Studies Of Transition Metal Carbonyl Clusters Using Laser Desorption Ionisation And Electrospray Ionisation Mass Spectrometry

Christopher Whyte

ABSTRACT

Transition metal carbonyls are frequently used as catalysts in organic synthesis, and it has been suggested that clusters of transition metal carbonyls can be used as models to study the reactions and processes that occur at the active sites of the catalyst. Large cluster species have been associated with molecular fragments of bulk material, and given their increased surface area should be more potent as catalytic species. However, the production of large multi-nuclear transition metal clusters by traditional synthetic methods can be quite complex.

In the work described in this thesis a different approach has been used. Stable, readily available, transition metal cluster carbonyl compounds, such as $Os_3(CO)_{12}$, $Ir_4(CO)_{12}$, $Rh_6(CO)_{16}$, have been shown to easily aggregate into multi-nuclear supraclusters following exposure to pulsed ultraviolet laser radiation (laser desorption ionisation, LDI) in the source region of a mass spectrometer. The aggregation process has been studied from the resulting mass spectra, using both of time-of-flight mass spectrometry (TOF MS) and Fourier transform ion cyclotron resonance mass spectrometry (FT-ICR MS). Larger cluster precursors tend to aggregate via the stepwise addition of whole metal cores, whereas the smaller tri-nuclear osmium cluster can produce supraclusters with variable numbers of metal atoms present. Interestingly, laser desorption/ionisation of $Os_3(CO)_{12}$ leads to the formation of prominent dodecaosmium cluster negative ions, such as $[Os_{12}(CO)_{23}]^-$. As far as we are aware, no homoleptic dodecaosmium carbonyl species has been prepared via traditional synthetic methods, highlighting the future potential of this approach if techniques for stabilising these complexes and isolating them can be developed. . The LDI spectra also exhibit prominent metastable decay products, corresponding to evaporative carbonyl ligand loss, a phenomenon known as post-source decay. The rates of metastable decay have then been determined for the mono-isotopic rhodium supraclusters.

In addition the transition metal carbonyl precursors used in the aggregation experiments have been studied by electrospray ionisation using quadrupole and Fourier transform ion cyclotron resonance mass spectrometers. In this case clusters require derivatisation with an alkoxide agent to produce a carbomethoxy ligand ($[COOCH_3]^-$) on the cluster, providing them with the necessary charge for mass spectrometric detection. The recently introduced technique of Energy Dependent Electrospray Ionisation mass spectrometry (EDESI-MS) has been used to investigate the relative strengths of the metal-to-carbonyl bonds using a process known as in-source collision-induced dissociation. From this data bond dissociation energies for the sequential removal of carbonyl ligands from the transition metal cluster precursor have been determined. FT-ICR MS experiments confirm the presence of a second decay channel leading to the formation of metal carbonyl hydride species, produced from the activation of the carbomethoxy ligand. Preliminary studies of these coordinatively unsaturated transition metal carbonyls with hydrocarbons have also been carried out.

For my Mother and Alison

It is not good to settle into a set of opinions. It is a mistake to put forth effort and obtain some understanding and then stop at that. At first putting forth great effort to be sure that you have grasped the basics, then practicing so that they may come to fruition is something that will never stop for your whole lifetime. Do not rely on following the degree of understanding that you have discovered, but simply think, "This is not enough."

Tsunetomo Yamamoto, *Hagakure: The Book Of The Samurai*.

Table Of Contents

1 Introduction

1.1 The Concept Of Clusters

Cluster species are a neutral or charged species in which there is a polycyclic array of atoms. These macromolecules may be either hetero- or homo-atomic, naked with no peripheral atoms, or contain a central core around which several ligands may be bonded [1]. A more precise definition of transition metal clusters was composed by Frank Albert Cotton, one of the early leading figures in cluster chemistry [2].

> *"Metal atom cluster compounds can be formally defined as those containing a finite group of metal atoms which are held together entirely, mainly, or at least to a significant extent, by bonds directly between the metal atoms even though some non-metal atoms may be associated intimately with the cluster."*

In the case of transition metal carbonyl clusters the associated non-metal atoms are the carbonyl ligands that surround the metal core.

A significant part of this thesis is concerned with large transition metal carbonyl clusters, with metal nuclearities frequently in excess of ten atoms, surrounded by a carbonyl ligand shell. Such species can be termed as *supraclusters.* The high nuclearity of supraclusters places them somewhere between the atomic/molecular and the bulk limits, and hence between the quantum mechanical control of molecules and the classical regime of large molecular or bulk material [3;4]. This is a problem in that one cannot simply predict the physical properties of supraclusters from the extrapolation of either of these models. Even smaller scale clusters with a total nuclearity of the order of 10 atoms cannot be accurately described by the quantum model, and complete computer simulations are notoriously difficult for transition metal clusters due to the high electron density and the complexities of the multiple filled d-electron shells.

Clusters are of great fundamental interest to both chemists and physicists who have high expectations of their unique position in the molecular scale giving them exotic physical properties. In addition they may also further the current understanding of

the relationship between molecular and condensed matter since clusters sit so comfortably between the two, allowing us to "*look at both ends from the middle*" [5].

There has been a great deal of research into the field of clusters, with perhaps the most notable highlight being the Award of the Nobel Prize in Chemistry in 1996 to Robert Curl Jr., Sir Harry Kroto, and Richard Smalley for the discovery of the third solid state of carbon: the spherical forms of C_{60} and C_{70}, better known as Buckminster Fullerenes, or "Bucky Balls" [6;7], from which more work has followed [8-13]. Despite this, the current knowledge and understanding of the properties of clusters in the way that they are formed and can subsequently react is at best incomplete, or at worst still unknown. Therefore cluster research continues apace so that the properties of these species can be determined and exploited.

1.2 Clusters As Catalysts

The exceptional size of cluster systems means that they have generated much interest in the field of catalysis where their surface area is estimated to be similar to that of active sites found on catalysts [14]. Indeed, it has been found in a number of cases that the geometry of clusters match the geometry of atoms on a bulk surface [15]. Thus many clusters have been used both as catalysts and as models for the active sites on catalysts: a topic that shall be covered in more detail in the following chapter. Some of the most prominent catalytic materials are the transition metals. Small transition metal clusters, stabilised by a carbonyl ligand shell, have found prominent use in the catalytic promotion of organic transformations due to their abilities to make and break hydrocarbon bonds as well as interact with other organic species [15-34].

Therefore transition metal carbonyl species have become a popular topic of research. However, the best-known transition metals with catalytic properties, such as platinum, are very expensive making the production of platinum clusters for experimentation quite costly. As such, interest has broadened to the examination of the properties of the other transition metals, but while small transition metal carbonyl

species can be bought commercially their manufacture can often be a demanding process.

1.3 Traditional Synthetic Methods Of Transition Metal Carbonyl Clusters

Conventional inorganic synthetic methods to generate transition metal clusters can be long and laborious, requiring several synthetic steps, and sometimes involving extreme temperatures or pressures. The basic premise is usually the same: the use of a fundamental precursor, or building block, to assemble a larger cluster molecule. Most of these precursors must also be synthesised. As an example, the synthesis of iron penta-carbonyl is documented in Equation 1-1, which involves high pressures and reasonable temperatures [16].

$$Fe + 5CO \xrightarrow{P=97\,atm,\quad T=150°C} Fe(CO)_5 \qquad (1\text{-}1)$$

From this point, there are two synthetic steps to generate a larger multi-nuclear cluster, tri-iron dodeca-carbonyl [16], as given in Equation 1-2.

$$Fe(CO)_5 \xrightarrow{NaOH^-} Na[HFe(CO)_4] \xrightarrow{MnO_2} Fe_3(CO)_{12} \qquad (1\text{-}2)$$

Two other examples of these mechanisms are given in Equation 1-3 [17] and Equation 1-4 [16].

$$RuCl_3.xH_2O + CO \xrightarrow{MeOH,\quad P=50\,atm,\quad T=400\,K} Ru_3(CO)_{12} \qquad (1\text{-}3)$$

$$\begin{matrix} 2CoCO_3 \\ +2H_2 + 8CO \end{matrix} \xrightarrow{CO,\quad P=290\,atm\quad T=130°C} \begin{matrix} Co_2(CO)_8 \\ +2CO_2 + 2H_2O \end{matrix} \qquad (1\text{-}4)$$

The use of high temperatures (a technique known as pyrolysis) and reducing agents induces ligand loss in the cluster. This generates small labile species suitable for the aggregation into larger clusters. While these methods are effective, the clusters that are produced are still relatively small, consisting mostly of metal dimers or trimers. The production of the large, multi-nuclear supraclusters is considerably more difficult by traditional inorganic synthetic methods. While the smaller clusters have been associated with properties as catalysts and the models of catalytic sites on

surfaces, little is known on the properties of larger transition metal carbonyl supraclusters since there have been few cases of their production in sufficient quantities to allow subsequent analysis. .

1.4 Novel Synthetic Routes To Transition Metal Carbonyl Clusters

The generation of labile species and their subsequent reaction can be attained by other, less traditional and often simpler, methods of synthesis. Such examples include the gas-aggregation source [35], which evaporates a metal into a reservoir of cooled carrier gas to induce single atom collisions to form clusters, typically in excess of 10000 atoms [36-44]. Another is the sputtering source [45], which produces a cluster ion beam through the bombardment of a metal with high-energy inert-gas atoms such as Xenon or Krypton. This technique can often produce clusters of around 100 atoms [46-49]. Finally there is the Pulsed Arc Cluster Ion Source (PACIS) [50], which uses a high current discharge to produce metal clusters from the degradation of the metal electrode [49;51-55]. While these techniques are successful in the generation of naked metal clusters, their usefulness for transition metal carbonyl clusters is unknown.

The use of a laser to generate clusters offers many advantages over these other sources. The laser can be used on mostly any species in any natural state, and it is only the species itself that is targeted, thus negating the need for furnaces and cooling systems required by the gas aggregation source. Indeed, there has already been much successful research performed on the viability of using lasers for the generation of metal [5;56-73] and transition metal carbonyl clusters [71;74-80]

The pulsed nature of the laser and the relative ease with which they can be interfaced to time-of-flight mass spectrometers provides an all in one production and detection system. Many time-of-flight systems have nitrogen laser desorption ionisation sources already fitted making laser assisted cluster aggregation undoubtedly the

quickest and easiest method to produce high nuclearity clusters [81]. There is an additional benefit in that there is already an extensive library of metal carbonyl complex precursors available for experimentation.

1.5 Properties Of Small Unsaturated Transition Metal Carbonyl Clusters

As stated previously, the smaller transition metal carbonyl clusters are known for their properties as catalysts and the associated models. Obviously such properties are only valid when the cluster is coordinatively unsaturated. Despite the obvious usefulness, there would appear to be little qualitative data on the metal-ligand binding energies for varying sizes of ligand shell. Such data could be of enormous use in assessing the viability of such clusters as catalysts and the production of stable clusters with a fixed size ligand shell. A recently developed and suitable technique for investigating this area is Energy Dependent Electrospray Ionisation Mass Spectrometry. This uses a systematic process of collision-induced dissociation to gradually remove the ligand shell from the cluster, producing a complete picture of the dissociation products and their relative stability and points of formation. The clusters must necessarily be charged prior to analysis, which is achieved by the derivatisation of the cluster with an organic nucleophilic agent. It should prove interesting to observe the stability and possible reactions between the saturated and unsaturated cluster and the organic derivativisation agent.

1.6 Aims Of The Thesis

There are two primary topics that this thesis wishes to address. Firstly the physical processes behind the aggregation and reactivity of transition metal supraclusters is to be explored. The first task therefore is to generate these supraclusters from a series of available smaller transition metal carbonyl clusters, utilising a laser field to induce

the aggregation reactions. It is hoped that a standard laser desorption ionisation source attached to a mass spectrometer will generate and analyse the supraclusters *in situ*, which may provide an insight into the method by which the aggregation reaction occurs. In addition the stability of the supraclusters shall also be studied, since an unstable cluster would not be a viable option as a catalyst. It therefore follows that the supraclusters be coordinatively unsaturated such that there is a suitable space in the surrounding ligand shell, and a vacant bonding site on the metal, for future reactants to bind to.

Secondly the properties of the smaller transition metal carbonyl clusters used as the precursors for the laser-induced aggregation reactions shall be investigated, using Energy Dependent Electrospray Ionisation Mass Spectrometry. This research should hopefully generate some useful information regarding the physical stability of the unsaturated clusters. It is further hoped that some quantitative values for the metal-ligand bond energies can be determined, as there currently exists little published data in this area. The reaction of the cluster with the derivatisation agent could also highlight the reactive properties of transition metal carbonyls with organic species.

1.7 Reference List

1. Housecroft, C. E. *Cluster Molecules of the p-block Elements*, 1st ed.; Oxford University Press Inc.: New York, 1994.

2. Cotton, F. A. *Quarterly Reviews of the Chemical Society* **1966**, *20*, 389-402.

3. Castleman, A. W.; Mark, T. D. *Gaseous Ion Chemistry and Mass Spectrometry*, John Wiley And Sons, Inc.: New York, 1986; 259-303.

4. Stein, G. B. *Physics Teacher* **1979**, *17*, 503.

5. Whetten, R. L.; Cox, D. M.; Trevor, D. J.; Kaldor, A. *Surface Science* **1985**, *156*, 8-35.

6. Kroto, H. W.; Heath, J. R.; O'Brien, S. C.; Curl, R. F.; Smalley, R. E. *Nature* **1985**, *318*, 162-163.

7. Kroto, H. W. *Nature* **1987**, *329*, 529-531.

8. Hare, J. P.; Kroto, H. W.; Taylor, R. *Chemical Physics Letters* **1991**, *177*, 394-398.

9. Hawkins, J. M.; Lewis, T. A.; Loren, S. D.; Meyer, A.; Heath, J. R.; Shibato, Y.; Saykally, R. J. *The Journal Of Organic Chemistry* **1990**, *55* , 6250-6252.

10. Meijer, G.; Bethune, D. S. *Chemical Physics Letters* **1990**, *175*, 1-2.

11. Pradeep, T.; Rao, C. N. R. *Materials Research Bulletin* **1991**, *26*, 1101-1105.

12. Wang, S.; Buseck, P. R. *Chemical Physics Letters* **1991**, *182* , 1-4.

13. Wilson, M. A.; Pang, L. S. K.; Willett, G. D.; Fisher, K. J.; Dance, I. G. *Carbon* **1992**, *30*, 675-693.

14. *Catalysis by di- and polynuclear cluster complexes*, John Wiley and Sons Inc: New York, 1998.

15. Dyson, P. J.; McIndoe, J. S. *Transition Metal Carbonyl Cluster Chemistry*, Gordon and Breach Science Publishers: 2000.

16. Bochmann, M. *Molecular Organometallics 1 Complexes with Transition Metal-Carbon σ-Bonds*, 3rd ed.; Oxford University Press: Avon, 1999.

17. Housecroft, C. E. *Metal-Metal Bonded Carbonyl Dimers and Clusters*, 1st ed.; Oxford University Press Inc.: New York, 1995.

18. Agrawal, M. C.; Upadhyay, S. K. *Journal Of Scientific and Industrial Research* **1983**, *42*, 508-517.

19. Fukuoka, A.; Kosugi, W.; Morishita, F.; Hirano, M.; McCaffrey, L.; Henderson, W.; Komiya, S. *Chemical Communications* **1999**, 489-490.

20. Heiz, U.; Sanchez, A.; Abbet, S.; Schneider, W.-D. *Chemical Physics* **2000**, *262*, 189-200.

21. Kaneda, K.; Fujita, K.; Takemoto, T.; Imanaka, T. *Bulletin Of The Chemical Society Of Japan* **1991**, *64*, 602-612.

22. Kaneda, K.; Mizugaki, T. *Organometallics* **1996**, *15*, 3247-3249.

23. Lewis, L. N. *Chemistry Reviews* **1993**, *93*, 2693-2730.

24. Sánchez-Delgado, R. A.; Andriollo, A.; Puga, J.; Martín, G. *Inorganic Chemistry* **1987**, *26*, 1867-1870.

25. Weber, W. A.; Gates, B. C. *Journal Of Catalysis* **1998**, *180*, 207-217.

26. Yamamoto, S.; Lewis, R. M.; Nabata, Y.; Hotta, H.; Kuroda, H. *Inorganic Chemistry* **1990**, *29*, 4342-4344.

27. Oiestad, A. M. L.; Uggerud, E. *Chemical Physics* **2000**, *262*, 169-177.

28. Anstock, M.; Taube, D.; Gross, D. C.; Ford, P. C. *Journal of the American Chemical Society* **1984**, *106*, 3696-3697.

29. Geusic, M. E.; Morse, M. D.; Smalley, R. E. *Journal of Chemical Physics* **1985**, *82*, 590-591.

30. Gross, D. C.; Ford, P. C. *Journal of the American Chemical Society* **1982**, *21*, 1702-1704.

31. Gross, D. C.; Ford, P. C. *Journal of the American Chemical Society* **1985**, *107*, 585-593.

32. Kaldor, A.; Cox, D. M. *Journal of the Chemical Society Faraday Transactions* **1990**, *86*, 2459-2463.

33. Riley, S. J. *Berichte der Bunsen-Gesellschaft fur Physikalische Chemie*, *96*, 1104-1109.

34. Trautman, R. J.; Gross, D. C.; Ford, P. C. *Journal of the American Chemical Society* **1985**, *107*, 2355-2362.

35. Sattler. *Physical Review Letters* **1980**, *45*, 821.

36. Abe, H.; Schulze, W.; Tesche, B. *Chemical Physics* **1980**, *47* , 95-104.

37. Brechignac, C.; Cahuzac, P.; Leygnier, J.; Tigneres, I. *Chemical Physics Letters* **1999**, *303*, 304-310.

38. Frank, F.; Schulze, W.; Tesche, B.; Urban, J.; Winter, B. *Surface Science* **1985**, *156*, 90-99.

39. Koga, K.; Sugawara, K. *Surface Science* **2003**, *529*, 23-35.

40. Mahoney, W.; Andres, R. P. *Materials Science and Engineering A* **1995**, *204*, 160-164.

41. Min, H.; Zhaoye, W.; Pingping, C.; Shengwen, Y.; Guanghou, W. *Nuclear Instruments and Methods in Physics Research Section B: Beam Interactions with Materials and Atoms* **1998**, *135*, 564-569.

42. Xenoulis, A. C.; Trouposkiadis, P.; Potiriadis, C.; Papastaikoudis, C.; Katsanos, A. A.; Clouvas, A. *Nanostructured Materials* **1996**, *7*, 473-486.

43. Yamada, Y.; Castleman, J. *Chemical Physics Letters* **1993**, *204*, 133-138.

44. Yamada, Y.; Deng, D. H.; Snyder, E. M.; Castleman, J. *Chemical Physics Letters* **1993**, *203*, 330-336.

45. Woste. *Physics Review B* **1986**, *33*, 6792.

46. Greene, J. P. *Nuclear Instruments and Methods in Physics Research Section A: Accelerators, Spectrometers, Detectors and Associated Equipment* **2002**, *480*, 119-123.

47. Ishii, K.; Amano, K.; Hamakake, H. *Journal of Vacuum Science & Technology A-Vacuum Surfaces and Films* **1999**, *17*, 310-313.

48. Kanter, M. *Nuclear Instruments & Methods in Physics Research Section B- Beam Interactions with Materials and Atoms* **1992**, *70*, 200-204.

49. Yoshida, Y.; Ohnishi, T.; Hirofuji, Y.; Ikeda, T. *Review of Scientific Instruments* **1990**, *61*, 598-600.

50. Siekmann, H. R.; Luder, C.; Faehrmann, J.; Lutz, H. O.; Meiwes-Broer, K. H. *Zeitschrift fur Physik D-Atoms Molecules and Clusters* **1991**, *20* , 417-420.

51. Blessing, N.; Burkart, S.; Gantefor, G. *European Physical Journal D* **2001**, *17*, 37-41.

52. Gantefor, G.; Siekmann, H. R.; Lutz, H. O.; Meiwes-Broer, K. H. *Chemical Physics Letters* **1990**, *165*, 293-296.

53. Gantefor, G.; Siekmann, H. R.; Lutz, H. O.; Meiwes-Broer, K. H. *Chemical Physics Letters* **1990**, *165*, 293-296.

54. Klipp, B.; Grass, M.; Muller, J.; Stolcic, D.; Lutz, U.; Gantefor, G.; Schlenker, T.; Boneberg, J.; Leiderer, P. *Applied Physics A-Materials Science & Processing* **2001**, *73*, 547-554.

55. Lu, W. Y.; Huang, R. B.; Ding, J. Q.; Yang, S. H. *Journal of Chemical Physics* **1996**, *104*, 6577-6581.

56. Alford, J. M.; Williams, P. E.; Trevor, D. J.; Smalley, R. E. *International Journal of Mass Spectrometry and Ion Processes* **1986**, *72*, 33-51.

57. Arzumanian, G. M.; Bogdanov, D. D.; Bykowsky, Y.; Rodin, A. M.; Silnov, S. M.; Ter akopian, G. M. *International Journal of Mass Spectrometry and Ion Processes* **1985**, *64*, 255-264.

58. Faust, P.; Brandstattner, M.; Ding, A. *Biomedizinische Technik.Biomedical Engineering* **1990**, *35*, 225-226.

59. Freiser, B. S. *Talanta* **1985**, *32*, 697-708.

60. Freiser, B. S. *Analytica Chimica Acta* **1985**, *178*, 137-158.

61. Giardini-Guidoni, A.; Teghil, R.; Mele, A. *Spectrochimica Acta Part A: Molecular Spectroscopy* **1990**, *46*, 503-504.

62. Gord, J. R.; Buckner, S. W.; Freiser, B. S. *Chemical Physics Letters* **1988**, *153*, 577-582.

63. Jentsch, T.; Drachsel, W.; Block, J. H. *International Journal or Mass Spectrometry and Ion Physics* **1981**, *38*, 215-222.

64. Loh, S. K.; Hales, D. A.; Armentrout, P. B. *Chemical Physics Letters* **1986**, *129*, 527-532.

65. Mark, T. D. *International Journal of Mass Spectrometry and Ion Processes* **1987**, *79*, 1-59.

66. Mele, A.; Consalvo, D.; Stranges, D.; Giardini-Guidoni, A.; Teghil, R. *Applied Surface Science* **1989**, *43*, 398-401.

67. Melinon, P.; Monot, R.; Zellweger, J.-M.; van den Bergh, H. *Chemical Physics* **1984**, *84*, 345-358.

68. Moini, M.; Eyler, J. R. *Chemical Physics Letters* **1987**, *137* , 311-314.

69. Rastopov, S. F.; Sukhodol'sky, A. T. *Physics Letters A* **1990**, *149*, 229-232.

70. Döppner, T.; Teuber, S.; Schumacher, M.; Tiggesbäumker, J.; Meiwes-Broer, K. H. *International Journal of Mass Spectrometry* **1999**, *192* , 387-391.

71. Duncan, M. A.; Dietz, T. G.; Smalley, R. E. *Journal of the American Chemical Society* **1981**, *103*, 5245-5246.

72. Smirnov, M. B.; Krainov, V. P. *Physica Scripta.* **2001**, *63*, 157-163.

73. Teghil, R.; Giardini-Guidoni, A.; Piccirillo, S.; Mele, A.; Polla-Mattiot, F. *Applied Surface Science* **1990**, *46*, 220-224.

74. Critchley, G.; Dyson, P. J.; Johnson, B. F. G.; McIndoe, J. S.; O'Reilly, R. K.; Langridge-Smith, P. R. R. *Organometallics* **1999**, *18*, 4090-4097.

75. Dale, M. J.; Dyson, P. J.; Johnson, B. F. G.; LangridgeSmith, P. R. R.; Yates, H. T. *Journal Of The Chemical Society-Dalton Transactions* **1996**, 771-774.

76. Dyson, P.; Johnson, B. F. G.; McIndoe, J. S.; Langridge-Smith, P. R. R. *Inorganic Chemistry* **2000**, *39*, 2430-2431.

77. Dyson, P. J.; Hearley, A. K.; Johnson, B. F. G.; McIndoe, J. S.; Langridge-Smith, P. R. R. *Inorganic Chemistry Communications* **1999**, *2*, 591-594.

78. Dyson, P. J.; McGrady, J. E.; Reinhold, M.; Johnson, B. F. G.; McIndoe, J. S.; Langridge-Smith, P. R. R. *Journal Of Cluster Science* **2000**, *11*, 391-401.

79. Jackson, P.; Fisher, K. J.; Dance, I. G.; Gadd, G. E.; Willett, G. D. *Journal Of Cluster Science* **1992**, *13*, 165-187.

80. Lee, G. H.; Huh, S. H.; Jung, H. I. *Journal of Molecular Structure* **1998**, *440*, 141-145.

81. Lee, G. H.; Huh, S. H.; Jung, H. I. *Journal of Molecular Structure* **1998**, *440*, 141-145.

2 Transition Metal Carbonyl Clusters

2.1 Introduction

The field of organometallic chemistry has been one of the most rapidly developing areas of inorganic chemistry over the last 40 years, proving itself to be of fundamental interest to the understanding and development of catalysts and their behaviour, as well as the generation of new synthetic methods and materials [1]. A large part of this work has focussed on the generation and properties of organometallic clusters. There is much expected of these clusters due to the properties displayed by *d*-block metals within molecular surfaces and solid state systems. For instance the bulk surface of transition metals are well noted for their high, metal-specific, catalytic activity for the transformation of organic molecules [2;3]. In addition organometallics are renowned for their variable oxidation states and their optical/photochemical properties [2].

In comparison to such clusters as C_{60}, which consist only of skeletal atoms, transition metal clusters in the condensed phase are most often surrounded by a stabilising shell of ligands, the size of which can vary depending upon the cluster species at hand. Various ligands can be used [4], but this work shall be focussing on transition metal clusters surrounded by a shell of carbonyl ligands.

2.2 General Properties Of Transition Metal Carbonyl Clusters

2.2.1 Structure

A triangular network of metal atoms is the most common basic unit found in many transition metal clusters which can be built into complex three-dimensional polyhedra [5]. Above six metal atoms, the geometry of the cluster cores tend to be composed of condensed tetrahedral and octahedral sub-clusters, with an increase in the occurrence of metal capping of polyhedron faces [6]. This is a direct consequence of the properties of the metal trigonal unit. The bonding between metal atoms is not

purely confined to the edges but can also occur within the trigonal array itself, leading to capping. In a trigonal array there is a degree of orbital overlap at the centre allowing the bonding of a metal atom to the face of the trigoanl array [5]. This is not always spatially possible with square arrangements of atoms.

There is an observed tendency for finite metal clusters to adopt close-packed structures [5]. As the metal nuclearity increases from double figures, the metal atoms have been observed to be arranged in such a way as to resemble a fragment from of a bulk metal lattice with a variety of close packing structures (such as body-centred cubic, hexagonal close-packed, and cubic close-packed lattices) [6]. This can be directly observed from the cluster $[Rh_{13}(CO)_{24}H_{5-n}]^{n-}$ (n=2,3) [7]. The structure of this cluster features a central rhodium atom surrounded by a dodecahedron of 12 rhodium atoms, a structure that corresponds to the smallest possible unit of a close-packed structure. It can therefore be seen that relatively small transition metal clusters can soon approximate the form of their bulk analogues. This also demonstrates that the metal skeleton of a cluster can be regarded as approximating a round surface [5].

The size of the cluster, in terms of the number of constituent metal atoms, defines many of the cluster's properties. Small transition metal carbonyl clusters are more akin to discrete molecular fragments, where nearly all of the metal atoms are on the surface of the metal core. As the clusters become larger, there will be a corresponding increase in the number of metal atoms that lie beneath the surface, bonded only to other metals. Nonetheless, for transition metal carbonyl clusters with approximate metal nuclearities of 100 atoms or less the majority of the metal atoms will be on, or very near to, the surface [2]. Thus larger transition metal carbonyl clusters are likely to have a larger metal-to-ligand ratio than the much smaller clusters, owing to the larger number of purely metal-metal bonds that exists in the larger clusters.

The formal coordination of metal atoms in clusters is variable and unusually high. The metal-metal bonds have a partially metallic character, such that they cannot be represented by directional vector bonds (2-electron sharing) [5]. This leads to an

unsymmetrical distribution of bonds around the metal centres, permitting the formation of the rounded structures observed for the larger metal clusters. The metallic character of the metal-metal bonds increases as the cluster core becomes larger; the valence electrons of the metal atoms are not localised at each metal atom, but instead belong to the entire cluster as a whole. Therefore the cluster can be thought of being constructed from an array of positive metal ions immersed in a sea of mobile free-electrons [8]. Correspondingly an increased number of metal atoms become the overwhelming source of valence electrons to the cluster system, and so those provided by ligands are less important to the structural integrity of the cluster. It is regarded that the chemical properties of the smaller clusters are governed by the effects determining the stability of the cluster [2;9]; i.e. the clusters are most stable when fully ligated, such that their coordination sites are saturated, limiting their possible reactivity. Conversely, the larger clusters, which appear as relatively more unsaturated species, are more likely to show reactive properties.

The nature of these unsymmetrical bonds within transition metal carbonyl clusters limits the ability to determine *a priori* possible structures of given cluster configurations. While the system may seem relatively simple, with its finite number of metal atoms, the bonding is complicated by the interactions among the combinations of σ, π, and π^* orbitals of the carbonyl ligands with the suitable combinations of the metal orbitals. Such techniques as Linear Combination of Atomic Orbitals – Molecular Orbitals (LCAO-MO) are made incredibly complicated by the sheer number of independent parameters that these bonding formalisms create. In addition, only the smallest of clusters with three of four metal atom cores are known to consistently obey the 18-electron rule: the configuration that gives each metal atom a filled valence shell, similar to that of the inert gases [5]. Various theoretical models have been conjectured to determine cluster structures, the most well-known being Wade's rules, also known as Polyhedral Skeletal Electron Pair Theory (PSEPT). The rules are composed from formal analogies between the electronic structures of carboranes and polyboranes and those of metal carbonyl clusters [10]. However, all of the models have their own restrictions and so

characterisation of cluster species is best performed from direct measurement and comparison with known structures.

2.2.2 Reactivity

As the first transition metal carbonyl clusters were prepared and isolated in the laboratory they were discovered to have useful reactive properties, the most prominent being their ability to allow ligands to become bonded to multiple metal centres, allowing for the weakening and subsequent cleavage of the bridging bond (as discussed in Chapter 1.2). This property has the potential to be used n catalysing specific organic reactions, such as the Fischer-Tropsch reaction, which converts mixtures of carbon monoxide and hydrogen (also known as '*synthesis gas*') into hydrocarbons. The conversion of carbon monoxide into hydrocarbons first requires the cleavage of the carbon-oxygen bond, followed by the addition of hydrogen and the formation of bonds between other, similarly cleaved, carbon monoxide molecules. The formed product is then removed into the gas phase by hydrogenolysis. A depiction of the reaction scheme is given below in Figure 2-1 [1].

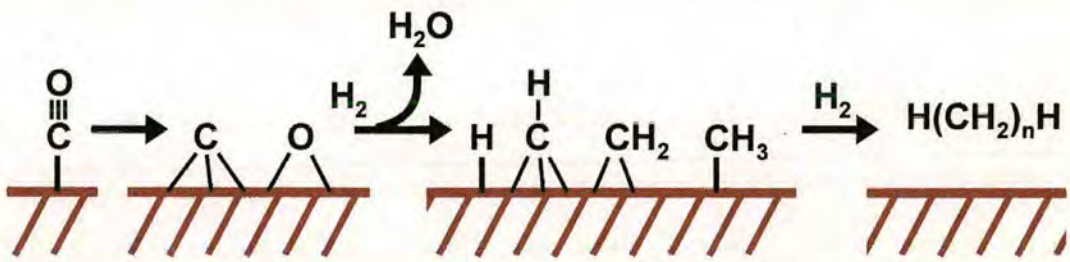

Figure 2-1 The progression of the Fischer-Tropsch reaction on a surface. Diagram adapted from Reference 1.

Transition metal carbonyl clusters have been instrumental in the elucidation of the process by which this reaction is heterogeneously catalysed by iron or ruthenium under high temperature and pressure, from analogies made between the absorption of carbon monoxide onto bulk metal surfaces and ligated transition metal carbonyl clusters. Indeed it has been suggested that organometallic cluster species can be regarded as models for transition metal surfaces, being used as a means to explore the mechanism of catalytic reactions [2;11-13]. This is known as the cluster-surface

analogy. It is presumed that the surface of a bulk material can be shown to consist of combinations of discrete cluster units, as shown below in Figure 2-2. Unfortunately, the veracity of this analogy has not been wholly confirmed by experimental evidence [2]. This is in many ways due to the saturated nature of the clusters since they are surrounded by a stabilising ligand shell. The catalytic properties of the metal surfaces are present due to the their unsaturated nature, giving a number of vacant sites for the bonding and subsequent manipulation of organic and other species. The question is now one of producing unsaturated clusters that can be experimented upon. Stable coordinatively unsaturated metal species are not readily synthesised from scratch, and so the practical alternative is to remove ligands from a saturated cluster, something that will be attempted in Chapter 6.

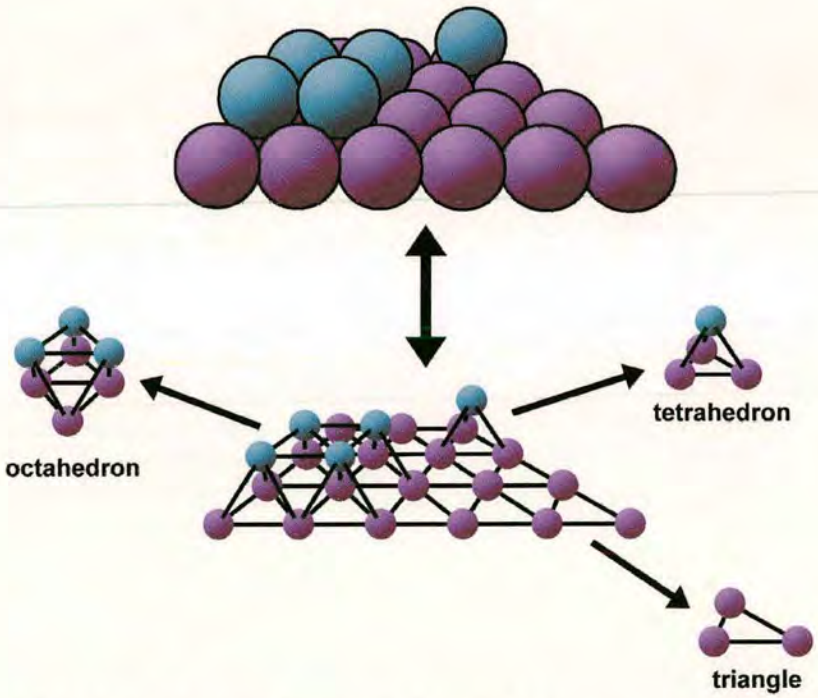

Figure 2-2 A depiction of a bulk surface, from which several small transition metal cluster cores can be found amongst the array of metal atoms. Diagram adapted from Reference 4

2.3 Clusters Under Study

Three small transition metal carbonyl clusters are used throughout the work presented in this thesis, used as both precursor species for laser-induced aggregation experiments, and investigated in a series of collision-induced dissociation experiments to probe the properties of unsaturated cluster species. These clusters are tetrairidium dodecacarbonyl, $Ir_4(CO)_{12}$, triosmium dodecacarbonyl, $Os_3(CO)_{12}$, and hexarhodium hexadecacarbonyl, $Rh_6(CO)_{16}$.

2.3.1 Tetrairidium Dodecacarbonyl

The structure of $Ir_4(CO)_{12}$ was first accurately determined in 1978 by Churchill and Hutchinson [14]. The structure is shown below in Figure 2-3.

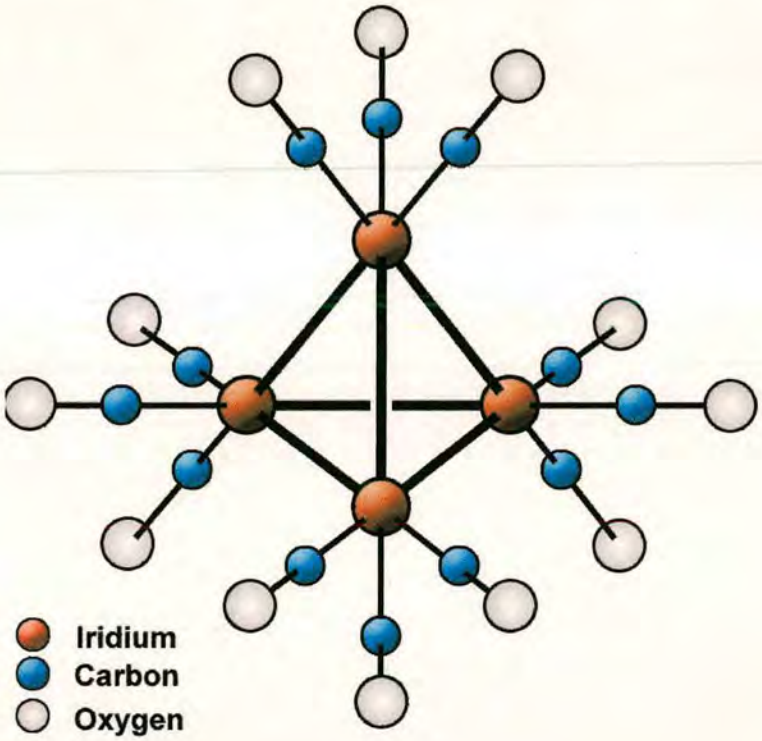

Figure 2-3 The XRD structure of $Ir_4(CO)_{12}$. Diagram adapted from Reference 14.

This structure features a regular tetrahedral arrangement of iridium metal atoms, with the arrangement of carbonyl ligands around the core giving the cluster T_d symmetry.

Unfortunately, this structure is not the only geometry the cluster can adopt. In the solid state crystal form the cluster exhibits small quantities of several other disordered states, the structure of which differs greatly from this form [14]. Since this behaviour appears to be associated only with the condensed phase structure of the species, one can assume that the desorbed species produced for all of the gas-phase experiments will adopt the above, most common geometry.

The chemistry of polynuclear iridium carbonyl clusters has not been studied in any great degree of detail previously[5], presenting the oppurtunity to possibly explore some uncharted chemistry of this species.

2.3.2 Triosmium Dodecacarbonyl

The solid state structure of the $Os_3(CO)_{12}$ cluster was determined by X-ray crystallography to have the form given in Figure 2-4 by Churchill and DeBoer [15].

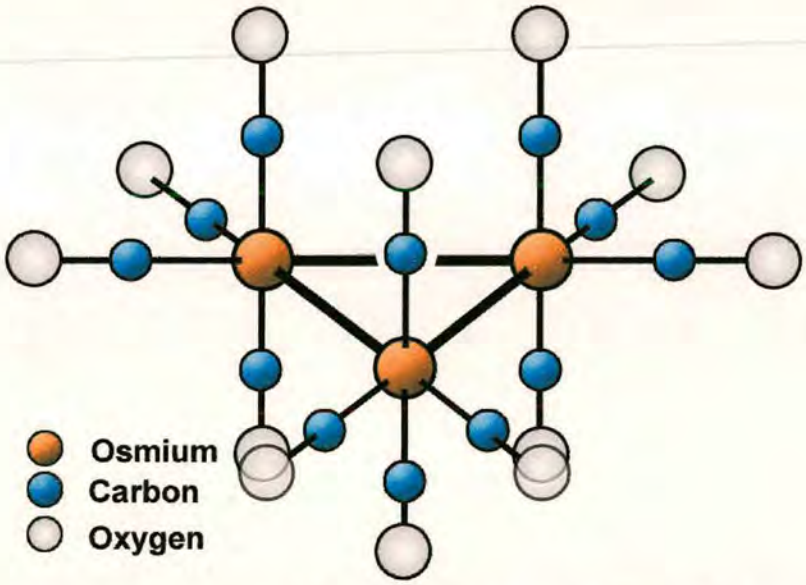

Figure 2-4 The XRD structure of $Os_4(CO)_{12}$. Diagram adapted from Reference 15.

The cluster features a trigonal arrangement of metal atoms surrounded by the carbonyl ligand shell. Osmium has previously been used as a precursor for larger

cluster aggregates in pyrolysis experiments [5;16], and so should prove to be potent in the laser-induced aggregation experiments.

2.3.3 Hexarhodium Hexadecacarbonyl

The cluster $Rh_6(CO)_{16}$ was correctly identified in 1963 by Corey and Dahl, after the species had previously been identified as $Rh_4(CO)_{11}$ [17]. The solid state structure of the cluster, as determined from crystallographic methods is shown in Figure 2-5.

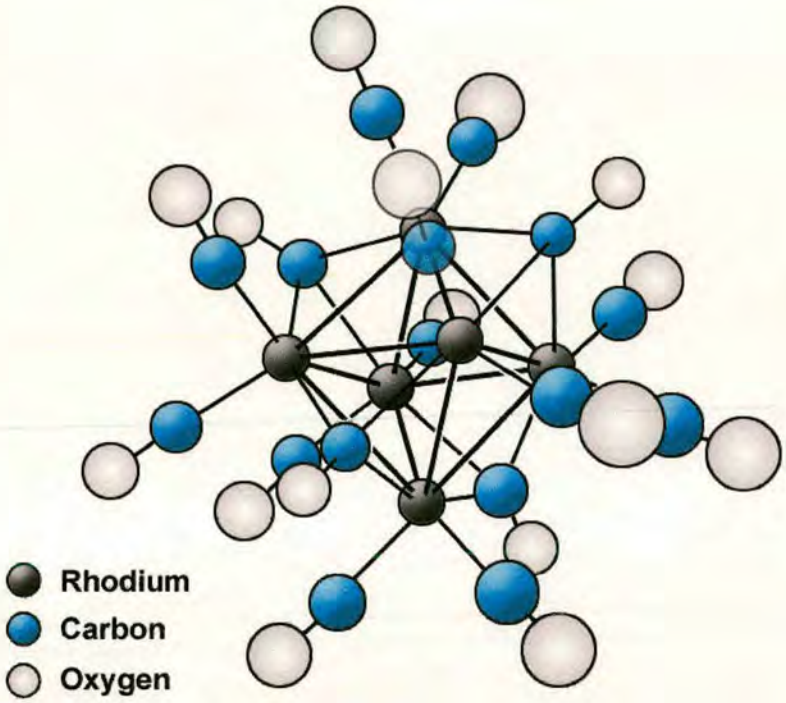

Figure 2-5 The XRD structure of $Rh_6(CO)_{16}$. Diagram adapted from Reference 17.

This structure is rather more complicated than those of the previous structures. The metal core is a regular octahedral arrangement of rhodium metal atoms. There are four capping carbonyl ligands on the faces of the octahedral, arranged such that they directed towards the vertices of a tetrahedron. The remaining 12 carbonyl ligands are terminal [17]. The overall arrangement gives an icosohedral arrangement of oxygen atoms around the central metal octahedral core [5]. In direct contrast to the previous clusters, the chemistry of this rhodium cluster has been much more thoroughly

examined. For a review the reader is directed towards an excellent, albeit slightly dated review in Reference 5.

2.4 Preparing Transition Metal Carbonyl Clusters For Electrospray Ionisation Mass Spectrometry

A feature of the work presented in this thesis is the analysis of the above clusters using electrospray ionisation as a means to introduce the ions into a mass spectrometer, as reviewed in Chapter 3.4.2. This requires the clusters to be in the form of ions in a non-volatile solution before they can be analysed. However, the transition metal carbonyl species under study are all in the zero oxidation state and carry no net charge. The saturation of the clusters means that it is very difficult to ionise any one of the metal atoms in the core. While it is possible to protonate transition metal carbonyl species in the gas phase (via the reaction of the species with a suitable proton donor such as methane under electron bombardment conditions [18;19]) such a reaction is made more difficult in solution chemistry. This is due to the low Brønsted acidity/basicity of the carbonyl ligands. Thus, traditional methods of solution phase protonation using an acetonitrile/water solution do not work for the transition metal carbonyl clusters.

Thus an alternative method of ionisation is through a ligand substitution reaction, replacing one of the carbonyl ligands with a charged adduct. The problem with ligand substitution is the effect it may have on the cluster itself. An alteration to the electron arrangement within the cluster can, and often will, have a direct effect on its chemistry. How this change would manifest itself is something that could only be explored by experimentally comparing the chemistry and physical properties between the neutral transition metal carbonyl cluster and the substituted cluster. For the purposes of this thesis it would be better to not significantly "corrupt" the cluster by altering its composition and instead have a charge placed on the solvated clusters by some means that invokes as little physical change to the cluster as possible. One

possible method is to exploit the physical properties of the carbonyl ligands themselves.

2.4.1 Alkoxylation of Transition Metal Carbonyl Clusters

Carbon has a Pauling electronegativity of 2.5, whereas oxygen has a value of 3.5 [20]. Thus the oxygen pulls more of the electron density towards it, making the carbon slightly positive. A nucleophilic attack on the carbon by an anionic adduct would then provide the necessary charge required for electrospray analysis, and should hopefully have a less significant effect on the chemistry of the cluster compared to direct ligand substitution. Such reactions are well known in transition metal carbonyl chemistry [5]. One such suitable adduct is an alkoxide anion, OR^-, where the R represents a hydrocarbon.

The addition reaction of an alkoxide anion to a carbonyl ligand is a well-known reaction in organometallic chemistry. The late Paolo Chini and his group were principally responsible for the characterisation of novel organometallic species in the seventies, including the production and crystallographic identification of transition metal carbonyl systems with an activated carbonyl through the addition of alkoxides and other reagents [5;21;22]. This early work was then capitalised upon by the work of D.C. Gross and P.C. Ford in the early eighties. The focus of their research was the investigation of the water gas shift reaction (WGSR), the industrial generation of hydrogen from carbon monoxide and steam, as given in Equation 2-1 [1].

$$CO_{(g)} + H_2O_{(g)} \longrightarrow CO_{2(g)} + H_{2(g)} \qquad (2\text{-}1)$$

In particular, they investigated the possible catalytic properties of transition metal carbonyl systems, ranging from a single metal atom core to cluster sized systems, towards this reaction. It had been proposed that the nucleophilic activation of a carbonyl ligand played an integral role in WGSR catalysis, and thus the chemistry of the addition of nucleophilic reagents such as alkoxides was comprehensively investigated [23-28;28].

Some ten years later, the scope for using the nucleophilic activation of a coordinated carbonyl ligand was used as a means to permit the study of transition metal carbonyls

by electrospray ionisation mass spectrometry by Henderson *et al.* Organometallic species had previously been analysed by electrospray ionisation mass spectrometry, but for the most part they did not feature carbonyl ligands and were cations taken from organometallic salts [29]. Henderson's group implemented the first reported analysis of nucleophilically activated transition metal carbonyl cluster systems by electrospray ionisation mass spectrometry via their derivatisation with methoxide [30].

2.4.2 A Closer Look At Methoxide Derivatisation – Making The Carbomethoxy Ligand

The production of an alkoxide anion is a relatively simple affair. In the case of simple alcohols, for example methanol and ethanol, the addition of an alkali metal such as sodium, can promote the formation of the basic alkoxide anion as shown for methanol in Equation 2-2.

$$2Na_{(s)} + 2CH_3OH_{(l)} \longrightarrow 2\left[Na^+\right]\left[OCH_3^-\right]_{(l)} + H_{2(g)} \qquad (2\text{-}2)$$

The addition of sodium methoxide, $NaOCH_3$, to a non-aqueous solution of the transition metal carbonyl cluster has been shown to only nucleophilically attack one of the coordinated carbonyls on a variety of different cluster species [23;24;27;28], including $Ir_4(CO)_{12}$ [31], $Os_3(CO)_{12}$ [26], and $Rh_6(CO)_{16}$ [32], regardless of changes in relative concentrations. The reaction is rapid and thermodynamically favoured in all cases. Infrared spectroscopy on species derivatised with sodium methoxide, including $Os_3(CO)_{12}$, displayed stretching frequencies consistent with the presence of a CO_2CH_3 group, known as a carbomethoxy ligand, and a negative charge [26]. Thus the methoxide adduct is directly bonded to the carbon on the carbonyl ligand as shown in Figure 2-6.

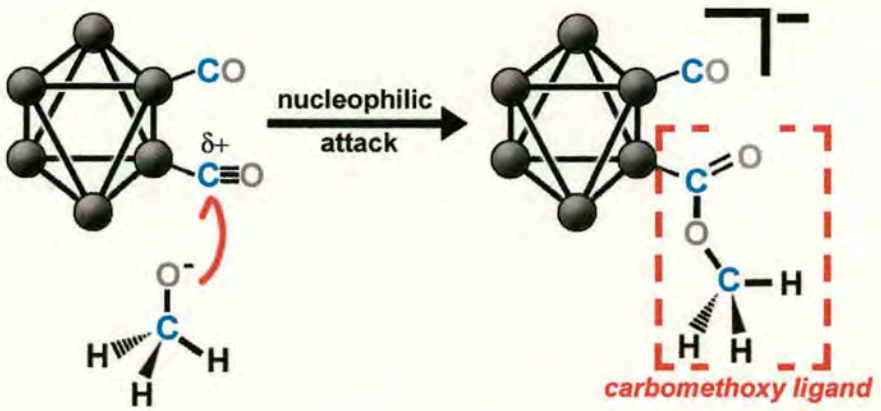

Figure 2-6 An example of the derivatisation of a transition metal cluster by the nucleophilic attack of the methoxide anion towards a coordinated carbonyl ligand, creating the carbomethoxy ligand as shown. The overall effect is to leave the cluster with a negative charge.

The formation of the bonds between the methoxide nucleophile, the carbonyl ligand and the metal must be determined to judge the effect the carbomethoxy ligand has on the physical and chemical properties of the cluster. One could try and determine the molecular orbitals formed from the addition of these species, but such a process would be very time consuming and very awkward due to the lack of symmetry within the final product. An alternative is to break down the problem into a series of stages:

1. The methoxide anion;
2. The carbonyl ligand;
3. The addition of the methoxide to the carbonyl.

The Methoxide Anion

The bonding within the methoxide anion can be understood by splitting the species up into two parts, the methyl group and its bond with the oxygen. The structure of the methyl group is similar to the planar boron tri-hydride molecule: two *2p* orbitals (p_x and p_y) and the single *2s* orbital of the carbon, shown in Figure 5-2a) combine to form three sp^2 hybridised orbitals [33;34]as shown in Figure 2-7 b) [34]. The sp^2 orbitals then bond to the *s* orbitals of the hydrogen, Figure 2-7 c).

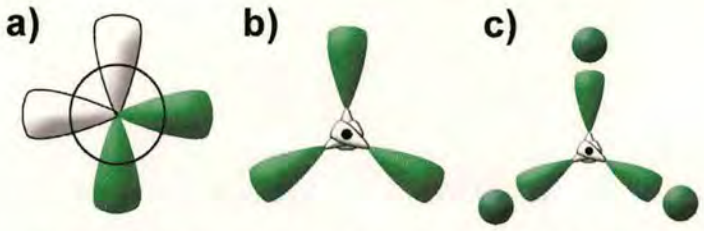

Figure 2-7 a) The unhybridised *2s* and two *2p* orbitals of carbon. b) The sp^2 hybridised orbitals of carbon. c) The overlap between the sp^2 and hydrogen *1s* orbitals.

The molecular orbital diagram for methyl is shown in Figure 2-8. The possible combinations of hydrogen 1*s* orbitals around the carbon have been built from symmetry-adapted orbitals. The diagram reveals that the $2p_z$ orbital of the carbon is non-bonding and partially filled. This orbital is of the correct geometry to bond to one of the partially filled 2*p* orbitals of an oxygen atom (electron arrangement $1s^2\,2s^2\,2p^4$) via a p-σ bond as depicted in Figure 2-9. Finally, the methoxide is anionic, and the additional electron can be accommodated in the last remaining partially filled oxygen 2*p* orbital, giving the oxygen a full complement of 2*p* electrons. The presence of the oxygen also acts to slightly push the hydrogen bonds down and out of the plane.

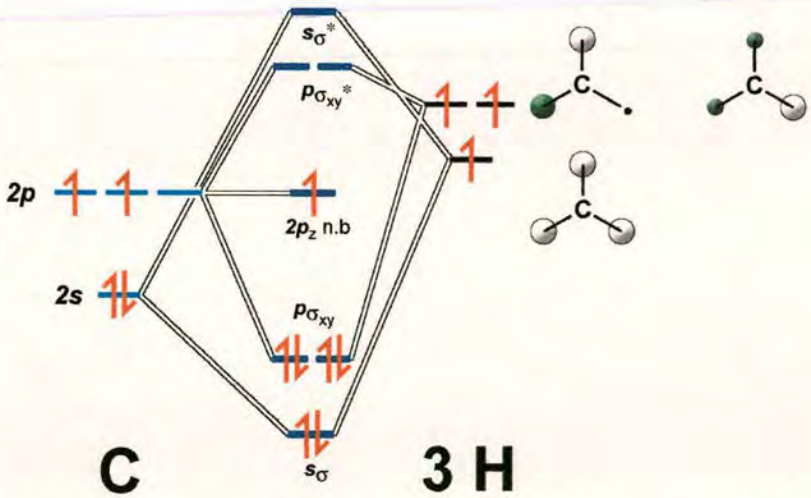

Figure 2-8 The molecular orbital diagram of the methyl group. The various symmetry adapted hydrogen orbitals are also shown. Although this diagram does not account for the sp^2 hybridisation the overall effect is the same, with the $2p_z$ non-bonding orbital containing a single electron. Diagram adapted from Reference 34.

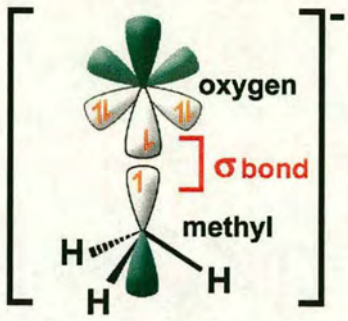

Figure 2-9 The methoxide anion, as constructed from the addition of oxygen to a sp^2 hybridised methyl group. Due to the electron sharing in the bond between the methyl and the oxygen and the negative charge the oxygen of the methoxide has a full 2*p* shell.

The Carbonyl Ligand

The molecular bonding diagram for an uncoordinated carbonyl ligand, is shown in Figure 2-10 [1;34]. The overall bond order of the carbon-to-oxygen bond is three from the combination of the electron pair in the two σ bonds and the two π bonds, and the subtraction of the $s\sigma^*$ anti-bonding electron pair.

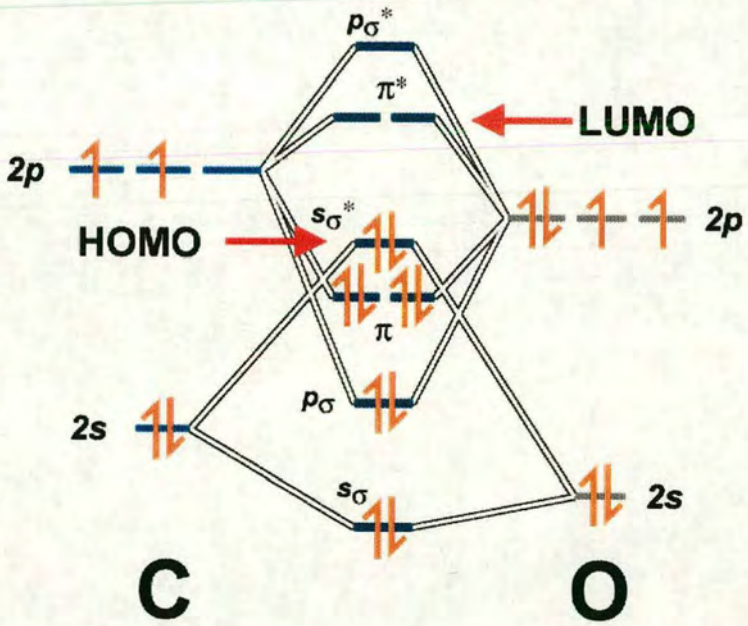

Figure 2-10 The molecular bond energy level diagram for free carbon monoxide. The lowest unoccupied molecular orbital (LUMO) and the highest occupied molecular orbital (HOMO) are indicated on the diagram.

The $s\sigma^*$ electron pair is situated on the carbon atom, and is used to form a *dative* σ bond to a metal coordination site in a metal carbonyl complex [1], as depicted in Figure 2-11a). The anti-bonding π^* orbitals are of a suitable geometry to accept electrons from occupied metal *d* orbitals, an occurrence known as *back-bonding*, which has the overall affect of increasing the strength of the metal-to-carbonyl bond, depicted for one of the π^* orbitals in Figure 2-11b). The back-bonding strengthens the bond to the metal at the expense of the carbon-to-oxygen bond, which is weakened due to the acceptance of electron density into anti-bonding orbitals thereby lowering the bond order. It should be noted that in a transition metal carbonyl cluster orbital hybridisation shall also occur, since localised bonding schemes cannot account for the number of bonds supported by one metal atom and the geometry of the cluster as a whole. The ratio of orbital mixing in the hybridisation is dependent upon the number of bonds and the geometry. For example both $Ir_4(CO)_{12}$ and $Os_3(CO)_{12}$ feature metal atoms bonded to six other species. The *s* and *p* orbitals can only provide four bonds so two *d* orbitals must be included to produc d^2sp^3 hybridised orbitals. For $Rh_6(CO)_{16}$ each metal centre is fully bonded to six other species, while sharing a carbonyl ligand with two other metal atoms (the capping carbonyl ligands). Thus the choice of hybridised orbitals is made somewhat more difficult since the bonding character is between d^2sp^3 and d^3sp^3 orbitals. However, for ease of illustration of the dative and back-bonding, Figure 2-11 shows only normal *d* orbitals

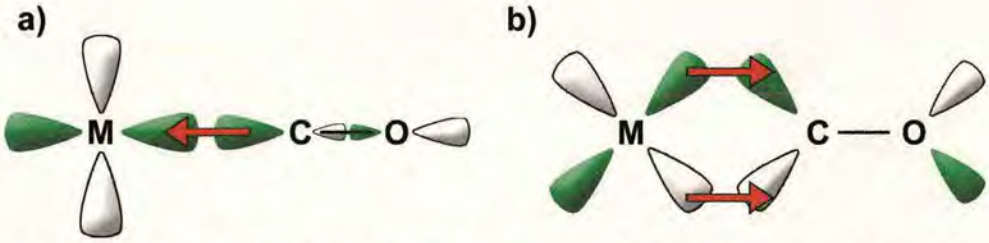

Figure 2-11 a) This shows the dative bond, with the lone pair on the carbon bonding to the metal via a σ bond. b) This shows the back-bonding between a filled *d* orbital on the metal and one of the anti-bonding π^* on the carbonyl, creating a π bond. The red arrows in each case denote the motion of electron density between the two species.

The degree of back-bonding is dependent upon the electron density of the metal: the greater the atomic number of a metal, the greater the degree of back-bonding that occurs. The effect of back-bonding can be observed through infrared spectroscopy, which measures the individual molecular vibrational frequencies on exposure to varying wavelengths of infrared radiation. As back-bonding increases the bond order of the carbonyl bond decreases. This has the overall effect of increasing the carbon to oxygen bond length, and thereby decreasing the vibrational stretching frequency of the carbonyl molecule.

Bonding Of Methoxide And Carbonyl

As discussed above, the oxygen of the methoxide anion has a full 2*p* shell, where two of the filled 2*p* orbitals are not involved in the bonding of the system. Either of these orbitals is of the correct symmetry to bond to the vacant 2*p* orbital of the carbon within the carbonyl. The new electron arrangement for the carbomethoxy ligand can be explored by adding a pair of electrons into the carbon 2*p* atomic orbitals in the molecular orbital diagram for carbonyl, as shown in Figure 2-12.

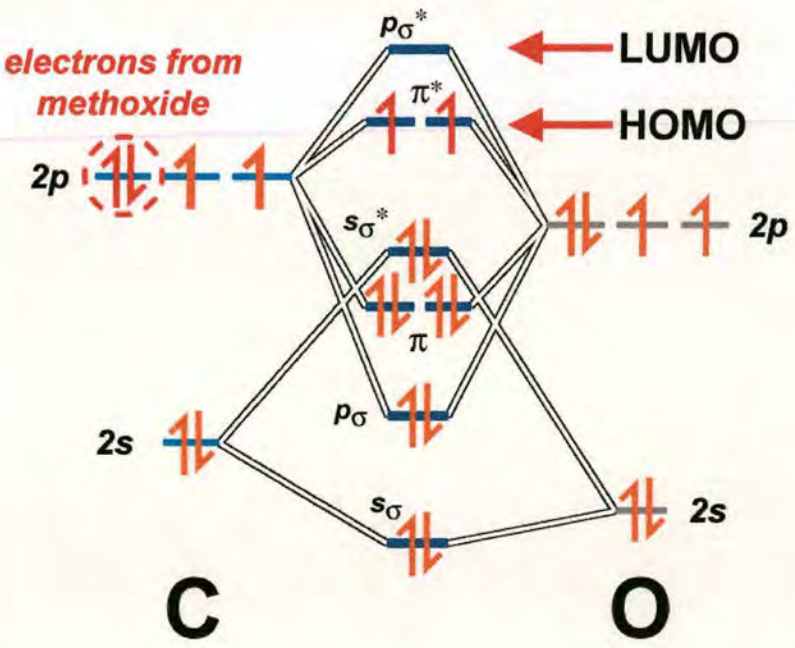

Figure 2-12 A revised carbonyl energy level diagram with the introduction of a lone pair of electrons into carbon *2p* orbital from the bond with the methoxide anion.

The nearest available vacant molecular orbital is the anti-bonding π^* orbital. The s_σ* lone pair on the carbon are still free to bond unhindered to the metal, but the partial occupancy of the anti-bonding π^* orbitals means that the degree of back-bonding with the metal has been reduced. The extra electrons in the π^* anti-bonding orbitals reduces the bond order of the carbonyl ligand to two. The CO stretching vibrational frequency shows a characteristic decrease for transition metal carbonyl species derivatised with the methoxide anion in comparison to the underivatised species [26], confirming this arrangement.

2.4.3 The Effect of The Carbomethoxy Ligand On The Cluster

X-ray diffraction studies on methoxide derivatised $Ir_4(CO)_{12}$ and $Rh_6(CO)_{16}$ to produce $[Ir_4(CO)_{11}(CO_2CH_3)]^-$ and $[Rh_6(CO)_{15}(CO_2CH_3)]^-$ respectively, have been able to show the direct bonding of the methoxide to the carbon on a carbonyl ligand to produce the carbomethoxy ligand [22;32]. The X-ray diffraction data provides a wealth of information on the effect that the presence of the carbomethoxy ligand has upon the cluster, specifically in the way the electron density is shifted and alters the average bond lengths between the atoms within the cluster.

$[Ir_4(CO)_{11}(CO_2CH_3)]^-$

In the case of the iridium cluster, the carbomethoxy ligand has a profound effect to the structure of the underivatised cluster. Despite the trouble with generating a single crystal structure of $Ir_4(CO)_{12}$, the generally accepted form is that of a tetrahedron arrangement of iridium atoms, each of which feature three terminal carbonyl ligands [35;36]. However the presence of the carbomethoxy induces a structural rearrangement, resulting in the generation of bridging and terminal carbonyl ligands [22], as can be seen in a re-illustration of their data in Figure 2-13.

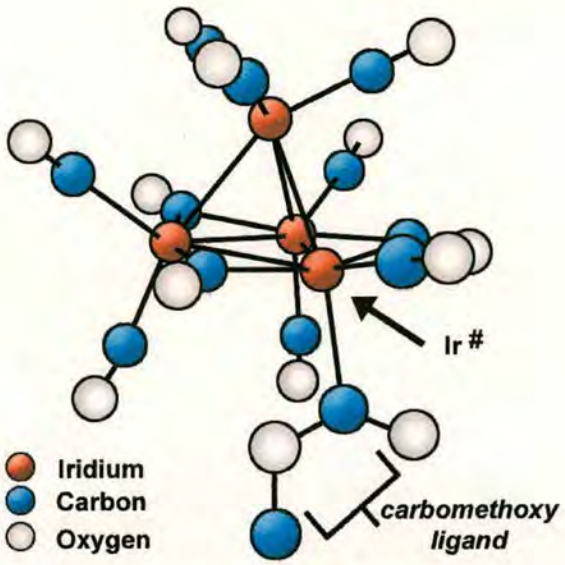

Figure 2-13 A representation of the X ray diffraction data of methoxide derivatised $Ir_4(CO)_{12}$. The presence of carbomethoxy promotes some carbonyls to form bridging bonds between iridium atoms on one plane of their tetrahedral arrangement. Diagram adapted from Reference 22.

The iridium atom to which the carbomethoxy ligand is bonded is denoted as $Ir^{\#}$. As expected, the methoxide bonds to a terminal carbonyl to form the carbomethoxy ligand, but the presence of bridging ligands is slightly worrying due to the fact that one of the main reasons for choosing derivatisation with a nucleophilic agent like methoxide is that it was hoped they would not significantly alter the physical properties of the cluster species under study. However, it has previously been noted that the basic structure of $Ir_4(CO)_{12}$ is not retained when a carbonyl ligand is substituted with other neutral and anionic ligands, such as iodine anion, I^- and chlorine anion, Cl^- [22;32], producing a similar rearrangement of the structure. It would then seem that many of the viable ligand substitutes designed to place charge upon the cluster would have produced a similar effect upon the iridium cluster as the carbomethoxy ligand. Therefore the decision was made to continue the use of the carbomethoxy ligand to ionise the iridium cluster, to maintain similar conditions between this and the other clusters for comparison, and because of the possibility of investigating elements of the water gas shift reaction so associated with the carbomethoxy ligand.

Despite the alteration in ligand arrangement the iridium core remains essentially the same compared to the underivatised cluster. However, it is observed that the bond length between the first carbon of the carbomethoxy ligand (2.20Å) is slightly greater than the bond lengths to the other terminal carbonyls (2.00Å) [22]. Such an increase in the metal-to-carbonyl bond length is evidence of the hindrance posed to back bonding by the partial occupation of the anti-bonding orbitals of the carbomethoxy ligand. This provides some degree of confirmation to the suspected electron arrangement for the carbomethoxy ligand with the longer bond length between $Ir^{\#}$ and the first carbon of the carbomethoxy ligand. The carbonyl ligands bonded to $Ir^{\#}$ do not seem to be affected by the carbomethoxy ligand, with their bond lengths remaining very similar to those bonded to the other iridium atoms, and likewise for the bridging carbonyls [22].

$[Os_3(CO)_{11}COOCH_3]^-$

To date there has been no evidence that the structure of the methoxide derivatised osmium cluster has been characterised (according to SciFinder Scholar and Web of Knowledge). It is assumed that the methoxide will bond to one of the many terminal carbonyl ligands on the cluster, with resultant unknown changes to the cluster geometry.

$[Rh_6(CO)_{15}(CO_2CH_3)]^-$

In the case of the rhodium cluster the methoxide has been shown to bond to one of the terminal carbonyl ligands [32]. This is to be expected, as there is no free electron available on the carbon of a capping carbonyl ligand for forming a bond to the methoxide. A re-illustration of this X-ray diffraction data can be seen in Figure 2-14 [32].

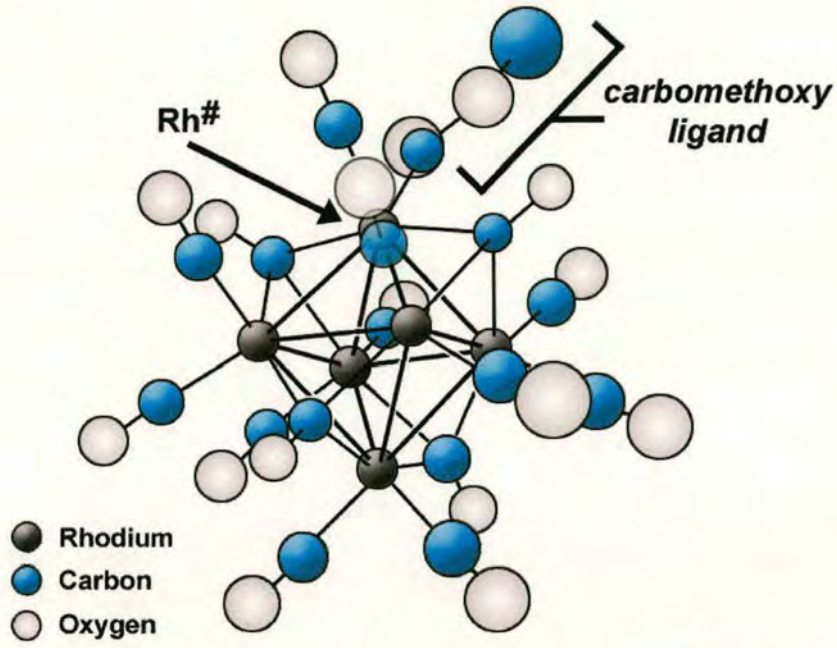

Figure 2-14 A representation of the X ray diffraction data of methoxide derivatised $Rh_6(CO)_{16}$. Diagram adapted from Reference 32.

The presence of the more electronegative carbomethoxy ligand distorts the arrangement of the capping carbonyls bonded directly to $Rh^{\#}$, pushing the arrangement slightly out of their normal symmetric tetrahedral conformation with the other two capping ligands. Once again the bond between $Rh^{\#}$ and carbomethoxy has been found to be slightly longer than that of a terminal carbonyl, being 1.96Å in length, compared to 1.86 Å on the plain cluster [17]. This provides further weight to the presence of additional electron density within the anti-bonding orbitals of the carbomethoxy ligand.

Finally the metal-metal bonds have been slightly reduced from 2.776Å [37] to 2.765Å [32], a difference of less than half a percent. This indicates a minor shift in the electron density within the cluster core, leading to the core becoming slightly more compact and the strengthening of the metal-to-metal bonds. Overall, this does not represent too much of a change to pose a significant change in the clusters chemical properties.

2.5 Conclusion

The general properties of transition metal carbonyl clusters have been reviewed, from their structural characteristics to their known reactivity and relationship with the bulk materials. In addition each of the clusters that will be used in the work presented within this thesis has been introduced, looking at their structure in the solid state and after derivatisation with the methoxide adduct, where such data exists. This knowledge, combined with the evaluation of the mechanism of the derivatisation reaction itself, will assist the experimental process and the subsequent interpretation of the data, allowing for more insightful reviews and conclusions to be drawn.

2.6 Reference List

1. Bochmann, M. *Molecular Organometallics 1 Complexes with Transition Metal-Carbon σ-Bonds*, 3rd ed.; Oxford University Press: Avon, 1999.

2. Whetten, R. L.; Cox, D. M.; Trevor, D. J.; Kaldor, A. *Surface Science* **1985**, *156*, 8-35.

3. Madley, T. E.; Yates, J. T.; Sandstorm, D. R.; Voorhoeve, R. J. *Treatise Solid State Chemistry* **1976**, *6B*, 1.

4. Dyson, P. J.; McIndoe, J. S. *Transition Metal Carbonyl Cluster Chemistry*, 1st ed.; Gordon and Breach Science Publishers: 2000.

5. Chini P.; Longoni, G.; Albano, V. G. 1974; pp. 285-344.

6. Housecroft, C. E. *Metal-Metal Bonded Carbonyl Dimers and Clusters*, 1st ed.; Oxford University Press Inc.: New York, 1995.

7. Albano, V. G.; Ceriotti, A.; Chini, P.; Ciani, G.; Martinengo, S.; Anker, M. *Journal of the Chemical Soicety Chemical Communications* **1975**, 859.

8. Mahan, B. M.; Myers, R. J. *University Chemistry*, 4th ed.; The Benjamin/Cummings Publishing Company, Inc.: 1987.

9. Collman, J. P.; Hegedus, L. S. *Principles and Applications of Organotransition Metal Chemistry*, University Science Books: Mill Valley, California, 1980.

10. Wade, K. J. *Journal of the Chemical Society Chemical Communications* **1971**, 792.

11. Muetterties, E. L. *Bulletin de La Societe Chimique de Belgique* **1975**, *84*, 959.

12. Muetterties, E. L. *Bulletin de La Societe Chimique de Belgique* **1976**, *85*, 451.

13. Muetterties, E. L.; Rhodin, T. N.; Band, E.; Brucker, C. F.; Pretzer, W. R. *Chemical Reviews* **1979**, *79*, 91.

14. Churchill, M. R.; Hutchinson, J. P. *Inorganic Chemistry* **1978**, *17*, 3528-3535.

15. Churchill, M. R.; DeBoer, B. G. *Inorganic Chemistry* **1977**, *16*, 878-884.

16. Eady, C. R.; Johnson, B. F. G.; Lewis, J. *Journal Of Organometallic Chemistry.* **1972**, *37*, C39.

17. Corey, E. R.; Dahl, L. F. *Journal Of The American Chemical Society.* **1963**, *85*, 1202-1203.

18. Chapman, J. R. *Practical Organic Mass Spectrometry*, 2nd ed.; John Wiley & Sons, Inc.: 1998.

19. Ekeberg, D.; Hagen, S. I.; Hvistendahl, G.; Schulze, C.; Uggerud, E.; Vedde, J. *Organic Mass Spectrometry* **1993**, *28*, 1547-1554.

20. Stark, J. G.; Wallace, H. G. *Chemistry Data Book*, 2nd Edition in SI ed.; John Murray (Publishers) Ltd: London, 2001.

21. Ciani, G.; Sironi, A.; Chini, P.; Martinengo, S. *Journal Of Organometallic Chemistry.*. **1981**, *213*, C37-C40.

22. Garlaschelli, L.; Martinengo, S.; Chini, P.; Canziani, F.; Bau, R. *Journal Of Organometallic Chemistry.*. **1981**, *213*, 379-388.

23. Anstock, M.; Taube, D.; Gross, D. C.; Ford, P. C. *Journal Of The American Chemical Society.* **1984**, *106*, 3696-3697.

24. Gross, D. C.; Ford, P. C. *Inorginc Chemistry.* **1982**, *21*, 1702-1704.

25. Gross, D. C. *Journal Of The American Chemical Society.* **1986**, *108*, 6100.

26. Gross, D. C.; Ford, P. C. *Journal Of The American Chemical Society.* **1985**, *107*, 585-593.

27. Powell, P.; Stephens, M.; Yassin, K. H. *Journal Of Organometallic Chemistry..* **1986**, *301*, 313-319.

28. Trautman, R. J.; Gross, D. C.; Ford, P. C. *Journal Of The American Chemical Society.* **1985**, *107*, 2355-2362.

29. Katta, V.; Chowdhury, S. K.; Chait, B. T. *Journal Of The American Chemical Society.* **1990**, *112*, 5348-5349.

30. Henderson, W.; McIndoe, J. S.; Nicholson, B. K.; Dyson, P. J. *Chemical Communications.* **1996**, 1183-1184.

31. Angoletta, M.; Malatesta, L.; Caglio, G. *Journal Of Organometallic Chemistry..* **1975**, *94*, 99-106.

32. Ciani, G.; Sironi, A.; Chini, P.; Martinengo, S. *Journal Of Organometallic Chemistry..* **1981**, *213*, C37-C40.

33. Atkins, P. W. *Physical Chemistry*, 6th ed.; Oxford University Press: 1998.

34. Winter, M. J. *Chemical Bonding*, 3rd ed.; Oxford University Press: Avon, 1996.

35. Churchill, M. R.; Hutchinson, J. P. *Inorganic Chemistry.* **1978**, *17*, 3528-3535.

36. Holland, G. F.; Ellis, D. E.; Tyler, D. R.; Gray, H. B.; Trogler, W. C. *Journal Of The American Chemical Society.* **1987**, *109*, 4276-4281.

37. Corey, E. R.; Dahl, L. F. *Journal Of The American Chemical Society.* **1963**, *85*, 1202-1203.

3 Mass Spectrometry

3.1 Introduction

The International Union of Pure and Applied Chemistry (IUPAC) define the mass spectrometer as [1]:

> *"An instrument in which the beams of ions are separated (analysed) according to the mass/charge ratio and the ions are measured electrically."*

Such analysis occurs within the gas phase and necessarily deals with ionic species. The separation of ions of differing mass and charge is achieved through the manipulation of electric and/or magnetic fields, which permits the determination and differentiation of ionic species and their isotopes.

The origins of mass spectrometry can be traced back to the late 19th and the early 20th century, when in 1886 the German physicist Eugen Goldstein discovered the existence of positively charged particles, generated from gaseous samples as they were exposed to a perforated cathode [2;3]. Over a decade later in 1898 physicist Wilhelm Wien demonstrated that the rays of positive ions could be deflected in the presence of strong electric fields, and be differentiated by their charge and mass, and that different ionic species could be detected simultaneously [4]. However, it wasn't until 1905 that the first model mass spectrometer instrument was conceived and built by the noted English physicist Joseph John Thomson at Cambridge University [5]. Thomson developed the discoveries of Goldstein and Wien to construct an instrument that could take any sample gas, ionise it and use strong electric and magnetic fields to separate the ions by their charge and mass. The ions formed parabolic beams, which were focussed onto photographic plates to record the mass spectrum. The equations of motion that defined the parabolic path of the ions were expressed in terms of the charge-to-mass ratio, e/m of the ion (where e denotes the charge of an electron and m is the mass of the particle). Figure 3-1 is a theoretical depiction of one of the first mass spectra Thomson recorded from a mixture of hydrogen and oxygen. The spectrum shows sharp parabolas that corresponded to the appropriate e/m values of H^+, H_2^+, O^+, O^{2+}, and O_2^+, and also weak indications of H^- and O^- [5].

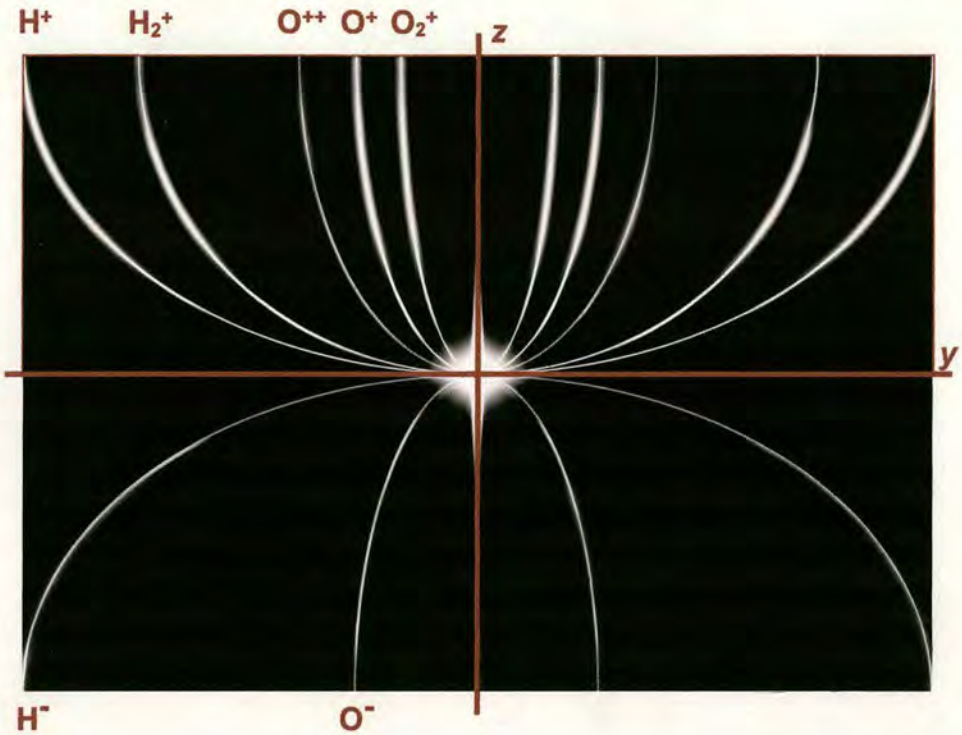

Figure 3-1 A theoretical reproduction of a parabola mass spectrum as recorded for hydrogen and oxygen on a photographic plate. This diagram has been adapted from Reference 5.

Within years of its creation, the mass spectrometer was instrumental in the discovery and characterisation of the stable isotopes of the elements [6;7] and was soon finding uses for organic identification and structural elucidation in the petrochemical industry and pharmaceuticals. Since then mass spectrometry has evolved into one of the most important analytical tools for the investigation of complex biological systems. The progression of new technology, such as more reliable and sophisticated electronics, vacuum systems and fabrication processes, has permitted the rapid development of mass spectrometry to extend far beyond the scope of Thomson's instrument. As a result, several distinct mass spectrometry techniques have been devised and created, each using different principles to produce ions and achieve ion separation by charge and mass, creating a family of instruments that form the mass spectrometry genus. To this extent no less than three mass analyser systems have been used in the research within this thesis, including two separate ionisation

processes, all of which shall be reviewed in this chapter, beginning with a brief overview of the basic principals of mass spectrometry.

3.2 The General Operating Principles Of Mass Spectrometry

3.2.1 The General Components Of A Mass Spectrometer

Each variant of mass spectrometer can be split into five distinct parts, as shown in Figure 3-2.

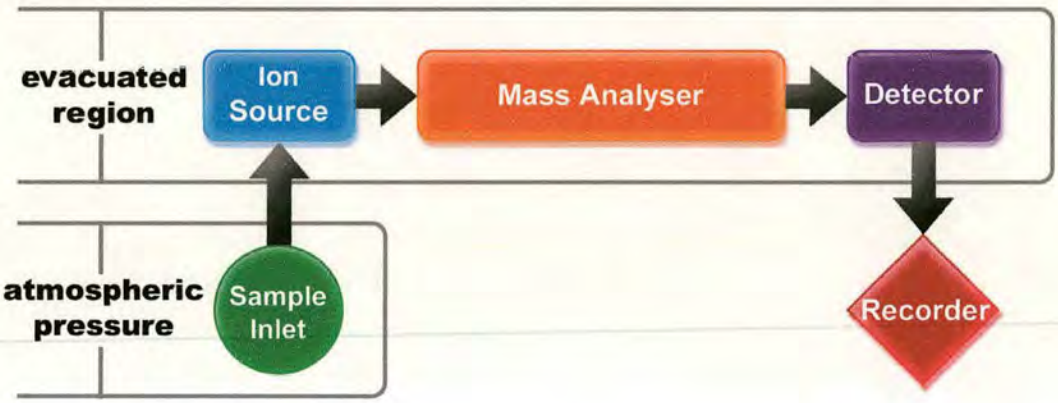

Figure 3-2 The essential components of every mass spectrometer. Diagram adapted from Reference 8.

The function of each stage is as follows:

The Sample Inlet: Transfers the sample (solid, liquid or gaseous) from the ambient pressure of the laboratory to the ion source. The sample inlet may vaporise the sample into the gas phase before entry into the ion source.

The Ion Source. Converts the sample into gaseous ions, provides the ions with kinetic energy and collimates them to form either a continuous ion beam, or a tight ion packet (a collection of ions confined to a finite volume).

The Mass Analyser. The analyser exposes the ions to electric or magnetic fields, or even a mixture of both. The fields are controlled so as to control the motion of the ions, separating them out in terms of their mass-to-charge ratio.

The Detector. The detector is usually a form of electron multiplier. On reaching the detector, the mass-charge separated ions strike the multiplier, which generates a gradual cascade of electrons to produce a current that can be measured and then amplified [9]. Alternatively some detectors can detect the minute current generated from the motion of the ions past a system of electrodes, which is then amplified. The amplified signal is then processed to generate data corresponding to the ion current at given mass-to-charge values.

The Data Recorder. Plots the mass spectrum. In the early days this would take the form of a chart recorder. All modern instruments use a specially configured desktop computer system to operate the mass spectrometer and process, record and store the mass spectra for future reference and manipulation.

As can be seen from Figure 3-2, the majority of the mass spectrometer is operated under vacuum. A gas-phase ion in the presence of any other gaseous species will experience collisions with the molecules of that gas, and be slowed by those collisions. The number of collisions is dependent upon the velocity of the ions and the pressure of the gas. The higher the pressure of the gas, the more collisions will occur and the ions will have a slower resultant speed. Thus employing vacuum reduces the number of collisions, facilitating the transfer of ions from the ion source to the detector. Quite often the earlier stages of the mass spectrometer, such as the ion source, necessarily operate at higher pressures than the rest of the instrument. A system of differential pumping is used to reduce the pressure along the remainder of the instrument to bring the analysis region to the highest vacuum. The motion of the ions is maintained by a system of *ion optics,* which are covered in the following section. The vacuum is also a necessary state to ensure clean analysis of the sample. Any stray neutral species that enters the analyser can coat the walls and perhaps even

the electronic instruments that produce the electric and magnetic fields to achieve ion separation. Such an occurrence can severely hamper the effectiveness of the mass analyser by disrupting the homogeneity of those fields, and can remain as a contaminant within the instrument. The vacuum maintained within the instrument can vary with the requirements of each instrument, but is typically in the region of several millionths to one billionth of atmospheric pressure (10^{-6} – 10^{-10} mbar) [8].

A general convention is to label the spatial *z*-axis as that which travels the length of the instrument. Many mass spectrometers are linear, in that the ion beam travels along the *z*-axis from the ion source to the analyser, and all of the above described components act parallel to the *z*-axis. There are some instruments that are not linear, and all those components that do not act parallel to the *z*-axis are termed to be *off-axis*. Thus the motion of the ions does not absolutely define the *z*-axis of the instrument.

A review of the pertinent sample introduction and ionisation techniques that are used in the work of this thesis is given in Chapter 3.5 followed by a similar review of the mass analysers in Chapters 3.4 and 3.5.

3.2.2 Ion Optics

Analogies can be made between the motion of a beam of charged particles and that of a light beam. Both can be directed and focussed to distinct spatial positions and planes, and if the particles fall under quantum mechanic rules, they can both be diffracted and refracted from their wave-particle characteristics. Where the light beams are manipulated through lenses and prisms, ion beams are manipulated by electrostatic and/or magnetic fields, applied by *ion optics*. These are integral components of any mass spectrometer, focussing and directing the ion beam to the mass analyser. The ion optics can range from very sophisticated systems of specially designed electrodes to simple metal plates, all of which are connected to power supplies configured to generate the necessary electric field for the correct function of the ion optic, e.g. focussing, transmission etc. Quite often the user has a degree of

control over the operation of the ion optics, allowing the mass spectrometer to be tuned to the best possible conditions for the analysis of different ionic species.

Kinetic Energy And Ion Optics

Within this thesis the ion optics feature quite prominently as a control of the translational motion of the ions. It is therefore worthwhile to examine the physics that will determine the translational/kinetic energy of the ions.

The electric potential energy, U, is the energy of a charged particle within an external electric field (i.e. not the electric field generated by the charged particle). The external electric field, $\boldsymbol{E}$, is a vector quantity since the field acts in a specific direction. If a charged particle moves between two points within the electric field the difference in the particle's electric potential energy between those points is the negative of the work done by the electrostatic force, via the electric field, on the charged particle during it's motion. The potential energy of the charged particle is dependent upon both the magnitude of the charge and the electric field [10].

However, the potential energy per unit charge of the field is significantly different in that it has a unique value at any point within an electric field, and is independent of the magnitude of the charge, q. This is known as the *electric potential*, V, and is measured in joules per coulomb, or volts, where

$$V = \frac{U}{q} \tag{3-1}$$

Therefore the difference in electric potential, ΔV, between any two points in an electric field is equal to the difference in the electric potential energy, ΔU, per unit charge between these points [10]. Defining these points as i and f (denoting initial and final) then it can be seen that the change in the electric potential energy between i and f is the negative of the work done, W_{if}. The potential difference is then equal to:

$$\Delta V = V_f - V_i = -\frac{W_{if}}{q} \tag{3-2}$$

If the potential difference is known, then the work done by the electrostatic force in moving the particle from points i to f is equal to:

$$W_{if} = -q\Delta V \tag{3-3}$$

This equation is extremely useful as a first step to determining the kinetic energy of ions as they move through ion optics. Consider a simple array of ion optics consisting of a linear array of two identical planar metal plates, separated by a distance *s*, with a small central orifice through which ions can pass, as depicted in Figure 3.3.

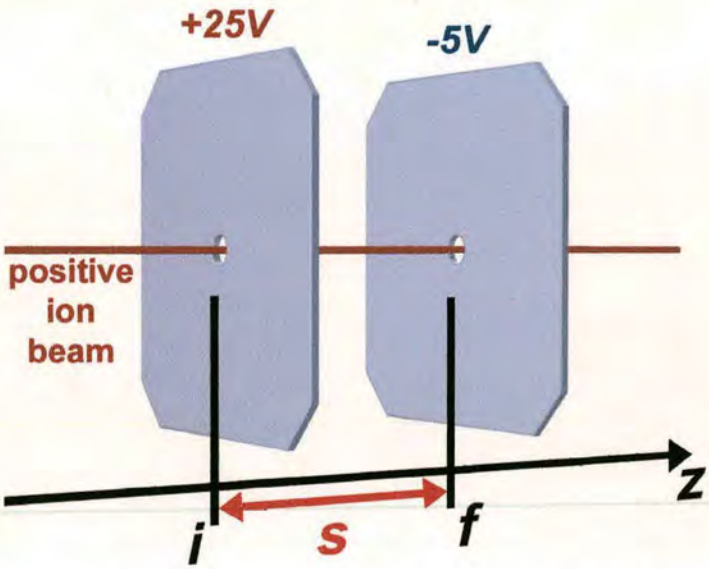

Figure 3-3 A positive ion beam travelling through narrow apertures in identical metal plates at points *i* and *f*. An electric potential is applied to each plate, as indicated, to create a potential difference ΔV.

It can be assumed to a good approximation that the electric field at the centre of each plate is the same as that for the ideal infinite surface, such that the field that exists between the centres of the two plates is homogenous. If the initial plate is connected to a 25 V d.c. power supply, and the final plate is connected to a –5 V d.c. supply, then the potential difference, ΔV is –30 V. If the ions have a uniform charge equal to the magnitude of the charge of an electron, *e* (1. 602 x10^{-19} C), then the work done by the electric force on an ion between *i* and *f* is

$$W_{if} = -(1.602\times10^{-19})\times(-30) = 4.806\times10^{-18}\,\text{J} \tag{2-4}$$

This answer can be simplified by replacing the joule units of energy with the *electronvolt* (*eV*), which is the energy equal to the work required to move a single

elementary charge e, through a potential difference of one volt. One electronvolt is equal to 1.602×10^{-19} J. Thus the above value of work is simply 30 eV. The work is a measure of the kinetic energy gained (or lost) from the motion of the ion through the potential difference. If the ion is initially at rest, the work defines the final kinetic energy of the ion at point f.

Therefore the kinetic energy, KE, gained in moving from i to f is determined by the relationship:

$$\underset{i \to f}{KE} = -q.(V_f - V_i) = -q.\Delta V \tag{3-4}$$

The external electric field, $\boldsymbol{E}$, between i and f can then be determined from the potential difference from the following relationship, given without proof [10]:

$$\Delta V = -\int^{f} \boldsymbol{E} \bullet d\boldsymbol{s} \tag{3-5}$$

Thus the potential difference between points i and f in an electric field is equal to the negative of the line integral of $\boldsymbol{E} \bullet d\boldsymbol{s}$ from i to f. In a linear electric field as described in the above example, the electric field strength, E, is simply equal to the potential difference divided by the separation, s.

Skimmer Cones

Many of the ion optic systems that are of interest within this thesis are not planar, but conical in shape. These are known as *skimmer cones* and, as well as being used for ion guidance, they provide another indispensable function for mass spectrometry. Skimmer cones are normally applied as the interface between different regions moving from higher to lower pressure.

A gas is made to pass from an atmospheric region through a small orifice into an evacuated region. On entering the evacuated region the gas forms a free jet, and the enthalpy of the gas is converted into directed bulk flow translational energy, such that the gas molecules are accelerated and the gas expands into the evacuated region. The conversion of the enthalpy results in a decrease in the local gas temperature throughout the free jet, meaning that the local speed of sound of the gas also decreases. As the gas molecules accelerate their velocity will, at some point within

the free jet, exceed the local speed of sound [11]. From this phenomenon, the motion of gas from atmosphere to vacuum is often described in terms of a supersonic expansion.

The occurrence of the free jet creates problems if the gas has to enter another separate region through a narrow orifice. A free jet is terminated by a shockwave, known as a Mach disk in which the motion of the gas molecules will be re-randomised. If the gas prematurely hits a blunt diaphragm, such as a planar plate featured in Figure 3-3 it will force the early formation of a shock wave, and little of the gas molecules will be transmitted into the next region [11]. The problem is countered by the introduction of a conical shaped metal plate, the skimmer cone, positioned such that the tip penetrates into the free jet area before the formation of the Mach disk. Thus the gas molecules will be able to continue on into the next region. A typical example of a skimmer cone is shown in Figure 3-4.

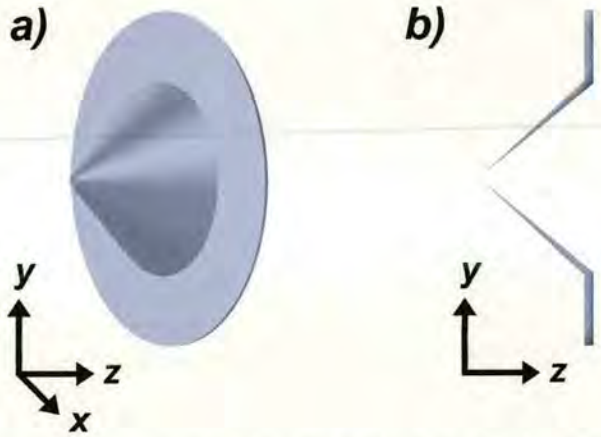

Figure 3-4 a) and b) show an elevation and side view of a typical skimmer cone. The skimmer is a precision made hollow cone punched onto a thin planar sheet, usually making the skimmer quite fragile. The central aperture is typically of the order of only one or two millimetres.

A linear array of skimmer cones can be used to accelerate gaseous ions in an analogous manner to that covered in the previous section with planar electrodes. Although the electric field generated by the skimmer cones will be substantially different, the electric potential at the tips of the two skimmers, at points *i* and *f* will

just be that provided by the power supplies. Therefore the equations used to determine the kinetic energy of the gas ions moving between skimmers at *i* to *f* are the same as that for the planar electrodes in Equation 3-4.

3.3 The Anatomy Of The Mass Spectrum

3.3.1 The Units Of Mass Spectrometry

When photographic plates were used to record parabola mass spectra, the quantity of interest was the charge-to-mass ratio, *e/m*, not only for its appearance in the equations of ion motion but also because the early researchers were more interested in the study of charged particles than gathering chemical data on the composition of unknown species. As the instruments evolved into a method of chemical analysis, the term charge-to-mass ratio was not particularly useful in interpreting a mass spectrum and determining the mass of the sample. Thus the term *mass-to-charge ratio*, *m/z* was formally adopted as the principal unit of measurement.

There are several units that are commonly used when interpreting mass spectra. It is common to find the mass-to-charge ratio taken to be the absolute value of the mass of the analyte species, i.e. equal to *u*, but this neglects the possibility of multiply charged species. A mass spectrum showing a peak recorded at a mass-to-charge value of 44 could be interpreted as being due to singly charge carbon dioxide, CO_2^+ (mass-to-charge = 44/1), or doubly charged pentan-1-ol, $[CH_3CH_2CH_2CH_2CH_2OH]^{2+}$ (mass-to-charge = 88/2 = 44). Another common unit is the Dalton, *Da*, named after the English chemist John Dalton, and is often used to represent one mass-to-charge unit, and is equal to one gram per mole (also the value of *u*). Once again this is only really equal to mass. To remove any ambiguity it is best to quote the mass-to-charge value, which is also denoted by the *Thomson* unit, *Th*, named after the founding figure of mass spectrometry. Thus doubly charged pentan-1-ol is 44 Th, and singly charged benzene is 78 Th.

3.3.2 The Mass Spectrum

The mass spectrum is a two-dimensional plot that displays the mass-to-charge value on the *x*-axis and the relative intensity on the *y*-axis. It is common practice for mass spectra to be normalised to the most intense peak on the spectrum, known as the *base peak*, such that all smaller peaks are shown relative to the base peak [8]. Ideally, every mass spectrum would be composed of vertical single-point lines pertaining to the precise mass-to-charge ratio of each species analysed. In reality, most mass spectra are composed of slightly curved peaks. Figure 3-5 shows a simulation of a mass spectrum to illustrate this point , showing the peaks relating to singly charged toluene ($C_6H_5CH_3$) and normal heptane ($CH_3CH_2CH_2CH_2CH_2CH_2CH_3$) (Simulation generated by the MassLynx software).

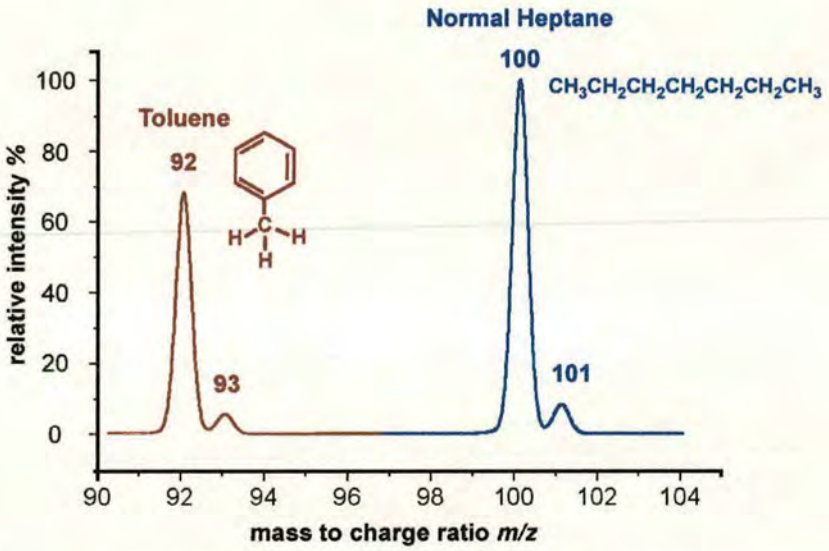

Figure 3-5 A simulation of the mass spectrum of toluene and n-heptane.

The mass spectrum shows peaks at 92 and 93 for toluene, and 100 and 101 for normal heptane. As can be seen heptane is the most abundant species present and is the base peak: toluene has an abundance of approximately 70% of heptane. The minor peaks at 93 and 101 mass-to-charge units belong to the proportion of the hydrocarbons that contain the heavier and rare isotopes of carbon and hydrogen, ^{13}C, and to a much lesser extent ^{2}H. Since 1.1% of all carbon is ^{13}C and only 0.015% of all hydrogen exists as ^{2}H [12], the probability of being able to detect species with more

than one heavy isotope within the molecule is virtually nil. Thus the mass spectrum has only recorded the presence of one heavier atom in each species, most likely ^{13}C, and the abundance of these heavier isotopes is approximately 10% of the most abundant isotope peaks. Most species have a characteristic isotope "fingerprint", allowing for rapid visual identification of species from the mass spectrum. It is also possible to simulate the isotope distribution for any molecular formula, with the isotope model being constructed from the weighted summation of the known isotope distribution of each constituent atom, producing the expected isotope pattern for that molecule. Thus isotope models can be used to confirm the assignments made in a mass spectrum.

The breadth of the peaks is an indication of the quality of the mass spectrum and the abilities of the mass analyser: the broader the peaks the poorer the standard of mass spectrum. The mass spectrum in Figure 3-5 can be regarded as being of a mediocre standard. This is a factor known as the *resolution* of the mass spectrometer.

3.3.3 Resolution

IUPAC defines the mass resolving power of a mass spectrometer as [1]:

> *"The ability to distinguish between ions differing in the quotient mass/charge by a small increment."*

Thus the resolution of a mass spectrometer can be regarded as the capacity of the system to separate ions of adjacent mass-to-charge ratios, although no standard definition of that separation has been formally adopted by the mass spectrometry community [9]. At the most basic level, the resolution, R, required to separate two ions of mass-to-charge values m_1 and m_2, where $m_2 = m_1+\Delta m$, as shown in Figure 3-6, is given by [9]:

$$R = \frac{m_1}{\Delta m} \tag{3-6}$$

A large resolution value corresponds to a greater resolving power of the mass spectrometer. The resolution can also be expressed in terms of *parts per million*, leading to the equation [9]:

$$R(ppm) = 10^6 \frac{\Delta m}{m_1} \qquad (3\text{-}7)$$

When dealing with parts per million, the lower the value of R, the greater the resolving power of the mass spectrometer.

A complication arises in determining the resolution in that the operating principles of some types of mass analysers force the definition of resolution for that instrument. As an example a *quadrupole* mass analyser (which shall be examined in Chapter 3.6.1) works by maintaining the value of mass separation, Δm, throughout the mass range. As such, if the mass separation is held at 1 Th, then the resolution of a peak at 2000 Th will be 2000, and a peak at 200 Th will have a resolution of 200. The constant mass separation represents the limiting factor in the resolution of quadrupole analysers. Other mass spectrometer types face similar constraints to the resolution, which shall be discussed in Chapter 3.5. Therefore the resolution of a mass spectrometer is dependent upon the mass-to-charge value of the species being measured and the method by which it is being measured. . It is valid to say that mass spectrometers should only be classed in terms of their overall resolving abilities, rather than any quantitative value, unless those values are quoted from the analysis of example species.

The method of operation within the quadrupole mass analyser means that resolution can be measured from just one peak. This can be done from the mass spectrum by measuring the width of a peak at half of the height of that peak, known as the *Full Width at Half Maximum*, of *FWHM* [9]. This is also shown in Figure 3-6 for a peak at m_1 Th.

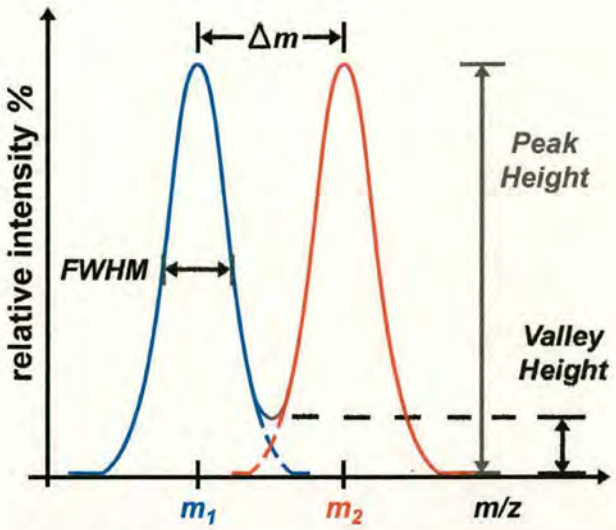

Figure 3-6 A mass spectrum showing two peaks of equal intensity for ions of mass-to-charge values m_1 and m_2. The various parameters for determining the resolution of the spectrum, such as the valley height and the full-width at half-maximum height (FWHM) of m_1 are shown. Diagram adapted from Reference 9.

If two peaks are quite close together they can overlap, and the superposition creates a valley in-between the peaks, as shown in Figure 3-6 for peaks on a mass spectrum at m_1 and m_2 Th. This introduces a problem in that, if the valley height (defined as the distance between the base of the valley and the *m/z* axis) is too large in relation with the height of the peak, one cannot distinguish one peak from its neighbour without any ambiguity. One rule that is used to clarify the definition of a resolved peak in such a situation is the 10% valley definition of resolution: two peaks of equal intensity are regarded to be resolved if they are joined by a valley that has a height of, at most, 10% of the height of either peak, and each peak contributes equally to the valley (i.e. the point of peak intersection should be half the height of the valley for the peaks to have an equal contribution to the formation of the valley) [9]. A definition of the parameters is shown in Figure 3-6. This rule is rather laborious, but it's basic tenets can be judged by eye, rather than detailed measurement. Some analysers, such as *magnetic sectors* use this method to determine the resolution of the spectrum, quoting the valley height as the resolution achieved [9].

3.3.4 Parent And Fragment Ions

The formation of ions and the conditions to which the gas phase ions are exposed to as they traverse the mass spectrometer can sometimes promote the dissociation of certain bonds within the analyte species. Far from being a problem such an action can reveal a lot of useful information on the structure of the species. A *parent* ion is defined as [1]:

> *"An electrically charged molecular moiety which may dissociate to form fragments, one or more of which may be electrically charged, and one or more neutral fragments."*

The ionic fragments resulting from a dissociation reaction are termed to be *daughter* ions. It is possible for daughter ions to dissociate further to produce other charged and neutral molecular moieties of successively lower molecular weight.

Quite often the dissociation reactions do not result in the complete depletion of the parent ion population, allowing for their detection on the mass spectrum. Obviously the intensity of the parent ion reflects the proportion of parent ions that did not dissociate. The distribution of daughter ions can provide information on the overall structure of the parent ion, with the relative intensity of the parent and daughter ions revealing information on the proportion of parent ion that fragments and the efficiency of the reaction. In addition, the abundance and number of fragment ions can provide information on the likely locations of the charge on an ionised molecule from the evaluation of the neutral fragments: if one region of the molecule is continuously lost as part of the neutral fragment, then that part is never ionised.

An example of how fragmentation can provide structural information on analyte species can be taken from the case of two hydrocarbon isomers, normal heptane and 2,2-dimethylpentane. Both have been ionised by electron impact (the interaction of gaseous sample molecules and an electron beam formed from the heating of a metal filament [13;14]) generating positive ions from the loss of electrons. The electron energy is 70 electronvolts, which has lead to both the ionisation and fragmentation of the molecules. Both of the parent molecules have the same empirical formula –

C_7H_{16}, but are structurally different, hence producing different populations of fragment ions. A simulation of the mass spectrum of heptane is shown in Figure 3-7, as is the structure of the molecule and the simplified fragmentation pathway. A similar simulation of the mass spectrum of 2,2-dimethylpentane is given in Figure 3-8 with a simplified fragmentation pathway.

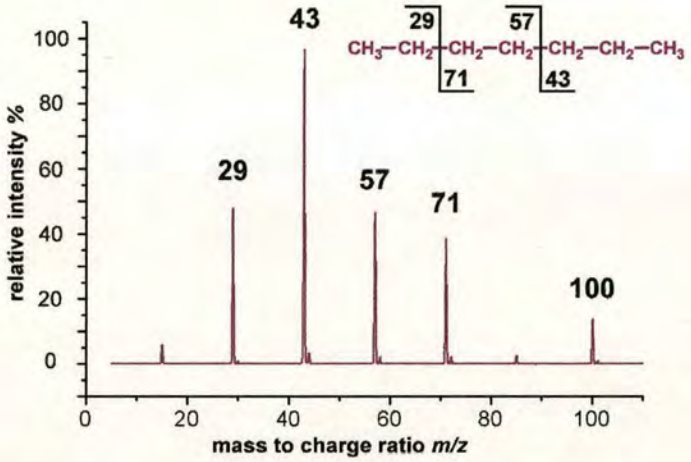

Figure 3-7 A simulated mass spectrum of heptane, alongside the suspected bond dissociations and the masses of the subsequent fragments. Example adapted from Reference 8.

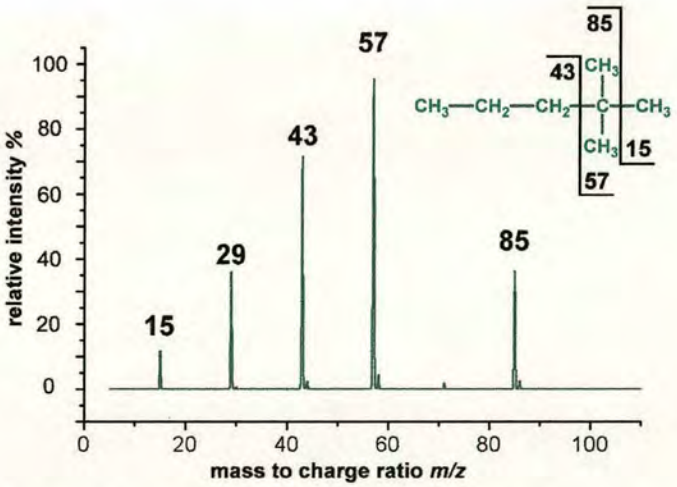

Figure 3-8 A simulated mass spectrum of 2,2-dimethylpentane, alongside the suspected bond dissociations and the masses of the subsequent fragments. Example adapted from Reference 8.

Although many of the fragments have the same mass, the relative population of the ions reveals which of the isomers the spectra belong to. In particular it is the absence of the $CH_3(CH_2)_4$ fragment (of mass 71*u*) that reveals the spectrum of Figure 3-8 to belong to 2,2-dimethylpentane. It is also interesting to note that there is no peak corresponding to the parent ion of 2,2-dimethylpentane, revealing that the presence of the tertiary carbons along the back of the molecule make it particularly more fragile.

As discussed previously, it is possible for daughter ions to undergo an additional dissociation reaction. Thus the original daughter ion has now become a parent ion for another fragment. The original species (the source of all generations of daughter ions) is referred to as the *molecular* ion [1]:

> *"An ion formed by the removal from (positive ions) or addition to (negative ions) a molecule of one or more electrons without fragmentation of the molecular structure."*

By using this term, one can then differentiate the source species from all the subsequent parent ions formed through multiple dissociation reactions .

Dissociation of bonds within a species can only occur if energy has been transferred to the species in excess of the internal bond dissociation threshold. This can occur as a by-product of the ionisation process if energy in excess of the ionisation energy is imparted into the molecule. Alternatively, dissociation can be brought about by the use of collisions to sufficiently excite the sample ions. A common example is the technique of *Collision-Induced Dissociation* (*CID*), where the ions are brought to collide with inert gas molecules to promote energy transfer and dissociation. The technique is deservedly popular as it is possible to control the dissociation reaction(s) through the target gas pressure and the velocity of the ions.

3.4 Sample Introduction And Ionisation Techniques

The techniques of sample introduction and ionisation are as important as the abilities of the mass analyser. The past three decades has seen the development of at least seven new and unique methods of ionisation and sample introduction, mostly all created to facilitate the analysis of fragile biological compounds [8].

Prior to these innovations, the principal method of generating gaseous sample molecules was by simple vaporisation through heating. This worked well for volatile organic hydrocarbon molecules and some inorganic species that could then be ionised by high impact collisions with an electron beam. Biological species such as proteins and peptides are not only non-volatile, but also very fragile, and the act of vaporisation would produce a catastrophic decomposition of the species [15]. This problem initiated the development of new methods to generate gaseous ions suitable for the processing of fragile and unwieldy species, methods that would later become known as *soft ionisation*.

Various soft ionisation methods were created, providing novel ways of "extracting" intact gaseous ions from solid or liquid phase samples. Soft ionisation techniques are not limited to the analysis of biological or any other fragile species, and have been particularly useful in the analysis of all types of sample, from organic to inorganic. There are two distinct categories of soft ionisation: *energy sudden* methods, such as *laser desorption ionisation* [15] and *field desorption* methods, such as the technique of *electrospray ionisation*. Both of these ionisation techniques are used in this thesis, and are reviewed below.

3.4.1 Laser Desorption Ionisation Mass Spectrometry

The Origins of Laser Desorption Ionisation

The principles of energy sudden methods for ionisation of fragile systems were originally developed from the theoretical propositions made by Beuhler and his colleagues [16] in the mid 1970's. The rate theory of unimolecular decomposition

shows that the rate constant for vaporisation is greater than that for decomposition at higher temperatures [9]. Therefore a rapid heating process would be able to vaporise large molecules in a time frame so small that the decomposition of the molecule had insufficient time to occur [15;16]. The propositions were supported by experimental evidence that showed the fragmentation of large species reduced with increased heating rates. These findings eventually lead to researchers at the FOM laboratories in Amsterdam developing the use of laser radiation to flash-desorb sample molecules on a metal surface [17;18]. The modern techniques of *laser desorption ionisation* (*LDI*) evolved from these first pioneering experimental forays.

The Mechanisms of Laser Desorption In Mass Spectrometry

Laser desorption ionisation generates gaseous ions from a solid surface. The species to be analysed is dissolved and spotted onto a small dot on a metal or ceramic sample plate. It is often not a problem if the analyte is not fully dissolved, but the solvent should be reasonably volatile since it must evaporate with little or no additional heating before the sample is ready for analysis. The sample molecules are physisorbed onto the surface and bound to it by weak van der Waals type bonds [19;20]. The plate is then placed into a chamber that is subsequently evacuated for interfacing with the mass spectrometer. A pulsed laser beam is fired at the sample to promote the desorption and ionisation of the sample molecules. The majority of mass spectrometers use a single laser to perform desorption and ionisation, although it is possible to separate these processes using two independent lasers. A time delay is normally made between ion formation and extraction into the analyser. Regardless of the pulse length (typically of the order of nanoseconds), the frequency at which the laser pulses is normally of the order of ten hertz, providing more than enough time between pulses for the chemical and physical reactions that occur as a consequence of the laser pulse to proceed to completion.

Two distinct mechanisms have been proposed to describe desorption of molecules from a solid surface. The mechanisms can be considered as thermal and non-thermal phenomena, and are dependent upon the wavelength of the laser, and the thickness of the sample deposited onto the sample plate [9;21]. Broadly speaking the thermal

mechanism has been observed for infrared radiation, and thick sample layers, whereas the non-thermal mechanism is associated with ultraviolet radiation, and thin sample layers. Since only ultraviolet lasers are used for the ionisation of samples within this thesis the thermal process shall be ignored for now. A nitrogen laser is used to provide the ultraviolet radiation, with a wavelength of 337 nm, which corresponds to an individual photon energy of 5.87 E^{-19} J. The laser pulse has a typical power density of 10^{10} Wcm^{-1} [21]. This beam is so powerful that it forces the complete explosive decomposition of the molecules at the focus of the beam by direct heating of the molecules. This catastrophic form of irradiation is also known as ablation, and can prompt the release of molecular fragments and even electrons from the sample molecules. It is also likely that the ejected material may also form a plasma above the focus [21], which can adsorb some of the other incident photons and partially shield the molecules beneath. The ablation of the sample molecules produces a shockwave that travels across the sample surface via energy dissipation, which vibrationally disrupts the binding potentials between the sample molecules and the surface of the plate [21]. The mechanism of this process is therefore described as non-thermal, and although those molecules at the focus of the laser beam are catastrophically fragmented, the vast remainder desorb from the surface as intact neutrals and ions. Evidence exists to support the occurrence of non-thermal desorption in this manner from the measurement of the kinetic energy of desorbed ions. Ions desorbed with an ultraviolet laser have been observed to have kinetic energies of the order of tens of electronvolts, far too high to have been produced by a thermal evaporation process [9;21].

It is reasonable to assume that a combination of the thermal and non-thermal processes can occur simultaneously given the correct mixture of parameters, such as the ultraviolet irradiation of thick sample layers. In such circumstances it is likely that the two processes will occur within the same time scale, but be laterally separated [21].

Sample Ionisation

The desorbed neutral molecules will be vibrationally excited to some degree after being forced from the sample plate. The distance of the molecules from the laser focus will dictate the excitation of the neutral, and so the neutrals shall feature a distribution in their internal energies. Therefore those close to the laser focus will probably have enough energy to auto-ionise and lose an electron. It is also possible that the desorbed neutrals shall be irradiated by an ultraviolet photon and be ionised in that way. The process of ionisation by electron loss can be thought of as a special case of dissociation from a molecule and so can be understood from the review of dissociation in Chapter 4.4. While these mechanisms explain the formation of cations, it is known that anions can be produced from laser desorption ionisation as well. An excited desorbed neutral species may not ionise, but instead dissociate in some way. This creates a vacancy in the molecular orbitals suitable for the scavenging of the free electrons produced from the ablation site and those lost from the cations.

Although the energy of the photon cannot be changed the intensity of the laser beam can by increased through the use of focussing optics. The intensity of the beam is dependent upon the number of photons per unit time and area [22], and a greater intensity can increase the number of species excited by the laser. It is normally the case that a molecule can only interact with a single photon at a time, but an intense beam can possibly promote multiple photon absorption [22]. By varying the intensity it is possible to reduce the power of the beam and thus lower the extent of activation of the molecules. This can be used to restrain the amount of neutral fragmentation from the ablation site and beyond, but may have a correspondingly detrimental effect on the quantity of ions produced. The technique of matrix-assisted laser desorption ionisation (also denoted as *MALDI*) was designed to counter this problem by placing the analyte species into a solvent containing small polar organic molecules that form the matrix. The organic molecules are chosen so that they have a strong absorption at the chosen laser wavelength. The solvent is evaporated leaving behind mixed crystals of the analyte in the matrix. Irradiation of the sample mixture leads to electronic excitation of the matrix molecules, which transfer their excess energy to

the analyte in a more controlled fashion to generate cations that are desorbed from the surface. A quantity of the matrix is also desorbed from the sample plate, and can prevent any interaction occuring between the sample ions [9]. However, it is these very reactions between the activated clusters shall be used to promote the formation of larger supra clusters, thereby negating the need for matrices.

Sample Preparation

Samples are normally prepared by a process known as *evaporative layers*. The sample is dissolved in a suitable volatile solvent, or a matrix for MALDI, and deposited onto a sample tile. The tile is a relatively small metallic plate, which contains a number of small dimples, measuring only a millimetre or two across, into which the sample is placed in volumes of only one microlitre or less. The solvent is left to evaporate, leaving a small layer of the sample. The process is repeated to build up a layer that covers the dimple. The tile is transferred into the ion source, which is then evacuated.

3.4.2 Electrospray Ionisation Mass Spectrometry

The Conception Of Electrospray Ionisation

Electrospray ionisation uses a strong electrostatic field to extract ions from solution and desorb them into an ambient bath gas or vapour. [9;15]. It was discovered in 1951 that the electric field present at sharp points of an electrode, such as the ends of a fine metal filament, held at a high potential within a vacuum, was sufficiently powerful to ionise and desorb molecules placed on, or even near to, those sharp points [9;15;23;24]. The intensity of the electric field at these sharp points distorts the potential energy profile for the interaction between the adsorbed sample and the metal surface of the electrode generating a finite probability that an electron from the sample molecule can tunnel into the emitter [9;25]. Under these conditions the energy that is necessary for the desorption of an ion is made considerably less than that required for the evaporation of the neutral molecule. Despite the high electric potential and field on the electrode, the energy transferred to the internal energy of the ionised molecule is quite small, typically of the order of a fraction of an electronvolt, giving the ion a minimal excess internal energy and limiting the fragmentation of the species [9].

Unfortunately, in using high potentials applied to the electrodes, the ions are often desorbed from the surface into vacuum with a high kinetic energy, dependent upon the potential applied. Thus in many cases the energy would be of the order of kiloelectronvolts [9;15].

It was subsequently found that the application of a high voltage to the surface of a non-volatile liquid in a vacuum would produce a similar effect [15;26]. The competing forces of the electric field and the surface tension of the liquid force the liquid into a stable tapering cone, known as a Taylor cone [26-28]. The electric field at the tip of the liquid cone is sufficiently strong to desorb ions containing charge-bearing molecules and clusters of the solvent in an analogous way to the process described above, i.e. the ions are 'extracted' from the liquid by the field and made free, thus producing gaseous ions. To counter the broad kinetic energy range of the ions, the droplets of solvated ions were desorbed into an inert *bath gas* instead of a vacuum, based on work pioneered by Dole [29;30]. The presence of the gas acts to regulate the ion velocity and provide a means to aid the desolvation and desorption process by acting as a source of enthalpy. Thus collisions between the droplets and the gas molecules transfer heat to the droplets and promote their evaporation [15]

The Elements Of The Electrospray Ionisation Process

Electrospray ionisation is actually a misnomer: electrospray does not generate ions. Instead the mechanism requires the ions to be in solution prior to any analysis [9]. Dole was able to ionise biological macromolecules, such as peptides and proteins, through the use of simple solution chemistry. Proteins and peptides all feature many amino acid groups that are sufficiently basic to be protonated (H^+). This is not the only method of charging the analyte molecules. Any number of electrophilic or nucleophilic species can be used to attach positive or negative charge carrying adducts onto the analyte species. Therefore any analyte solution for use in electrospray is a highly polar liquid, with equal proportions of positive and negative ions.

Electrospray ionisation can be considered as a powerful and *"unnatural"* [28] desolvation process in that it takes ions from solution to the gas phase without a phase transition. As such the electrospray process is endoergic[28]. The electrospray mechanism is split into two stages: the dispersal of highly charged droplets into a bath gas of approximately atmospheric pressure (otherwise known as droplet formation), followed by the evaporation of the solvent, freeing the analyte ions (also known as ion formation). Before examining the mechanics behind these processes, it is useful to turn to the apparatus arrangement that makes up the electrospray source.

The Electrospray Source

The electrospray source is built into a gas-tight housing, preventing any contaminants getting in and also any potentially dangerous samples or by-products out, with an aperture leading directly to the mass analyser. The source consists of three items.

Spraying Capillary this is a narrow bore capillary (generally 0.1 mm inner diameter) that is normally made from metal or has been metal coated, and is tapered at one end. The spraying capillary sits within the electrospray source and emits the analyte solution into the source. The analyte solution itself is held externally within a gas tight syringe. A syringe pump provides a low, constant flow of the liquid, normally between 1-50 μl/min, which travels through narrow bore capillary tubing into the spraying capillary from where the solution is emitted.

Ion Optics these provide the necessary potential difference (usually of the order of several kilovolts) to create the high electric field required to promote ion desorption from the analyte solution. Skimmer cones are prominent to separate the pressurised region of the electrospray source from the evacuated region of the mass analyser and to collimate the ions into an ion beam by the application of an electric potential. While the apertures in the ion optics would allow all molecules to be transmitted, both ion and solvent, the electric fields maintain the motion of

ions through to the analyser and prevents them from being removed by the pumps that remove the solvent molecules from the following stages.

Inert Bath Gas the inert bath gas is vital for the production of ions from the analyte solution and the viability of connecting the ion source to a mass spectrometer. The most common bath gas is nitrogen, N_2, and the bath gas can be introduced into the source by a direct flow into the source region. Flow rates vary depending upon the volume of the electrospray source housing and the recommendations of manufactures. A typical working pressure within an electrospray source will be several times atmospheric pressure.

Different arrangements of these components have been developed, but the overall function remains the same. There are two main types of electrospray source, which generate the electric field in different ways.

One method is to use a metal spraying capillary to which a high electric potential is directly applied, and positioning it close to a counter electrode, held at ground or a much lower potential. The electric field then generally acts to propel the ions in the direction of the mass analyser. The potential applied to both the spraying capillary and the counter electrode is the same as the polarity of the analyte ions in solution. A general schematic is given in Figure 3-9 showing the spraying capillary and a planar counter electrode with a small aperture to transmit the ions, followed by a skimmer cone. The bath gas is introduced via a channel that surrounds the spraying capillary and provides a coaxial flow of gas parallel to the flow of liquid. This is often referred to as *Ion Spray* [9;15;31;32].

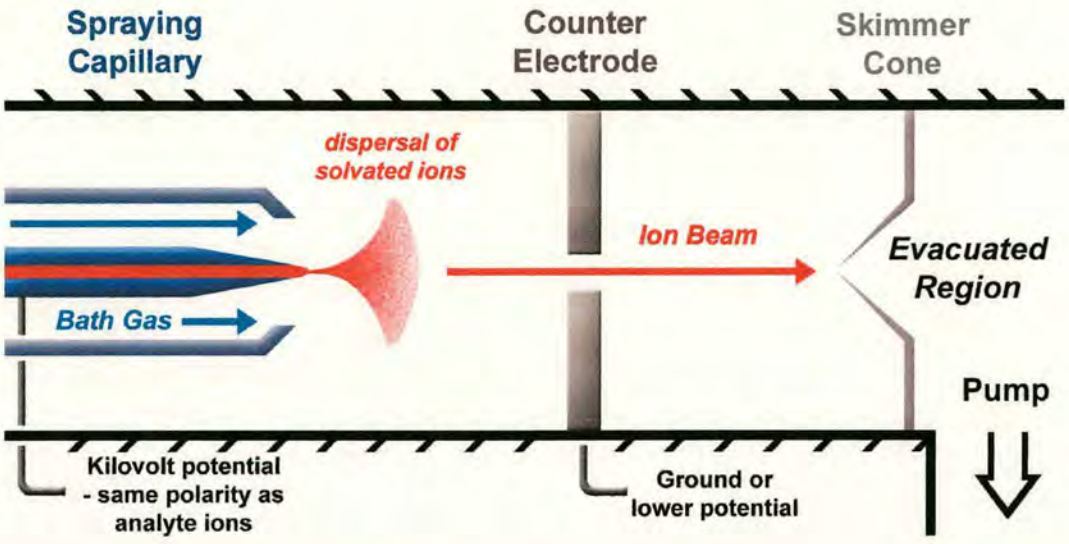

Figure 3-9 A general example of one type of electrospray source where the electric field is generated by the direct application of an electric potential to the spraying capillary. The skimmer cone can also have a potential applied to collimate the ion beam. Diagram adapted from Reference 9.

An alternative mechanism involves spraying the solution from a grounded metal needle into a surrounding metal cylindrical electrode to which a high kilovolt potential is applied of opposite polarity to the analyte ions. The electric field generated is different from the first example due to the geometry of the cylindrical electrode, but the overall result is the same in that the ions are propelled in the direction of the analyser. This is shown in Figure 3-10. This type of electrospray source will normally also feature a glass capillary within the first evacuated region. The ends of the capillary have been metal coated to allow a potential difference to be set up across the capillary. The inlet is set at a potential that is around one kilovolt greater than that on the cylindrical electrode, while still being of the opposite polarity of the analyte ions. The exit is set at a low potential of the sample polarity as the analyte ions, normally 50V [15]. The ions and the bath gas are pushed through the capillary, where the enclosed volume forces lots of collisions between the solvated analyte ions, the inert bath gas molecules and the walls of the capillary, aiding the desolvation process.

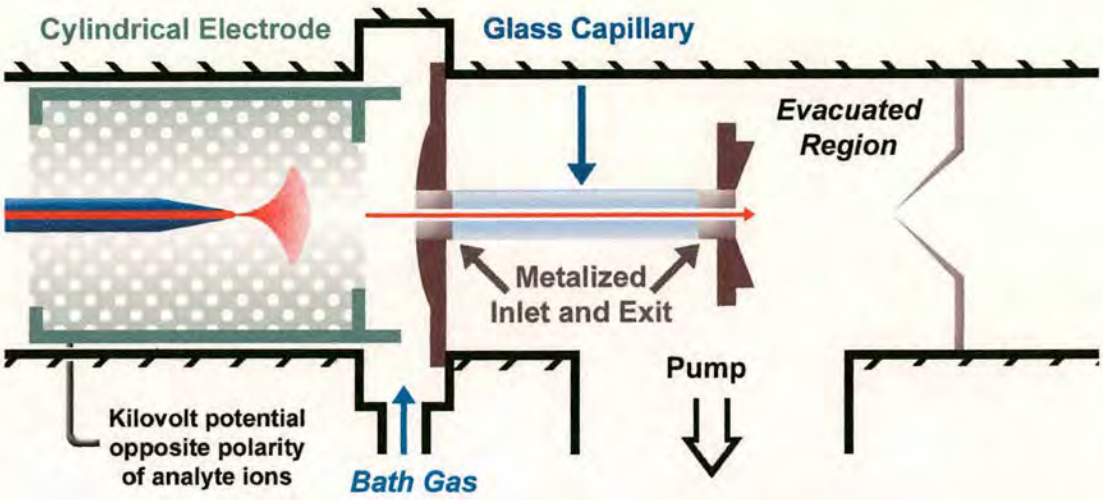

Figure 3-10 An alternative electrospray source. In this example the metal capillary is held at ground, while the electric field is applied to a cylindrical electrode that surrounds the capillary. Diagram adapted from Reference 15.

Now that the means by which the electrospray process works is set out, the mechanism by how it all works can be explored. To simplify the discussion, it shall be assumed that in all the following descriptions the analyte ions are negative, matching the polarity of the ions under study in this thesis.

Droplet Formation

The electric field created in the first stage of the electrospray source partially penetrates the liquid present at the tip of the spraying capillary. When dealing with negative ions the field causes the negatively charged analyte ions to drift towards the surface of the liquid, while the positively charged counter ions present within the solution move away from the surface. The redistribution of charge continues until the electric field inside the liquid is effectively cancelled out[28].

The accumulation of negative charge destabilises the surface of the liquid because the negative ions are drawn down the electric field but are unable to escape from the liquid, forcing the liquid to be drawn out into the Taylor cone. The electric field acting at the tip of the Taylor cone makes the cone unstable, and a fine thread of liquid, with an approximate diameter of a few micrometers, is emitted from the tip of the cone. The surface of this liquid filament is enriched with the negative ions [28]. At

some point downstream, the filament becomes unstable and forms individual droplets. The surfaces of the droplets are also enriched with the negative analyte ions, but there are no positive counterions within the surface of the droplet, giving the surface an excess negative charge density.

The droplets begin to evaporate, losing solvent molecules. As the volume of the droplet decreases the surface charge density increases until it reaches *Rayleigh limit* [9;33]: the point at which the combined forces due to the electrostatic repulsion between the analyte ions on the droplet surface is equal to the force of the surface tension [15;33]. On exceeding the Rayleigh limit the droplet becomes extremely unstable and the droplet breaks up, forming much smaller droplets, further acting to desolve the ions from the solution. This event is sometimes referred to as a *Coulomb Explosion*[9;15;32;34]. The same process occurs again with the smaller droplets, setting up a cascade reaction of ensuing Coulomb explosions.

The presence of the bath gas provides extra assistance to the desolvation process. The neutral bath gas molecules strike the droplet, transferring a portion of the relative kinetic energy of the collision pair into thermal energy. This increases the thermal energy of the entire droplet, and given sufficient collisions can prompt the evaporation of the volatile solvent molecules from the droplet. Collisions between the droplets and the inert bath gas molecules are facilitated by the existence of a considerable ion-molecule attraction that exists between the charged droplets and the gas, the nature of which is discussed in Chapter 4.2.1. Despite the energetic collisions, the collisions with the bath gas also serve to quench the excess internal energy of the analyte ions, and it has been experimentally verified that the analyte ions are internally relaxed after the similar collision conditions [35]. In addition, the collisions remove a portion of the translational energy of the droplet/ions. With the bath gas pressure being such that the gas molecules are far in excess of the number of droplets/ions the charged species never reach their theoretical maximum kinetic energy dictated by the electric field between the spraying capillary and the sample cone. The kinetic energy of the ions is then kept at a level corresponding to the

natural velocity distribution of the gaseous molecules at the given source temperature [15]. The ions are thus described as being *thermalised.*

It is worthwhile to illustrate this point by determining an order of magnitude value for the number of collisions that would occur within the source region of the electrospray ion source. This shall be done using a hard sphere model for working out the collision cross section, and thus the mean free path. While there are more accurate methods of determining the collision cross section, such as the Langevin model used for collisions between charged species and neutrals (as covered in Chapter 4.2.2), they shall not be used here since the number of charges on the initial droplets is very high and not known. Thus the mean free path is determined from Equation 3.8:

$$\lambda = \frac{1}{\sqrt{2}\sigma}\left(\frac{V}{N}\right) = \frac{1}{\sqrt{2}\sigma}\left(\frac{k_B T}{p}\right) \tag{3-8}$$

Where σ represents the collision cross section. For the hard-sphere model of gas particles the collision cross section is determined as:

$$\sigma = \pi . d^2 \quad \Rightarrow \quad d = \frac{1}{2}\left(d_{droplet} + d_{N_2}\right) \tag{3-9}$$

where $d_{droplet}$ is the diameter of the emerging droplet, and d_{N2} is the diameter of the nitrogen molecule, (1.09 Å = 1.09E^{-10} m), the most common type of bath gas. To begin with the ions emerge as large droplets, and at the end are considerably smaller free ions, thus the mean free path will get larger as desolvation occurs. The pressure within the ion source can be taken to be one atmosphere, which converted to SI units is roughly 100,000 Nm^{-2}, while the temperature is taken to be 90°C (363 K) and Boltzmann's constant k_B is 1.38E^{-23} JK^{-1}. Assuming a conservative first droplet size of around 2 μm diameter [28] the initial mean free path for the droplet can be determined to be of the order of 10^{-15} m. Conversely, for a free ion with a diameter, d_s, of 10 Å, the mean free path is of the order of 10^{-9} m. Given that the separation between the counter electrode and the spraying needle is normally of the order of millimetres, the number of likely collisions will be between several thousand billion to hundreds of thousands of collisions within this region.

The above calculation overestimates the number of collisions by some degree, since it does not account for the existence of the pressure gradient that will exist between the pressurised source region and the adjacent evacuated stage. Thus the majority of the nitrogen gas density will be situated nearer the spraying capillary. In addition the heated neutral bath gas is normally continuously pumped into the instrument, and therefore the gas molecules carry an additional kinetic energy above the thermal level. However, under such an overwhelming number of collisions it is clear that the free ions will never be able to reach the velocity that would be attainable in vacuum, and so the velocity of the ions will be slowed to comparable levels with the neutral gas flow. The resultant velocity of the ions on exiting the sample cone will then be similar to that of the gas flow velocity.

Ion Formation

The topic of ion formation within the electrospray process is a contentious issue. There are currently two major theories for just how the ions are finally freed from their solvated state, each with their own list of defenders and reasoning.

The first is that envisaged by Dole himself. The cascade of Coulomb explosions occurs until finally the ions are entirely released from the droplets and made free, while all the solvent molecules have been desorbed into the bath gas, providing that the charge is still held by the analyte ion and has not been lost in the desorption process [9;15;28;32]. This process is sometimes referred to as a *charge residue* mechanism [15], and is reasoned to be the most favourable on energetic grounds [28].

The second theory of gas-phase ion production is based on the work of Iribane and Thomson [36] and is an implicit form of field desorption [9]. The analyte ion is evaporated from the small and highly charged droplets. The repulsion between the ions in the droplet essentially force an analyte ion out from the droplet in what can be considered as an evaporation process[9], and it becomes a free ion [32;36]. Iribane and Thomson suggested that the necessary field required for direct ion evaporation could be achieved without exceeding the Rayleigh limit [9;15;36]. This theory also supports the observation of distributions of multiply charged ions recorded by mass

spectrometry. It is thought that only by direct ion evaporation could the ions maintain their numerous charge states [9;15;32].

The precise mechanics of the process is a matter that is unlikely to be resolved any time soon, and certainly has no obvious bearing on the results of this thesis. The strength of each case is dependent upon the conditions within the source and the solutions used, but at the end of the day the ions are made free from the solvent ions and ready to be analysed by mass spectrometry. For those that are interested there have been some excellent and very thorough reviews of each of the proposed mechanisms in the literature, although each chooses and defends its own preferred mechanism [15;28;32;37].

Collision-Induced Dissociation Within Electrospray

The electrospray mechanism is largely dependent upon collisions between the solvated ions and an inert bath gas to produce free ions before entry into the evacuated region prior to analysis. However, the first evacuated region within most electrospray sources is usually of the order of tenths of a millibar, since it acts as an interface between the atmospheric conditions of the source and the rigorous vacuum required by the analyser (with a pressure of at the very least 10^{-5} millibar, and often much lower). This intermediate pressure suggests that there is a sufficient partial pressure of bath gas still present that could be made to react with the free ions.

The inclusion of accelerating ion optics within the first evacuated region after the source provides a means of providing the ions with sufficient initial kinetic energy to endure dissociating collisions with the neutrals prior to analysis. If the ions are internally cool on leaving the electrospray source, as suggested earlier [15;38], then the only activating collisions will occur outside of the pressurised region. It is generally considered that the most efficient collision-induced dissociation occurs in the intermediary region between the electrospray source and the analyser, and their corresponding extremes of pressure [9;39-41].

However, it is possible that the most efficient region for activating collisions may well occur beyond this region. Many electrospray interfaces feature an r.f. only hexapole (similar to the quadrupole but with a symmetric arrangement of six rods) as an ion guide just between the intermediary region discussed above and the analyser itself. The pressure surrounding the hexapole is nominally just less than that of the analyser. Work performed by the noted mass spectrometrist Dick Smith in America had suggested that the most efficient region for activating collisions and dissociations is positioned just after the hexapole [41], work that has recently been corroborated by a team of French researchers [40].

In either case the use of collision-induced dissociation in electrospray, also known (inaccurately to a degree) as *in-source* dissociation, has been used extensively to provide a quick means of extracting structural information from a variety of species, and as a "warm-up" procedure for subsequent, more stringent, collision-induced dissociation conditions [9;32;42-47]. However, since the technique is not a true MS/MS method, the resultant fragment ions observed could be from any number of possible parent ions, which does place a limit on certain types of analysis that would be possible.

3.5 Mass Analysers

The mass analyser is undoubtedly the working end of the mass spectrometer, but its importance today has been matched by sample introduction and ionisation: a direct result of the push for the analysis of biological materials. The process of separating an assembly of ions by their charge and mass need not be overly complicated in terms of the application of the electric and/or magnetic fields, nor by the processing that follows to generate the mass spectrum. Although numerous mass analyser types exist, no single one could be described as being dominant in the abilities it offers. Each mass analyser has its own distinct advantages, ranging from such properties as ease of operation and maintenance, and inherent high resolution.

Across the work of this thesis, three different types of mass analyser have been used to study the transition metal carbonyls. Each varies in its method of operation and its overall abilities, and therefore each shall be looked at in detail in the subsequent sections.

3.5.1 Time-Of-Flight Mass Spectrometer

Principles of Time-Of-Flight

The *time-of-flight mass spectrometer* (*TOF-MS*) is by far the most conceptually simple model of analyser that is in current use today. The operating principles of time-of-flight are such that the analyser does not explicitly measure the mass-to-charge value of gaseous ions, but instead measures their momenta. The principle behind such measurement is that a population of gaseous ions, with a distribution of mass and charge, that travel in the same direction with constant kinetic energy will have a corresponding distribution of velocities, where the velocity is inversely proportional to the square root of the mass-to-charge ratio [48]. Whereas scanning mass analysers separate ions spatially the time-of-flight analyser separates ions temporally. A commonly used axiom regarding time-of-flight mass spectrometry is [48]:

"it matters just as much when the ions are as where they are."

Measuring ion momentum can be performed by means of a simple arrangement of electrodes. An external electric field, created by the potential difference between two electrodes, can be made to accelerate ions in a given direction. For the sake of this review it shall be assumed that initially the ions are at rest and so commence acceleration at the same point in time and from a spatial plane perpendicular to the acceleration vector. The ion source is placed within the acceleration region of the time-of-flight instrument, which can lead to the entire accelerating electrode arrangement being referred to as the source region. After extraction the ions enter the *drift region*, or *field-free region*, where no external electric field operates. Both areas are evacuated, with the drift region normally evacuated to a higher degree than

the source. The ions travel through the drift region with the velocity defined by the field and their mass and charge, before reaching the detector.

A general schematic of a linear time-of-flight instrument is shown in Figure 3-11 analysing two ionic species, A and B, each carrying unit charge, but having different masses, m_A and m_B respectively. In this scheme, $m_A < m_B$. Thus the mass-to-charge value of the ions can be taken as their mass. Ions of the same mass-to-charge value form discrete ion packets, temporally separated from all other ions. The motion of the ions A and B as they travel through the instrument is shown in Figure 3-11 at evenly spaced points in time, denoted from t_1 through to t_8. The mass spectrum is then constructed from the arrival times of the ion packets at the detector. As such the entire procedure of analysis is usually pulsed. The potentials are applied to the accelerating electrodes at time $t = t_o$ for a given length of time, normally of the order of microseconds before being switched off again. The observed time-of-flight is thus recorded respectively of $t = t_o$. The record of ion abundance against time is then converted into a mass spectrum.

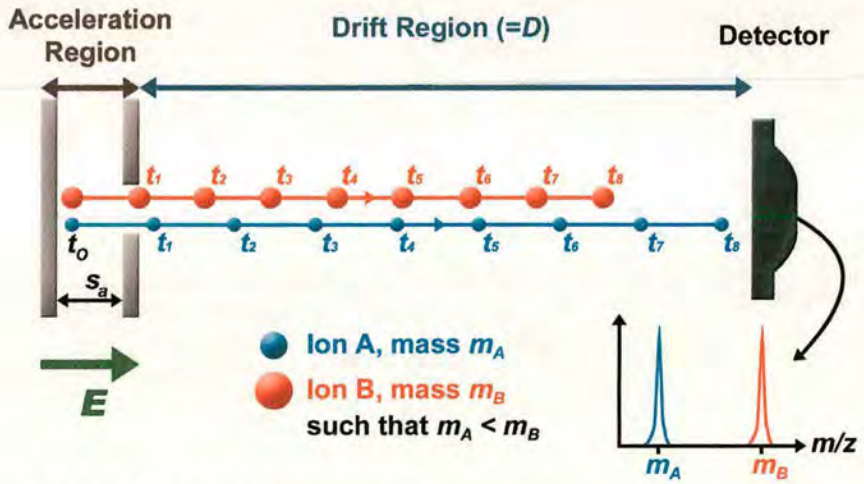

Figure 3-11 A general schematic of a linear time-of-flight mass spectrometer, showing the motion of identically charged ions A and B through the instrument. The vector of the electric field is represented by ***E***. The term s_a represents the distance travelled within the accelerating region. The length of the drift region is denoted by *D*. The terms $t_{1\text{-}8}$ relates to evenly spaced snapshots in time. Thus the motion of the ions is shown for the progression in time. It can be seen that the lighter ion A has a greater velocity and shall reach the detector before the heavier ion B.

The pulsed nature of the instrument means that time-of-flight instruments cannot work with a continuous flow of ions, such as that produced from an electrospray source, unless some means of forming the ions into coherent ion packets is first employed, i.e. a linear RF multipole (details of which in the following chapter on linear quadrupole mass analyser). Laser desorption ionisation naturally works by producing plumes of gaseous ions from a pulsed laser beam, and as such laser desorption ionisation is one of the most common ionisation mechanisms for time-of-flight mass spectrometry.

The controlling physics behind the temporal separation of the ions is quite uncomplicated. The velocity of the ions never reaches relativistic levels, and so Newtonian physics are perfectly adequate to determine the equations of motion for the ions [48]. The following is a look at the equations of motion of an ion in a linear instrument. The overall goal is to determine the total time-of-flight of the ion, from the beginning of the pulse at $t = t_o$, to detection.

An ion has charge $q = z.e$, where z is the number of positive or negative charges on the ion, and e is the magnitude of the charge of the electron. The ion is placed between two electrodes at a point denoted as s_o. Potentials applied to the electrodes generate a potential difference, ΔV, which creates an electric field. The electric field strength, E, is equal to the potential difference between the electrodes, divided by the distance travelled by the ion under the influence of the field, denoted by s_a.

$$E = \frac{\Delta V}{s_a} \tag{3-10}$$

The potential difference defines the kinetic energy of the ion, and thus its maximum velocity. Thus the ion is accelerated from an initial starting velocity, u_o, to the maximum allowable velocity before the ion enters the field-free drift region. Therefore the ions travel though the drift region with the maximum possible velocity, which should theoretically remain constant. This is defined as the *drift velocity*, u_D, such that:

$$KE = q\Delta V = qEs_a = \tfrac{1}{2} mu_D^2$$

$$u_D = \sqrt{\frac{2qEs_a}{m}} \tag{3-11}$$

The force, F, experienced by the ion in the presence of an electric field, E, is equal to:

$$F = Eq$$

This force accelerates the ion in the direction of the electric field. The acceleration can be determined from Newton's second law of motion:

$$F = ma \quad \therefore \quad a = \frac{Eq}{m}$$

The acceleration must be determined so that one can calculate the time spent by the ion accelerating to the drift velocity. The acceleration is defined as the differential of the velocity with respect to time:

$$a = \frac{\mathrm{d}u}{\mathrm{d}t} = \frac{\mathrm{d}}{\mathrm{d}t}\left(\frac{Eq}{m}\right)$$

$$\therefore \quad u = \int\left(\frac{Eq}{m}\right)\mathrm{d}t$$

$$\therefore \quad u = u_o + \left(\frac{Eq}{m}\right)t \tag{3-12}$$

This equation determines the velocity of the ion at any time, t, under constant acceleration. Since the kinetic energy is fixed by the one electric field the ion can only accelerate to its maximum drift velocity. The time required for acceleration from u_o to u_D can be calculated by:

$$t_a = \frac{u_D - u_o}{E}\left(\frac{m}{q}\right) \tag{3-13}$$

If one can assume that the ions are initially at rest before acceleration, then $u_o = 0$ and the acceleration time is readily determined purely from the electrode parameters and the mass and charge of the ion. For completeness it is often assumed that the ions take a finite time to respond to the action of the force, t_o, from $t = 0$ when the potential is applied to the electrodes. The determination of this value is possible but is often overlooked due to its negligible effect to the total flight time of the ion.

The time taken to traverse the drift region, t_D, is simply the length of the drift region, D, divided by the drift velocity:

$$t_D = \frac{D}{u_D}$$

$$t_D = \left(\frac{m}{2qEs_a}\right)^{1/2} D \quad = \quad \left(\frac{m}{2q\Delta V}\right)^{1/2} D \tag{3-14}$$

Finally, one may wish to also include the response time of the detector, t_d although again this is likely to have a negligible effect upon the overall flight time, and its inclusion is dependent upon the desired accuracy of the research.

Therefore the time-of-flight, TOF, is equal to [48]:

$$TOF = t_o + t_a + t_D + t_d$$

$$= t_o + \left[\frac{u_D - u_o}{E}\left(\frac{m}{q}\right)\right] + \left[\left(\frac{m}{2q\Delta V}\right)^{1/2} D\right] + t_d \tag{3-15}$$

Whereas the ion velocity is inversely proportional to the square root of the mass-to-charge ratio, the dependence of the flight time on the mass-to-charge ratio is more complicated. In most time-of-flight instruments the drift time, t_D, is far greater than the acceleration time, t_a. Indeed the drift time is often far greater than the sum of the acceleration time, the response time, t_o, and the detection time t_d, meaning the relationship for the drift time in Equation 3-14 is a good approximation to the flight time of the ions.

Resolution In Time-Of-Flight Mass Spectrometry

In time-of-flight mass spectrometry it is just as valid to measure the resolution from the time domain as it is from the mass domain [48]. Given that the drift time is the dominant factor in the time-of-flight, it can be seen from Equation 3-14 that the mass is directly proportional to the square of the time, thus it is possible to define:

$$m = \mathrm{A}t^2 \quad \therefore \quad \frac{\mathrm{d}m}{\mathrm{d}t} = 2\,\mathrm{A}\,t$$

where A is a constant of proportionality. It then follows that

$$\Rightarrow \quad \frac{dm}{m} = \frac{2dt}{t} \quad \therefore \quad \frac{m}{\Delta m} = \frac{t}{2\Delta t} \tag{3-16}$$

Both the time interval Δt and the mass interval Δm are measured as the full-width at half maximum of the peak.

The resolution is dependent upon the flight time of the ions, which in itself is dependent upon the geometry of the electrodes, the surrounding volume of the source, and most importantly the kinetic energy of the ions [9;48]. Ideally, each ion of a given type would be accelerated to the exact same kinetic energy and reach the detector at exactly the same time as a very tight ion packet. However, this does not always occur, and the ions are frequently given a range of kinetic energies, producing broad ion packets. The size of the ion packet is important for the resolution of the mass spectrum. A broad ion packet will strike the detector over a greater interval of time than a tight ion packet. The longer this time interval is the broader the corresponding peak appears on the mass spectrum, as shown in Figure 3-12.

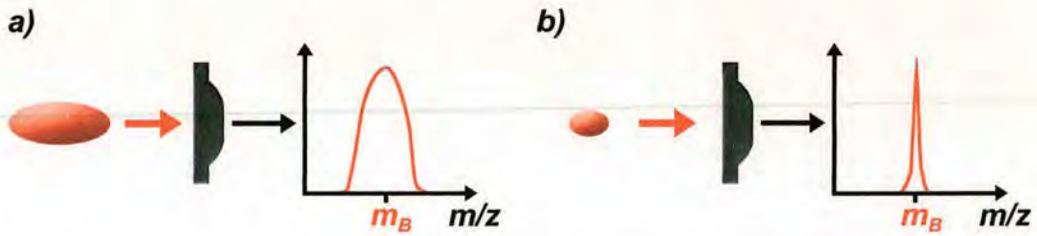

Figure 3-12 a) A broad ion packet will strike the detector and be registered over a longer amount of time. This results in a broad peak in the subsequent mass spectrum centred on the mass-to-charge value of the ion. b) A tight ion packet striking the detector will produce a much higher resolution peak in the mass spectrum.

The broadening of the ion packet can occur from a number of different sources. For example ions that are produced from a species already in the gas phase cannot be localised to a single fixed position prior to acceleration, making the assumptions proposed in determining the time-of-flight in the previous section untenable. Although the motion of gaseous ions is not purely chaotic, the ions are subject to a distribution of velocities. Put simply this means that not all of the ions present

within the ion source will initially be travelling in the desired direction toward the analyser when the accelerating force is applied. The portion of the ions travelling in the opposite direction will be decelerated from their initial velocity to zero, and then accelerated to the drift velocity. The time taken to perform this manoeuvre is defined as the *turn-around time*. All the ions will reach their drift velocity because the time spent traversing the acceleration region is greater than the turn around time, but the ions that were moving towards the detector will be spatially separated from those that had to turn around, broadening the ion packet [48].

Where the ions are produced from a solid surface, via laser desorption ionisation for example, the problem of turn-around time is appreciably reduced. The majority of ions travel the same distance in the acceleration field from the same point in time. However, the ions ejected from the surface will emerge with a distribution of kinetic energy that contributes to the final kinetic energy of the ions after acceleration. The initial kinetic energy is much less than that given to the ions from the accelerating field and so can be assumed to have a negligible addition to the total time-of-flight.

Numerous new technologies have emerged to improve the resolution and accuracy of time-of-flight measurements, with two in particular being the most widely implement, both of which aim to improve the resolution by *energy focussing*.

Time-lag Focussing

Time-lag focussing, developed by Wiley and McLaren [49], is an arrangement of electrodes that is used to accelerate the ions while compensating for the different positions and velocities of the ions [9]. The extraction of the ions is split into a two-part acceleration process, using a series of three electrodes. The first electrode is a planar electrode, which shall be labelled the *source* electrode, while the remaining two electrodes are a delicate system of fine and taught meshes constructed from metal wires. These shall be labelled the *extraction* electrode and the *focus* electrode. The ionisation event occurs between the source and extraction electrodes. Gaseous ions can be formed from laser desorption ionisation from a solid sample on a target plate or from direct introduction of a gas into the volume between the source and

extraction electrodes. A typical arrangement of the electrodes is given in Figure 3-13.

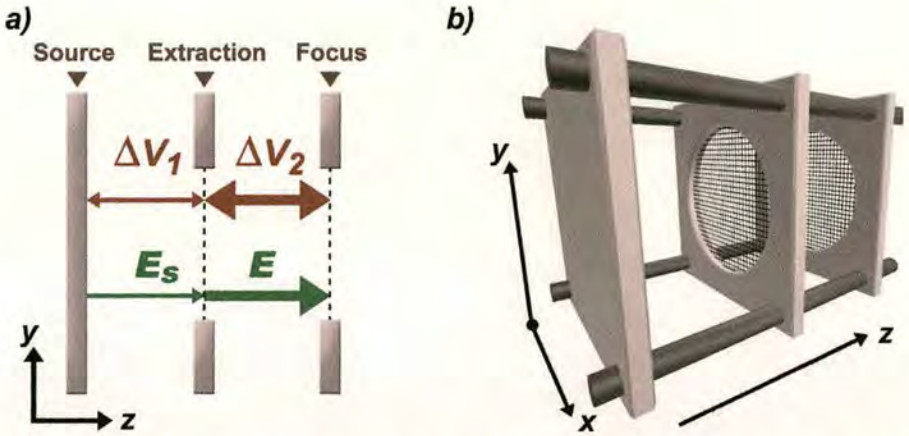

Figure 3-13 An example of a generic Wiley and McLaren style ion source and acceleration electrodes. a) The potential differences applied between the source and extraction electrodes, ΔV_1, is much smaller than the potential difference between the extraction and focus electrodes, ΔV_2. As such the electric field strength E_s is correspondingly smaller than E. Note that gaseous ion production occurs between the source and extraction electrode. b) A three-dimensional representation of the electrode arrangement to aid visualisation.

The mesh electrodes, also known as *grids*, are constructed so as to transmit ions through them while carrying the necessary potential to generate the electric field with the other electrodes. Although a grid electrode does not have a planar surface the field generated is very close to homogeneous with fringe-field effects having a minor detrimental effect upon the homogeneity of the field and the ion velocity [48].

The potentials applied to the source and extraction electrodes are such that the potential difference, ΔV_1 is quite small, for example V_{source} = 20kV, and $V_{extraction}$ = 19.95kV, making a potential difference ΔV_1 = 50V. Therefore the electric extraction field E_s is also small. The ions then enter the main acceleration stage where the potential difference is much greater, of the order of several kilovolts. The electric field strength E, is also much greater and accelerates the ions to their final energy [9].

The small initial extraction field is part of the process in focusing the ions into tight ion packets. Ions that are positioned at the back of the electrode arrangement, near the source electrode, will acquire slightly more kinetic energy than those located near the extraction electrode [9], although this difference in kinetic energy will be relatively small given the small nature of the extraction field strength E_s. A time lag is made between the ionisation event and the first acceleration event, of the order of several microseconds for a typical microsecond ionisation pulse. The time lag provides enough time for the portion of ions that initially move away from the detector after ionisation to get to positions where the extraction field, E_s will give them more kinetic energy than those that are moving towards the detector and are nearer the extraction electrode. Thus after the final extraction stage the final kinetic energies of the ions will be such that minor energy disparities have allowed those ions that initially moved away from the detector to catch up with those that initially moved toward it, so that all ions ultimately reach the detector at the same time. The efficiency of this mechanism is dependent upon the extraction field strength and the period of the time lag, both of which can be tuned to maximise resolution [9].

Reflectron Ion Mirror

An alternative mechanism to improve resolution is to make the more energetic ions follow a longer trajectory by means of a retarding field with the *reflectron* being the most common example [50]. The reflectron can be thought of as an 'ion mirror', a retarding field that reflects incoming ions out towards a desired location. The field is generated from a series of grid electrodes to which potentials are applied to create a linearly increasing electric field, E_R. The reflectron is angled slightly off the centre of the z-axis so that the ions are not reflected back upon themselves and that the detector can be placed in a position in which it will not interfere with the motion of the incident ions. A diagram of a typical reflectron is shown in Figure 3-14.

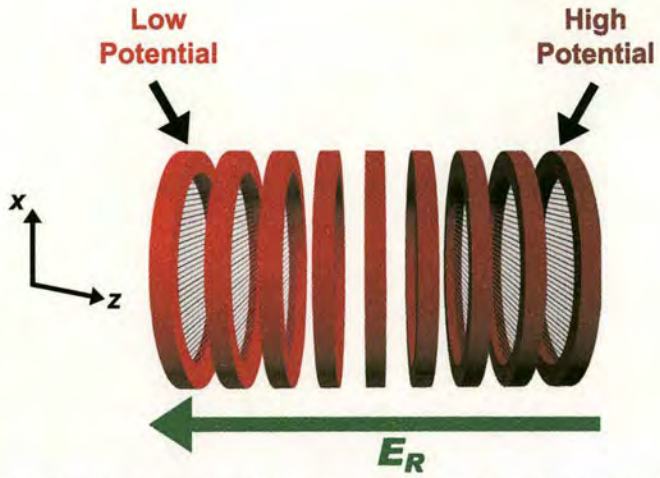

Figure 3-14 A top-down view of an array of cylindrical electrodes to make a reflectron. To generate a linear retarding field E_R, the potential difference between each adjacent electrode is made constant so that the potential increases linearly to the maximum value at the rear of the assembly. The reference axes show how the reflectron is at a slight angle to the *z*-axis.

In operation, those ions that have greater kinetic energies will penetrate deeper into the reflecting field than less energetic ions, and thus take longer to be reflected. The result is that a properly tuned reflectron can ensure that the more energetic ion of a given mass-to-charge value reaches the detector at the same time as the less energetic equivalent ion, as depicted in Figure 3-15. This reflectron is then said to be operating in *full correction* mode.

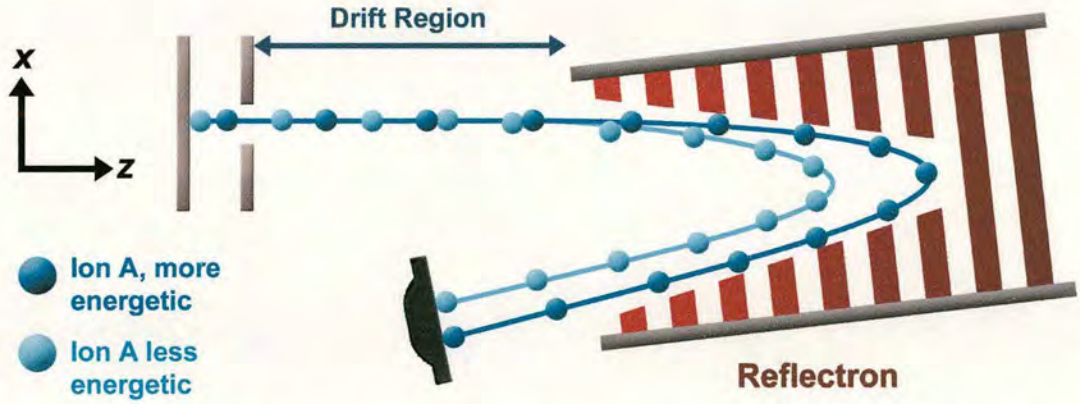

Figure 3-15 The reflectron working in full correction mode to focus ions of the same mass-to-charge value at the detector. A section has been removed from the reflectron so that the trajectory of the ions can be seen as they move through the reflecting field.

In addition to the reflectron producing a more coherent ion packet, it also significantly lengthens the flight times of all the ionic species. In doing so, ions of different mass-to-charge shall have a greater degree of spatial separation by the time they reach the detector, also improving the overall resolution of the entire mass spectrum.

Most commercial instruments feature a combination of Wiley-McLaren double acceleration sources and a reflectron to get the best possible resolution from the instrument. It is also common to see a detector placed behind the reflectron to allow ions to be analysed in a linear system with the reflectron inactive. There have been a number of new developments in time-of-flight mass spectrometry to further improve resolution, with the most notable being the orthogonal acceleration time-of-flight mass spectrometer [51-53], but as yet these have only just entered into commercial instruments.

Ion Fragmentation In Time-Of-Flight Mass Spectrometry

Time-of-flight mass spectrometry is unique in that it is one of the few mass analysis tools that can adequately detect metastable ion fragmentation during the analysis procedure. A metastable ion can be defined as: [1]

> *"An ion which is formed with sufficient excitation to dissociate spontaneously during its flight from the ion source to the detector."*

A defining factor for metastable ions is that the lifetime of the ion prior to the dissociation, is longer than an unstable ion, defined as [1]:

> *"An ion that is sufficiently excited to dissociate within the ion source."*

Similarly, the lifetime of the metastable ion is shorter than that of a corresponding stable ion [1]:

"An ion which is not sufficiently excited to dissociate spontaneously into a daughter ion and associated neutral fragment(s) or to react further before reaching the detector."

Metastable ions are thus observed to dissociate within the mass analyser, with the dissociation event known as *post-source decay.*

As can be seen, the most critical factor for the stability of the ion is its internal energy. A general plot of the internal energy distribution for ions formed in a generic ion source of a mass spectrometer is given below in Figure 3-16.

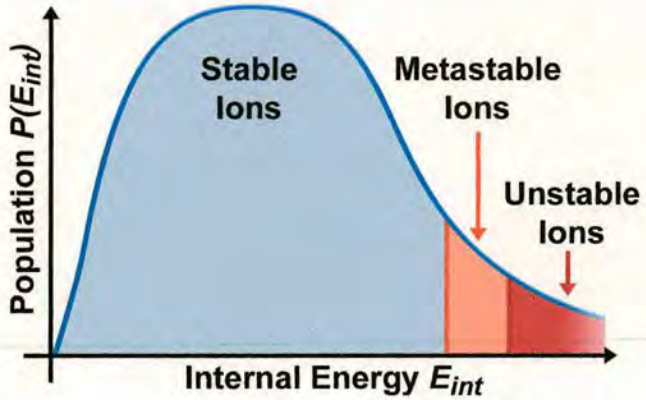

Figure 3-16 A theoretical internal energy distribution of ion population against internal energy. The energy ranges that lead to stable, metastable and unstable ions are indicated. Diagram adapted from Reference 54.

As can be seen from Figure 3-16, stable ions can have a broad range of internal energy, but the metastable ions have an intermediate internal energy, and therefore dissociate with intermediate rate constants. Most metastable polyatomic ions are vibrationally excited ions with internal energies slightly above the threshold for dissociation, and dissociate via vibrational predissociation, the details of which are discussed in Chapter 4.4.1. It is also the case that metastable species decay through the weakest bonds within the molecule [55;56].

A metastable ion of mass m_p and unit charge dissociates to produce a daughter ion of mass m_d and a neutral of mass m_n. The kinetic energy, and hence momentum, p_p, of the metastable ion is fixed by the electric fields of the acceleration region. Therefore

if the metastable ion performs post-source decay and dissociates within the field free region of the mass spectrometer, the conservation of momentum dictates that the sum of the momenta of the products must be equal to the momentum of the parent ion, since there are no other external forces present. In the absence of any changes made to the kinetic energy of the ion resulting from the fragmentation reaction, both the daughter ion and the neutral fragment should have the same velocity, u, as their parent ion. However, this does not account for the scattering of the fragments, which shall leave with different trajectories. Therefore there exists a distribution of fragment velocities, but for convenience only those fragments that maintain their motion toward the reflectron shall be considered since these shall be the only ions that will be detected, and in which instance the velocity of the fragments and parents do match. Therefore if post-source decay occurs within the field free region of a linear instrument the dissociation event will be undetectable. After dissociation both fragments continue to travel with the same velocity as that of the metastable parent ion, and arrive at detector at the corresponding time. Thus the fragment ion would appear on the mass spectrum as having a mass-to-charge value identical to that of its parent, as shown in Figure 3-17.

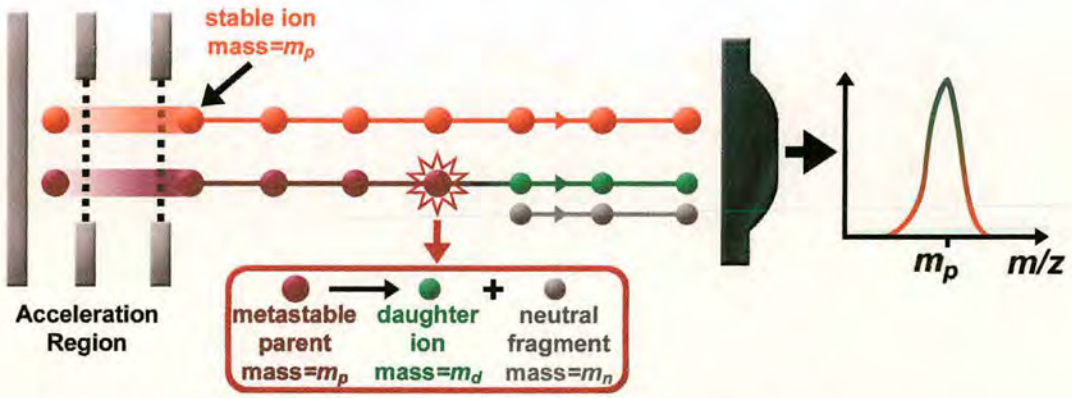

Figure 3-17 Post-source decay occurring in a linear time-of-flight mass spectrometer. Singly charged ions of mass m_p are shown being analysed, one stable, and the other metastable. After the dissociation event the conservation of momentum dictates that the fragments carry the same velocity as that of the stable and metastable ions. Therefore the metastable daughter ion arrives at the detector at the same time as the stable ion, and both register on the mass spectrum as mass m_p.

Now consider the case of post-source decay in a reflectron time-of-flight mass spectrometer, looking at two ionic species, A and B. Firstly assume that the entire population of 'A' ions are stable with each ion having a mass of m_A, and carrying unit charge for simplicity. The mass of each B ion is m_B, where $m_A < m_B$, and they also have unit charge. The population of B ions is not entirely stable and features a small fraction of metastable ions, denoted as B′. The drift velocity of ion A is u_A and the drift velocity of ion B (including both stable and metastable forms) is u_B such that $u_A > u_B$. When the metastable ion B′ fragments, the daughter ion, which shall be denoted as ion C, carries the same charge as its parent ion, and has a mass that is equal to that of ion A, $m_A = m_C$. Thus stable ion A and daughter ion C have the same mass-to-charge value and are equivalent, but not necessarily identical, species.

If the dissociation event occurs in the first field-free region of the instrument, the daughter ion C will have the same velocity as the parent, u_B, as discussed above. The kinetic energy of daughter ion C will therefore be lower than that of its parent, B′ due to its smaller mass, and also lower than that of the equivalent ion A, due to its slower velocity. Thus on entering the reflectron daughter ion C will not penetrate as far into the reflecting field as ion A, allowing C to 'catch up' with A. Running the reflectron in *partial correction* mode allows the metastable daughter ions to almost catch up with the equivalent ion before reaching the detector, so the ions can be detected separately as demonstrated in Figure 3-18. If the reflectron was operated in full correction mode, ion A and ion C would arrive at the detector at the same time, and the dissociation event would not be observed.

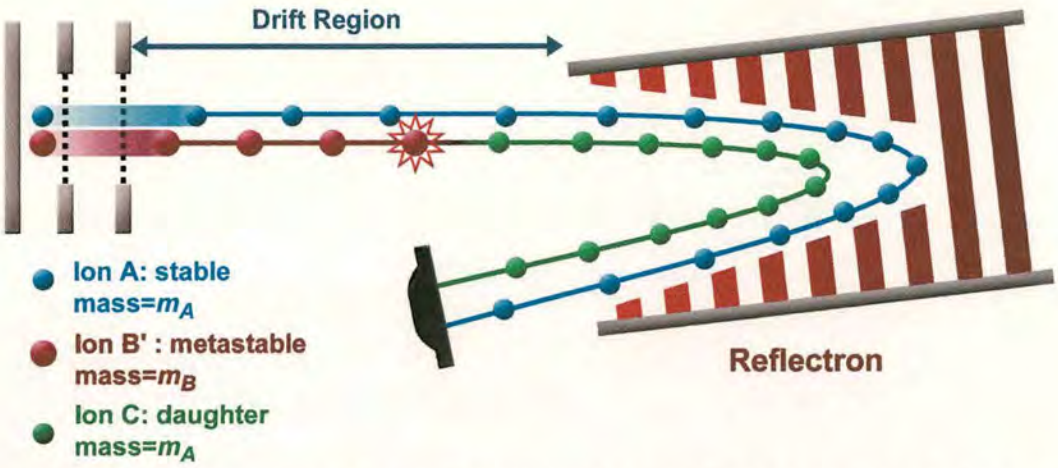

Figure 3-18 Post-source decay of metastable ion B' to daughter ion C in a reflectron time-of-flight mass spectrometer. The motion of the parent and daughter ion is compared to that of ion A. Since all the ions carry the same unit charge, and ion C shares the same mass as ion A, the two ions are equivalent in their mass-to-charge value. Therefore the reflectron is run in partial correction mode so that the daughter ion C can be detected separately from stable ion A.

Not shown in Figure 3-18 is the motion of stable B ions. The kinetic energy of these ions is identical to that of ion A if it is assumed that they are both formed at the same point in the acceleration region. Thus ion B would follow the same path through the reflecting field as ion A, albeit at a slower initial velocity, and arrive at the detector behind ions A and C. The resultant mass spectrum would therefore look something like the theoretical example shown in Figure 3-19.

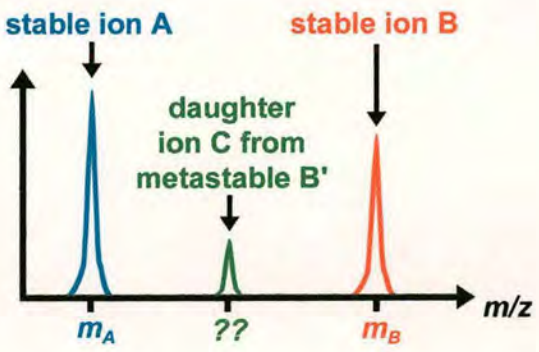

Figure 3-19 A theoretical reproduction of the mass spectrum produced from Figure 3-18. The position of daughter ion C on the mass spectrum is between that of the ion of equivalent mass-to-charge value, in this case ion A, and the stable variant of the parent ion, B.

The exact position of the daughter ion is dependent upon a number of factors. The mass of the fragment ion determines its kinetic energy, and thus the turn around time in the reflectron. A small fragment ion will have a much smaller kinetic energy, and spend less time in the reflecting field. It should then be detected with a mass-to-charge value close to its actual value. This is also dependent upon the strength of the reflecting field and how well tuned it is, i.e. if it is running close to full correction mode for that particular ion. The relative intensity of each peak in Figure 3-19 reflects the reduced population of ion B due to the decay of the metastable ions, with the intensity of ion C providing information of the relative quantity of B ions that were metastable.

However, this review of metastable decay has so far neglected the possibility of any increase in kinetic energy emerging from the dissociation reaction. The phenomenon of *kinetic energy release* is a known consequence of any dissociation process where the internal energy is above the dissociation threshold. Part of the excess internal energy is partitioned into the kinetic energy of the products [57;58]. The metastable daughter ions will therefore have a slight difference in their kinetic energy after dissociation. While this does effect the mass-to-charge values at which all daughter ions are detected, the extent of this change to the kinetic energy is not particularly severe and the principles of the above arguments hold true to a good approximation. A review of kinetic energy release is covered in Chapter 4.4.3.

3.5.2 Quadrupole Field Mass Filter

In 1953 the German physicists Wolfgang Paul and Hans Dehmelt published their research into the use of quadrupolar electrical fields for the separation of ions for mass spectrometry, work that would later earn them the Nobel Prize for physics in 1989 [8;59;60]. The quadrupolar field can be generated by two electrode arrangements. One option is a collection of three electrodes – an equatorial ring electrode and two end-cap electrodes with hyperbolic cross-section, which together make a hollow region in the centre where the ions are stored. This is a *quadrupole field ion trap*, but is more commonly referred to by the term ion trap.

The second option of generating a quadrupole field is from an arrangement of four parallel metal rods that are symmetric to the *z*-axis. This arrangement is a *linear quadrupole mass filter*, but is commonly shortened to the term *quadrupole* in mass spectrometry. It is this type of quadrupole field mass analyser that is used in some of the work featured in this thesis. An example of a typical quadrupole set-up is shown in Figure 3-20. The rods can have either hyperbolic or circular cross-section, and the distance between the centre of the face of the rods and the *z*-axis is r_o.

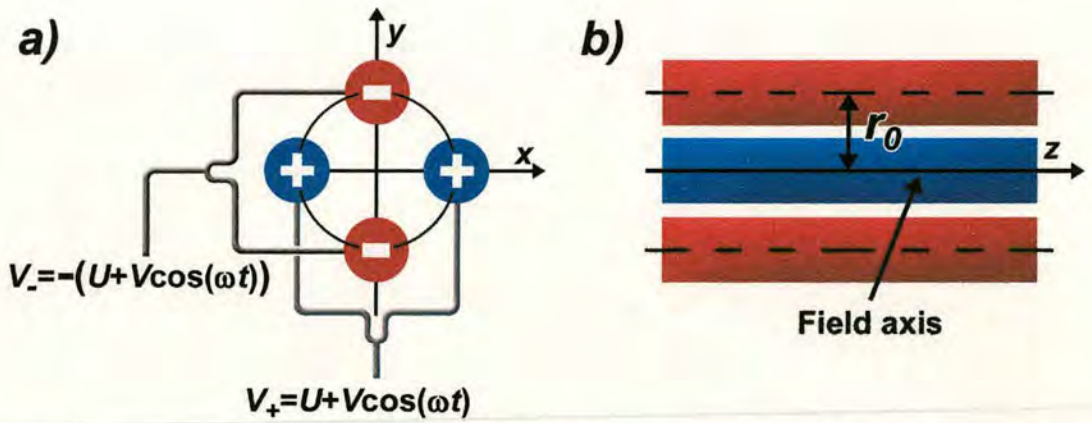

Figure 3-20 A general schematic of a linear quadrupole mass analyser with rods of circular cross-section. a) The arrangement of rods and the respective potentials applied to the vertical and horizontal pair of electrodes are shown. b) The separation between the centre of the rods and the *z*-axis, r_o can also be thought of as the radius of curvature of the quadrupole. Diagram adapted from Reference 9.

The Quadrupole Field

The voltage supplied to the electrode rods has two components:

1. A direct current (d.c.) component, U,
2. A radio-frequency (r.f.) component $V\cos(\omega t)$. This voltage component has a time dependent sinusoidal form, with an amplitude that varies between zero and the maximum voltage, denoted by V_o. ω is the angular frequency of this component, such that the frequency is equal to $\omega/2\pi$.

The electrodes can be split into horizontal and vertical pairs. The potential applied to the horizontal pair on the *x*-axis is [9;34]:

$$V_+ = U + V\cos(\omega t) \tag{3-17}$$

Similarly, the potential applied to the vertical pair of electrodes on the *y*-axis is [34]:

$$V_- = -U + V\cos(\omega t + \pi)$$

$$\therefore \quad V_- = -[U + V\cos(\omega t)] \tag{3-18}$$

As can be seen from these equations, and Figure 3-20, opposite sets of electrodes have the same charge, but are biased with d.c. voltages of opposite polarity, and the r.f. components are out of phase by 180° [34].

A superposition of constant and periodic components to the potential is necessary for the assembly to function as a mass analyser. If only a constant potential was applied the ions would travel in simple harmonic motion in the *xz*-plane with finite amplitude. However, the amplitude of the oscillatory motion in the *yz*-plane would gradually increase, and the ions could crash out onto the walls of the quadrupole rods or otherwise be lost from the assembly. The ion motion in the *xz*-plane is defined as *stable* ion motion since the ions would stay within the quadrupole, whereas the ion motion in the *yz*-plane is defined as *unstable* ion motion [61].

If the potential were a periodic function of time the motion of ions in both the *xz*-plane and *yz*-plane would oscillate around the *z*-axis. The ion motion could be stable in both planes if the periodicity of the field was short enough, and the mass-to-charge ratio of the ion sufficiently large, that the ion would respond slowly to the outward motion of the field and stay within the quadrupole [61].

A combination of a constant and periodic potential provides the ideal control of ion stability. Ions moving in the *x*-direction with a particularly low mass-to-charge value will have unstable trajectories when the magnitude of the periodic potential component exceeds that of the constant potential. Thus the ion will oscillate with an increasing amplitude and eventually be lost. Therefore ions with large mass-to-charge values can be transmitted through to the detector with no problem, and so the *x*-direction is termed a *high-pass mass filter*. Correspondingly, ions moving in the *y*-direction with a large mass-to-charge value would be unstable because of the presence of the constant potential. However, ions with small mass-to-charge values

are stabilised by the periodic component if the amplitude and frequency are such that they can correct the trajectory of the ion when its oscillatory amplitude is increasing. Therefore the *y* direction is termed a *low-pass mass filter* [61].

Combining the motion of the ions in the two directions generates a sophisticated mass filter with a controllable size of *band-pass*: the range of mass-to-charge values, Δm/z, that correspond to stable ion motion. Thus the quadrupole can be used for the separation of ions of different mass-to-charge. The overall motion of the ions is to travel in the direction of the *z*-axis while oscillating in the *xy*-plane, with a frequency that is dependent upon the mass-to-charge value of the ion, and a stability that is dependent upon the oscillation frequency, the amplitude of the applied components of the potential and the geometry of the quadrupole rods. Ions with a mass-to-charge value that falls within the defined band-pass shall travel through the quadrupole to the ion detector, while all other ions shall have unstable ion motion and be lost, as depicted in Figure 3-21.

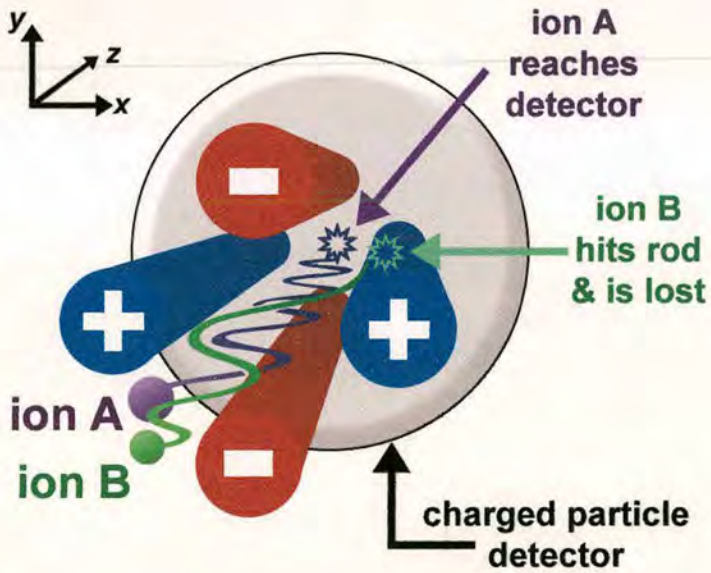

Figure 3-21 Ion A has the correct mass-to-charge value to traverse the field with stable motion and reach the detector. Ion B is outwith the band-pass, consequentially exhibiting unstable motion in the *x*-direction and is eventually lost on one of the quadrupole rods. Note that for simplicity, only the oscillatory motion of the ions in the *xz*-plane has been depicted for ease of illustration and visualisation. It can be assumed for this example that motion in the *yz*-plane is stable for both ions.

Determining Stable Ion Motion In A Quadrupole Field

The equations of motion that describe stable and unstable ion trajectories had existed for over a century [62] before the development of the quadrupole mass analyser. In the mid-nineteenth century, the mathematician Mathieu determined solutions for describing regions of stability and instability on vibrating stretched skins [63], equations that are now known as Mathieu equations. These same equations were applied to define the limits of stability for ion motion through the quadrupole. The processing of these equations to prove their validity for quadrupole fields and determining the equations of ion stability is beyond the scope of this thesis. However, processing of the Mathieu equations yields two parameters, known as *operating points*: a and q [61]. These are defined by [9]:

$$a = \frac{8zU}{mr_0^2\omega^2} \tag{3-19}$$

$$q = \frac{4zV_o}{mr_0^2\omega^2} \tag{3-20}$$

The operating points define the values of the potentials for an ion of a particular mass-to-charge value and r.f. frequency, ω, to pass through the quadrupole field and reach the detector [61]. A plot of q against a generates the quadrupole stability diagram, also known as a Mathieu diagram, in which it is shown what values of a and q produce stable and unstable ion oscillations. A quadrupole stability diagram is given in Figure 3-22.

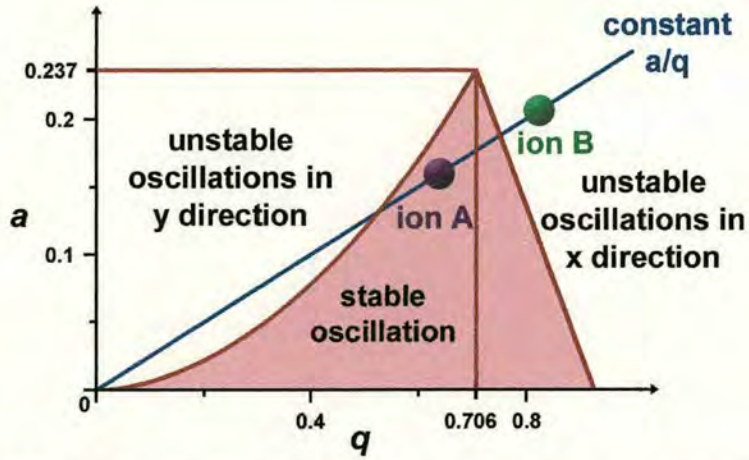

Figure 3-22 A stability diagram for a linear quadrupole mass analyser. The regions of ion stability and instability in the respective directions of motion are shown. Diagram adapted from Reference 9.

It can be seen from Equations 3-19 and 3-20 that the ratio a/q is equal to $2U/V_o$, independent of the mass-to-charge ratio. Therefore the operating points for all ions lie on the same line of constant a/q, as shown in Figure 3-22, which passes through the origin of the stability plot. This is known as the *mass scan* line [61]. Figure 3-22 shows that when the a parameter is non-zero, only the ions that appear in the stability region will pass through the quadrupole and reach the detector. In correlation to Figure 3-21, the stability diagram shows ion A within the stable oscillation region, whereas ion B has an unstable oscillation in the x-direction. By increasing the value of the U/V_o ratio, the mass scan line approaches closer to the tip of the stable region, resulting in a narrower band of mass-to-charge values that will be stable [61].

The equations for determining ion stability are devised for the ideal conditions that the rods have infinite length, an unlimited cross-section and are placed at exactly the right symmetrical points around the z-axis. These criteria cannot be met in reality, due mainly to the finite dimensions of the rods, and so the quadrupole field generated is imperfect due to fringe field effects and rod misalignment from the theoretical ideal. Despite these problems the quadrupole still performs as an effective mass analyser [61].

Quadrupole Operation

A quadrupole mass analyser is an example of a *scanning* mass analyser. The range of mass-to-charge values that is to be examined, which shall be refered to as the experimental window, is selected before the analysis begins. The magnitude of the band-pass, $\Delta m/z$, can also be controlled, and remains constant throughout the analysis procedure. The band-pass is gradually moved between the upper and lower limits of the experimental window and only those ions that fit within the confines of the band-pass will be detected, while all other ions are lost. A constant flow of ions is necessary for a mass spectrum to be recorded, a fact that reflects the popularity of interfacing electrospray ionisation sources to quadrupole mass analysers. In addition, the quadrupole can only operate with ions injected into the array at relatively low speeds, normally achieved by an accelerating voltage of 10-20 V [9]. Again the electrospray ionisation source can fulfil this criterion since the temperature of the bath gas controls the velocity of the ions and can easily maintain the ions at the necessary low kinetic energies prior to the final evacuated transfer region directly before the analyser. Here another R.F. only multipole, typically a hexapole, will accumulate the ions into a coherent packet for sending into the quadrupole analyser.

In a standard quadrupole the mass spectrum is generated by maintaining a constant r.f. frequency, ω, and varying both the magnitude of the constant potential, U, and the maximum magnitude of the r.f. potential, V_o simultaneously while keeping the ratio of U/V_o constant [9;34]. The recorded mass-to-charge values are proportional to V_o, such that a linear increase in this parameter provides an easily calibrated linear mass-to-charge scale [9]. It is possible to generate a mass spectrum by varying the r.f. frequency while keeping both U and V_o constant, but this option is not particularly convenient to perform.

Resolution Of The Quadrupole Mass Analyser

The magnitude of the band-pass, which correlates to the mass separation, Δm, directly controls the resolution of the quadrupole, which itself is controlled by the d.c. voltage U. A high resolution corresponds to a high value of the a/q ratio, where a considerable proportion of the selected ions oscillate with just enough amplitude to be lost, reducing the overall transmission of the ions. The band pass at lower values

of *a*/*q* is broader, and so the resolution is decreased as the transmission increases. It is theoretically possible to run a quadrupole at very high resolution by operating at a value of *a*/*q* that is close to the apex of the triangular stable region as depicted in the stability diagram in Figure 3-22. However, this is not feasible in practice, since the maximum possible resolution is dependent upon the initial ion velocities in the *x* and *y* directions, and the positions at which the ions enter the quadrupole. Therefore the quadrupole is regarded as being a low-resolution mass filter, but one that is more than adequate for a wide variety of analyte species and research programmes [9].

3.5.3 Fourier Transform Ion Cyclotron Resonance Mass Spectrometer

Origins Of FT-ICR MS

The *ion cyclotron resonance* (ICR) principle was first described by E.O. Lawrence in the early 1930's [64;65], to explain the motion of charged particles within a uniform magnetic field, ***B***. The motion of the ions is dependent upon the mass and the charge of the ion, (as shall be discussed later) and so it was a logical progression to implement the ICR principle to mass spectrometry. This was first done with the creation of the omegatron, built in 1949 by Hipple, Sommers, and Thomas [66;67]. The technique developed quite quickly, with the next generation of ICR mass spectrometers featuring a trapped ion cell, first developed by McIver [68]. The ion cell used an electric field in addition to the magnetic field, to constrain the ions to a three-dimensional volume. This allowed an improvement in instrument resolution, and an increase in the potential of the system to be used as a reaction "test-tube", due to the stability of the of the ions within the cell. The first implementation of the Fourier transform ion cyclotron resonance mass spectrometer came in 1974, when Comisarow and Marshall used an oscillating electric field with a linearly varying frequency to perform the trapping operation of the ion cell [69]. The motion of the ions induced an electric current (known as an *image current*) in a system of electrodes. This current was converted to an oscillating voltage, amplified and then digitised to give a time-domain signal (i.e. the variation of ions signal with time). The Fourier transform is a numerical algorithm that can be applied to discrete data sets for the conversion of a time-domain signal into a frequency spectrum. The speed at which

this operation can be performed is of the order of milliseconds for even the largest of data sets, allowing the instrument to be tuned and record mass spectra in real time [70].

The Ion Cyclotron Resonance Cell And The Motion Of Ions

The construction of the ICR cell and the motion of the ions within is fundamental to the way in which the ions are detected and the mass spectrum is recorded. A good general starting point for this study is to examine the general configuration of the ICR cell. The cell consists of a system of electrostatic plates, of which there are many different possible configurations in use today [71]. The following appraisal of the workings of the FT-ICR MS shall be constrained to those applied in the Bruker® instruments used within this thesis. Thus the ICR cell is an ion trap consisting of a series of four electrodes arranged in a cylinder, with two end-cap electrodes. The cylinder itself is placed within a large super-conducting magnet (the magnetic field must necessarily be of the order of Tesla's). A general schematic of the ICR cell is given in Figure 3-23. The dimensions of the cell are of the order of centimetres. The electrodes can be divided up into three pairs of electrodes with shared functions, each of which shall be looked at in turn. The ions formed at the ion source are focussed into a discrete ion packet and sent to the ICR cell via an arrangement of ion optics. They enter the cell with a velocity $\boldsymbol{v}$ through the small aperture in the front end-cap, parallel to the direction of the magnetic field $\boldsymbol{B}$, and once in the cell, the ions undergo ion cyclotron motion. The presence of the magnetic field constrains the ions to move in a circular motion, the plane of which is perpendicular to the magnetic field lines, due to the inward-directed Lorentz magnetic force [70;71]. Over the length of the ICR cell the magnetic field is virtually uniform.

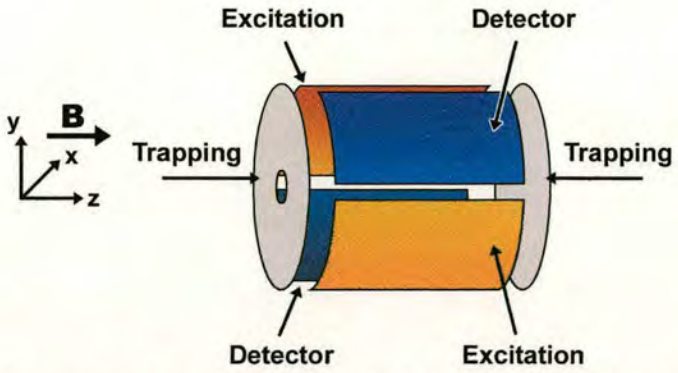

Figure 3-23 The arrangements of the excitation, detector and trapping electrodes in a cylindrical ion cyclotron resonance ion trap cell.

The Lorentz force can be defined from the following equation:

$$\boldsymbol{F} = m\boldsymbol{a} = m\frac{d\boldsymbol{v}}{dt} = q\boldsymbol{v} \times \boldsymbol{B} \tag{3-21}$$

The direction of motion is dependent upon the charge of the ion, as depicted in Figure 3-24.

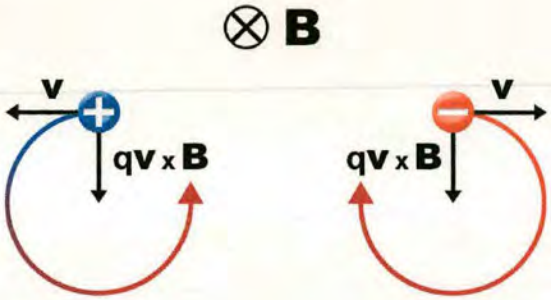

Figure 3-24 The path of ions moving with velocity **v** in the plane of the paper is bent into a circular path by the influence of the magnetic field applied perpendicular to the plane of the paper, which produces an inward-directed Lorentz magnetic force. It can be seen that ions of opposite polarity orbit in opposite senses. Diagram adapted from Reference 71.

The velocity in the *xy* plane (perpendicular to the magnetic field) can be defined as $v_{xy} = \sqrt{v_x^2 + v_y^2}$. The angular acceleration of the ion is then equal to v_{xy}^2/r, where r is the radius of the circular motion. By replacing the acceleration term in Equation 3-21 with the angular velocity, one acquires:

$$\frac{mv_{xy}^2}{r} = qv_{xy}B \tag{3-22}$$

The angular velocity, ω, measured in radians per second, is defined by $\omega = v_{xy}/r$. Substituting this into Equation 3-22 gives:

$$m\omega^2 r = qB\omega r$$

$$\rightarrow \quad \omega_c = \frac{qB}{m} \tag{3-23}$$

where ω_c is the cyclotron frequency of the ion. It can be seen from Equation 3-23 that the cyclotron frequency is unique for any given mass-to-charge ratio, and that for any charge state the cyclotron frequency decreases with increasing mass. In addition the cyclotron frequency increases proportionally with the magnetic field. Therefore it is possible to use this as the basis of a mass spectrometer. From Equation 3-23 the cyclotron radius of the ions in the magnetic field can be determined as:

$$r = \frac{mv_{xy}}{qB} \tag{3-24}$$

From Equation 3-24 it can be seen that the greater the mass-to-charge of the ion, the greater the ion cyclotron radius. It can be determined that a singly charged ion at equilibrium with its surroundings at room temperature, undergoing ion cyclotron motion within a magnetic field of 3 Tesla can have a cyclotron resonance of between approximately 0.08mm (for an ion of mass = 100u) to approximately 0.8mm (for an ion of mass = 10000u) [71].

The end cap electrodes have a static potential applied to them to produce an electric field, which acts to confine the ions to the relatively small volume of the cell. The ions thus move in a trapping motion, moving back and forth along the length of the ICR cell (while still undergoing the cyclotron motion), the frequency of which is dependent upon the strength of the field, the geometry of the ICR cell and the mass and charge of the ion [70;71]. The presence of the electric field complicates the motion of the ions even further by inducing a third motion of the ions, in addition to the cyclotron and trapping motion. The magnetron motion is circular with a defined frequency, and occurs along the lines of constant electrostatic potential within the

field. The magnetron motion is centred around the central axis of the cell, while the cyclotron's instantaneous centre is the circle of the magnetron motion [72]. Thus the motion of the ions within the cell is very complicated, but can be considered as the superimposition of the circular cyclotron motion over the helical motion generated by the superposition of the magnetron motion and the trapping motion. This helical motion is illustrated in Figure 3-25 for the motion of ions moving from the front capping electrode to the end.

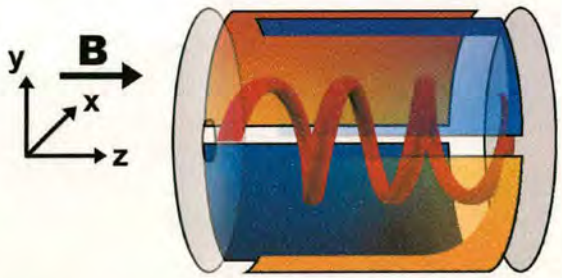

Figure 3-25 An illustration to depict the motion of ions due to the superposition of the magnetron and trapping motion. Diagram adapted from Reference 9.

The cyclotron motion is then superimposed onto the helix, which is demonstrated in Figure 3-26, which looks at the motion along the *z*-axis.

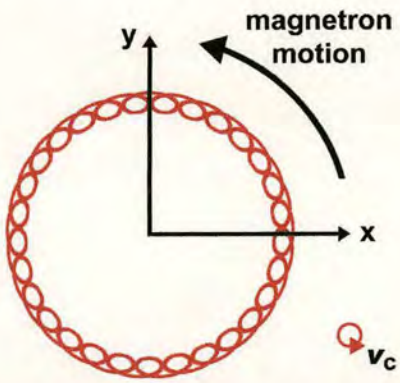

Figure 3-26 An example of the overall motion of the positive ions through the ICR cell as viewed from the *z*-axis. The circular cyclotron motion, with velocity $\boldsymbol{v}_c$, can be seen to move with the circular magnetron motion, as indicated. Diagram adapted from Reference 71.

The radius of the magnetron motion is virtually independent of the ion mass-to-charge ratio, but does increase with the amplitude of the trapping electric field, while the magnetron frequency is usually three orders of magnitude lower than the cyclotron frequency [72].

The motion of the ions can be used to generate an electrical current as they pass the detection plates within the ICR cell, however it is only the small cyclotron frequency that is a measure of the mass-to-charge ratio. At this current stage the measure of the cyclotron frequency cannot be readily measured due to the fact that the cyclotron radius is too small to induce a significant differential current on the detection plates, and the distribution of the cyclotron motion as it travels along the magnetron and trapping motion is likely to induce a net zero current. To overcome this problem a spatially uniform r.f. electric field is applied to the excitation plates of the ICR cell. The frequency of the field is swept through a given range such that when the frequency of the field matches the cyclotron frequency of the ions, the ion receives an increase in its kinetic energy, manifested by an increase in its orbital cyclotron radius. In addition the cyclotron angular phases of ions of the same mass-to-charge become synchronised, such that the ions are moving together coherently [9;70;71]. From this it can be seen the term "resonance" can be applied to the motion of the ions. The field is carefully controlled such that the excited cyclotron radius does not exceed the radius of the ICR cell. The motion of the ions is depicted in Figure 3-27.

Figure 3-27 A depiction of ion cyclotron resonance. The ions are given kinetic energy by the electric field generated by the excitation plates (orange), and are made into a spatially coherent ion packet. As the ions pass the detector plates (blue) a current is induced, which can be transformed into a time domain ion signal. Diagram adapted from Reference 71.

As the ions pass the detector plates they induce a small current, which is converted into an oscillating voltage, amplified, digitised and recorded to form a time domain ('*transient*') signal. This is a superimposition of sinusoidal functions of different amplitudes and initial phases, and whose frequencies correspond to the cyclotron frequencies of the ions in the cell. Thus by quickly sweeping the exciting electric field through a range of frequencies (known as a '*chirp*') one can obtain a time domain signal for all the ions in the cell, from which the fast Fourier transform can deconvolute the dataset to give the cyclotron frequencies and ultimately the mass-to-charge values.

Resolution of FT-ICR MS

The resolution of the FT-ICR mass spectrometer can be evaluated by determining the first derivative with respect to mass of the relationship between the cyclotron frequency and the mass-to-charge ratio (Equation 3-23) [71].

$$\frac{d\omega_c}{dm} = \frac{-qB}{m^2} = -\frac{\omega_c}{m} \qquad (3\text{-}25)$$

From this relationship it can be seen that

$$\frac{\omega_c}{d\omega_c} = -\frac{m}{dm} \qquad (3\text{-}26)$$

where $d\omega_c$ and dm refer to the full-width at half maximum peak height. It can therefore be seen from Equation 3-26 that the resolving power of the FT-ICR mass spectrometer is the same for both the frequency and mass domain (asides from the minus sign). Since it is known from Equation 3-23 that the cyclotron frequency is dependent upon the magnetic field strength, it can be seen that the stronger the magnetic field the greater the resolution that can be achieved in the frequency and mass domain.

Ion Isolation

The method by which the ions are excited by the oscillating electric field can be exploited to perform ion isolations. It is possible to specify a cyclotron frequency range that encompasses the mass-to-charge range of the ions to be isolated. All the

other ions that have cyclotron frequencies outwith this band will be accelerated by the excitation field to a cyclotron radius in excess of that of the ICR cell, and will be ejected from the instrument, as depicted in Figure 3-28.

Figure 3-28 Ions of a given mass-to-charge value, and hence cyclotron frequency are given an excess of kinetic energy by the exciting electric field such that they are given a cyclotron radius in excess of the ICR cell radius, and are lost from the cell. Diagram adapted from Reference 71.

One is limited by the minimum frequency range over one can chose for isolation, and still obtain a high resolution. A mass spectrum containing ions with masses upwards of 1000 amu, recorded on an instrument using a three Tesla superconducting magnet will typically have a cyclotron frequency ranging to tens of thousands of Hertz. Thus an isolation range of a couple of amu will have a frequency range of only 100Hz or so, which is difficult to maintain. Fortunately there is a solution. One can specify a broader isolation range to encompass the ion of interest, and any additional ions that are present but not wanted can be removed. The cyclotron frequency of each of the surplus ions can be determined from their m/z value, from which one can program a series of excitation "chirps" that excite these ions into having cyclotron radii in excess of that of the cell radius and be lost from the cell. This technique is known as using *shots* to remove the unwanted ions.

Tandem Mass Spectrometry

Once the ion(s) is isolated it is possible to perform tandem mass spectrometry by exposing the ion to either a collision gas or laser radiation. A low pressure of a neutral inert gas (of the order of mbar back pressure) can be pulsed into the cell to promote CID, but there are a number of ways in which the CID can be assisted by

controlling the ion motion within the cell. The first is by exciting the ions into a higher kinetic energy and cyclotron radius with an on-resonance r.f. pulse (i.e. frequency matching the cyclotron frequency of the ion) from the excitation plates. By exciting the ions in such a way the energy of collision with a neutral bath gas molecule is increased above what would be possible with unexcited ions, and so after just one or several collisions the unimolecular dissociation of the ion can occur (a full review of collision-induced dissociation is provided in Chapter 4). This method is known as *on-resonance irradiation* CID (ORI CID) and normally works best for relatively simple ions of low mass (less than 500 Th), but for larger ions the energy imparted on one or two collisions can be quickly dissipated into the many vibrational modes of the ion, such that a more rapid and efficient increase in internal energy is needed to promote the dissociation of the ion. The internal energy of the large ion can be gradually increased in a series of stages by setting the excitation electric field to periodically excite and de-excite the ion in the ICR cell by modulation of the r.f. frequency. The cyclotron radius is thus increased and decreased and the ion experiences conditions concomitant with large-scale multiple collisions, allowing the gradual build up of the internal energy of the ion. This technique is called *sustained off resonance irradiation* CID (SORI-CID) [71]. Similarly one can use the ICR cell as a reaction vessel, reacting the isolated ions with low pressures of reagent gases to induce ion-molecule reactions.

It is also possible to perform photodissociation within the ICR cell, typically by focussing a carbon dioxide laser (wavelength = 10.6 μm) through an aperture in the rear trapping electrode of the ICR cell. The ions are "slowly heating" leading to fragmentation [71]. This technique is typically known as *infrared multiple photon dissociation* (IRMPD).

3.6 Reference List

1. *Compendium of Analytical Nomenclature, Definitive Rules*, 3rd ed.; International Union Of Pure and Applied Chemistry: 1997.

2. Goldstein, E. *Berlin Akd.Monatsber.* **1876**, 279.

3. Goldstein, E. *Berlin Akd.Monatsber.* **1886**, *II*, 691.

4. Wien, W. *Ann.der Physik* **1902**, *8*, 244.

5. Thomson, J. J. *Proceedings of the Royal Society* **1913**, *A89*, 1-20.

6. Aston, F. W. *Nature* **1919**, *104*, 393.

7. Aston, F. W. *Nature* **1920**, *105*, 617.

8. Brenna, J. T.; Busch, K. L.; Caprioli, R. M.; Cotter, R. J.; Grigsby, R. D.; Judson, C. M.; Ramanathan, R.; Siuzdak, G.; Story, M. S.; Thomas, J. J.; Willoughby, R. C.; Yergey, A. L. *Measuring Mass. From Positive rays To Proteins.*, 1st ed.; Chemical Heritage Foundation: 2002.

9. Chapman, J. R. *Practical Organic Mass Spectrometry*, 2nd ed.; John Wiley & Sons, Inc.: 1998.

10. Halliday, D.; Resnick, R.; Walker, J. *Fundamentals of Physics Extended*, 4th ed.; John Wiley & Sons, Inc.: New York, 1993.

11. Schneider, B. B.; Chen, D. D. Y. *Analytical Chemistry.* **2000**, *72*, 791-799.

12. Stark, J. G.; Wallace, H. G. *Chemistry Data Book*, 2nd Edition in SI ed.; John Murray (Publishers) Ltd: London, 2001.

13. Dempster, A. J. *Physics Review* **1921**, *18*, 415.

14. Nier, A. O. *Review of Scientific Instruments* **1947**, *18*, 398.

15. Fenn, J. B.; Mann, M.; Meng, C. K.; Wong, S. F. *Mass Spectrometry Reviews.* **1990**, *9*, 37-70.

16. Beuhler, R. J.; Flanigan, E.; Green, L. J.; Friedman, L. *Journal Of The American Chemical Society.* **1974**, *96*, 3990.

17. Posthumus, M. A.; Kistemaker, P. G.; Meuse, T. N. *Analytical Chemistry.* **1978**, *50*, 985.

18. Unsöld, E.; Hillenkamp, F.; Nitsche, R. *Analysis* **1976**, *4*, 115.

19. Zare, R. N.; Levine, R. D. *Chemical Physics Letters* **1987**, *136*, 593-599.

20. Zare, R. N.; Hahn, J. H.; Zenobi, R. *Bulletin of the Chemical Society of Japan* **1988**, *61*, 87-92.

21. Lindner, B.; Seydel, U. *Analytical Chemistry.* **1985**, *57*, 895-899.

22. Wayne, C. E.; Wayne, R. P. *Photochemistry*, 2nd ed.; Oxford University Press Inc.: New York, 1999.

23. Müller, E. W. Z. *Physik* **1951**, *131*, 136.

24. Inghram, M.; Gomer, R. J. *Journal Of Chemical Physics.* **1954**, *22*, 1279.

25. Beckey, H. D.; Schulten, H.-R. *Agnew.Chem.Int.Ed.Engl.* **1975**, *14*, 403.

26. Evans, C. A. J.; Hendricks, C. D. *Review Of Scientific Instruments* **1972**, *43*, 1527.

27. Taylor, G. I. *Proceedings of the Royal Society London A* **1964**, *A280*, 383.

28. Kebarle, P.; Tang, L. *Analytical Chemistry.* **1993**, *65*, 972 A-986 A.

29. Dole, M.; Mach, L. L.; Hines, R. L.; Mobley, R. C.; Ferguson, L. P.; Alice, M. B. *Journal Of Chemical Physics.* **1968**, *49*, 2240.

30. Mach, L. L.; Kralik, P.; Rheude, A.; Dole, M. *Journal Of Chemical Physics.* **1970**, *52*, 4977.

31. Bruins, A. P.; Covey, T. R.; Henion, J. D. *Analytical Chemistry.* **1987**, *59*, 2642.

32. Gaskell, S. J. *Journal Of Mass Spectrometry.* **1997**, *32*, 667-688.

33. Lord Rayleigh. *Philos.Mag,* **1882**, *14*, 184.

34. Hofstadler, S. A.; Bakhtiar, R.; Smith, R. D. *Journal Of Chemistry Education.* **1996**, *73*, A82-A88.

35. Douglas, D. J. *Journal Of Physical Chemistry* **1982**, *86*, 185-191.

36. Iribane, J. V.; Thomson, B. A. *Journal Of Chemical Physics.* **1976**, *64*, 2287.

37. Fenn, J. B. *Journal Of The American Society Of Mass Spectrometry.* **1993**, *4*, 524-535.

38. Douglas, D. J. *Journal Of Physical Chemistry* **1982**, *86*, 185-191.

39. Micromass *Platform II Users Guide.*

40. Serani, L.; Lemaire, D.; Laprévote, O. *International Journal Of Mass Spectrometry* **2002**, *219*, 403-408.

41. Smith, R. D.; Loo, J. A.; Baringa, C. J.; Hedmonds, H. R. *Journal Of The American Society Of Mass Spectrometry.* **1990**, *1*, 53.

42. Akashi; Naito; Takio. *Analytical Chemistry.* **1999**, *71.*

43. Song, H. W.; Yue, G. H.; Lu, Y.; Yang, P. Y.; Wang, H. H. *Chinese Journal Of Chemistry* **2002**, *20*, 467-473.

44. Williams, T. M.; Kind, A. J.; Houghton, E.; Hill, D. W. *Journal Of Mass Spectrometry.* **1999**, *34*, 206-216.

45. Lindh, I.; Griffiths, W. J.; Bergman, T.; Sjovall, J. *International Journal Of Mass Spectrometry and Ion Processes* **1997**, *164*, 71-79.

46. Wang, P. P.; Bartlett, M. G.; Martin, L. B. *Rapid Communications in Mass Spectrometry* **1997**, *11*, 846-856.

47. Hao, C.; March, R. E.; Croley, T. R.; Smith, J. C.; Rafferty, S. P. *Journal Of Mass Spectrometry.* **2001**, *36*, 79-96.

48. Guilhaus, M. *Journal Of Mass Spectrometry.* **1995**, *30*, 1519-1532.

49. Wiley, W. C.; McLaren, I. H. *Review of Scientific Instruments* **1955**, *26*, 1150.

50. Mamyrin, B. A.; Karataev, V. I.; Schmikk, D. V.; Zagulin, V. A. *Soviet Physics JETP* **1973**, *37*, 45.

51. Migorodskaya, O. A.; Shevchenko, A. A.; Chernushevich, I. V.; Dodonov, A. F.; Miroshnikov, A. I. *Analytical Chemistry.* **1994**, *66*, 99-107.

52. Coles, J.; Guilhaus, M. *Trends in Analytical Chemistry* **1993**, *12*, 203-213.

53. Dawson, J. H. J.; Guilhaus, M. *Rapid Communications in Mass Spectrometry* **1989**, *3*, 155-159.

54. Busch, K. L.; Glish, G. L.; McLuckey, S. A. *Mass Spectrometry/Mass Spectrometry: Techniques And Applications Of Tandem Mass Spectrometry*, 1st ed.; VCH Publishers, Inc.: New York, 1988.

55. Pilling, M. J.; Seakins, P. W. *Reaction Kinetics*, 1st ed.; Oxford University Press Inc: New York, 1997.

56. Levine, R. D.; Bernstein, R. B. *Molecular Reaction Dynamics and Chemical Reactivity*, 1st ed.; Oxford University Press Inc: New York, 1987.

57. Laskin, J.; Lifshitz, C. *Journal Of Mass Spectrometry.* **2001**, *36*, 459-478.

58. Lifshitz, C. *European Journal Of Mass Spectrometry* **2002**, *8* , 85-98.

59. Paul, W.; Steinwedel, H. *Zeitschrift fur Naturforsch.A* **1953**, *8*, 448.

60. Paul, W.; Reinhard, H. P.; von Zahn, U. *Zeitschrift fur Physik* **1958**, *152*, 143.

61. Introduction To Mass Spectrometry. http://www.larimaxinstruments.com/new_page_2.htm . 6-11-2001.

62. March, R. E. *Journal Of Mass Spectrometry.* **1997**, *32*, 351-369.

63. Mathieu, E. *J.Math.Pure Appl.(J.Liouville)* **1868**, *13*, 137.

64. Lawrence, E. O.; Livingston, M. S. *Physical Review* **1932**, *40*, 19.

65. Lawrence, E. O.; Edlefsen, N. E. *Science* **1930**, *72*, 376.

66. Sommers, H.; Thomas, H. A.; Hipple, J. A. *Physical Review* **1951**, *82*, 697.

67. Hipple, J. A.; Sommers, H.; Thomas, H. A. *Physical Review* **1949**, *76*, 1877.

68. McIver, R. T. J. *Review of Scientific Instruments* **1970**, *41* , 555.

69. Comisarow, M. B.; Marshall, A. G. *Chemical Physics Letters* **1974**, *25*, 282.

70. Dinca, A. Gas-Phase Studies of Transition Metal-Containing Ions: Investigations into their Structure and Reactivity Using Fourier Transfrom Ion Cyclotron Resonance Mass Spectrometery. The University Of New South Wales, 2002.

71. Marshall, A. G.; Hendrickson, C. L.; Jackson, G. S. *Mass Spectrometry Reviews.* **1998**, *17*, 1-35.

72. Schweikhard, L.; Marshall, A. G. *Journal Of The American Society Of Mass Spectrometry.* **1993**, *4*, 433.

4 The Physics Of Ion–Molecule Reactions, Molecular Activation And Fragmentation

4.1 Introduction

An overwhelming feature of all the experiments presented in this thesis is the occurrence of ion-molecule collisions. It is through these collisions that cluster species aggregate into supraclusters [1-3], and the cluster precursors accumulate energy leading to their fragmentation. In the case of the aggregation experiments the reactions are dependent upon the production of gaseous ions and neutral cluster species with sufficient energy to meet and form bonds, a dependency that is met through the use of laser desorption of a solid sample of the cluster precursors.

This chapter aims to look at all of the critical factors crucial to the experimental processes, starting with the ion-molecule collisions so vital to the experiments, through to the methods of molecular activation, and finally the processes of dissociation from those activated species.

4.2 Ion-Molecule Reaction Systems

4.2.1 The Interaction Potential

All molecules can experience one of a number of different attractive and repulsive forces, and as such they all interact with one another. Ions shall obviously experience Coulombic attractions and repulsions due to the electric field they generate, but interactions are not just limited to those of ions.

The Attractive Ion-Neutral Potential

A neutral molecule can experience a strong interaction with a charged ionic molecule. The charge, q, carried by an ion generates an electric field, $\mathcal{E}$ as characterised by the Coulomb expression:

$$\mathcal{E} = \frac{q}{4\pi\varepsilon_0 R^2} \tag{4-1}$$

where ε_0 is the vacuum permittivity constant (ε_0=8.85419x10^{-12} J^{-1}C^{2}m^{-1}), and R is the distance between the centres of the molecules, referred to as the *inter-nuclear distance*. The field induces a dipole moment, denoted as μ_{ind}, in the neutral molecule, which interacts with the field and orientates itself with the direction of the field, the most favourable position to lower the free energy of the system. In addition there exists a long-range attractive polarisation force between the ion and the neutral molecule. This can be seen for the case of a cation in Figure 4-1.

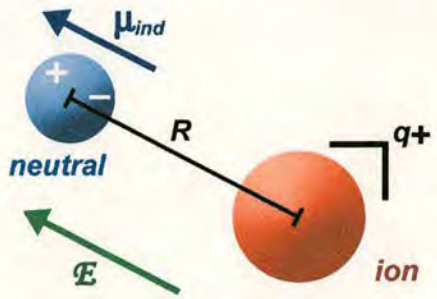

Figure 4-1 The induced dipole moment of a neutral molecule due to the electric field,E, generated by a cation with charge q+. The green arrow marks the direction of the field, and the induced dipole is orientated with the electric field.

The induced dipole moment μ_{ind} is proportional to electric field, and the proportionality constant is the *polarisability*, α, defined as the readiness that a dipole moment will be induced in the presence of an electric field. Therefore the induced dipole has the following relationship:

$$\mu_{ind} = \alpha\mathcal{E} \tag{4-2}$$

The polarisability is an intrinsic property of all atoms and does not vary appreciably from the order of 10^{-39} J^{-1}C^{2}m^2 [4]. Within a molecular framework the total polarisability can often be approximated from the addition of all the atomic values.

The induced dipole interacts with the electric field and in doing so lowers it to an amount equal to $-\mu_{ind}\mathcal{E}$. The interaction energy, V, also known as the polarisation energy can be determined as shown below:

$$V_{polsn}(R) = V_{I-M}(R) = -\left[\frac{1}{2}\frac{\alpha q^2}{(4\pi\varepsilon_0)^2}\right]R^{-4} = -C_4/R^4 \qquad (4\text{-}3)$$

The coefficient C_4 is the combination of all the terms within the square brackets in Equation 4-3. While the value of the polarisability is small it is sufficiently potent to attract molecules from a broad range of impact parameters at low collision energies.

The Repulsive Nuclear Potential

The interaction potential between an ion and a neutral molecule is not purely attractive. As two species approach one another there comes a point at which the attractive potential is countered by the nuclear repulsion that exists between each collision partner, and to a far lesser extent the repulsion between the shells of electrons of each collision partner. This Coulombic repulsion potential has the form:

$$V_{I-I}(R) = \frac{q_1 q_2}{4\pi\varepsilon_0 R} \equiv C_1/R \qquad (4\text{-}4)$$

where q_1 represents one nuclear charge, q_2 is the second nuclear charge, and R is the separation between them. The interaction energy for the Coulombic repulsion decreases far less rapidly with increasing distance than that for the polarisation attraction. Thus the nuclear repulsion forms a local minimum in the potential between the two species at an inter-nuclear separation of R_{min}. From this point energy is needed to push the collision partners closer together and overcome the repulsion, presenting an energy barrier to the reaction. The collision partners must overcome the energy barrier if a reaction is to occur since the electron shells must meet and rearrange as the course of the reaction dictates.

Therefore the interaction potential between an ion and a neutral molecule features a superposition of the ion-molecule attraction $V_{I\text{-}M}(R)=-(C_4/R^4)$, and the electrostatic repulsion between of electron shells, given by $V_{I\text{-}I}=(C_1/R)$. It is assumed that, initially, the collision partners are at an infinite separation where the potential between the two is zero. Therefore the interaction potential curve for the superimposition of the attractive and repulsive components has the form of that given

initially, the collision partners are at an infinite separation where the potential between the two is zero. Therefore the interaction potential curve for the superimposition of the attractive and repulsive components has the form of that given in Figure 4-2. R_{min} is shown on the plot, as is R_0, which denotes the separation between the collision partners that must be reached for a collision to occur.

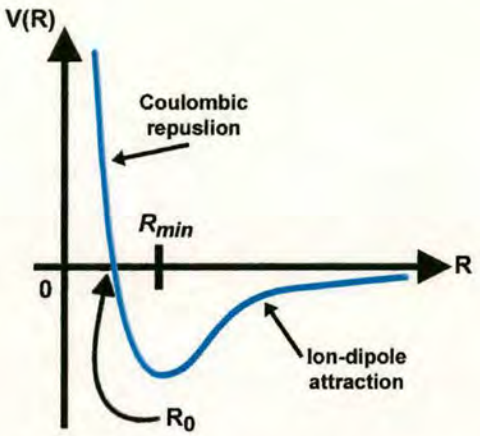

Figure 4-2 A comparison of the varying interaction potential energy V(R) with inter-nuclear separation R for an ion-molecule collision pair.

Of course, reaction mechanisms are not two-dimensional processes and the reactions proceed along a three-dimensional potential surface, which in this case can be created by sweeping the potential curve around the $V(R)$ axis.

The Centrifugal Energy Barrier

The repulsion between electron shells is not the only energy barrier that must be considered. There exist other intrinsic barriers to a successful collision between two molecules. Consider a collision pair, A and X, with an inter-nuclear separation R, and an impact parameter b (the distance of closest approach between the mass centres of the two molecules and orthogonal to the line of motion) as illustrated in Figure 4-3.

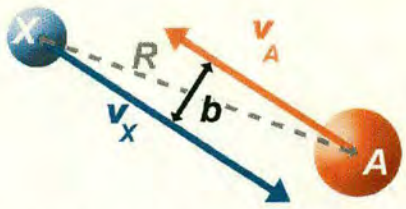

Figure 4-3 A collision pair, A and X, with impact parameter b and internuclear separation R.

It should be noted that while the velocity vectors in Figure 4-3 are almost parallel such a condition is not necessary for a collision to occur. The parallel velocities are purely for ease of visualisation, as is the fact that the species are depicted as spheres. The collision can be described using classical mechanics in terms of the total energy of the system, E_{tot}, i.e. the sum of the kinetic and potential energy that exists between the collision partners:

$$E_{tot} = KE + V(R) = \frac{1}{2} m_A v_A^2 + \frac{1}{2} m_X v_X^2 + V(R) \tag{4-2}$$

The relative kinetic energy of the collision system can be considered to be that of a particle with a mass equalling the reduced mass of the collision pair, and a velocity equal to the relative velocity, v_{rel} of the collision pair.

$$E_{tot} = \frac{1}{2} \mu v_{rel}^2 + V(R) \tag{4-5}$$

Assuming that A and X are infinitely separated initially, the potential energy between them is zero. Therefore the expression for the total energy can be equated to the initial relative kinetic energy of the collision pair, E_{rel}.

$$E_{tot} = E_{rel} = \frac{1}{2} \mu v_{rel}^2 \tag{4-6}$$

From the conservation of energy, the sum of the kinetic and potential energy as the internuclear separation R gets smaller shall always be equal to the initial relative kinetic energy. It is also known that after the collision the molecules shall experience a deflection in their motion and be scattered, which introduces an angular dependence to the motion of the collision partners in the form of the scattering angle θ_s. It is possible to define a plane through which the centres of both of the collision pair lie, i.e. the collision plane, and in doing so one can adequately monitor the

collision process through two-dimensional polar coordinates, as shown in Figure 4-4a) and b).

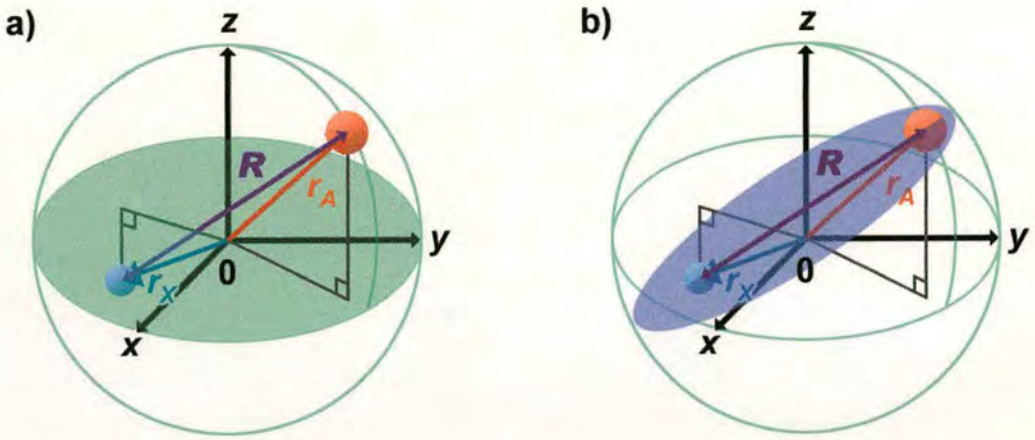

Figure 4-4 a) The collision pair A and X defined at a moment in time in three-dimensional space by their respective position vectors r_A and r_X. The xy plane is denoted by the green shaded ellipse, which shows that A lies in positive space, while X is in negative space with respect to the origin. b) The purple ellipse defines the collision plane in which the centres of A and X lie. In defining a two-dimensional coordinate system on this plane simplifies the handling of the angular dependence of the scattering.

The position of the collision pair, expressed in polar coordinates on the collision plane, is shown in Figure 4-5. Note that the axes are arbitrarily defined and labelled x and y for convenience. By using polar coordinates the scattering angle can be directly incorporated into the equations of motion for the collision.

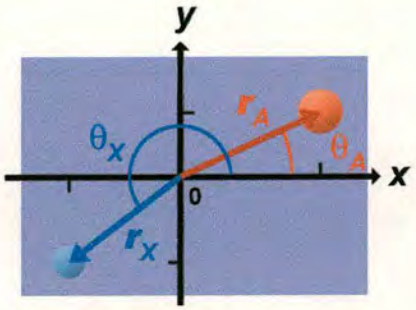

Figure 4-5 The position of the example collision pair defined by polar coordinates. The axes lie on the collision plane as described in Figure 4-4.

As both the ion and the molecule move the position vector for each changes correspondingly, and the rate of change of the position vector with time gives the velocity. This velocity can be broken down into two mutually perpendicular components, v_{rad} and v_θ. The velocity component v_{rad} acts in the radially outwards direction and is linear. The other velocity component, v_θ, always acts perpendicular to v_{rad}.

The term v_{rad} is used to define a component of linear momentum, p, and v_θ to define the component of *angular momentum*, L, where

$$L = m.r.v_\theta \tag{4-7}$$

The relative velocity of the collision pair can now be split up into its radial and angular parts:

$$E_{tot} = KE + V(R) = \frac{1}{2}\mu\left(v_{rad}^2 + v_\theta^2\right) + V(R) = E_{rel} \tag{4-8}$$

$$E_{rel} = \frac{1}{2}\mu v_r^2 + \frac{L^2}{2\mu R^2} + V(R) = E_{rad} + E_{cf} + V(R) \tag{4-8}$$

The first term on the right is the associated kinetic energy of the relative motion of A and X towards one another, known as the *radial kinetic energy*, E_{rad}. The second term is the energy associated with the orbital motion of the collision pair, known as the *centrifugal kinetic energy*, E_{cf}. V(R) remains unchanged from before. Assuming that both the magnitude and direction of the orbital angular momentum are conserved (i.e. are constant) during an elastic collision between A and X, the magnitude of the orbital angular momentum can be defined by the relative velocity and the impact parameter, in place of the internuclear distance and the radial velocity respectively:

$$L = \mu v_{rel} b \tag{4-9}$$

Thus the centrifugal kinetic energy, E_{cf}, becomes:

$$E_{cf} = \frac{1}{2}\mu v_{rel}^2 \frac{b^2}{R^2} \quad \text{and} \quad E_{rel} = \frac{1}{2}\mu v_{rel}^2 \tag{4-9a}$$

$$\therefore E_{cf} = E_{rel}\frac{b^2}{R^2} \tag{4-9b}$$

The relative kinetic energy of Equation 4-9 can now be expressed as [5]:

$$E_{rel} = E_{rad} + E_{rel}\frac{b^2}{R^2} + V(R) \tag{4-9}$$

$$\Rightarrow E_{rad} = E_{rel}\left(1 - \frac{b^2}{R^2}\right) - V(R) \tag{4-9}$$

$$\Rightarrow E_{rad} = E_{rel} - V_{eff}(R) \tag{4-10}$$

where

$$V_{eff} = V(R) + E_{rel}\frac{b^2}{R^2} \tag{4-11}$$

The effective potential is the sum of the potential energy and the centrifugal kinetic energy. Therefore, even in the absence of any potential field or barrier, the centrifugal kinetic energy provides a permanent repulsive centrifugal barrier dependent upon the impact parameter, despite the fact that the potential between the collision pair of A and X shall be attractive to some degree. Therefore there is a local maximum in the effective potential created by the centrifugal barrier, and the translational kinetic energy must be sufficient to surmount the barrier before a collision can even take place.

The effective potential is expected to be substantially different from the potential plot of Figure 4-2. The variation of the effective potential with impact parameter is shown below in Figure 4-6, where it is assumed that the collision pair will collide with a known value of relative kinetic energy, E. Figure 4-6 a) shows the effective potential energy curve for the impact parameter b_{orb}, a specific value of impact parameter for which the relative kinetic energy of the collision pair is exactly countered by the centrifugal barrier. Therefore the incoming particle becomes caught on the barrier and orbits its collision partner at a separation of R_{orb}. This is often referred to as an *orbiting collision*. Figure 4-6 b) shows the effective potential for a larger impact parameter value, for which the energy is insufficient to cross the centrifugal barrier and the collision pair can get no closer than the R_{max}. Finally, the effective potential for a small impact parameter is shown in Figure 4-6 c), where the energy is sufficient for the incoming particle to cross the barrier and meet for reaction. As an aside, a head-on collision, for which the impact parameter has a zero

value, presents no centrifugal barrier to the collision pair, and the potential curve has the form of that in Figure 4-2.

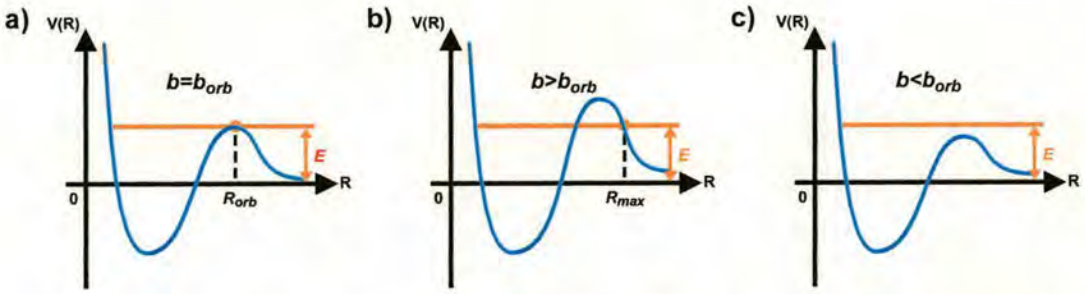

Figure 4-6 Variation of effective interaction potential with changing impact parameter, b.. a) $b=b_{orb}$: relative kinetic energy of collision is such that it gets caught on the centrifugal barrier and one molecule orbits its collision partner. b) $b>b_{orb}$: energy is insufficient to cross the centrifugal barrier, and the collision pair can only get as close as R_{max}. c) $b<b_{orb}$: Energy sufficient to cross the barrier and therefore reaction is likely.

Thus the importance of the value of the kinetic energy and impact parameter in ensuring a collision occurs can be seen, but the attraction that exists between ions and neutral molecules can assist in bringing collision partners overcoming the centrifugal barrier [6].

4.2.2 Ion-Molecule Collisions

A reaction between two molecules cannot occur unless those two species are brought into contact. Therefore the rate of collisions between the two reactant species can provide a good measure for the rate of reaction. The attractive nature of the ion-molecule interaction means that a collision between species with a large impact parameter is feasible. As such the rate of collisions between an ion and a molecule is greater than would be predicted by a traditional hard-spheres model, where it is assumed that no interaction exists. A measure of the rate of reaction can be made from the collision cross-section, σ, which defines a target area for each individual molecule, for which another molecule must pass through for a collision to occur. For hard-sphere models the cross-section can be determined from the sum of the hard-sphere radii, but for a more realistic appraisal of the collision cross section for ion-molecule reactions one must account for the interaction potentials that exists between

the collision partners. In including such factors as this, the cross section is defined as the *reaction cross section*, σ_R, which can be regarded as a microscopic reaction probability that is related to the rate constant for a reaction at a specific kinetic energy [6].

Langevin Model

The Langevin model can be used to determine the maximum possible impact parameter for collisions between ion and molecules to occur. The model accounts for the interaction between the ion and molecule and its subsequent effect in allowing collisions to occur for larger impact parameters than would be allowed with hard spheres. The full effective potential can be determined from the centrifugal energy barrier given in Equation 4-11 and the ion-molecule interaction potential given in Equation 4-3. Thus the effective potential has the form [7]:

$$V_{eff}(R) = -\frac{1}{2}\frac{\alpha q^2}{(4\pi\varepsilon_0)^2 R^4} + E_{rel}\frac{b^2}{R^2} \tag{4-12}$$

In order for a collision to occur the relative kinetic energy of the collision pair must be sufficient to cross the centrifugal barrier. The intermolecular separation at this point is labelled as R_{max}, and can be determined from the relationship:

$$\frac{d}{dR}V_{eff}(R_{\max}) = 0 \tag{4-13}$$

$$\therefore \quad R_{\max}^2 = \frac{\alpha q^2}{(4\pi\varepsilon_0)^2 E_{rel} b^2} = \varphi\frac{1}{E_{rel} b} \tag{4-13}$$

It then follows that the maximum possible impact parameter will be when the relative collision energy is equal to the maximum of the effective potential.

$$b = b_{\max}, \quad V_{eff}(R_{\max}) = E_{rel} \tag{4-14}$$

The maximum effective potential can then be determined from R_{max}.

$$V_{eff}(R_{\max}) = -\frac{1}{2}\varphi\left(\frac{\left(E_{rel} b_{\max}^2\right)^2}{\varphi^2}\right) + \frac{\left(E_{rel} b_{\max}^2\right)^2}{\varphi} \tag{4-14}$$

$$V_{eff}(R_{\max}) = \frac{1}{2}\frac{1}{\varphi}E_{rel}^2 b_{\max}^4 \tag{4-14}$$

It then follows that:

$$E_{rel} - V_{eff}(R_{\max}) = 0 \tag{4-15}$$

$$E_{rel} - \frac{1}{2}\frac{1}{\varphi} E_{rel}^2 b_{\max}^4 = 0 \tag{4-15}$$

$$\frac{1}{E_{rel}} = \frac{1}{2}\frac{1}{\varphi} b_{\max}^4 \tag{4-15}$$

$$\therefore \quad b_{\max}^2 = \frac{q}{4\pi\varepsilon_0}\sqrt{\frac{2\alpha}{E_{rel}}} \tag{4-15}$$

Thus the reaction cross section, σ_R, is now equal to:

$$\sigma_R = \pi b_{\max}^2 \tag{4-16}$$

However, the cross section given in Equation 4-16 is only valid if there is no energy barrier to the reaction. In the case of ion-molecule activating collisions this criteria holds, since any reaction that occurs as a consequence of the collision happens a finite time after the collision once a sufficient level of internal energy has been achieved. In the case where there exists an energy barrier to reaction, such as may be expected for any bond-forming aggregation reaction, the threshold energy for the reaction must be accounted for. This requires knowledge of the energy imparted into the collision pair on collision, which can be determined from the *line-of-centres model*.

Line Of Centres Model

The line of centres model is most often used with hard sphere models of atoms and molecules. While the current treatise on ion-molecule collisions has avoided the use of such assumptions, the line of centres model can legitimately be used here. The basic assumption of the line of centres model is that only the relative kinetic energy of the collision pair that acts along the line between the centres of the two species can be used to overcome the reaction barrier, as depicted in Figure 4-7.

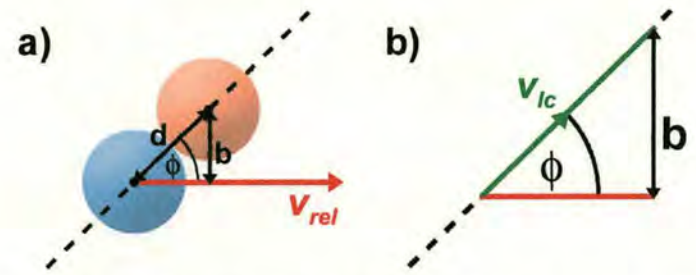

Figure 4-7 a) The orientation of species in a given collision. The relative velocity of the collision pair is shown, as is the impact parameter b, and the inter-nuclear separation d. b) a closer view of the collision to show the direction of the velocity that acts along the line of centres of the collision pair, v_{lc}, in relation to the impact parameter and the angle ϕ between the centres of the molecules and the direction of relative motion. Diagram adapted from Reference 8.

It can be taken from Figure 4-7 that the component of velocity that acts along the line of centres, v_{lc}, is equal to cosine(ϕ). It then follows from elemental trigonometry that

$$v_{lc} = v_{rel}\left[\frac{d^2 + b^2}{d^2}\right]^{\frac{1}{2}} \qquad (4\text{-}17a)$$

Therefore the component of energy that acts along the line of centres is:

$$E_{lc} = E_{rel}\left[\frac{d^2 + b^2}{d^2}\right]^{\frac{1}{2}} \qquad (4\text{-}17b)$$

It follows from Equation 4-17b that an increase in the impact parameter results in a decrease in the amount of energy that can be transferred along the line of centres for a given relative energy. In addition the line of centres energy is at its maximum for a head on collision, where b=0. This is the point at which the line-of-centres model has a correlation with real molecular species as the efficiency of energy transfer is at its most when molecules meet head on, and not along the molecular axis [8].

Therefore, if the reaction has a threshold energy of E_0 then the reaction can only occur for a given energy E provided that the impact parameter b is less than the maximum b_{max}. Thus:

$$E^0 = E_{rel}\left[\frac{d^2 - b_{\max}^2}{d^2}\right] \tag{4-18}$$

$$\therefore \quad b_{\max}^2 = d^2\left(1 - \frac{E_0}{E_{rel}}\right) \tag{4-19}$$

It can be seen that for a collision that occurs with a relative kinetic energy of E_{rel} and at impact parameters greater than b_{max}, the energy along the line of centres will be less than the threshold energy. From these arguments the reaction cross section for reactions with an energy barrier is re-evaluated as [7;8]:

$$\sigma_R(E_{rel}) = \pi b_{\max}^2 = \begin{cases} 0 & E_{rel} \le E_0 \\ \pi d^2(1 - E_0/E_{rel}) & E_{rel} > E_0 \end{cases} \tag{4-20}$$

4.2.3 Unimolecular Reactions

While ion-molecule reactions form the basis of most of the work within this thesis, another prominent feature is the unimolecular reactions that follow the ion-molecule collisions. The following is a review of the main elements of the unimolecular reaction theory as it applies to both the collision-induced dissociation reactions and the cluster aggregation reactions.

Collision Activation And Dissociation

According to Lindemann theory of unimolecular reactions in gas-phase kinetics, collisional activation and the following reaction of the activated species are two distinct processes separated in time [9]. Thus:

$$A + X \underset{k_2}{\overset{k_1}{\rightleftarrows}} A^* + X \tag{4-21a}$$

$$A^* \xrightarrow{k_3} products \tag{4-21b}$$

Each step has its own unique rate constant: k_1 for the forward activation reaction, k_2 for the backward quenching reaction, and k_3 for the final reaction of the activated species into products. This separation of the bimolecular collision and the unimolecular reaction also holds true for collision-induced dissociation [10-13] provided that the relative velocity of the ion and target gas molecule is such that after the collision the ion and the neutral have become well separated before the

fragmentation step occurs [14]. Thus the collision activation and dissociation steps for the ligated metal cluster ions can be split up like so [15]

$$LM^- + N \longrightarrow (L - M^-)^* + N \qquad \text{(4-22a)}$$

$$(L - M^-)^* \longrightarrow M^- + L \qquad \text{(4-22b)}$$

where L represents the neutral ligand, M represents the metal carbonyl cluster ion, and N represents the neutral target gas. If the ion and target molecule are not well separated by the time of fragmentation then the target molecule has a direct influence on the dissociation reaction [14].

The collision-induced dissociation of an ion occurs in accordance with the tenets of the *quasi-equilibrium theory* of unimolecular reactions [11;13;14;16;17]. Quasi-equilibrium theory was first applied to the calculation of mass spectral fragmentation patterns by Rosenstock, Wallenstein, Wahrhaftig, and Eyring [18]. The quasi-equilibrium theory concerns the rate of unimolecular reactions and assumes that after a collision between an ion and neutral, the ion's internal energy is equilibrated among all the degrees of freedom before the ion dissociates [10;18]. It should be noted that this assumption is also a key factor in RRK and RRKM theory for unimolecular reactions where intramolecular vibrational redistribution means that even if the internal states of an energised species are not initially equally populated, the vibrational energy flows so rapidly around the internal vibrational modes in comparison to the reaction rate that one can assume that all the internal states are equally accessible [5;8].

Thus the subsequent dissociation of the ion is determined only by the amount of energy it contains (i.e. the sum of any prior internal energy and the energy acquired on collision) and is independent of the initial state in which the ion is formed. Therefore the internal energy of the parent ion is statistically redistributed prior to dissociation. By separating the reaction in this way one can approach and analyse the dissociation mechanism independently, by assuming that the ion or molecule has been activated by some mechanism to a suitable energy above the critical energy for dissociation. While the nature of the excitation step is endothermic and the

fragmentation is exothermic, the overall reaction may be endothermic, exothermic or thermoneutral [14].

Association Reactions

In the instance where two species meet and form bonds between each other, it is likely that the new species will decay back to give the original reactants:

$$A + B \underset{\longleftarrow}{\longrightarrow} AB \qquad (4\text{-}23)$$

Thus one can see that the reaction is reversible, and as such the association reaction can be adequately described by unimolecular theory [8]. As the reactants meet they start to form a new bond between them. This can be said to be the activated complex, the intermediary species that occupies the highest point on the potential energy surface of the reaction system. Potential energy is released on the bond formation, and therefore the new AB molecule will be highly excited since the total energy of the A+B system must be conserved. As mentioned previously, energy will flow freely around the internal modes of the new AB molecule until, at some point, enough energy is located at the new bond and unimolecular dissociation occurs, reforming the original reactants A and B.

$$A + B \underset{\longleftarrow}{\longrightarrow} AB^* \qquad (4\text{-}24)$$

However, the dissociation of the new molecule can be avoided if the excess internal energy can be lost in some other way such as from collisional quenching provided by a third body, X, which could be an inert molecule or another reactant, such that the overall reaction can be classed as an exoergic association reaction [7]:

$$AB^* + X \longrightarrow AB + X \qquad (4\text{-}25)$$

In the case of the cluster aggregation reactions, which are most likely to occur as sequential steps, the mechanism is more likely to have the form:

$$
\begin{aligned}
M + M + X &\longrightarrow M_2 + X \\
M_2 + M + X &\longrightarrow M_3 + X \\
&\;\;\vdots \\
M_{n-1} + M + X &\longrightarrow M_n + X
\end{aligned}
\qquad (4\text{-}26)
$$

where M represents one of the transition metal carbonyl clusters. As the species involved in the association reaction get larger, the need for quenching by the interaction of a third body grows less since the exoergicity can be efficiently absorbed by the numerous vibrational degrees of freedom of the cluster molecule. Alternatively if either of the reactants is a polyatomic species, as is the case with the transition metal carbonyl clusters on display here, the removal of excess internal energy may be achieved by the preferential dissociation of other bonds within the cluster, such as carbonyl ligands.

4.3 Mechanisms Of Molecular Activation

The factors affecting collisions between ions and molecules having been established, it is now time to consider what occurs when the two species meet in more detail. This topic primarily concerns the processes of molecular activation on collision, and as such begins with a brief review of the modes of activation and the selection rules that govern the excitation mechanisms. This is then followed by an examination of the ion-molecule complex formed at the point of collision.

4.3.1 Modes Of Activation

The activation of a molecule involves the promotion of the molecule to a higher energy state. Molecules store their internal energy in the arrangement of the electrons in the molecule, the vibration of the molecular bonds, and the rotational motion of the molecule, referred to as the electronic, vibrational, and rotational modes of the molecule respectively. The energy of each of these modes is quantised and exists in discrete states, which can be though of as levels. The following is a brief review of their properties and origin [19]. Figure 4-8 depicts the relative energy scale and separation of each of these modes.

Electronic Modes: The allowed energy states for electronic modes pertain to the electron occupancy of the molecular orbitals. As the molecule becomes excited the electrons enter more energetic molecular orbitals, which tend to be anti-bonding. As the molecule becomes more excited the bond lengths are increased. The separation between the electronic levels decreases as the state of excitation increases, due to the internal energy approaching the dissociation limit for the bond, beyond which the energy is viewed as the classical continuum. The energy separation for electronic levels is typically of the order of 10^{-18} J. Each different electronic level has its own associated vibrational and rotational modes.

Vibrational Modes: The allowed energy states for vibrational modes are dependent upon the masses of the constituent atoms and the rigidities (strength and therefore length) of the bonds linking them. Because the vibrations are anharmonic the energy level separation decreases as the level of excitation increases. The energy separation for vibrational levels is typically of the order of 10^{-20} J. Each different vibrational level has its own associated rotational modes.

Rotational Modes: The separation of the rotational energy levels is dependent upon the moment of inertia of the molecule. As the molecule rotates the bonds lengths are elongated due to centrifugal distortion, an effect that increases as the angular velocity increases. Therefore the separation between rotational levels increases as the state of excitation increases, with the separation typically of the order of 10^{-23} J.

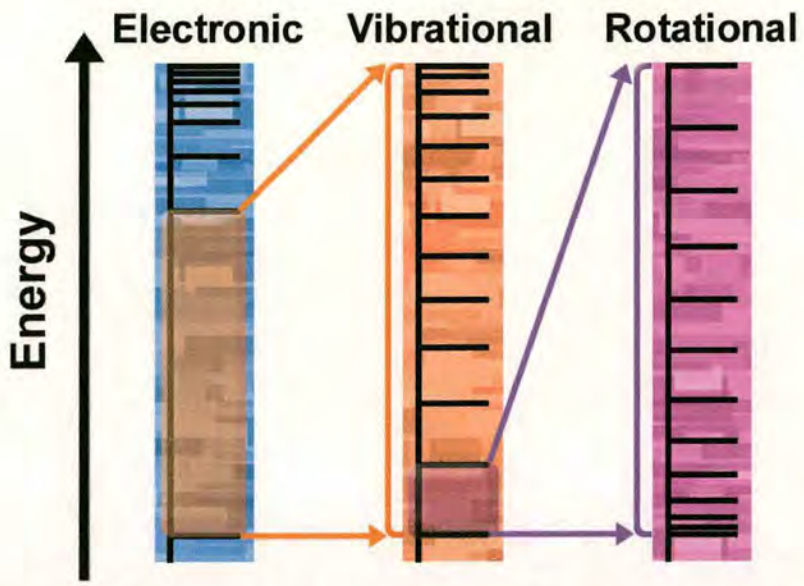

Figure 4-8 A schematic of the composition of the electronic, vibrational and rotational levels.

4.3.2 Allowed Transitions

The transitions that lead to activation can occur to any of the vibrational and rotational levels in an upper electronic state, although the close spacing and minute energy difference of the rotational levels often means that one concentrates on the electronic and vibrational modes only. The promotion of a molecule to an excited state cannot occur in just any fashion, and there are certain criteria that must be met for transitions to be allowed, known as *selection rules*. The selection rules incorporate such factors as the spin, orbital angular momentum and the symmetry properties of the two wavefunctions of the energy levels between which the transitions take place. However, these rules are not rigid, and can be broken in certain circumstances. For instance the system undergoing activation is assumed to be unperturbed, whereby the molecule is not undergoing any collisions and is in the absence of any electric or magnetic fields. All the experiments within this thesis are performed by mass spectrometry, where the gaseous ions/molecules are constantly exposed to collisions and electric/magnetic fields at some point. In addition the selection rules are only of particular use for small or simple molecules. The metal clusters experimented on within this thesis are reasonably large and complex, and the metal atoms feature a large nuclear charge which increases the effect of *spin-orbit*

coupling, the interaction between the spin and orbital angular momentum of the wavefunctions. Spin-orbit coupling causes the definition of some quantum numbers to break down, and as a result so do the selection rules based upon them [20]. Far from being a problem, the breakdown of rigid selection rules means that internal transitions that would be normally forbidden on the grounds of spin conservation, for example, are now possible presenting alternative routes to activation and fragmentation.

4.3.3 The Collision Complex

Now that the governing factors concerning the meeting of two molecules has been reviewed it is time to consider what occurs during the collision. When two molecules collide, a collision complex is formed. The collision complex exists for as long as the collision pair are in contact. During this time the two molecules may interact, with an electron on one of the molecules being excited by its interaction with the approaching nucleus of the other molecule, or from changes in the entire electronic structure that occur as the collision progresses [14], such as may occur from bond forming. Thus some form of energy transfer can occur that often leads to the lifetime of the collision complex being referred to as the *Interaction Time*, which shall be discussed in more detail later. If no bonds are formed between the collision pair, then energy transfer will occur. In this instance the post-collision kinetic energy is less than that before the collision, and thus the collision is regarded as being partially inelastic, with a finite interaction time. A purely inelastic collision is one where the collision partners stick together and move as one, an occurrence only likely to occur if there is a bond-forming reaction.

For any given ion-molecule collision one of three things can be considered to occur to the ion:

1. Excitation: The ion shall be excited by the collision with the neutral, as a portion of the relative energy of the collision is converted to internal energy of the ion. The form of the excitation can be electronic, rotational or vibrational.

2. De-excitation: A previously activated ion shall have its excess internal energy quenched by the collision with a neutral molecule, with the neutral molecule now being excited.
3. Neutralisation: For cations this shall probably occur through charge transfer, with the neutral becoming ionised. In the case of anions, excitation of the ion will most often promote the dissociation of the electron. This is a common reaction as the extra electron is normally more loosely bound than an electron on the neutral analogue.

For any reaction to occur, be it bond forming between the ion-molecule pair or the fragmentation of the ion, energy is required. The internal energy of the reactive collision partner is the most important consideration for the quantification of the reaction kinetics. The kinetic energy of the collision pair is considered as playing a secondary role as an energy reservoir for the excitation of the ion [10], despite being of intrinsic importance in bringing the collision partners together.

The excitation of the ion is necessarily an endothermic process, with a portion of the relative translational energy, δE, that is lost to the transformation into internal energy of the ion [14]. However, the internal energy uptake of the molecule *after* the collision, or rather the endothermicity of the activation, is defined separately as the parameter Q. This is because the state of the ion after excitation can often be different from the initial state occupied at the point of the excitation transition [14] and thus have a separate value of energy. The internal energy of the excited molecule can be defined as the sum of energies in the vibrational and internal rotation of a molecule or ion above the zero point energy.

The energy used to effect an internal transition within a molecule is dependent upon the relative velocity of the collision pair and the impact parameter, as discussed in Chapter 4.2.2, usually thought of in terms of the angle of scattering. The exact value of both δE and Q are difficult to define precisely, but there is a calculable maximum amount of energy that can be transformed into internal energy.

4.3.4 Centre-of-Mass Energy

A Brief Introduction To The Centre-Of-Mass Frame

The study of molecular collisions using classical mechanics is made simpler by observing the collision from the *centre-of-mass coordinate system,* or *CM frame*, whose origin is situated on the centre-of-mass of the collision partners and moves with it as the collision progresses. This differs from *Laboratory* or *LAB frame* of reference, which can be considered as being the viewpoint the experimenter would have of the collision process, from his (stationary) position in the laboratory. Thus the origin of the LAB frame remains fixed from the experimenter's perspective.

Parameters of the collision process, such as the initial velocity of one of the molecules, are defined from the LAB frame, and require transformation into the CM frame. It may seem a redundant complication to transfer the coordinate system around, but the centre-of-mass coordinate system offers many benefits to ultimately simplify the understanding of the collision. The chief benefit is that within the CM frame the momentum is conserved: the total momentum is always equal to zero, because the momenta of two colliding particles are equal and opposite at all times [14;21;22 23].

As an example a simple collision between two species, A and B, shall be looked at from both the CM and LAB frame of reference. Molecule A has a mass m_A, and prior to the collision it is situated at coordinates $\boldsymbol{r}_A$ from the LAB origin. Similarly molecule X which is lighter than A, has mass m_X, and is situated at coordinates $\boldsymbol{r}_X$ from the LAB origin before the collision. The molecules have the form of hard spheres. The position of the centre-of-mass of the collision pair at this time prior to the collision is given by the coordinates $\boldsymbol{r}_{CM}$ from the LAB origin. The positions of molecules A and X from the centre-of-mass are $\boldsymbol{r}_{c(A)}$ and $\boldsymbol{r}_{c(X)}$ respectively, where the subscript "c" is used to denote a parameter that is defined in the CM frame. All of the above is depicted in Figure 4-9 a).

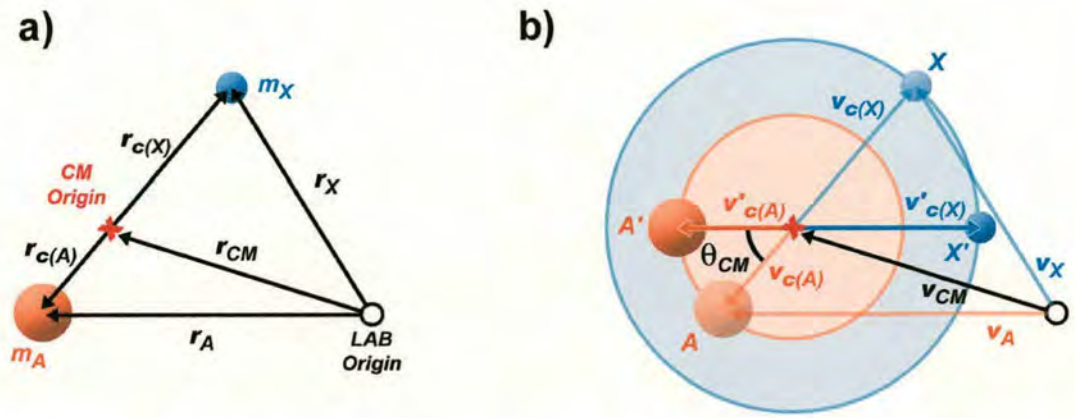

Figure 4-9 a) Viewing a collision pair from both the LAB origin and the CM origin, (marked with a black ring and a red cross respectively) prior to the collision. The positions of the molecules from the different origins are differentiated by the use of a subscript "c" to denote a parameter measured in the CM frame. b) A Newton diagram shows the outcome of the collision using the velocity vectors of the molecule before and after the collision (denoted by a prime). Diagram adapted from Reference 14.

The outcome of the collision can be represented by a Newton diagram [14;23], which shows the outcome of a collision through the velocity vectors of the molecules. An example of a Newton diagram for the example collision system is shown in Figure 4-9 b). The velocity vectors as measured from the CM frame are given for each molecule before the collision ($\boldsymbol{v}_{c(A)}$,and $\boldsymbol{v}_{c(X)}$) and after the collision ($\boldsymbol{v}'_{c(A)}$, and $\boldsymbol{v}'_{c(X)}$, where the prime is used to denote parameters measured after the collision). The properties of momentum conservation in the CM frame permit the marking out of the circular boundary regions from the CM origin that define the possible positions the molecules can occupy before and after collision. Thus, as can be seen in Figure 4-9 b) the molecules A and X are situated on the circumference of the respective coloured circles and are joined by a straight line that passes through the centre-of-mass. This ensures that the momenta are always equal and opposite.

The position of the centre-of-mass can be considered as the point of collision. From the LAB frame the position of the centre-of-mass, $\mathbf{r}_{CM}$ is in constant motion at a fixed velocity that is unaffected by the collision [14;21;24]. The velocity vector for the motion of the centre-of-mass $\boldsymbol{v}_{CM}$ is denoted in Figure 4-9 b) from the LAB origin.

The velocity of the centre-of-mass is determined from the differentiation of the position of the centre of mass with respect to time. The position of the centre-of-mass can be determined from the vector addition of the position vectors of molecule A and X in the LAB frame, with each position vector weighted against the ratio of the mass of it's parent molecule and the total mass of the collision pair. Thus:

$$\boldsymbol{v}_{CM} = {}^{d}\!/_{dt}\,\boldsymbol{r}_{CM} = \left[\frac{m_A}{m_A + m_X}\,{}^{d}\!/_{dt}\,\boldsymbol{r}_A\right] + \left[\frac{m_X}{m_A + m_X}\,{}^{d}\!/_{dt}\,\boldsymbol{r}_X\right] \qquad (7?22)$$

$$\boldsymbol{v}_{CM} = \frac{m_A\boldsymbol{v}_A + m_X\boldsymbol{v}_X}{m_A + m_X} \qquad (4\text{-}27)$$

In the instance that one of the particles is initially at rest, e.g. $\boldsymbol{v}_B$=0, then the velocity of the centre-of-mass becomes:

$$\boldsymbol{v}_{CM} = \frac{(m_A\boldsymbol{v}_A)}{(m_A + m_X)} \qquad (4\text{-}28)$$

The scattering of the collision partners is determined from the velocity vectors before and after collision, and is correspondingly called the centre-of-mass scattering angle θ_{CM}. This is shown in Figure 4-9 b) for the A molecule.

It can be seen from the Newton diagram that to calculate the post-collision velocity of molecule A from the LAB frame, $\boldsymbol{v}'_A$ (not shown in Figure 4-9) is to take the vector sum of the post-collision velocity of molecule A in the CM frame, $\boldsymbol{v}'_{c(A)}$, and the velocity of the centre-of-mass in the LAB frame, $\boldsymbol{v}_{CM}$.

$$\boldsymbol{v}'_A = \boldsymbol{v}'_{c(A)} + \boldsymbol{v}_{CM} \qquad (4\text{-}29)$$

The magnitude of the post-collision velocity vector of the ion in the LAB frame, $\boldsymbol{v}'_I$, is strongly dependent upon the scattering angle θ_{CM}.

To convert any parameter from LAB frame to the CM frame or vice versa follows a similar vector sum as shown in Equation 4-29. A parameter α_c in the CM frame can be converted to its analogue vector in the LAB frame, α, by the vector addition of the appropriate term for the centre-of-mass of the system α_{CM}. As an example to convert the post-collision momentum of molecule A, $\boldsymbol{p}'_{cA}$, in the CM frame to its LAB frame

analogue, $\boldsymbol{p}'_A$, requires only the addition of the momentum of the centre-of-mass of the collision system, $\boldsymbol{p}_{CM}$, where:

$$\boldsymbol{p}_{CM} = [m_A + m_X]\boldsymbol{v}_{CM} \qquad \& \qquad \boldsymbol{p}'_A = \boldsymbol{p}'_{cA} + \boldsymbol{p}_{CM} \tag{4-30}$$

The momentum of the centre-of-mass system can be thought of as the momentum of a single structure-less particle with a mass of the combined mass of the collision partners moving with the velocity of the centre-of-mass of the system, as described here.

The Centre-Of-Mass Energy And Collisions

It has been shown that in a partially inelastic collision a portion of the translational energy is lost in the conversion to internal energy, therefore the kinetic energy and hence the momentum are not conserved in the laboratory frame-of-reference (LAB frame). However, if the collision system is examined from the centre-of-mass frame-of-reference (CM frame), where the momentum is always conserved and equal to zero at all times, then the pre- and post-collision momenta for each collision partner is found to be equal and opposite. This fact can help in determining the maximum amount of energy that is lost to the transformation of internal energy, δE_{max}, [14;23] which should occur for a head on collision. Consider the collision between an ion of mass m_A and initial LAB velocity v_A, and a neutral of mass m_X that is initially at rest, but with a post collision velocity of v'_B in the LAB frame. Before the collision, the translational energy in the LAB frame is:

$$E_{LAB} = \tfrac{1}{2} m_A v_A^2 \tag{4-31}$$

And after the collision, the translational energy in the LAB frame is:

$$E'_{LAB} = \tfrac{1}{2} m_A v_A'^2 + \tfrac{1}{2} m_X v_X'^2 \tag{4-32}$$

It is possible to convert these energy terms into their equivalent values for the collision pair in the CM frame and describe them in terms of the translational energy of the collision pair in the centre-of-mass frame, E_c, and the translational energy of the centre-of-mass system, E_{CM}:

$$E_{LAB} = E_c + E_{CM} \tag{4-33}$$

$$E_{CM} = \frac{\left(\boldsymbol{p}_{CM}^2\right)}{2\left(m_A + m_X\right)} = \frac{\left(m_A + m_X\right)^2 \boldsymbol{v}_{CM}^2}{2\left(m_A + m_X\right)}$$

$$E_{CM} = \tfrac{1}{2}\left(m_A + m_X\right)\boldsymbol{v}_{CM}^2 \tag{4-34}$$

Substituting in the value of $\boldsymbol{v}_{CM}$ from Equation 4-28.

$$\boldsymbol{v}_{CM}^2 = \frac{\left(m_X \boldsymbol{v}_A\right)^2}{\left(m_A + m_X\right)^2}$$

$$E_{CM} = \frac{m_A^2}{2\left(m_A + m_X\right)}\boldsymbol{v}_A^2$$

$$E_{CM} = \left(\frac{m_A}{m_A + m_X}\right)E_{LAB} \tag{4-35}$$

As discussed earlier, the velocity of the centre-of-mass, $\boldsymbol{v}_{CM}$, does not change during the collision. Therefore the energy of the centre-of-mass system, E_{CM}, is conserved throughout the collision process, and cannot be converted into internal energy. Thus the energy of the collision pair in the centre-of-mass frame prior to collision, E_c, is the only source of energy for conversion to internal energy during the collision. Since the fraction of the initial LAB energy that is not converted to internal energy is known, it is a simple calculation to determine the fraction that is:

$$E_{LAB} = \left(\frac{m_A}{m_A + m_X}\right)E_{LAB} + E_c$$

$$1 = \left(\frac{m_A}{m_A + m_X}\right) + \frac{E_c}{E_{LAB}}$$

$$\frac{E_c}{E_{LAB}} = 1 - \left(\frac{m_A}{m_A + m_X}\right) = \left[\frac{m_A + m_X}{m_A + m_X} - \frac{m_A}{m_A + m_X}\right]$$

$$\frac{E_c}{E_{LAB}} = \left(\frac{m_X}{m_A + m_X}\right)$$

$$\therefore E_c = \left(\frac{m_X}{m_A + m_X}\right)E_{LAB} = \delta E_{\max} \tag{4-36}$$

Therefore the maximum amount of energy that can be converted into internal energy on collision, δE_{max} has been determined. This is a value that should be relatively simple to determine given that many of the parameters, such as the mass of the

collision partners will be known. If one can assume that the target neutral molecules are effectively stationary then the ion energy can be calculated from the acceleration of the ions from the source. However, this value only acts as a guide to the maximum quantity of energy that could be converted to internal energy, and in many instances only a fraction of this maximum will actually be converted. The value of δE_{max} in its current form only accounts for the relative velocity of the collision pair through the initial kinetic energy in the LAB frame, E_{lab}. However, the δE is also dependent upon the scattering angle. This is actually mathematically simple from the line of centres model used previously in Chapter 4.2.2, but difficult to account for under experimental conditions. It was established that the maximum efficiency of energy transfer occurs from head on collisions, and that the angular dependence, ϕ, of the energy transfer can be determined from the component of the velocity that acts along the line of centres:

$$v_c = v_{rel} \cos\phi \tag{3-27}$$

Thus, in the equations for an ion moving with velocity v_I hitting a stationary neutral target, E_c is determined as:

$$E_c = \delta E = \left(\frac{m_A}{m_A + m_X} \right) \left(\frac{1}{2} m_A v_c^2 \right) \tag{3-27}$$

$$= \frac{1}{2} \left(\frac{m_A^2}{m_A + m_X} \right) (v_{rel} \cos\phi)^2 \tag{4-37}$$

Unfortunately the angle ϕ is practically impossible to measure within the experiment unless specific equipment is available to detect ions scattered from single collisions at specific angles. It is possible to obtain an average value of δE by integrating Equation 4-36 over all possible angels of ϕ.

The energy in the centre-of-mass frame is greatest for a collision of a light ion with a stationary heavy target, and conversely least for a heavy ion colliding with a stationary light target.

4.3.5 Interaction Time And The Mode Of Activation

As discussed in Chapter 4.3.3 the duration of the collision complex is understood in terms of the interaction time. The interaction time has an important role to play in the excitation of a molecule on collision. The efficiency of excitation is controlled by a probability function. Both the probability and the form of the excitation that the molecule can experience are dependent upon the interaction time. The excitation of a molecule can promote a reaction, such as bond forming with the collision partner, or the fragmentation of an excited molecule. However, the precise mechanisms of activation of polyatomic ions is still not well understood [23].

The interaction time, denoted by the term t_c, can be controlled for an ion-molecule collision system through the variation of the relative velocity of the collision pair. The interaction time is not only dependent upon the relative velocity of the collision pair, but also the interaction potential that exists between them. As the relative velocity increases the interaction time is known to generally decrease, whereas the existence of an attractive potential between the collision partners can lead to the formation of a long-lived complex [10;11;14;16].

In the collision between ion A^- and neutral B, there are three excitation regimes that can occur to produce the activated product ion A^{*-}: direct electronic, direct vibrational excitation and a mixture of the two.

Electronic Excitation

The probability of excitation is dependent upon the interaction time in the form of *quasi*-resonance between the interaction time and the period of the electronic transition. If the interaction time is significantly different from the period of electronic excitation then the probability of electronic interaction is reduced and overall ion excitation is very inefficient. The dependency of electronic activation of the species upon the interaction time was quantified by Massey to form the *Adiabatic Criterion* [11;14;23;25].

$$R_M = \frac{t_c}{\tau} \tag{4-38}$$

The Massey Parameter, R_M, measures the ratio of the interaction time of the collision, and the characteristic period of the specific internal motion that shall be excited, τ. t_c can be determined by an interaction distance (usually taken as somewhere between 4-7Å) [23] divided by the relative velocity of the collision partners [14], whereas τ is equal to Planck's constant divided by the difference in electronic energy levels involved in the transition leading to excitation [23]. There are three schemes that can be considered:

1. If the interaction time is much greater than τ, such that $R_M \gg 1$ (lower keV velocities), the electrons adjust adiabatically to the perturbation from the interaction between the ion and the target to maintain the condition of lowest overall system energy, making an electronic transition unlikely [11;14;17;23;25].
2. If the interaction time is much less than τ, such that $R_M < 1$ (high keV velocities), the electronic transition time is now longer than the interaction time, an outcome that was originally believed to make transition unlikely [14;25]. However a small interaction time has been shown to be relatively efficient at exciting the ion, through the mixed mechanism of electronic/vibrational excitation, which shall be covered later.
3. If the interaction time is equivalent to τ, such that $R_M \approx 1$, (intermediate keV velocities) the probability and efficiency of ion activation is maximised [11;14;23]. Thus the probability can be considered to be analogous to resonance: the closer the interaction time and transition period the greater the efficiency of ion activation.

To accurately calculate the Massey parameter for any one collision necessitates intimate knowledge of the internal transitions that would occur from each collision, a factor that cannot always be determined prior to the experiment. It is therefore more usual to vary the relative collision velocity and determine the interaction time that results in the greatest overall ion activation.

The large separation between electronic levels corresponds to a small value of τ. Thus efficient electronic excitation will require a small interaction time, of the order of 10^{-15}-10^{-16} seconds. Such an interaction time is indicative of a fast relative velocity of the collision pair of the order of kiloelectronvolts. This has been corroborated by extensive experimental evidence [24;26-29] [13;17;30]. It follows that a small interaction time precludes momentum transfer between the collision pair. Thus the ion will experience virtually no change in its momentum perpendicular to the direction of flight, and consequentially scattering of the ion is limited to a narrow range [14].

An interaction time that is equivalent to the average time period for electronic excitation, such that $R_M \approx 1$, is much shorter than the time required for most nuclear motions. Therefore it can be reasoned that direct electronic excitation of the ion can occur at the interaction site through vertical Franck-Condon transitions [14;17;23;30]. The Franck-Condon principle states that the time required for an electronic transition in a molecule is much less than the vibrational period of the constituent nuclei of the molecule. One can then assume that during an electronic transition the nuclei effectively remain stationary with no change in their momenta [14;23;31]. A vertical transition therefore implies that an electronic transition occurs with no change in the nuclear geometry, and is drawn on a molecular potential energy diagram as a vertical line.

Thus the ion can be promoted to a higher energy state, usually a vibrationally excited state of an excited electronic state. However, the ion is unlikely to remain in this high energetic state and the molecule will redistribute the energy to leave the ion in a vibrationally activated state in the ground electronic state [11;14;17;23]. This process is illustrated on a molecular potential energy diagram in Figure 4-10. The potential energy of a molecule varies with the inter-nuclear separation. For a simple diatomic system the variation in the molecular potential can be plotted as a two-dimensional curve, similar to that of the collision-pair interaction potential curve in Figure 4-2. For further simplicity diatomic systems are used as models illustrating the activation processes. The electronic configuration of the molecule has a direct effect upon its

geometry and energy, so there exists a potential surface for each possible electronic configuration.

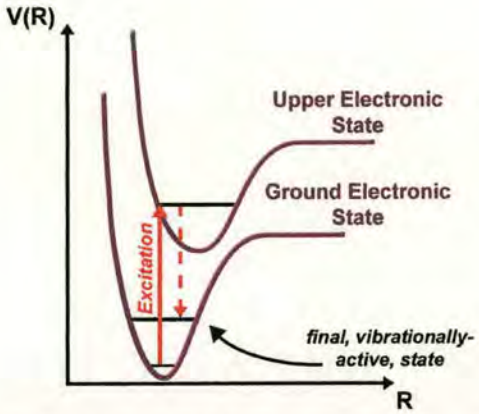

Figure 4-10 The molecular potential energy diagram of a diatomic system undergoing electronic excitation. The horizontal lines represent the vibrational levels associated with the molecular potential curves. The solid arrow indicates the vertical Franck-Condon transition, while the dashed arrow shows the result of the energy redistribution.

The mechanism by which the excited ion will lose the excess energy is through a rapid internal conversion process involving a radiationless transition to the final vibrationally activated state. The most common form of radiationless transition is thermal decay, where energy is transferred from the excited species to the molecules in the immediate environment, most likely into their vibrational modes [23;32].

This mechanism of excitation does not require the close approach of the nuclei of the ion and the neutral, and thus the nuclear-repulsive part of the interaction potential need not be sampled by the collision, an outcome that would result in momentum transfer. Therefore collisions with large impact parameters would produce minor scattering angles, corroborating expectations for negligible scattering with minimal momentum transfer.

It has been observed that the efficiency of ion excitation decreases rapidly with decreasing ion velocity [14;16;23], as may be expected with the corresponding increase in

interaction time, which would then move out of the necessary quasi-resonance with the transition time and hence lower the efficiency of excitation.

Vibrational Excitation

The separation between vibrational energy levels is much smaller than that for electronic levels. As such the corresponding value of τ is at least an order of magnitude greater for vibrational transitions than for electronic transitions. This then places the interaction time somewhere in the range of 10^{-13}-10^{-14} seconds for efficient vibrational excitation of an ion. Thus one would expect that vibrational excitation would be more prominent for slower moving ions with a reasonably strong attraction potential with the neutral target molecule. It has been observed that ions accelerated to kinetic energies of the order of $10 - 10^2$ electronvolts are the most efficient for vibrational activation of the ions [10;14;23;33;34].

Vibrational activation can occur through a number of different mechanisms [23]. One possibility is direct vibrational activation through the formation of a long-lived collision complex whose lifetime is greater than the time required for several vibrational transitions [11;14;16;34]. A long-lived collision complex can be formed if the interaction potential between the collision pair has a significantly deep potential well, such as may be found for an ion-molecule collision pair [23]. Should the complex be sufficiently long-lived the internal energy uptake Q will be distributed statistically among all the possible degrees of freedom of the collision complex [23;35-37]. Energy transfer in long-lived collision complexes has been measured to be as much as nearly 60% of the maximum centre-of-mass energy E_c [38].

A second possibility for vibrational excitation is through an impulse collision [23;39;40] for which the interaction time is required to be shorter than the vibrational transition period. In an impulsive interaction, only one part of the ion (an atom or a group of atoms) is directly involved in an elastic collision with the neutral, while the remainder of the ion acts as a spectator as depicted in Figure 4-11. Since the interaction time is less than the time required for the nuclei to adjust adiabatically (vibrationally) to the perturbation of the collision, a vibrational transition is likely

[11;14;15;23;41]. While the interaction time should be shorter than a vibrational period, it is still significantly longer than any electronic transition, otherwise electronic excitation would be favoured. It has been found that impulse collisions can occur for ions with an initial kinetic energy in the kiloelectronvolt range.

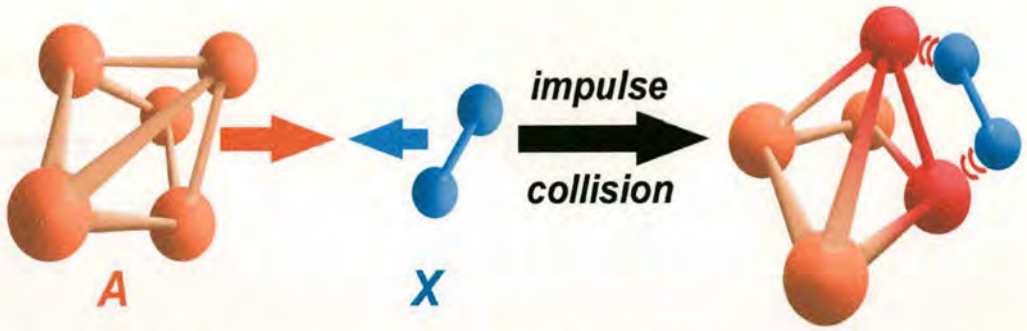

Figure 4-11 An impulse collision between molecules A and X. The collision affects only one part of the A molecule in an elastic collision, as shown by the red shaded atoms, while the remainder of the A molecule is considered as a spectator.

An impulsive collision samples the nuclear-repulsive part of the ion-molecule interaction potential, from which a considerable transfer of momentum can occur between the collision partners. Thus one would expect the scattering angles of the ion to be reasonably large in the centre-of-mass frame after the collision [23]. For the most part small impact parameters produce larger scattering angles since the collision pair encounters greater nuclear repulsion, and hence greater momentum transfer, with decreasing separation [42].

Since an impulsive collision involves only one part of the ion, the maximum energy available for conversion into internal modes is less than that accessible for an interaction between the neutral target molecule and the entire ion, due simply to the fact that in calculating the centre-of-mass energy, the mass of the ion is reduced to the mass of the atom(s) involved in the collision [15;41]. Uggerud and Derrick derived an equation to work out the mean internal energy uptake of a species in an impulsive collision, provided that the masses of the ion, target gas molecule, m_g, and sampled atom(s), m_a, were known[15].

$$\langle Q \rangle \approx \frac{1}{2}\chi E_c \quad where \quad \chi = 4\frac{m_a m_g}{(m_a + m_g)^2} \tag{4-39}$$

It can be seen that internal energy uptake will be maximised when the mass of the atom(s) struck is equal to the mass of the neutral target gas molecule (χ=1), and thus the maximum transferable energy will be the centre-of-mass energy. In most cases of polyatomic ions experiencing collisions with a neutral bath gas, the mass of the target gas will be much lower than that of the ion. This fact, coupled with the large angle scattering that is likely with such conditions means that the maximum amount of collision energy transfer will be much less than the 60% that has been observed for long-lived collision-complexes.

It has been proposed that the probability of an impulse collision increases with the collision energy, and hence the relative ion velocity, suggesting that the long-lived complex is only tenable at very low ion velocities [10;11;23]. Indeed the long-lived collision complex model is usually thought to be valid only when the relative translational energy of the collision pair is smaller than, or comparable to the binding energy of the collision complex, which for ion-molecule complexes is of the order of 1eV. Therefore one may expect a long-lived collision complex to occur for a centre-of-mass collision energy below 1eV [10]. In general the efficiency of vibrational excitation of the ion in a long lived complex has been observed to decreases with increasing ion velocity [10;11;14;33].

The overall outcome of vibrational excitation is to leave the ion vibrationally activated in the ground electronic state [12;14;16;17;30], similar to the general outcome of electronic excitation. However there will be differences between the final states of the ions produced by the two excitation mechanisms, most notably in the subsequent rotational energy of the ion, for which direct vibrational activation of the ion at low collision energies is expected to be more efficient at increasing.

Electronic/Vibrational Excitation

Given certain Franck-Condon factors vibrational excitation can occur with non-vertical electronic transition [23]. In a situation where the interaction time is slightly

less than the electronic transition period and the impact parameter is sufficiently small, an impulsive collision can occur. The mechanism is similar to that detailed for vibrational excitation, but instead stimulates an electronic transition due to the very small interaction time [17;23;43;44]. Therefore large angle scattering of the ion is expected, unlike the outcome of direct electronic excitation. To attain such a small interaction time the ions must normally be accelerated by a very high electric potential at the higher end of the keV scale.

Massey's adiabatic criterion cannot be justly applied to vibrational excitation or the mixed excitation mechanisms, as both feature maximum excitation efficiencies at interaction times that are greater or less than a vibrational or electronic transition. Nevertheless, one can employ the essence of Massey's argument for all forms of excitation: the magnitude of the interaction time is a gauge for the type of activation that is most likely to occur, and therefore must be in quasi-resonance for the average period of electronic or vibrational transitions, as shown in Figure 4-12.

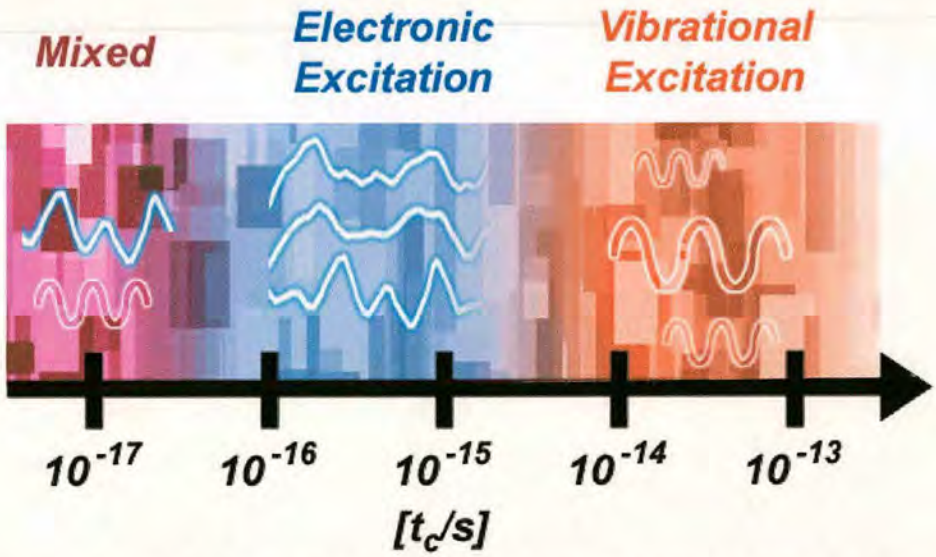

Figure 4-12 A guide to the typical excitation mechanisms for given interaction times

It is possible to determine the probability of excitation of an ion after a single collision, often referred as the probability of internal energy transfer [10], but it relies on knowledge of many intrinsic quantum variables such as the density of states with certain energy and the interaction matrix of the each collision [34], variables that are

unknown or incredibly difficult to calculate for the complex polyatomic transition metal carbonyl clusters under study.

4.3.6 Rate of Collision And The Rate of Activation

The presence of intrinsic potential energy barriers discussed in Chapter 4.2.1 has a direct effect on the rate of collisions, in some cases promoting and in others hindering collisions. As was discovered in Chapter 4.2.3 the reaction cross section for reactions with no energy barrier is larger than would be calculated for the hard-sphere model as it accounts of the ion-molecule attraction (Equations, 4-15 and 4-16). Where an energy barrier is present to reaction, the reaction cross section is dependent upon the relative collision energy being sufficient to overcome that energy barrier. With a value of the reaction cross-section, the rate constant can be determined from its product with the relative velocity of the reactants, v_{rel} [6]:

$$k(E) = \sigma_r v_{rel} \tag{4-40a}$$

Averaging this over a Maxwell-Boltzmann distribution produces [6]:

$$k(T) = \langle \sigma_r v_{rel} \rangle_{MB} \tag{4-40b}$$

The rate of collisions can provide a good measure of the rate of activation of the cluster ions. Since collision induced dissociation is a two-step process (bimolecular collision and activation, followed by dissociation) the two reactions can be separated. One can then define a separate rate for the activation of the cluster above the reaction threshold energy (for bond forming or bond dissociation depending upon the experiment), and a rate for the subsequent reaction.

Unfortunately the dependence of the reaction cross section on such factors as the impact parameter (which cannot be fixed in a reaction system), and the probability of steric factors (the necessity of a collision pair meeting at a specific orientation for a reaction to occur). While a probabilistic steric factor can be included to the reaction cross-section it can clearly be seen that to calculate *a priori* the reaction cross-section is made very difficult by the many different factors that must be included for accuracy. Attempts have been made to generate other means to quantify the reaction cross section by accounting for the intermolecular interactions. As already covered the attractive part of an ion-molecule potential can permit collisions from a broader

range of impact parameters than would occur for hard spheres, and thereby promote the efficiency of reaction and increase the reaction cross-section. Buttril derived a relation to define the reaction cross-section that quantitatively accounts for the increased possibilities of reaction that features a dependence upon the relative collision velocity v_{rel}, and not on the impact parameter [18]:

$$\sigma(v_{rel}) = \left[\frac{\pi}{v_{rel}}\right]\left[\frac{4e^2\alpha}{\mu}\right]^{1/2} \qquad (3\text{-}35)$$

In the expression μ is the reduced mass of the collision pair and α represents the polarisability of the neutral. The electronic charge on the ion is given by e. This equation is derived from balancing the dipole-induced attraction between the ion and the neutral collision pair against the centrifugal barrier. It is assumed that impact parameters that give orbiting or hard collisions, where $b < b_{orb}$, lead to the transfer of energy to activate the ion. However the above equation does not provide any information on the nature of the collision complex that is formed, and its validity is uncertain.

Fortunately, determination of the reaction cross section after the reaction has occurred can be made from the product ion peaks in the mass spectra, as covered in Chapter 4.4.4.

4.3.7 Multiple Collisions

To be able to extract accurate kinematic data from any collision-induced dissociation event requires the occurrence of a single collision between an ion and the target neutral molecule, for which there is a well-defined energy of the ion-molecule reaction. However, a single collision process can only occur if there is only one single neutral molecule present for collision, i.e. zero target gas pressure. Therefore there is always a finite probability that a series of sequential ion-molecule collisions will occur in any given collision-induced dissociation experiment. However, techniques have been devised that allow one to derive the reaction cross-section for a single collision event. As an example the Armentrout group calculate the reaction cross-section for a given ion-molecule collision-induced dissociation reaction at

different pressures of target gas. It is then possible to extrapolate the cross-sections to the corresponding value at zero pressure [6].

A multi-collision process can be thought of as a series of individual, single-collision events [10]. Each collision can be considered to be a separate, independent event, occurring between an ion and a 'fresh' neutral molecule. Thus the outcome of any one collision is independent of the state of the ion from the previous collision. The collision frequency increases linearly with target gas pressure and the relative velocity. When the ions have passed through the target gas the final state of the ion will represent a sum over the outcome of each collision. As an example the final trajectory of the ion is determined from the sum of all scattering angles (and hence the total momentum transfer to the ion) from each collision, and the reaction cross-section can be considered to be the sum of all individual reactive collision cross-sections. Every additional collision increases the variability in the distribution of the final state of the ion [6] and it would be impossible to construct a statistical model to accurately determine the outcome of the collision process. Therefore most *a priori* calculations correspond to an average over the possible outcomes for each collision.

Consequences Of Multiple Collisions

It is important that one consider the consequences of multiple collisions on the activation and subsequent dissociation of an ion in collision-induced dissociation. In a multi-collision process the ion increases its internal energy in a series of small increments with each collision [14]. Some collisions with the neutrals may be deactivating, but the overall effect is the excitation of the ion. An ion undergoing multiple collisions will accumulate more energy than it would with a single collision at the same ion kinetic energy (measured in the laboratory frame) [6]. It is therefore thought that a direct consequence of multiple collisions is that the threshold for product formation is shifted to lower energies [6] with the sequence of excitation halting as soon as the dissociation threshold is reached [14]. Therefore multiple collision-induced dissociation shall most often only provide data on the lower limits of the actual thermochemistry of the dissociation reaction [6].

Two thermal gases experiencing multiple collisions will maintain a thermal distribution of velocities. However, in a collision-induced dissociation experiment a large number of collisions can slow the ions down to thermal velocities, although this is an extreme scenario. For the most part the translational energy distribution of the ions is merely relaxed [16]. Since the collision frequency is linearly dependent upon the relative ion velocity, as is the maximum amount of possible energy transfer, E_{cm}, one can reason that the number and reactivity of collisions shall therefore decrease as the velocity is decreased, although one should stress that in most experiments this effect will not be overly prominent.

4.3.8 Laser Activation

The processes that occur during laser activation of molecules are in essence much simpler than collisional activation. A molecule that is struck by an incident laser beam shall absorb a photon, provided that the photon is of an energy that corresponds to the energy separation between the molecule's present energy level and an upper state. The transition that would occur between these two levels must also be permitted by the selection rules, but as mentioned earlier, these are very easily broken in the experimental system. Indeed with high laser fields the electric field of the radiation is strong enough to significantly shift the molecular energy levels of the incident molecule [7].

The energy of a photon is fixed from the following de Broglie relationship:

$$E = h \times \frac{c}{\lambda} \qquad \text{(2-??)}$$

where h represents Planck's constant, c is the speed of light, and λ is the wavelength of the photon. The lasers used within the experiments discussed within this thesis are of fixed wavelengths, and as such the photons are of a fixed energy. Therefore it is impossible to intentionally excite the molecule to specific excited states, although this ability is of little interest to this thesis.

The modes that are excited by the interaction between the photon and the molecule are dependent upon the wavelength of the photons. Long wavelength infrared lasers

are composed of low energy photons, suitable for the excitation of the closely spaced vibrational and rotational levels within one electronic state, whereas short wavelength ultraviolet lasers are composed of higher energy photons capable of interacting with the wider spaced electronic levels, as depicted in Figure 4-13. The interaction between the photon and the molecule usually occurs via the molecule's electric dipole (permanent or induced). Although it is possible for the photon to interact with electric quadrupoles, magnetic dipoles etc, these interactions tend to be much weaker [45].

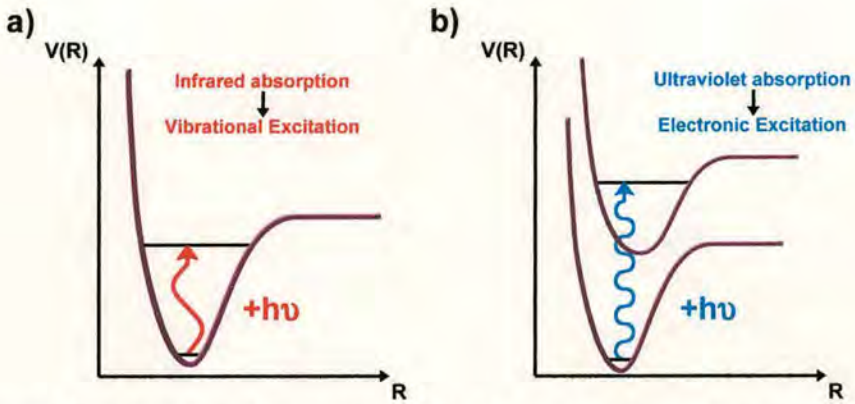

Figure 4-13 A depiction of the typical levels of activation for the two common laser wavelengths.

While the photon energy is fixed, the power of the laser beam is determined from the intensity: a factor related to the number of photons per unit time and area [45]. A greater intensity can increase the number of species excited by the laser, and while it is normally the case that a molecule can only interact with a single photon at a time, an intense beam can possibly promote multiple photon absorption [45]. For many polyatomic species multiphoton absorption is the only mechanism by which photo-induced dissociation of the molecule can occur. While the wavelength of any photon should be in resonance with the separation of the molecular energy levels, the electric field component of very intense laser beams can allow for non-resonant absorption. This reduces the specificity of the interaction, with the fixed wavelength photons able to be successfully absorbed by any species [7]. Extensive fragmentation is possible in intense laser beams, but experimental evidence suggests that such fragmentation is not due to direct fragmentation, but rather to a sequential

absorption/dissociation process. Such successive fragmentation occurs very quickly, often within the few nanoseconds of the laser pulse [46].

Intramolecular energy redistribution can occur between each photon absorption event, which can aid both multiphoton absorption and has implications for following photo-induced fragmentation. In the first instance, consider a resonant absorption event. The excited energy level occupied by the molecule may not be suitable to allow a second resonant absorption to a higher level. Energy partitioning moves the molecule to a lower energy state from where a second resonant absorption event can occur. In the case of fragmentation, energy partitioning ensures that all photo-activated species have had their internal energy equipartitioned around all the available degrees of freedom, permitting the use of RRKM theory with photo-induced dissociation [7]. The greater the density of states in a molecule, the faster the redistribution of energy will occur at higher energies. Thus the rates of redistribution will vary but they can be in the sub-picosecond range for high excitation energies [7]. It can thus be seen that in an analogous manner to collision-induced dissociation, where the difference in relative incident velocities only affects the type of excitation immediately experienced by an ion on collision and has no bearing on the final state of the ion or the subsequent fragmentation, the timescale for photon absorption and the wavelength of the photon have no influence on the subsequent dissociation step. It should be noted now that the process of photoionisation is analogous to that of photodissociation, with the products being a cation and an electron.

4.4 Dissociation Of Activated Species

It has been shown that in the case of both collisional and photo activation, rapid energy partitioning occurs, and thus all the fragmentation reactions can be considered to be independent of the manner in which the species was brought to the dissociation threshold, allowing for the treatment of the unimolecular dissociation by quasi equilibrium / RRKM theory. While the nature of the excitation step is endothermic

and the fragmentation is exothermic, the overall reaction may be endothermic, exothermic or thermoneutral [14]

4.4.1 Dissociation Mechanisms From Excited States

Dissociation can occur by one of three ways. The first possible mechanism is that the ion/molecule is excited through successive increases in the vibrational energy in the ground electronic state resultant from multiple collisions/photon absorptions, until it reaches the maximum allowed vibrational level (the energy of which is equal to the dissociation energy). If the system receives additional energy, dissociation will follow. This mechanism is likely to occur for multiple infrared photon absorption and multiple collisional activation. It is also possible, although unlikely with the large polyatomic species under study, that a single high-energy photon or energetic collision could also promote the species beyond the maximum vibrational level. The overall process is depicted on a molecular potential energy diagram for a model diatomic in Figure 4-14.

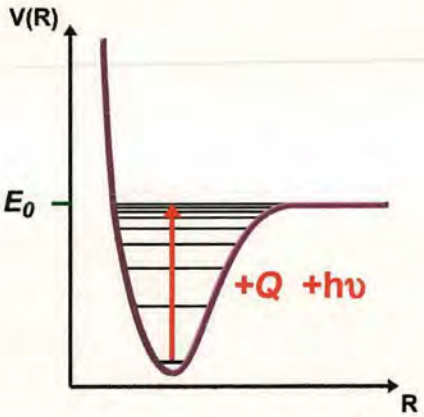

Figure 4-14 The molecular potential energy diagram for a model diatomic system undergoing vibrational activation up to the maximum allowed vibrational level, beyond which dissociation will follow. The vibrational levels of the ground electronic state have been included for reference. Diagram adapted from Reference 4.

The second possibility incorporates a transition to a vibrational state that exists above the dissociation threshold for an upper electronic level, a mechanism that is likely to occur for ultraviolet activation and is depicted in Figure 4-15 [20].

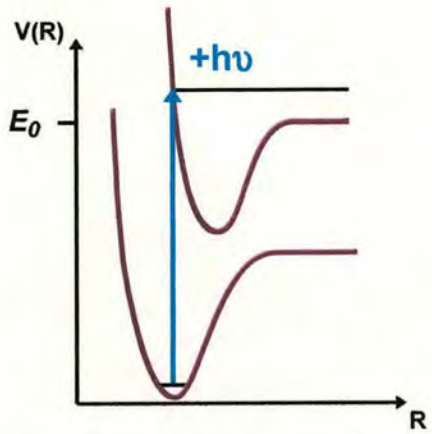

Figure 4-15 The molecular potential energy diagram for a model diatomic system undergoing an electronic transition to a vibrational level to a level in excess of the threshold energy for dissociation, denoted E_0. Diagram adapted from Reference 20.

The third possibility is that the ion/molecule is excited to a repulsive unbound electronic state [20]. This state exists from the electron occupancy of anti-bonding orbitals, leading to the dissociation of the bond, and is illustrated in Figure 4-16.

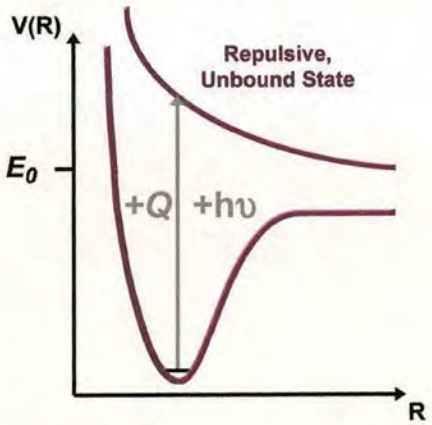

Figure 4-16 The molecular potential energy curves for a model diatomic system where the activation occurs to a repulsive, unbound state. The grey text denotes that activation can occur via collisional activation, or infrared and ultraviolet radiation. Diagram adapted from Reference 20.

It is possible for an ion/molecule complex to dissociate even if it occupies an excited state below the dissociation limit. An upper bound electronic state can be crossed by a dissociative repulsive state, causing the perturbation of the bound state. If the

ion/molecule is excited to a vibrational level close in energy to the point of intersection, the molecule may take on the dissociative character, via a *curve crossing* mechanism, and fragment. The overall activation and dissociative process is known as *predissociation* [20;32] and is illustrated for a model diatomic system in Figure 4-17. The curve crossing mechanism occurs by radiationless transitions, controlled by selection rules. However, a strong spin-orbit coupling greatly enhances the probability of curve crossing within the species by allowing transitions that would not be allowed by the selection rules. Thus the curve crossing mechanism occurs between two potential energy surfaces of different spin.

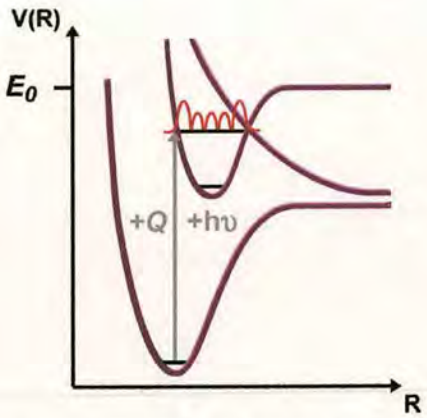

Figure 4-17 The molecular potential energy curves for a diatomic molecule undergoing predissociation. The excited vibrational state in the upper bond state has an energy below that of the critical energy, E_0 but lies close to the point of intersection with the repulsive unbound state. Diagram adapted from Reference 20.

The predissociation mechanism is particularly important in the photodissociation of large complex molecules. It is favoured over direct dissociation because such molecules do not normally undergo direct optical dissociation in the wavelength regions of their strongest absorption, and the molecules contain a large number of reasonably closely spaced electronic states, and a correspondingly large number of vibrational modes, which increases the probability of curve crossing [20]. It is important to realise that the outcome of predissociation may be different from the dissociation products from direct dissociation, since the fragments from predissociation are dependent upon the nature of the dissociative state that is involved in the curve crossing mechanism.

4.4.2 Energy Partitioning

The structural change associated with any dissociation step produces a new distribution of energy E within the fragments due to the movement of electrons, and the breaking of bonds. Thus the internal energy content of the daughter ion is significantly different from its parent. In terms of a consecutive dissociation reaction, such as:

$$W^- \xrightarrow{-neutral} X^- \xrightarrow{-neutral} Y^- \xrightarrow{-neutral} Z^- \qquad (4\text{-}25)$$

the internal energy content of each subsequent daughter ion will be smaller in comparison to its parent ion, and the unimolecular rate of dissociation for each dissociative step will be unique.

On dissociation, the energy of the parent ion will be partitioned between both the ionic and neutral fragments. The energy of the parent ion, daughter ion and neutral fragments can be separated into two independent components: the kinetic energy and the internal energy.

Kinetic Energy Partitioning

The total energy of the collision system shall be shared between the products after the reaction. The mechanism and energy of any reaction has a direct influence on the internal and kinetic energy distribution of the products, and these are determined by separate partitioning functions [10]. After the fragmentation of the excited reactant ion the resultant daughter ion and the neutral fragment will have a kinetic energy dependent upon the endothermicity of the reaction that formed it [14]. Kinetic energy partitioning is normally very simple since the kinetic energy is directly proportional to the relative mass of the products. Therefore for the unimolecular dissociation reaction:

$$A^{*-} \longrightarrow B^- + C \qquad (4\text{-}41)$$

the kinetic energy of the daughter ion B^- is:

$$E_{kin}\left(B^-\right) = \frac{m_{B^-}}{m_{A^{*-}}} E_{kin}\left(A^{*-}\right) \qquad (4\text{-}42a)$$

And for the neutral fragment C:

$$E_{kin}(C) = \frac{m_C}{m_{A^{*-}}} E_{kin}(A^{*-}) \qquad \text{(4-43b)}$$

Internal Energy Partitioning

The internal energy available to the fragmentation products is that which is in excess of the ground state of the products. The energy difference between the ground states of the parent and the products can be measured as ΔE_x, therefore making the internal energy of the products equal to E_{int}-ΔE_x as shown in the potential energy diagram for the dissociation reaction in Figure 4-18, which plots the variation in the potential energy of the system as the reaction progresses. This still holds true if the ion A^- is originally in an energy state, E_i, above the ground state before the collision excites to E_{int} (also shown in Figure 4-18).

The internal energy of the products can also be split into two independent components: the reverse activation energy and the non-fixed energy. The reverse activation energy is the energy that would be required by the fragmentation products to return to their original state, A^{*-}. The reverse activation energy can be determined from the energy difference between the ground state of the products and the critical energy, labeled as E_A^r. The non-fixed energy is the internal energy of the daughter ion and neutral fragment above the critical energy, denoted as E^t [14;23]. Both of these are shown Figure 4-18.

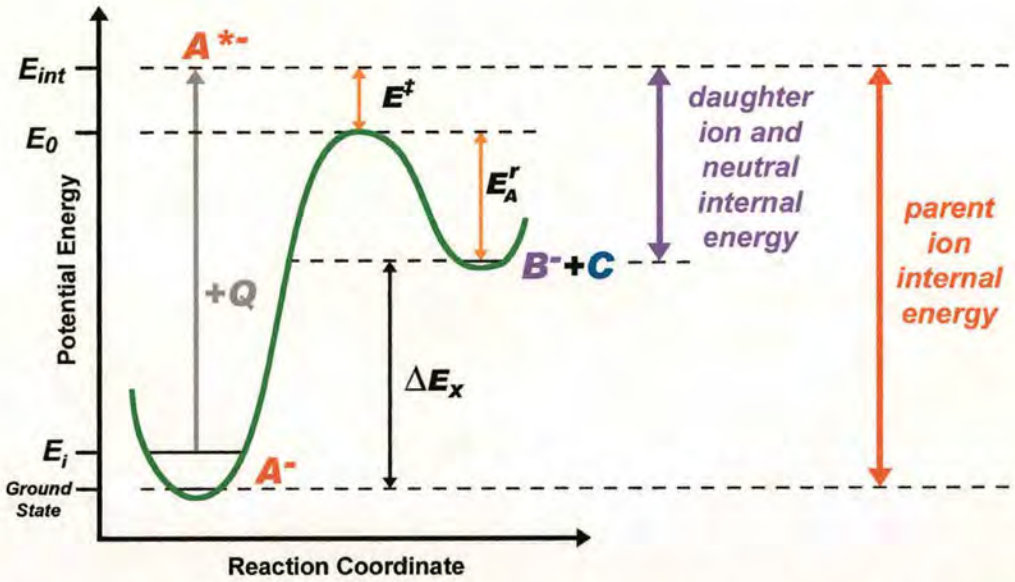

Figure 4-18 The progress of the dissociation following the change in the potential energy with reaction coordinate: the excited parent ion A^{*-} dissociates to produce the daughter ion B^- and neutral fragment C. The partitioning of the internal energy from parent to daughter is shown. Figure adapted from Reference 14. Note that this diagram applies for the process of collision-induced dissociation and photodissociation.

The partitioning of the internal and kinetic energy from parent ion to daughter ion and neutral fragment is made slightly more complicated by an associated phenomenon with the dissociation reaction. A fraction of the parent internal energy that is in excess of the ground state of the products is unavailable to the daughter ion and neutral, and is partitioned into the kinetic energy of separation of the fragments [23]. Thus the partitioning of kinetic energy is always modified by this extra translational energy known as *kinetic energy release* of the reaction [10;14;47;48].

4.4.3 Kinetic Energy Release

The kinetic energy release, T, can be considered in terms of the translational energy that is released in the fragmentation [14] due to excess internal energy above the dissociation threshold [47;48]. The kinetic energy release affects the resultant translational energy of all fragmentation products. Since fragmentation is isotropic in the centre-of-mass frame, the product kinetic energy distribution is equally likely

to be reduced or increase by the kinetic energy release when converting back to the laboratory frame of reference, generating a spread of product kinetic energies [23].

The value of the kinetic energy release in the centre-of-mass frame is rather small in comparison to the product kinetic energy, but on conversion to the laboratory frame of reference the kinetic energy release is 'amplified', allowing for its accurate measurement. This laboratory value can then be converted back to its centre-of-mass value [14;47;48]. Measurement of the kinetic energy release can be made from reflectron time-of-flight mass spectrometry measurements. The front plate of the reflectron is set to a voltage that is greater than the kinetic energy of the daughter ion but lower than the kinetic energy of the parent ion, with the values of the kinetic energy determined from the kinetic energy partitioning relationship (Equations 4-43). Because the kinetic energy release gives the ions a spread of kinetic energies, the peak shape of the daughter ion is broadened. Analysis of the peak shape then provides details on the kinetic energy release for the formation of that daughter ion.

Measurement of the kinetic energy release can provide useful information on the structure of the fragmenting species and the energetics, excitation mechanism and dynamics of the process [47;48]. The kinetic energy release also provides information on the amount of excess energy that is not partitioned to the fragments, and so provides a more accurate value of the daughter ion internal energy, a vital factor in determining the rate of the dissociation reaction. The total kinetic energy release is produced from contributions from the non-fixed energy, $E^{\ddagger}$, and the reverse activation energy E_A^r, denoted as $T^{\ddagger}$, and T^r, such that the total kinetic energy release, T, is equal to $T = T^{\ddagger}+T^r$ [14;23] as shown in Figure 4-19.

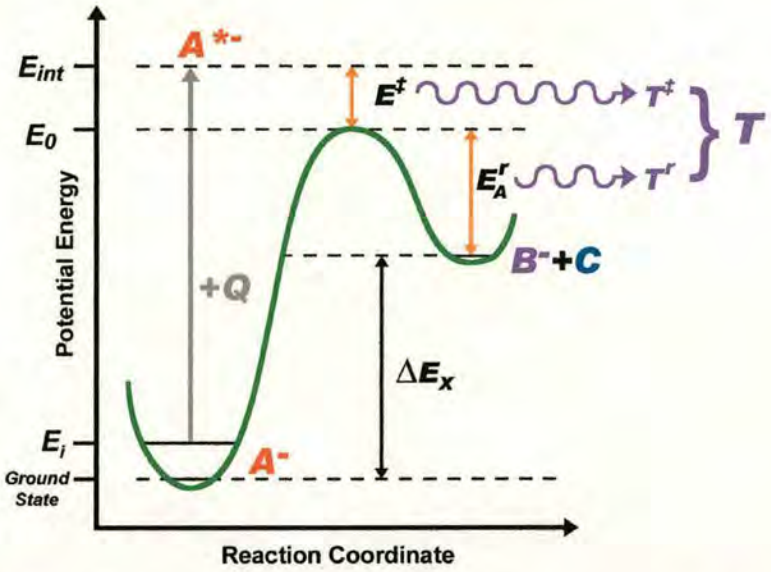

Figure 4-19 The potential energy diagram for dissociation, showing the contributions made from the non fixed energy $E^{\ddagger}$, and the reverse activation energy E_A^r to the kinetic energy release. Once again this diagram applies to both collision-induced dissociation and photodissociation.

4.4.4 Rate Of Dissociation

The rate of the fragmentation has a direct effect upon the abundance of the daughter ions detected in mass spectrometry. The finite time between the sample introduction and the analysis stage provides the time window within which the ions have to dissociate. The rate of dissociation will therefore determine the number of daughter ions produced, and the possible subsequent dissociation of the daughter ions [49].

The unimolecular nature of the dissociation stage of collision-induced dissociation therefore gives a unimolecular rate constant for dissociation. However, the fragmentation is itself dependent upon the bimolecular rate of the collisions to produce the necessary excitation. Since the dissociation step is known to occur some time of the order of 10^{-6} or 10^{-5} seconds after the excitation step [14;23]and that the dissociation reaction occurs on a much longer time scale in comparison to the activation step one can legitimately consider the fragmentation step as a separate entity and measure the unimolecular rate of the fragmentation using RRKM theory. In the case of photo-induced fragmentation, the fact that energy is observed to be

partitioned between all available energy modes prior to dissociation and that the dissociation reaction also occurs on a longer timescale in comparison to the activation step, the rate can also be evaluated from RRKM theory.

The internal energy-dependent reaction rate for the unimolecular dissociation can be defined by transition state theory, which uses the RRKM expression to derive the microcannonical rate constant [10]:

$$k(E_{\text{int}}) = \frac{n^{\text{dgn}} W(E_{\text{int}} - E_0)}{h\rho(E_{\text{int}})} \tag{4-43}$$

where n^{dgn} is the reaction path degeneracy, $W(E_{int}-E_0)$ is the sum of states of energy equal to (E_{int}-E_0), and $\rho(E_{int})$ is the density of states at energy E_{int} [10;48]. As discussed previously, knowledge of such an equation to determine the rate constant is not particularly useful when such quantum variables as the density of states are an un-determined quantity for the cluster species under study, and so rate calculations shall be reliant on measurements of the reaction cross-section. The reaction cross-section will thus provide the product of the bimolecular reaction cross-section for excitation and the unimolecular reaction cross-section for the subsequent dissociation.

As a further complication, the rate of reaction can have a degree of dependency on the overall rotation of the ion, such that the total angular momentum of the collision system must be conserved during the course of the reaction [10;14]. The problem can be overcome by treating the conservation of angular momentum as a rotational energy barrier, analogous to the centrifugal barrier in Chapter 4.2.1. The centrifugal barrier is associated with bimolecular reactions, but for the unimolecular fragmentation the rotational energy barrier is partially converted into the translational energy of the products, and thus lowers the value of the critical energy of the reaction. This is an effect that reduces with increasing molecular size, so its effects on the large cluster species under study shall most likely be negligible [10].

As discussed previously in Chapter 4.3.6 a measure of the rate of dissociation can be made from knowledge of the reaction cross section. Fortunately, it is often acceptable to measure the relative reaction cross-section of dissociation reactions

from the resultant daughter ion intensity and limit oneself to a comparative study of the different reaction cross-sections for the reactions of one particular species [14]. Thus the energy dependent reaction cross section can be determined from:

$$k(E) = \sigma_r v_{rel}$$

4.5 Reference List

1. Wronka, J.; Ridge, D. P. *Journal Of The American Chemical Society.* **1983**, *106*, 67-71.

2. Meckstroth, W. K.; Ridge, D. P.; Reents Jr, W. D. *Journal Of Physical Chemistry.* **1985**, *89*, 612-617.

3. Forbes, R. A.; Laukien, F. H.; Wronka, J. *International Journal Of Mass Spectrometry And Ion Processes* **1988**, *83*, 23-44.

4. Atkins, P. W. *Physical Chemistry*, 6th ed.; Oxford University Press: 1998.

5. Brouard, M. *Reaction Dynamics*, Oxford University Press: New York, 1998.

6. Armentrout, P. B. *Journal Of The American Society Of Mass Spectrometry.* **2002**, *13*, 419-434.

7. Levine, R. D.; Bernstein, R. B. *Molecular Reaction Dynamics and Chemical Reactivity*, 1st ed.; Oxford University Press Inc: New York, 1987.

8. Pilling, M. J.; Seakins, P. W. *Reaction Kinetics*, 1st ed.; Oxford University Press Inc: New York, 1997.

9. Lindemann, F. A. *Transactions of the Faraday Society* **1922**, *17*, 598.

10. Drahos, L.; Vékey, K. *Journal Of Mass Spectrometry.* **2001**, *36*, 237-263.

11. Chapman, J. R. *Practical Organic Mass Spectrometry*, 2nd ed.; John Wiley & Sons, Inc.: 1998.

12. Douglas, D. J. *Journal of the American Society of Mass Spectrometry* **1998**, *9*, 101-113.

13. McLafferty, F. W.; Bente, P. F.; Kornfeld, R.; Tsai, S. H. I. *Journal Of The American Chemical Society.* **1973**, *95*, 2120-2129.

14. Cooks R. G. *Collision Spectroscopy*; 1st ed.; Plenum Press: New York, 1978; Chapter 7, pp. 357-450.

15. Uggerud, E.; Derrick, P. J. *Journal Of Physical Chemistry* **1991**, *95*, 1430-1436.

16. Douglas, D. J. *Journal Of Physical Chemistry* **1982**, *86*, 185-191.

17. Horning, S. R.; Cooks, R. G. *Journal Of The American Chemical Society.* **1990**, *112*, 119-126.

18. Buttrill, S. E. *Journal Of Chemical Physics.* **1970**, *52*, 6174-6183.

19. Richards, W. G.; Scott, P. R. *Energy Levels In Atoms And Molecules*, 2nd ed.; Oxford University Press Inc.: New York, 1998.

20. Wayne, C. E.; Wayne, R. P. *Photochemistry*, 2nd ed.; Oxford University Press Inc.: New York, 1999.

21. Halliday, D.; Resnick, R.; Walker, J. *Fundamentals of Physics Extended*, 4th ed.; John Wiley & Sons, Inc.: New York, 1993.

22. Johnson, R. E. *Introduction to Atomic And Molecular Collisions*, Plenum Press: New York, 1982.

23. Busch, K. L.; Glish, G. L.; McLuckey, S. A. *Mass Spectrometry/Mass Spectrometry: Techniques And Applications Of Tandem Mass Spectrometry*, 1st ed.; VCH Publishers, Inc.: New York, 1988.

24. Kondrat, R. W.; Cooks, R. G. *Analytical Chemistry.* **1978**, *50*, 81a-92a.

25. Massey, H. S. W. *Reports on Progress in Physics* **1949**, *12*, 248.

26. Franchetti, V.; Freiser, B. S.; Cooks, R. G. *Organic Mass Spectrometry* **1978**, *13*, 106-110.

27. Bowie, J. H.; Blumenthal, T. *Journal Of The American Chemical Society.* **1975**, *97*, 2959-2962.

28. Wachs, T.; McLafferty, F. W. *International Journal Of Mass Spectrometry And Ion Physics.* **1977**, *23*, 243-247.

29. Fedor, D. M.; Cooks, R. G. *Analytical Chemistry.* **1980**, *52*, 679-682.

30. Kim, M. S.; McLafferty, F. W. *Journal Of The American Chemical Society.* **1978**, *100*, 3279-3282.

31. Sharp, D. W. A. *Dictionary of Chemistry*, 2nd ed.; Penguin Books Ltd: 1990.

32. Atkins, P. W.; Friedman, R. S. *Molecular Quantum Mechanics*, 3rd ed.; Oxford University Press Inc.: New York, 1997.

33. Refaey, K. M.; Chupka, W. A. *Journal Of Chemical Physics.* **1965**, *43*, 2544-2545.

34. Oref, I.; Tardy, D. C. *Chemical Reviews* **1990**, *90*, 1407-1445.

35. Eastes, W.; Toennies, J. P. *Journal Of Chemical Physics.* **1979**, *70*, 1644.

36. Eastes, W.; Toennies, J. P. *Journal Of Chemical Physics.* **1979**, *70*, 1652.

37. Greene, R. F.; Hall, R. B.; Sondergaard, N. A. *Journal Of Chemical Physics.* **1977**, *66*, 3171.

38. Harrison, A. G. *International Journal Of Mass Spectrometry And Ion Physics* **1983**, *51*, 353.

39. Boyd, R. K.; Kingston, E. E.; Brenton, A. G.; Beynon, J. H. *Proceedings of the Royal Society of London A* **1984**, *392*, 59.

40. Mahan, B. H. *Journal Of Chemical Physics.* **1970**, *52*, 5221-5225.

41. Cooper, H. J.; Derrick, P. J.; Jenkins, H. D. B. *Journal Of Physical Chemistry* **1993**, *97*, 5443-5444.

42. Hasted, J. B. *Physics of Atomic Collisions*, 2nd ed.; Elsevier: New York, 1972.

43. Durup, J. *Recent Developments in Mass Spectroscopy*, University Park Press: Baltimore, 1970.

44. Singh, S.; Harris, F. M.; Boyd, R. K.; Beynon, J. H. *International Journal Of Mass Spectrometry And Ion Physics.* **1985**, *66*, 131.

45. Wayne, C. E.; Wayne, R. P. *Photochemistry*, 2nd ed.; Oxford University Press Inc.: New York, 1999.

46. Dietz, W.; Neusser, H. J.; Boesl, U.; Schlag, E. W. *Chemical Physics.* **1982**, *66*, 105.

47. Lifshitz, C. *European Journal Of Mass Spectrometry* **2002**, *8* , 85-98.

48. Laskin, J.; Lifshitz, C. *Journal Of Mass Spectrometry.* **2001**, *36*, 459-478.

49. McLafferty, F. W.; Wachs, T.; Lifshitz, C.; Innorta, G.; Irving, P. *Journal Of The American Chemical Society.* **1970**, *92*, 6867-6880.

5 Laser Induced Aggregation Of Transition Metal Clusters

5.1 Introduction

As discussed in the Chapter 1, most synthetic routes to large transition metal carbonyl clusters can often require extreme conditions of heat and pressure, with little yield. Should any cluster species prove to have catalytic properties then mass manufacture would be desirable, and so research continues into facile ways in which large cluster species can be manufactured. One such possible method is the use of a laser incident upon a solid sample of smaller cluster precursors to produce labile clusters that can then aggregate into larger *supraclusters*. It is also possible that the rapid heating and photochemistry that can occur by using a laser may grant access to novel species of exotic geometry and properties.

Laser desorption ionisation has become a very popular ionisation source for the processing of biological samples though mass spectrometry. In using a system such as this the products of the laser induced aggregation of transition metal carbonyl clusters can be analysed simultaneously. The mass spectrometer of choice is a Micromass TofSpec 2E mass spectrometer, coupled with a nitrogen laser of 337 nm wavelength.

5.2 The Chemistry Of Laser Induced Cluster Synthesis

The act of irradiating a sample of cluster with a laser beam is in essence quite simple, but the process of aggregation involves many different physical processes such as the interaction between the clusters and the photons and the reactions between the subsequently excited molecules. Each of the processes governing the desorption of the cluster species and their activation and reaction has been covered in Chapters 3 and 4.

To review, for a sample deposited on a solid surface laser ablation occurs directly at the laser focus, causing the explosive decomposition of the analyte species. Molecular fragments, and even free electrons, are then ejected, which can possibly

form a plasma above the laser focus. A shockwave is created that moves across the surface forcing the desorption of intact sample molecules from the surface. The intact molecules near the laser focus will be internally excited, prompting ionisation and possibly some form of dissociation, most likely ligand loss from the transition metal carbonyl systems. In addition any neutrals produced from the surface will not be extracted by the ion optics to be analysed, and can remain in the source region where they can be exposed to more photons and collisions. The same can be said for ions of the opposite polarity to the ion mode of the instrument. The efficacy of photon absorption is a species dependent characteristic, and so it is possible that certain cluster species will be better absorbers of the ultraviolet photons than others.

A time delay of the order of microseconds between the laser pulse and the extraction allows sufficient time for reactive collisions to occur between labile cluster species in the gas phase. The cluster aggregation occurs via a series of ion-molecule association reactions [1-3], an occurrence that can be rationalised by the long range attraction that exists between these species. It is most likely that the neutral species shall be intact cluster precursor molecules desorbed from the surface. Due to the nature of the ion-molecule attraction it is assumed that all of the association reactions are bimolecular, that is only two species will meet and react at any one time. The involvement of another ion or molecule would disrupt the potential energy surface in a manner dependent upon the trajectories of the species. However, at the early stages of cluster aggregation the intervention of a third body, such as another cluster precursor, shall be vital in quenching the excess internal energy acquired by the reacting species to allow bond formation, as discussed in Chapter 4.2.3. It can be seen that ion or neutral species that carry an excess of internal energy will be less likely to undergo a successful association reaction. This is also true if the relative kinetic energy of collision is too great [4]. The ionic cluster precursors are most likely to have undergone one or several dissociation reactions, lowering the internal energy of the ion by some degree, and increasing the probability of a successful association reaction. As the clusters get bigger they will be given vibrational energy from the addition of further units to the cluster. This additional internal energy may lead to instability and should be removed, but such an act is not solely dependent upon

quenching collisions. Since the act of dissociation removes energy from the system the clusters can remove excess energy from the dissociation of the weakest bonds in the system, most likely the metal-ligand bonds. The production of small neutral molecules from the dissociation, and the reduction of the species internal energy that follows, has lead to this process being described as *evaporative cooling*. Thus the internal energy of the cluster species is likely to be reduced by collisional quenching and the evaporation of carbonyl ligands from the cluster surface. In extreme circumstances there could even be a dissociation of metal-metal bonds from the metal core, although this is less likely. However, with increasing cluster size the cluster becomes a much larger and more effective energy sink to hold the internal energy, lessening the need for cooling to occur to maintain cluster stability.

Indeed it is very likely that each of the cluster units will have experienced at least one evaporation process before being extracted to the time-of-flight analyser. The cluster population can then be modelled on the *evaporative ensemble* model developed by Cornelius Klots [5-13]. The evaporative ensemble model assumes that each cluster has experienced at least one dissociation event before being analysed, and so each detected cluster is smaller than it once was. It is also assumed that, except for very large clusters, the evaporation process proceeds via the sequential dissociation of only small regular units, such as carbonyl ligands [6;14]. While it is likely in a highly excited environment that many more dissociation events will occur, the unimolecular rate constants for consecutive losses from any given cluster tend to drop quickly. Thus each subsequent dissociation step occurs over a longer time scale than the previous one, such that the time spent in undergoing any dissociation prior to that of the immediate precursor can be ignored. A cluster ion with a great excess of internal energy will reduce its energy from the successive evaporation of ligands. Those losses that occur in the ion source will be very fast, and can be thought of as *prompt* dissociations. If the cluster ion still has an internal energy that lies within the metastable range (as discussed in Chapter 3.5.1) then the cluster ion will continue to evaporate ligands within the mass spectrometer, which can be detected as post-source decay. The cluster would then be identified as a metastable cluster undergoing post-source decay. However it is possible given the nature of successive

ligand loss that the dissociation rate will be suitably reduced that a necessary evaporation step would occur at a time after the ion has been detected, such that the ion will not be detected as being metastable. Therefore, through limits placed by the mass spectrometry, the definition of a metastable ion is constrained by the experimental time window, i.e. the flight time of the ion. An ion that has a lifetime that is only slightly longer than the flight time will reach the detector and be regarded as stable.

On a final note, it has been discovered that the success of ion-molecule association reaction to form progressively larger transition metal carbonyl clusters increases with increasing ligand desaturation correlating to the electron deficiency of the cluster ions [1-3]. Work on the clustering of iron pentacarbonyl found that depending upon the electron deficiency the reaction rate for cluster formation varies from requiring a thousand ion-molecule collisions to form just one cluster-cluster bond to association reaction occurring with nearly every collision.

5.3 The Micromass® TofSpec™ 2E Laser Desorption Ionisation Time-of-Flight Mass Spectrometer

The experiments were performed on a Micromass® TofSpec™ 2E laser desorption ionisation time-of-flight mass spectrometer at the ICI Wilton Materials Research Centre with the assistance of Dr. Tony Jackson. The instrument is fitted with a reflectron, and is also capable of running in linear mode. A schematic of the instrument is provided below in Figure 5-1.

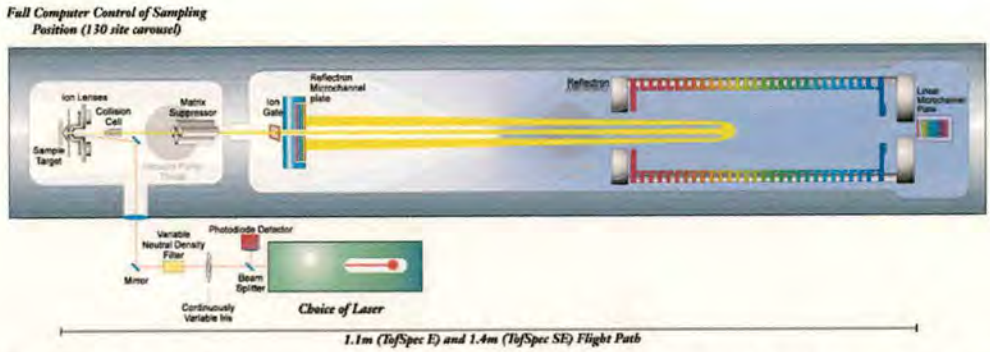

Figure 5-1 A schematic of the interior of the TofSpec instrument. Diagram adapted from Reference 15.

The controlling software for all Micromass mass spectrometer instruments is the MassLynx software suite. The software provides the user with the ability to control and fine-tune the experimental parameters as the mass spectra are being recorded. Real time control over the experiment in this way allows one to quickly tune the mass spectrometer for the best possible quality output, without having to stop and reload the sample each time a parameter is changed. There are a number of parameters that can be altered on this experiment that have a direct effect upon the nature of the ions produced, and the time the ions spend within the source and the field free region. These parameters include the laser beam intensity, and the potentials applied to the ion optics within the source. Each of these key parameters were manipulated to observe their influence on the aggregation of the clusters and the phenomenon of post-source decay.

5.3.1 Standard Parameters

Many of the instrument parameters were kept constant throughout all the experiments, and their values are given here. The experiments examined the effect of the laser intensity, and the focus electrode on the product clusters. The default values of these parameters have also been given below. The specific way in which these three parameters were altered in the experiments is described in detail in the relevant experimental sections.

The ion source region contains a Wiley McLaren style, three-stage accelerating ion optic system. The electrodes are known as the source, extraction and focus, as

discussed in the description of time-of-flight mass spectrometry in Chapter 3.51 and in Figure 3-13. However, the extraction and focus electrodes used in the instrument differ from those previously described in that they are skimmer cones, as opposed to wire meshes. The source electrode is the sample plate onto which the sample has been absorbed, and was throughout each experiment held at a potential of 20 kV. The extraction electrode is positioned approximately 3.5 mm[16] from the source electrode and was constantly held at a potential of 19950 V, creating a small potential difference of only 50 V. The focus electrode comes next and had a default value of 15500 V. Finally there is a ground electrode positioned approximately 25 mm[16] from the focus mesh. The pressure within the ion source was $6.61E^{-7}$ mbar.

The drift tube is 754 mm long from the ground electrode to the start of the reflectron (which can be taken as the length of the field free region), while the reflectron is 327 mm long. The linear detector is situated directly behind the reflectron. The detector used when operating in reflectron mode is positioned 405 mm from the reflectron in the field free region. This makes the total effective ion flight path approximately 2.3 m when operating in reflectron mode [16]. The reflectron potential was 26 kV, and the pressure within the analyser was $9.12E^{-8}$ mbar.

The laser beam is provided by a pulsed nitrogen laser, with a pulse length of 4ns. The intensity of the beam is controlled via two parameters within the software, known as *laser coarse* and *laser fine*. The laser coarse controls the first lens assembly from the laser. The laser fine is the second lens assembly and focuses the beam transmitted through the coarse optics onto the sample plate. As such the laser fine optics provide the most direct control over the intensity of the beam on the sample plate. The laser parameters are measured as percentage values by the software, with lower values pertaining to a tighter focus and more intense beam. The laser coarse was kept at 100%, while the default value for the laser fine was 25%. The repetition rate of the laser was 50 shots per scan. A single scan is comprised of the summation of the product mass spectra produced from the ions created from each shot. Thus the mass spectrum provides an average of the ion population over the

laser field conditions. The sample plate is moved by a system of stepper motors to move each spot into the region of laser focus

The instrument was run in both positive and negative ion mode, and the mass range of the instrument was set from 0 to 10000 Th.

5.3.2 Sample Preparation

Clusters species $Os_3(CO)_{12}$ and $Rh_6(CO)_{16}$ were available for use in these experiments. The transition metal species are not particularly soluble, but can be dissolved in a solution of dichloromethane, followed by sonication in an ultra-sonic bath. The absolute concentration of each solution is not important, given that the analysis of the experimental data will require no qualitative information. The sample was considered ready when there was complete coverage of the sample spot.

5.4 Effect Of Laser Intensity On Cluster Aggregation

The time-of-flight instrument was set up as above. The laser coarse value was set to 100% and the laser fine value was decreased in 25% intervals from 100% to 25%. By focussing the beam in such a way it is likely that differences in the cluster behaviour will be observed during the course of the experiment. The experiments stop at 25% because it was found that a laser fine value of 5% would produce no ions at all in either negative or positive ion mode. It is so far uncertain why such a high intensity beam would create such an effect. The high-energy conditions may prevent the aggregation of the cluster, as discussed above in Chapter 5.2, but one would still expect to see ions resultant from the ionisation and dissociation of the precursor cluster. However, by setting the laser fine value at 5% the mass spectra recorded the background electronic noise.

A total of ten scans were recorded for each laser fine level, followed by one scan at 5%. The first ten scans were summed to give an average mass spectrum, followed by the subtraction of the final scan at 5% to remove the background noise from the

spectrum and improve the clarity of the mass spectrum. The data was then smoothed by a mean, 3-channel, 2-pass method. Each of the operations was performed by the MassLynx software. In total four mass spectra were produced, one each for the different values of the laser fine parameter.

5.4.1 Positive Cluster Ions

The mass spectra recorded in positive ion mode were disappointing. A positive ion signal could not be achieved for the osmium clusters at all, for as yet unknown reasons. Figure 5-2 shows the mass spectrum recorded for the rhodium cluster with a laser fine value of 50%. The most intense peak does not pertain to any configuration of rhodium transition metal cluster, even accounting for doubly or triply charged species. In addition the peak is composed of other closely spaced peaks with a nominal separation of just 1 Th, suggesting isotope contributions of a singly charged species. If this is the case then the peak does not belong to a fragment of a rhodium cluster as there are too many isotope contributions. Surrounding the main contaminant peak are other lower intensity peaks, but there does not appear to be a pattern in the spacing between the peaks. It is therefore concluded that these peaks are resulting from some contaminant within the system. A closer view of the contaminant is given in in the inset spectrum in Figure 5-2. These erroneous early peaks hinder the detection of the rhodium supraclusters formed under the laser conditions. The mass spectrum in Figure 5-3 shows the collection of peaks corresponding to metal cluster cores of a fixed size.

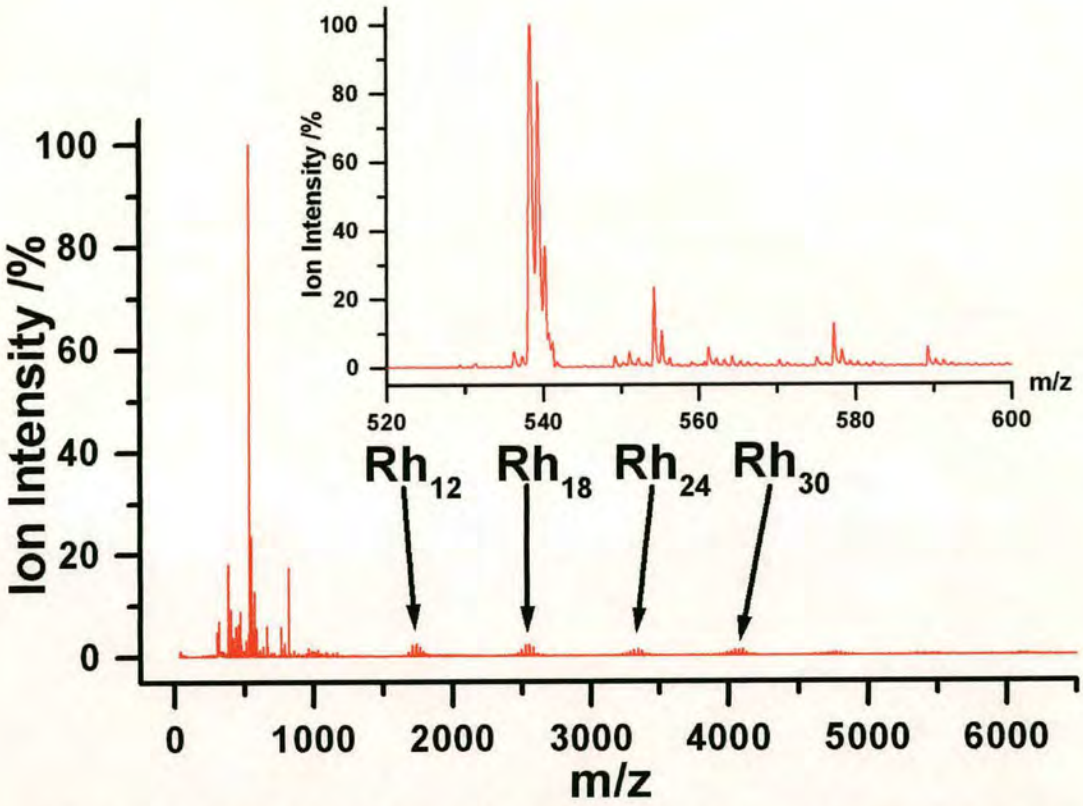

Figure 5-2 Positive ion spectrum for rhodium clusters recorded with a laser fine value of 50%. The nuclearity of the metal cores have been indicated. The inset mass spectrum shows a closer view of the suspected contaminants.

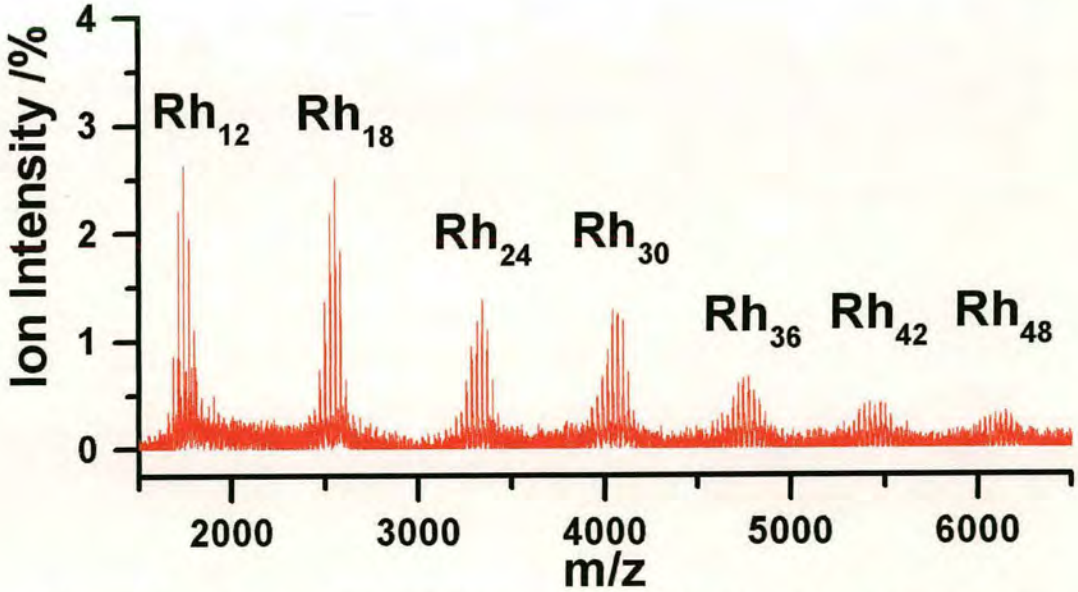

Figure 5-3 The rhodium supracluster peaks observed in the previous mass spectrum can be further resolved to show the variation in the size of the ligand shell surrounding the metal core

As can be seen from the mass spectrum in Figures 5-2 and 5-3, the supracluster metal cores are composed of multiples of the precursor cores. It can also be seen that there are a number of peaks associated with each metal cluster core nuclearity. These peaks are evenly spaced with a nominal mass difference between each peak of 28 Th, equivalent to the mass of a neutral carbonyl ligand. Thus the peaks represent clusters of a given metal nuclearity with a variation in the density of the carbonyl ligand shell. This variation in the number of ligands will result from differences in the size of the clusters meeting for reaction and the loss of carbonyl ligands from the evaporative cooling of the cluster. Figure 5-4 shows the individual clusters composed of 18 rhodium atoms. The designation of the peaks has been confirmed from isotope modelling.

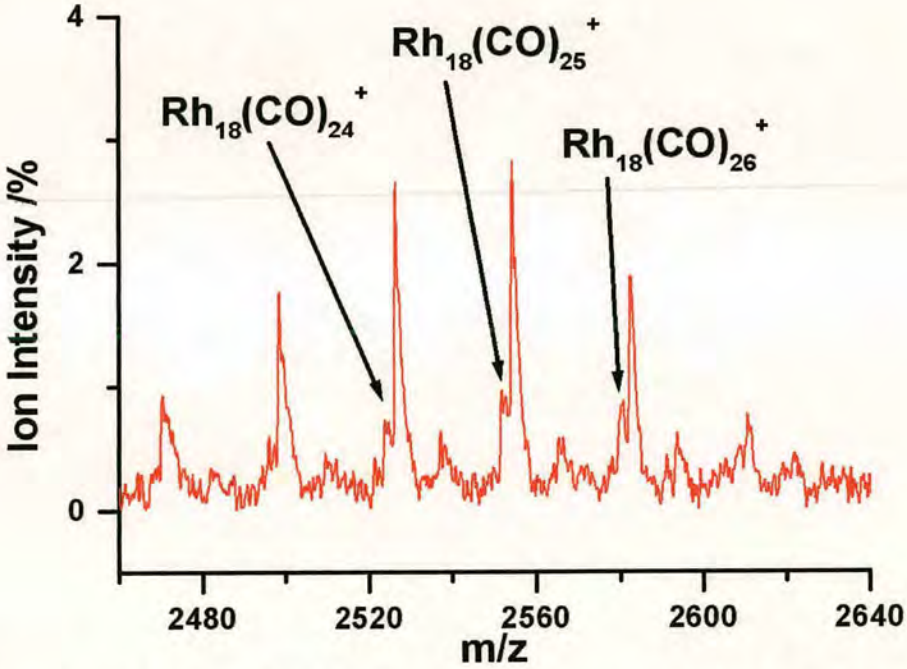

Figure 5-4 A close up of the Rh_{18} peak in the mass spectrum of Figure 5-2 which has been resolved to show these constituent peaks representing the different sizes of the ligand shell on clusters comprised of 18 rhodium atoms.

It can be seen from Figure 5-4 that there appears to be two peaks for each designated cluster ion. One slightly heavier, high intensity peak, and a lighter, lower intensity shoulder peak. This occurrence is believed to have occurred from post-source decay

of the supracluster ions. Isotope modelling (performed using the MassLynx software) proves that the smaller intensity shoulder peaks correspond to the designated cluster species, while the higher intensity peaks are generally 2 Th heavier. These more intense peaks are therefore the product of post-source decay. Unfortunately the resolution at this high value of the mass-to-charge, coupled with the low intensity of these peaks, means that observation of the stable and metastable species as two distinct peaks is not possible. Analysis of the post-source decay of the clusters will be performed later in the chapter. Virtually identical spectra were recorded for laser fine values of 75% and 100%.

The more intense beam at a laser fine value of 25% produced a greater intensity of larger clusters, but also showed indications of another contaminant, as can be seen in Figure 5-5. The contaminant is once again the most prominent peak in the spectrum, and cannot be attributed to any form of rhodium carbonyl cluster. However, its presence is not as significant, as a greater population of the supraclusters can be directly observed from the mass spectrum. Figure 5-5 shows the individual clusters composed of 24 rhodium atoms and their configuration.

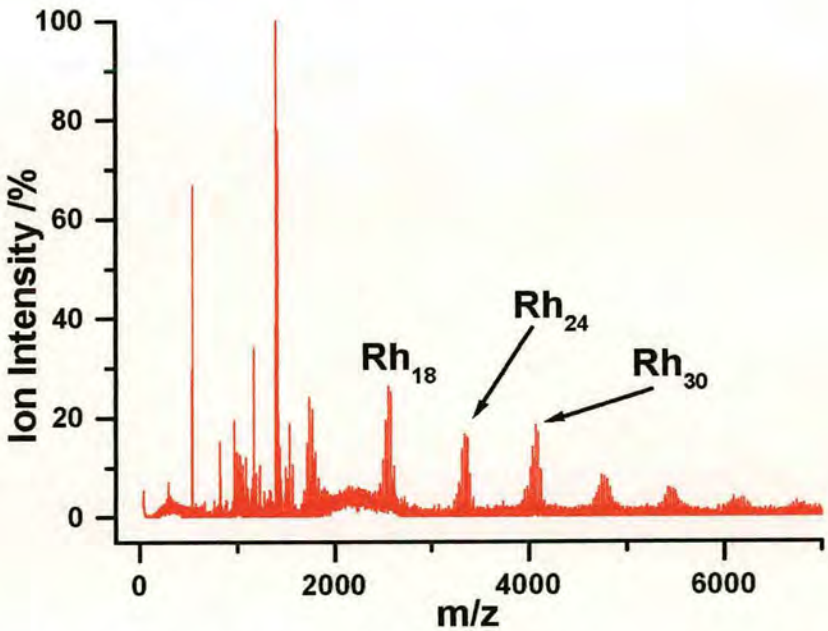

Figure 5-5 Positive ion spectrum for rhodium clusters recorded with a laser fine value of 25%.

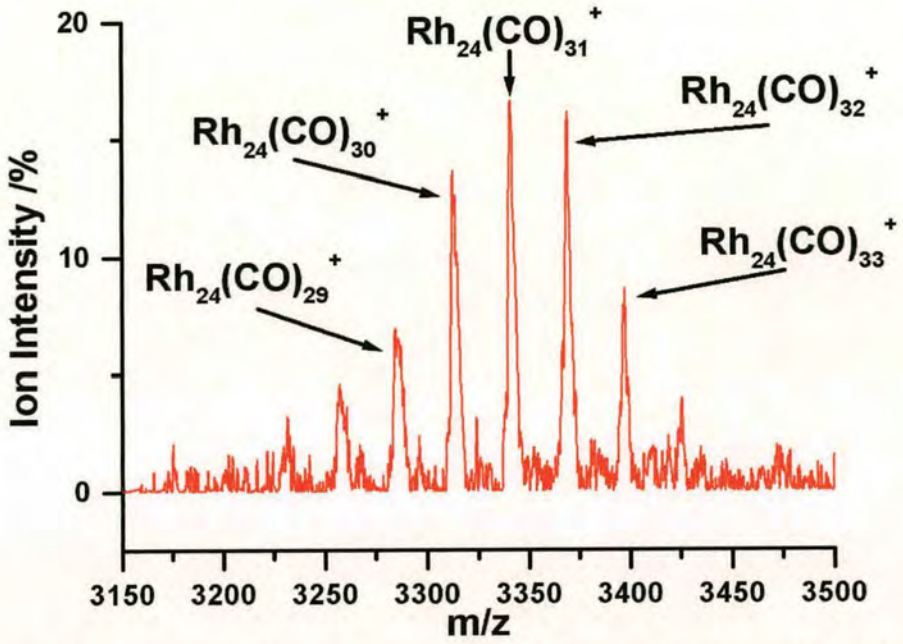

Figure 5-6 A close up of the mass spectrum of Figure 5-5 showing the different ligand shells for clusters comprised of 24 rhodium metals.

The mass spectrum in Figure 5-6 shows no evidence of the two peaks that were earlier associated to post-source decay. However, the width of each peak is around 8 Th. Since rhodium is monoisotopic, this peak width is quite large. It is therefore suspected that the resolution of this mass spectrum at this mass range is insufficient to resolve the stable and metastable peaks, and that both have been assimilated into the peaks observed in Figure 5-6.

5.4.2 Negative Cluster Ions

The negative ion data was far superior in quality. To begin with no contaminant species were observed, from which it can be assumed that the contaminants could only by positively ionised. Secondly the intensity of the heavier clusters was greater. Again the observed distribution of ions in the mass spectra changes little from laser fine values of 100% to 50%. Figures 5-7 and 5-8 show the mass spectra recorded for the negative ion rhodium clusters with laser fine values of 50% and 25% respectively.

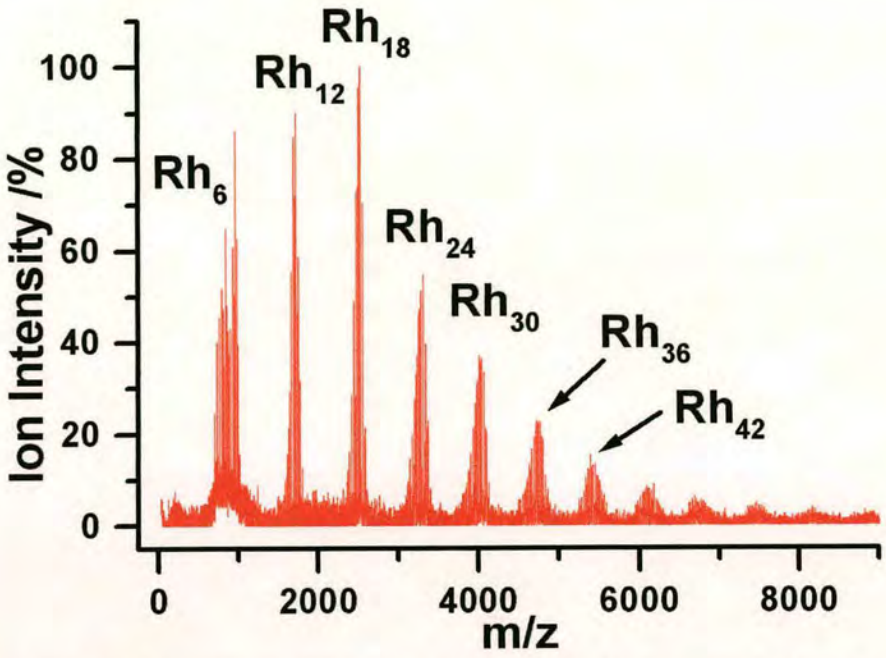

Figure 5-7 Negative ion mass spectrum for rhodium clusters recorded with a laser fine value of 50%. The switch to negative ion mode has resulted in a greater population of larger supraclusters.

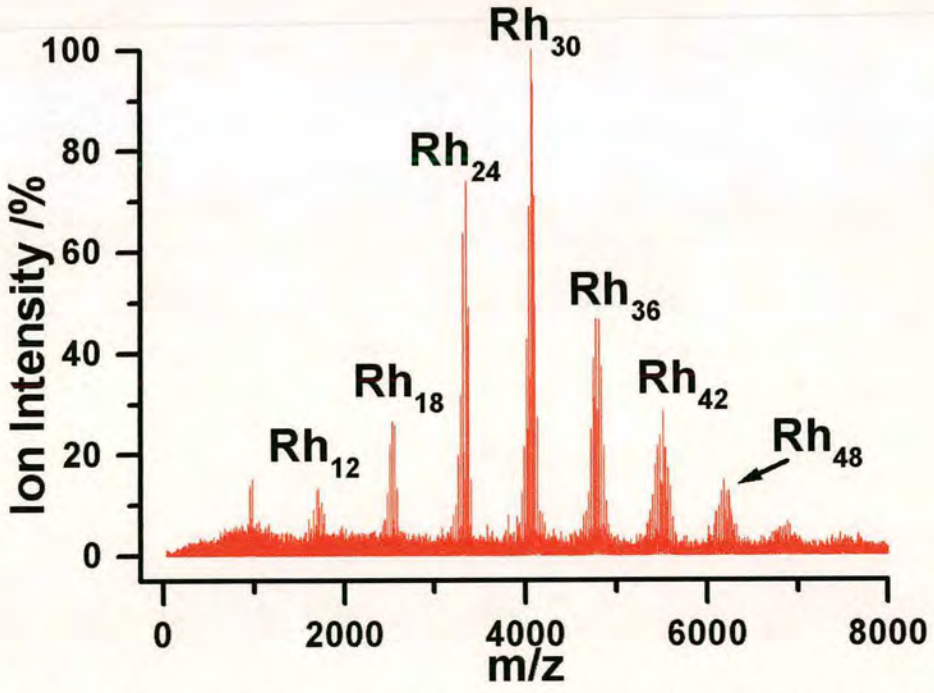

Figure 5-8 Negative ion mass spectrum for rhodium clusters recorded with a laser fine value of 25%. The increased intensity has increased the population of the larger clusters.

The spectra given in Figures 5-7 and 5-8 shows that supraclusters with metal nuclearities in excess of 50 atoms have been created by laser-induced synthesis, although the population of these heavier clusters is much smaller than the lighter Rh_{12} and Rh_{18} clusters. Comparisons between the positive and negative ion data suggest that the production of large negatively charged clusters is more facile. However it is also possible that the overwhelming high intensity contaminants present in the positive ion spectra hindered the detection of the cluster species, and distorting ones perception of the cluster growth.

At a laser fine value of 25% the distribution in cluster population shifts to the larger supraclusters, with the Rh_{30} clusters proving to be the most populated state, although there appear to be fewer of the low intensity heavier clusters in excess of 50 metal atoms on this spectrum. The lack of visible cluster species resulting from the fragmentation of the cluster precursor in Figure 5-8 suggest that these species have all been used in the generation of the larger cluster species. It would therefore seem that some threshold is breached between a laser fine value of 50% and 25% that promotes the greater production, and stability, of some of the larger cluster systems. It is possible that at the lower laser fine value the population of desorbed neutrals and desaturated cluster precursor ions is more suited to facile and prolific cluster reactions than at lower laser intensities. However, this phenomenon cannot just be attributed to greater laser intensity due to laser fine values of 5% producing no ions whatsoever. There is therefore obviously some need for balance to create the optimum conditions. It is possible that at the highest laser intensities the ablation is far more catastrophic, leading to the lack of an ion signal.

As before the peaks can be resolved to show the contributions from clusters with the same number of metal atoms but different sizes of ligand shells. Figure 5-9 and 5-10 show the peaks corresponding to clusters of 30 and 48 rhodium atoms respectively recorded with a laser fine value of 25%.

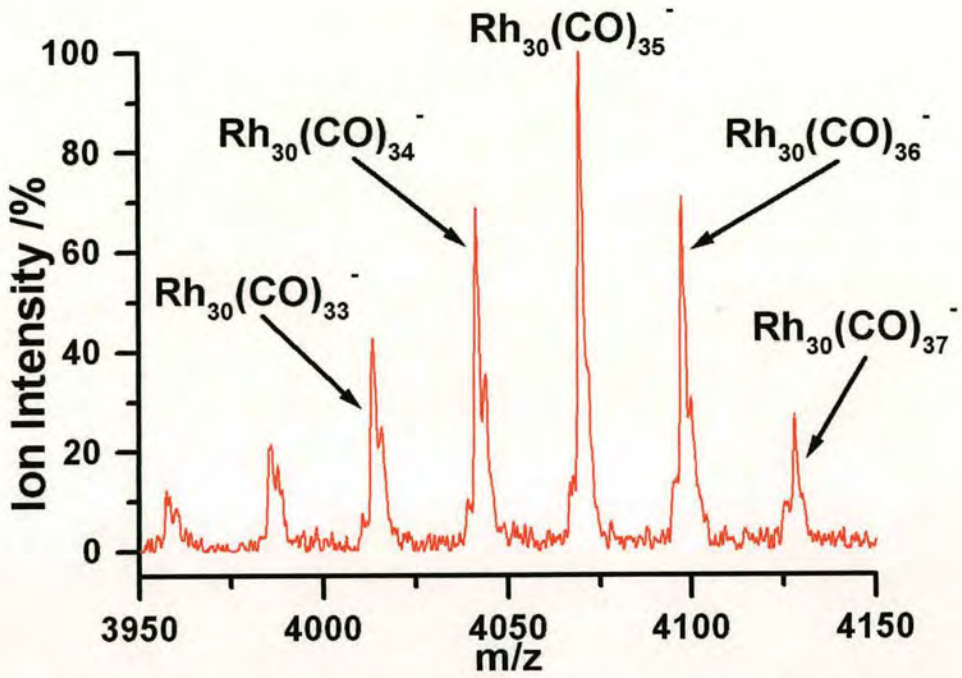

Figure 5-9 A close-up of the Rh_{30} peak from the mass spectrum in Figure 5-8,

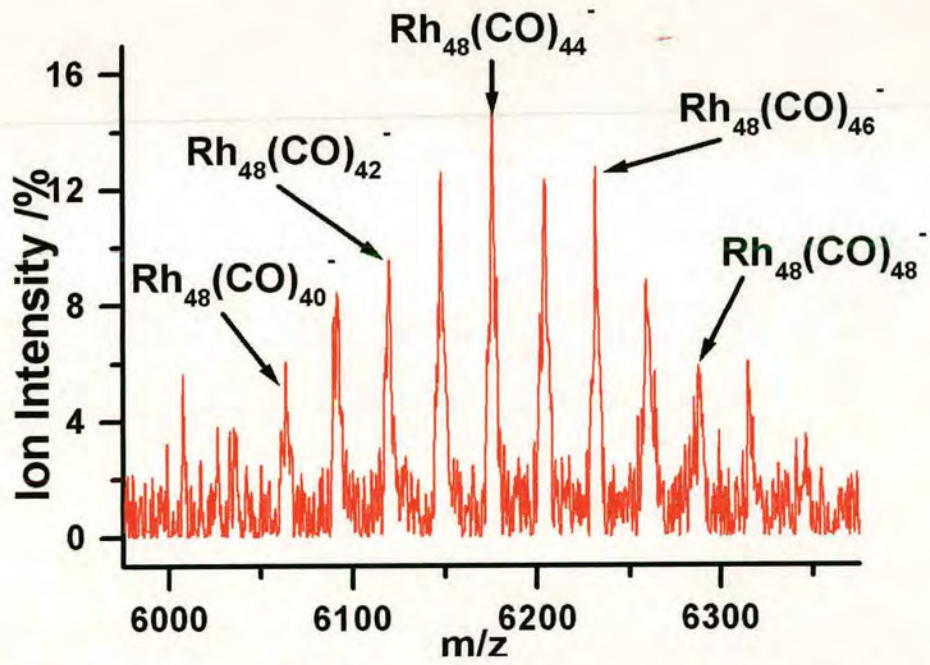

Figure 5-10 A close up of the Rh_{48} peak from the mass spectrum in Figure 5-8.

Similar patterns are apparent between the positive and negative rhodium cluster ions. The most obvious trend is that the cluster aggregation reaction for rhodium occurs through the step-wise addition of the metal core polyhedra as may be expected from

the results of similar clustering experiments [1-3]. It is not possible to say how this bonding occurs, whether through single or multiple metal-metal bonds. It is unlikely to involve bridging carbonyl ligands between metal atoms, as these bonds are very weak and the most likely to be evaporated from an excited supracluster. This issue shall be explored in more detail later.

The second trend is that as the cluster increases in metal size, the maximum number of carbonyl ligands on the cluster decreases, as can be seen in the spectra in Figures 5-4, 5-6, 5-9 and 5-10. The ratio of ligands to metals on the Rh_{18} cluster was around 1.5, a figure that steadily decreases, with the ratio for the Rh_{48} clusters reaching unity. Inspecting the low intensity Rh_{54} clusters reveals that the trend continues, with the ratio of ligands to metals getting ever smaller. These trends are represented in Figure 5-11.

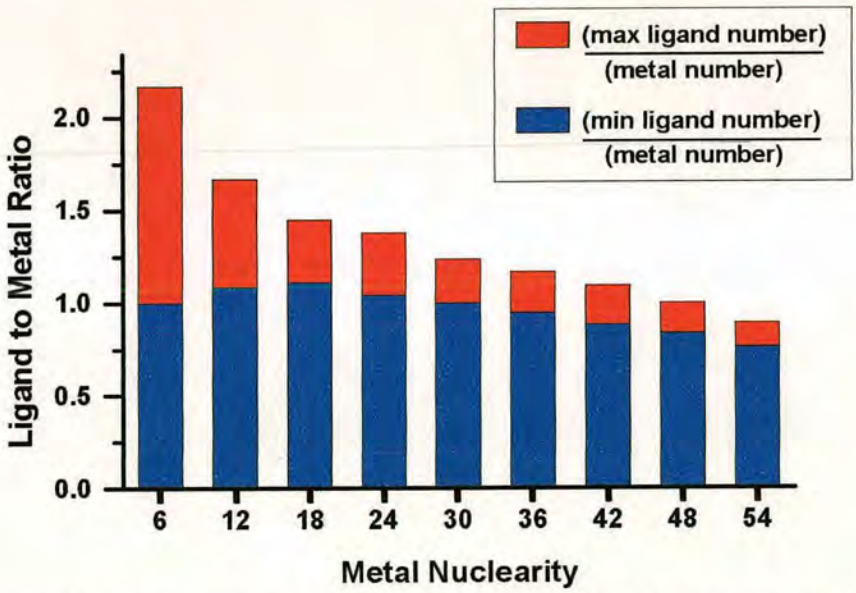

Figure 5-11 The variation in ligand to metal ratio for given cluster metal nuclearities. The ratios are shown for the maximum number of carbonyl ligands observed, and the minimum on each cluster species.

This trend suggests that the clusters are forming close-packed-like structures, with an increase in the number of internal metal atoms with multiple metal-metal bonds. Therefore the clusters are most likely approaching a rounded geometry as the aggregation reaction produces larger clusters, and that they have a more unsaturated

character than the original transition metal cluster precursors that formed them, as described in Chapter 2.2. In order for cluster cores to meet and bond, a significant number of ligands would have to be lost from each core such that the ligand shell would pose no steric hindrance to the aggregation of the metal cores. It was earlier reported that it has been found elsewhere that with iron pentacarbonyl species the rate of cluster formation increases with the decrease in coordinative saturation, which was tied in with the electron deficiency of the cluster [1-3]. Given that the degree of coordinative unsaturation can be shown to decrease as the clusters become larger, it could be hypothesised from the results on iron pentacarbonyl that the formation of progressively larger clusters will have a faster rate, and given that these species are large, will be able to effectively deal with the excess internal energy without recourse to fragmentation. However, the experimental results shown here show that the smaller clusters have a greater population than that of the larger supraclusters. It is possible that it is a simple matter that the clusters have insufficient time within the ion source to form equivalent populations of the larger supracluster species. It is also possible that relating electron deficiency to clustering reaction rate is not suitable for these large clusters. The observations made linking electron deficiency to clustering rate concerned mono-metal precursors, building to produce cluster with up to four metal atoms. For such small clusters the electron deficiency resulting from desaturation is significant. However, if the supracluster species formed here are closed polyhedral structures, the increase in metallic bonding character and delocalisation of electrons from the metal centres means that the electron deficiency brought about from ligand desaturation is far less significant to the electronic make up of the cluster. As such this may also limit the effect of the desaturation on assisting successful cluster formation.

It can also be seen that the resolution of the higher mass peaks becomes progressively worse. This is due to the limitations of the instrument (time-of-flight instruments are not capable of very high resolution to begin with, and the resolution decreases with increasing mass), the post-source decay of the clusters distorting the peaks, and the fact that the heavier clusters tend to have low intensities, lowering the

signal-to-noise of each peak. As an example the typical value of resolution for the Rh_{18} clusters is around 2000, while for the Rh_{48} clusters the resolution is nearer 600.

The results for the osmium clusters are fundamentally different from the rhodium clusters. Figures 5-12 and 5-13 show the mass spectra recorded for laser fine conditions of 50% and 25% respectively. These reveal that the trigonal metal framework has been broken to produce molecular fragments, which have bonded to produce new osmium clusters of four, five and even traces of six metal atoms with varying sizes of ligand shell, but with no sign of the extensive aggregation observed for the rhodium clusters.

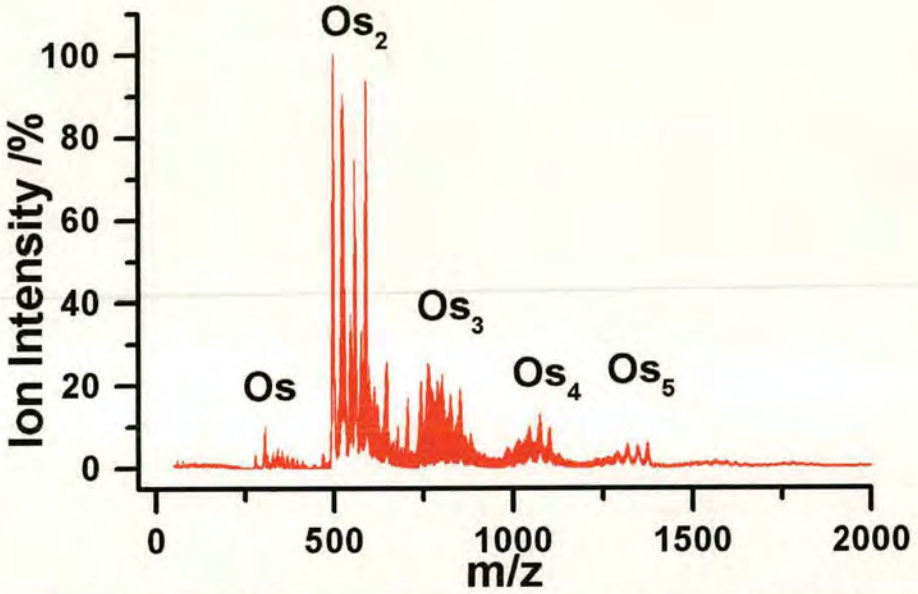

Figure 5-12 The production of molecular fragments and osmium tetramers resulting from moderate laser field conditions, with the laser fine parameter at 50%. Only the size of the metal core has been given, and not the size of the ligand shell on each cluster.

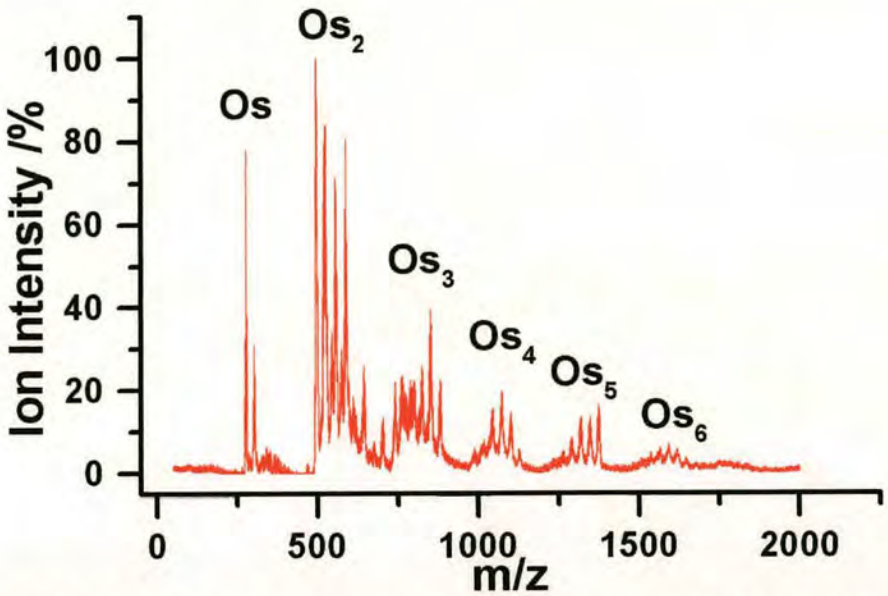

Figure 5-13 The production of molecular fragments and osmium tetramers, pentamers and traces of hexamers, resulting from more intense laser field conditions, with the laser fine parameter at 25%

Unfortunately the resolution of the cluster peaks is quite poor, to the extent that the isotope pattern of the osmium species is largely obscured by the resolution and the occurrence of post-source decay. An example of the effect of post source decay on the mass spectrum is given in Figure 5-14. The peak identified as $Os(CO)_3^-$ does not match the corresponding isotope model, but the observed pattern suggests that this is due to the overlap of the isotope distributions from stable and metastable ions. Once again the separation between the two is roughly two mass units. Taking this into account, an isotope model that is made two mass units heavier can be superimposed over the original model to try and recreate the observed pattern.

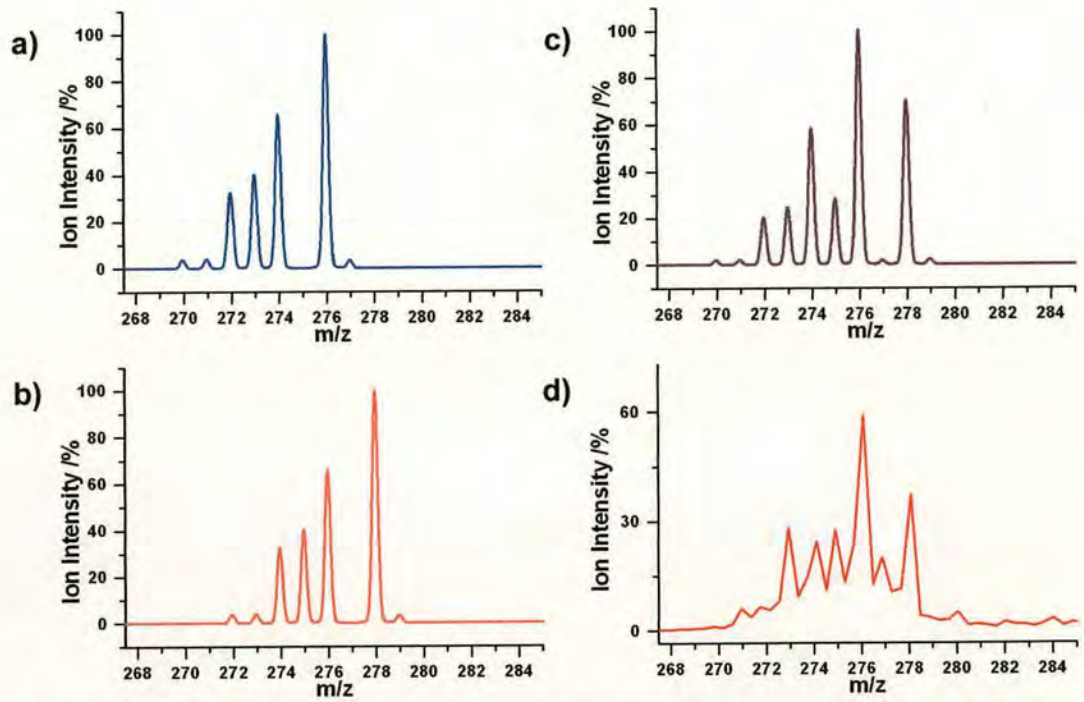

Figure 5-14 A reconstruction of the disruption caused to the isotope distribution of $Os(CO)_3^-$ by post-source decay. a) The isotope model of the ion $Os(CO)_3^-$. b) The same isotope pattern but made two mass units heavier (the average separation between the two peaks at this mass range) to represent the peak caused by metastable decay. c) The sum of the two isotope models, weighted so as to best match the recorded mass spectrum for $Os(CO)_3^-$, given in part d).

By working in this way the osmium ions were characterised as given in Figures 5-12 and 5-13.

5.5 Cluster Aggregation And Supracluster Geometry

It is clear from the data that there are extreme differences between the outcome of the experiment for the two species, due principally to the ease at which the osmium cluster was fragmented. The exact metal-metal bond strengths of the cluster species are unknown, but in a review of transition metal carbonyls by Lewis and Raithby, the average metal bond energy in a series of carbonyl derivatives was found to be $130kJmol^{-1}$ for osmium and $112kJmol^{-1}$ for rhodium [17]. Quite how relevant these values are for the clusters used within this thesis is unknown, but it does suggest that the fragmentation of the osmium cluster precursor was not simply due to a weaker

bond energy. It is more likely that the structure of the two cluster precursors had more bearing on their stability within the laser field. The trigonal structure of $Os_3(CO)_{12}$ means that each metal is only bound by two metal-metal bonds, whereas the octahedral structure of $Rh_6(CO)_{16}$ means that each metal is bound by four metal-metal bonds. It would therefore require much more energy to break a sufficient number of bonds within the rhodium cluster core to remove one metal atom. There are also a considerably greater number of internal energy modes available to the rhodium cluster within which to store excess internal energy, which will also have a potent effect on the stability of the rhodium cluster. It is also possible that the osmium cluster is a stronger absorber of the ultraviolet radiation than the rhodium cluster, which has allowed the osmium cluster to receive more energy from a given number of laser shots than the rhodium, leading to core fragmentation.

However the formation of the osmium fragments occurs, the process of cluster growth can be seen to be the same for both cases, namely through the aggregation of labile metal carbonyl units. In the case of osmium, the clusters have fragmented producing unsaturated single osmium atoms, dimers and trimers, which are able to react together. For rhodium the reaction can only occur through the step-wise addition of labile metal cores from the dissociation of ligands. The structures and geometry of the formed supraclusters cannot be readily determined from the mass spectrometry data. While certain large transition metal carbonyl systems have been produced through traditional synthetic methods and characterised by X-ray crystallography, it is unknown whether the supraclusters produced under the influence of strong laser field conditions will evolve along a different path, leading to novel structures. By looking at the known structures of clusters produced from traditional synthetic methods one may be able to rationalise whether the laser produced clusters will have a similar core geometry. At this stage it, however, the factors that affect cluster core geometry shall first be examined.

5.5.1 Influences On Cluster Core Geometry

There are several influences on cluster core geometry, which vary in importance as the size of the cluster core increases. The number of metal atoms will obviously

have the greatest effect on the cluster geometry, but there are a variety of ways in which a set number of atoms can be arranged to produce a stable geometry. The number of metal-to-metal bonds that a single metal atom can have is heavily dependent on the number of electrons within the *d*-shell. In a large multi-nuclear system, it is simpler to look at the number of electrons available to the cluster as a whole, rather than the individual contributions from each metal. Therefore the total number of electrons available to the metals can be determined from the number of electrons in the atomic *d*-shell in the zero oxidation state, the total number of ligands and the number of electrons they donate to the system (their nature; terminal, bridging or capping is not important when examining the system as a whole), and the overall charge of the cluster. For clusters of a given size and metal, a change in the number of ligands, and the charge, can have a tremendous effect upon the geometry the cluster core adopts, a topic that shall be reviewed later.

The mass spectra show that the ratio of carbonyl ligands to metal atoms is decreasing as the metal nuclearity increases. This suggests that the clusters are becoming more metallic like, as discussed in Chapter 2.2, with the cluster requiring less ligands to maintain the stability of the cluster and the integrity of the metal core. With regards to the evaporation processes that occur to the cluster as it cools following formation, it is likely that the loss of a small number of ligands will not result in a significant change to the cluster core geometry, as the principal source of electrons will be from the metal atoms.

5.5.2 Known Cluster Core Geometries

One can gain an insight into how metal cores can relax into different geometries through looking at the characterised clusters that have been generated from traditional synthetic methods. For instance, the pyrolysis of $Os_3(CO)_{12}$ at 483K is known to generate $Os_6(CO)_{18}$, but also generates species such as $Os_5(CO)_{16}$, $Os_7(CO)_{21}$ and $Os_8(CO)_{23}$ in minor quantities [18]. Each of these clusters has been identified, but for now only the pentametal and hexametal frameworks shall be examined.

The pentametal $Os_5(CO)_{16}$ forms a trigonal bipyramid structure, typical of many pentametal systems. However, pentametal osmium clusters with larger ligand shells have also been characterised, and the additional electrons brought by the ligands produces a dramatic change to the metal framework. The $Os_5(CO)_{18}$ has a planar structure, whereas $Os_5(CO)_{19}$ has a "bow-tie" configuration. Each of the pentametal cluster geometries described here are given in Figure 5-15.

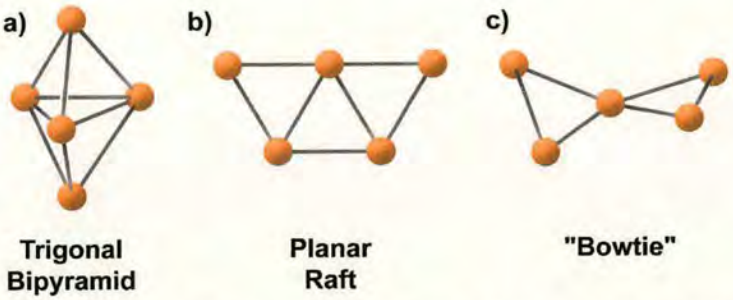

Figure 5-15 Examples of the various geometries of the osmium metal atoms in a pentametal clusters with varying ligand shells of 16, 18, and 19 carbonyls respectively. Diagram adapted from Reference 18.

Previous discussion indicated that the pyrolysis of $Os_3(CO)_{12}$ leads to the formation of $Os_6(CO)_{18}$. One would expect that the bringing together of two labile tri-osmium clusters would bond together to form an octahedral structure, as demonstrated in Figure 5-16 a). However, the crystallographically verified structure of $Os_6(CO)_{18}$ is a capped trigonal bipyramid structure, as given in Figure 5-16 b).

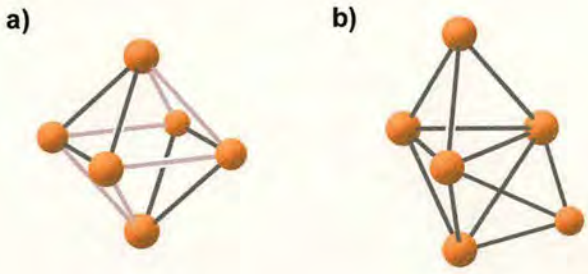

Figure 5-16 a) The expected octahedral form of $Os_6(CO)_{18}$ from the additional of two labile trigonal osmium clusters, and b) the actual form of $Os_6(CO)_{18}$ is a capped trigonal bipyramid structure.

The unusual structure of the $Os_6(CO)_{18}$ ion would certainly seem to support the earlier observation that as clusters increase in size they tend to form condensed polyhedra with an increase in the occurrence of capping metals. However, such a pattern is not uniform. The crystallographically verified structure of the cluster $[Rh_{12}(CO)_{30}]^{2-}$ is that of two octahedral metal cores linked by a single metal-metal bond [18], as demonstrated in Figure 5-17.

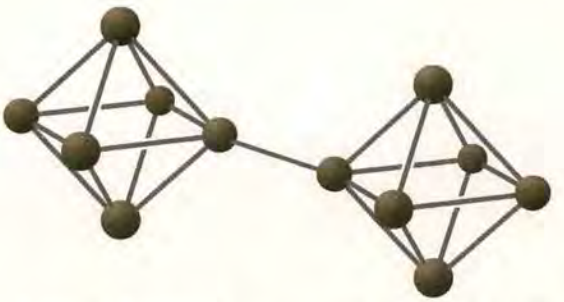

Figure 5-17 The dual octahedral structure of the $[Rh_{12}(CO)_{30}]^{2-}$ cluster Diagram adapted from Reference 18.

Such a structure exhibited by $[Rh_{12}(CO)_{30}]^{2-}$ does not relate to the expectation that large clusters form condensed polyhedron units.

It is possible that the aggregation of the smaller sub-units produce a myriad of different forms, with different metal connectivity dependent upon the geometry of the reacting pair when they meet. Another possibility is that there is a specific reaction path of minimum energy to produce identical stable cluster geometries. In any case it has been shown that the number of carbonyl ligands bonded to the cluster, and the charge, have a potent effect on the geometry of the cluster, providing necessary electrons for the creation and stabilisation of bonds.

5.6 Effect Of Laser Intensity On Post-Source Decay

Each of the cluster ions to emerge from the source is deemed to have undergone at least one unimolecular decay (most likely carbonyl loss) to assist in the de-excitation

of the species, such that the clusters can be represented by the evaporative ensemble model of Klots. The dissociation that occurs within the source can be considered as being prompt dissociation. The occurrence of post-source decay is evidence that many of the clusters have not been able to remove all of the excess energy within the source, and their internal energy is within the metastable range, as discussed in Chapter 3.5.1. While the occurrence of post-source decay can have a detrimental effect upon the clarity of the mass spectrum, it is possible to measure the unimolecular rate of metastable decay from the peaks within the mass spectrum by comparing the population of stable ions against metastable ions. In addition this information can also provide some details on the relative stability of the supraclusters produced.

5.6.1 Identifying Metastable Decay Peaks In The Mass Spectra

In Chapter 3.5.1 it was discussed that a metastable ion B (mass-to-charge of m_B) that dissociates post-source to give an ion A (mass-to-charge of m_A) will appear on a mass spectrum with a mass-to-charge value between m_A and m_B (as depicted in Figure 3-19). This permits the identification of the metastable from the prompt ions on the mass spectrum, an example of which is given in Figure 5-18.

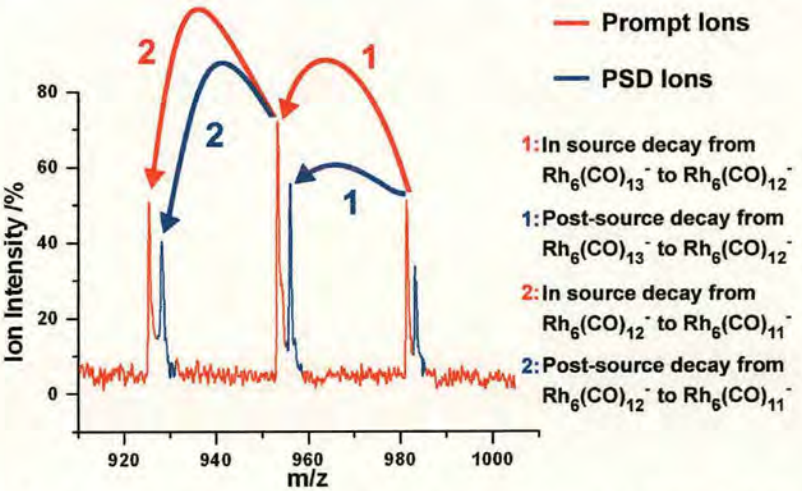

Figure 5-18 An example of the unimolecular decay channels occurring as a result of both in- and post-source decay in the rhodium cluster spectrum recorded at a laser fine value of 100%. The post-source decay and prompt ions have been colour coded to ease visualisation.

Given the broad and complicated isotope distribution of the osmium clusters, any work that involves the analysis of post-source decay will be made much easier by working solely with the mono-isotopic rhodium clusters, specifically the negative clusters due to the better spectra.

The rhodium mass spectra show that the relative intensity of the metastable peaks, compared to the corresponding stable peak, increases as the cluster core size increases. Such a trend is at first glance surprising given that a larger molecular system will have a greater number of internal modes in which more internal energy can be stored, such that a large cluster ion leaving the source may reach the detector intact. However, an increase in the number of internal modes not only results in a corresponding increase in the minimum energy necessary for the system to enter the metastable state, but also broadens the energy range of the metastable state, as can be seen in Figure 5-19. Thus a larger cluster ion can accumulate more energy before prompt dissociation occurs, resulting in the minimum amount of energy necessary to observe metastable decay shifted to higher energies, and a correspondingly broader range of energies at which the cluster ion can enter the metastable state [14].

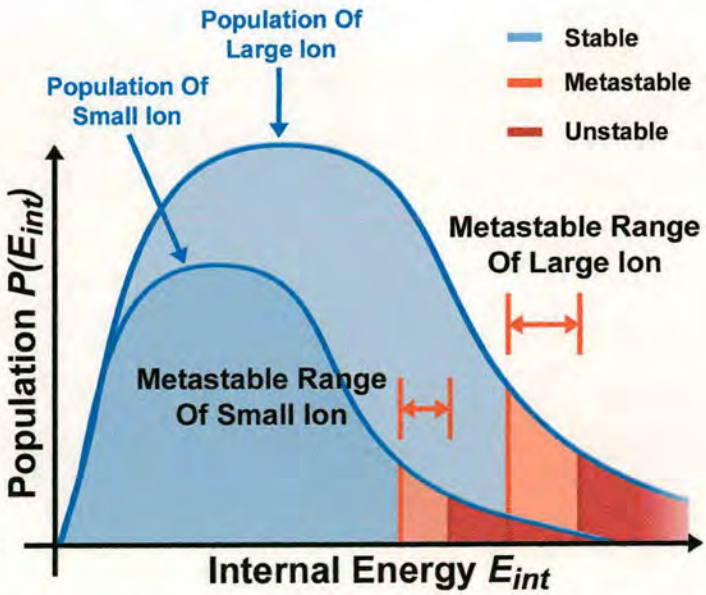

Figure 5-19 The metastable energy region for an a large multi-nuclear molecule can be seen to be larger than that for a smaller molecule.

Correspondingly, for the higher nuclearity clusters, a third peak can be observed that corresponds to an additional post-source decay channel. A particularly unstable ion that has already undergone post-source decay can evaporate another ligand again within the drift region. This is shown for Rh_{18} clusters in Figure 5-20.

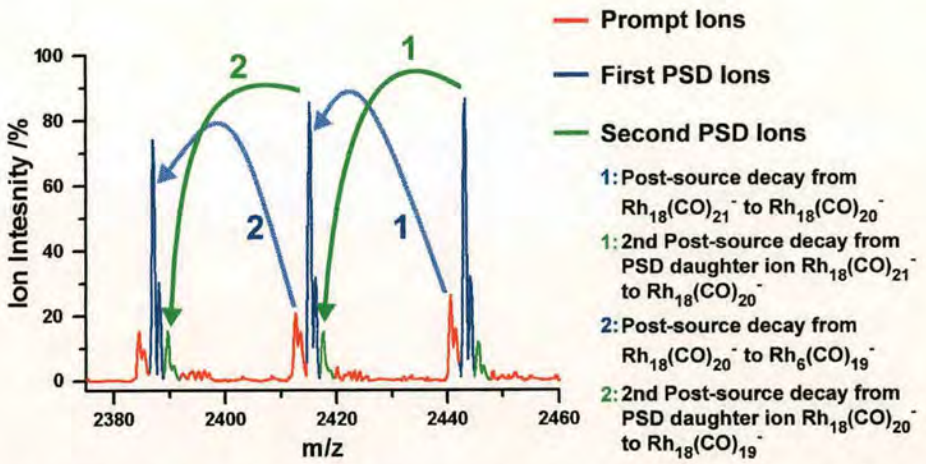

Figure 5-20 An example of the two post-source unimolecular decay channels observed for large nuclearity clusters. The first post-source decay ions are produced from the evaporation of a carbonyl ligand from a metastable ion. However, if this evaporation is insufficient to reduce the energy of the species to stable levels, then it can decay again, as indicated as the second post-source decay ions. Spectrum recorded with a laser fine value of 50%.

Figure 5-20 also shows the lower intensity of the stable ions for higher nuclearity clusters.

5.6.2 Determination Of The Metastable Rate Of Decay

The integrated intensity of each peak gives a measure of the population of that ion. The total population of one particular ion, produced at the ion source, can be determined from the sum of the integrated intensities of the prompt dissociation peak and the post source decay peak, as depicted in Figure 5-21.

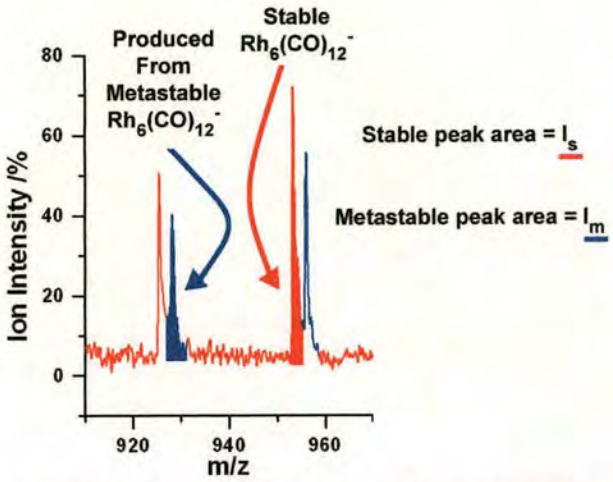

Figure 5-21 The shaded areas represent the peaks that correspond to the same cluster species. The stable peak (red, area = I_s) corresponds to $Rh_6(CO)_{12}^-$ that was produced from prompt dissociation within the ion source. The metastable peak (blue, area = I_m) shows the metastable proportion of $Rh_6(CO)_{12}^-$ that has decayed to $Rh_6(CO)_{11}^-$ within the field-free region. The sum of the integrated intensity of the two peaks ($I_s + I_m$) is therefore equal to the total population of $Rh_6(CO)_{12}^-$ that leaves the ion source.

If a secondary post-source decay channel is observed, then the metastable population is determined from the sum of all the relevant post-source decay peaks, as demonstrated in Figure 5-22.

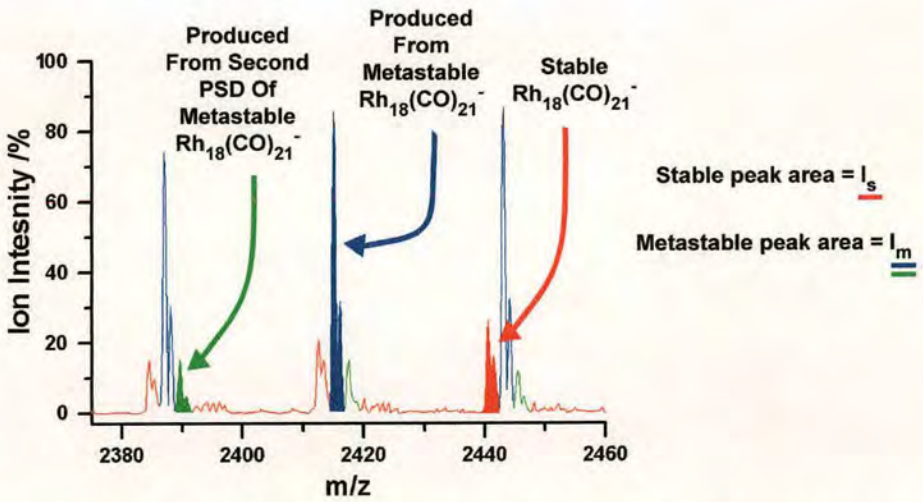

Figure 5-22 The shaded areas represent the peaks that correspond to the same cluster species that leave the ion source when secondary decay channels are observed. The metastable area, I_m, is determined from the sum of the first and second metastable peaks (blue and green respectively).

Assume that a generic rhodium cluster $Rh_n(CO)_x^-$, has a total population $P_x(t)$. A portion of this total population undergoes metastable decay within the time taken for the ion to travel from the ion source to the reflectron, denoted as t_{dr}. Metastable decay shall only be considered to occur within this window, due to the ease at which the drift time, t_{dr}, can be calculated. Thus the reaction can be regarded as occurring with a rate constant k_x, such that:

$$Rh_n(CO)_x^- \xrightarrow{k_x} Rh_n(CO)_{x-1}^- \tag{5-1}$$

The portion of the total population of $Rh_n(CO)_x^-$ that undergoes metastable decay is equal to the population of the resulting metastable daughter ion, $Rh_n(CO)_{x-1}$, at the end of the drift region. This can be denoted as $P_{x-1}(t_{dr})$, and can be determined from [14]:

$$P_{x-1}(t_{dr}) = P_x(t)[1 - \exp(-k_x t_{dr})] \tag{5-2}$$

Taking the integrated intensity as a measure of the population, $P_{x-1}(t_{dr})$ can be determined from area of the metastable daughter ion peak, I_{md}, and $P_x(t)$ from the sum of area of the stable parent ion and metastable peak, $I_{sp} + I_{md}$ (as described in Figure 5-20 and 5-21). Substituting these values into Equation 5-7 gives [14;19]:

$$I_{md} = (I_{sp} + I_{md})[1 - \exp(-k_x t_{dr})]$$

$$\therefore \quad \frac{I_{md}}{(I_{sp}+I_{md})} = [1 - \exp(-k_x t_{dr})]$$

$$\Rightarrow \quad \frac{I_{sp}}{(I_{sp} + I_{md})} = \exp(-k_x t_{dr}) \tag{5-3}$$

From this relatively simple equation one can determine the metastable unimolecular decay rate constant, k_x:

$$k_x = -\left(\ln\left[\frac{I_{sp}}{I_{sp} + I_{md}} \right] \right) \Big/ t_{dr} \tag{5-4}$$

The rate constant is a strong function of the internal energy of the cluster species. When looking at the metastable decay of ion $Rh_n(CO)_x^-$, the in-source dissociation reactions that produced this ion within the time spent in the ion source, t_s, can be safely ignored since these dissociation reactions originally occur on a much faster time scale (that becomes longer with each dissociation) than the subsequent

metastable decay within the field free region [14]. Therefore the rate k_x is a direct measure of the relative energy of the species $Rh_n(CO)_x$ at the point of decay, on which the internal energy of the ion's parent within the ion source, $Rh_n(CO)_{x+1}$, has little bearing.

The time the ions spend in the drift tube can be calculated from classical mechanics, since the velocity of the ions does not approach relativistic levels. The overall potential difference within the ion source is 20kV, which equates to an ion kinetic energy of 20keV, since the ions are singly charged (as discussed in Chapter 3.2.2). From the kinetic energy, the velocity of each ion as it leaves the source can be determined from $KE = \frac{1}{2}mv^2$. The distance from the ground electrode to the reflectron (equal to 754 mm) can be taken as the distance the ion travels from leaving the ion source to reaching the reflectron, from which the drift time, t_{dr}, can be evaluated for each cluster ion. However, from the energy calculation it is very clear that the drift time will be different for each cluster configuration due to their different mass, and thus the metastable time window is mass dependent. As the cluster size increases the time spent in the first field free region increases, giving more time for in-source dissociation. However, the time the ion spends within the field free region is also lengthened, providing a longer time window for post-source dissociation. Since the rate is determined from the ratio of the stable and metastable integrated intensities the relative rate values will be mostly unaffected.

Through the use of Equation 5-4 the metastable rates of decay k_x were determined for each ion where the post source decay peak could be clearly resolved. This was done for each mass spectrum recorded at laser fine values of 100% through to 25%. The integration of the peaks was performed in Microcal Origin. A plot of calculated rate against the mass-to-charge of the cluster is given in Figure 5-23.

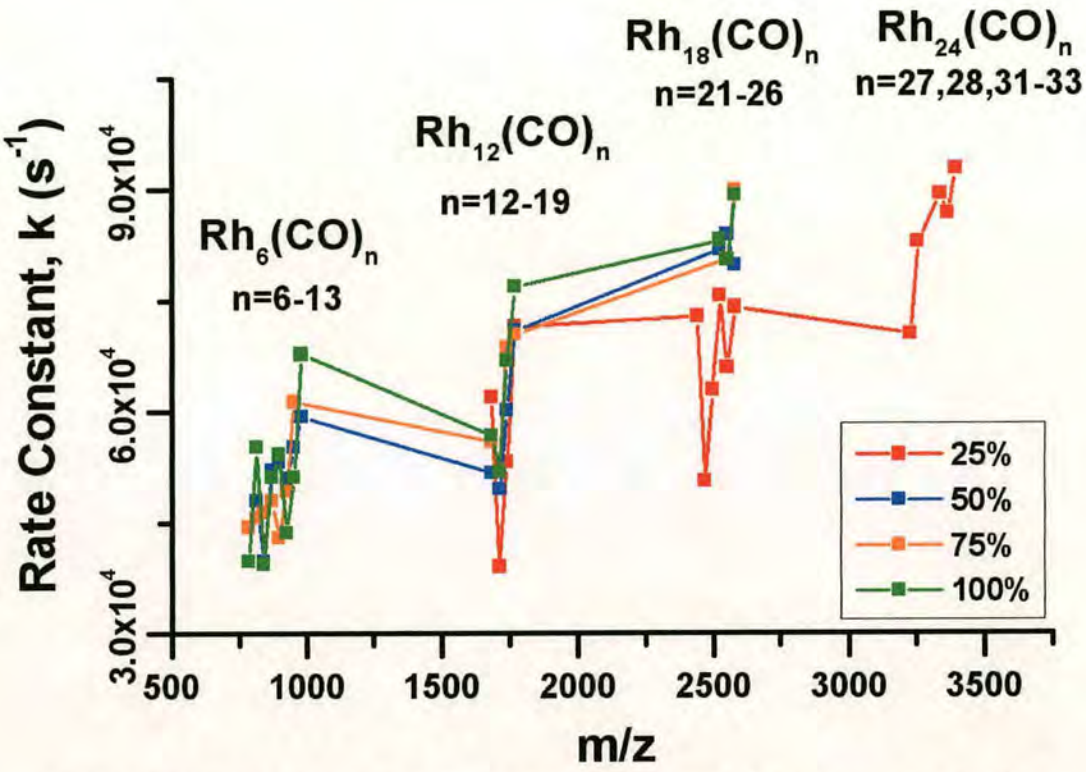

Figure 5-23 The change in metastable rate constant for various cluster sizes produced by different laser beam intensities.

Figure 5-23 shows that there is a general increase in the rate of metastable decay, which agrees with the earlier observation on the increase in the metastable peak intensity with cluster size. An increase in the population of metastable clusters with cluster size will obviously lead to an increase in the metastable decay. Such a trend can be rationalised by considering several key issues. Firstly, a larger cluster species will have a greater number of internal energy modes in which to store energy. Therefore in conditions where multiple, high energy, photon absorption is prevalent the smaller clusters will reach an unstable state of energy much sooner than the larger clusters. Thus the smaller clusters will evaporatively cool more frequently than the larger clusters, with the overall result that a greater population of the smaller clusters will have sufficiently cooled to remain stable during the analysis period in comparison to the larger clusters. In addition, for smaller cluster with an internal energy at the unstable limit the removal of one ligand will have a greater result on lowering the internal energy of that cluster than the removal of one ligand from a

similarly unstable larger cluster, since the unstable limit for the larger cluster will be greater. There is no evidence to suggest that the unstable cluster species feature core fragmentation, an event that would significantly reduce the internal energy of the cluster species.

It can also be seen that the higher laser intensity at laser fine values of 25% have a dramatic effect upon the rate of metastable decay. While the 50% to 100% rate values are quite bunched together, the 25% values are much lower. This occurrence could possibly be rationalised by considering that a greater intensity laser beam may excite the species more rapidly, and with more photons. If the ions are significantly excited they may decay more rapidly, and more frequently, within the ion source with the overall effect of there existing a greater number of ions that can remain stable during their time within the drift region, and lowering the number of metastable species. The dependency of the calculated rate on the population of the stable and metastable ions results in a lowering of the metastable rate of decay.

Figure 5-24 examines the variation of the rate of decay with cluster core and ligand size. For the precursor cluster, the rate of metastable decay is pretty erratic. There appears to be little in the way of any pattern in the variation in rate with ligand number, or any overall trend with the different laser fine values, with the possible exception of the $Rh_6(CO)_8$ anion. At laser fine values of 50% and 100% the metastable rate share a particularly low value of metastable rate. Such an occurrence suggests that this particular configuration has a greater population of stable ion than the other clusters of the same metal nuclearity. Moving on, the Rh_{12} clusters display a much more regular pattern of metastable rates, but there is strong evidence of similar local minimum for the cluster ion $Rh_{12}(CO)_{17}$. Once again this suggests that this ion has a more stable configuration than its counterparts, especially in contrast with the local maximum at $Rh_{12}(CO)_{19}$, which suggest the exact opposite.

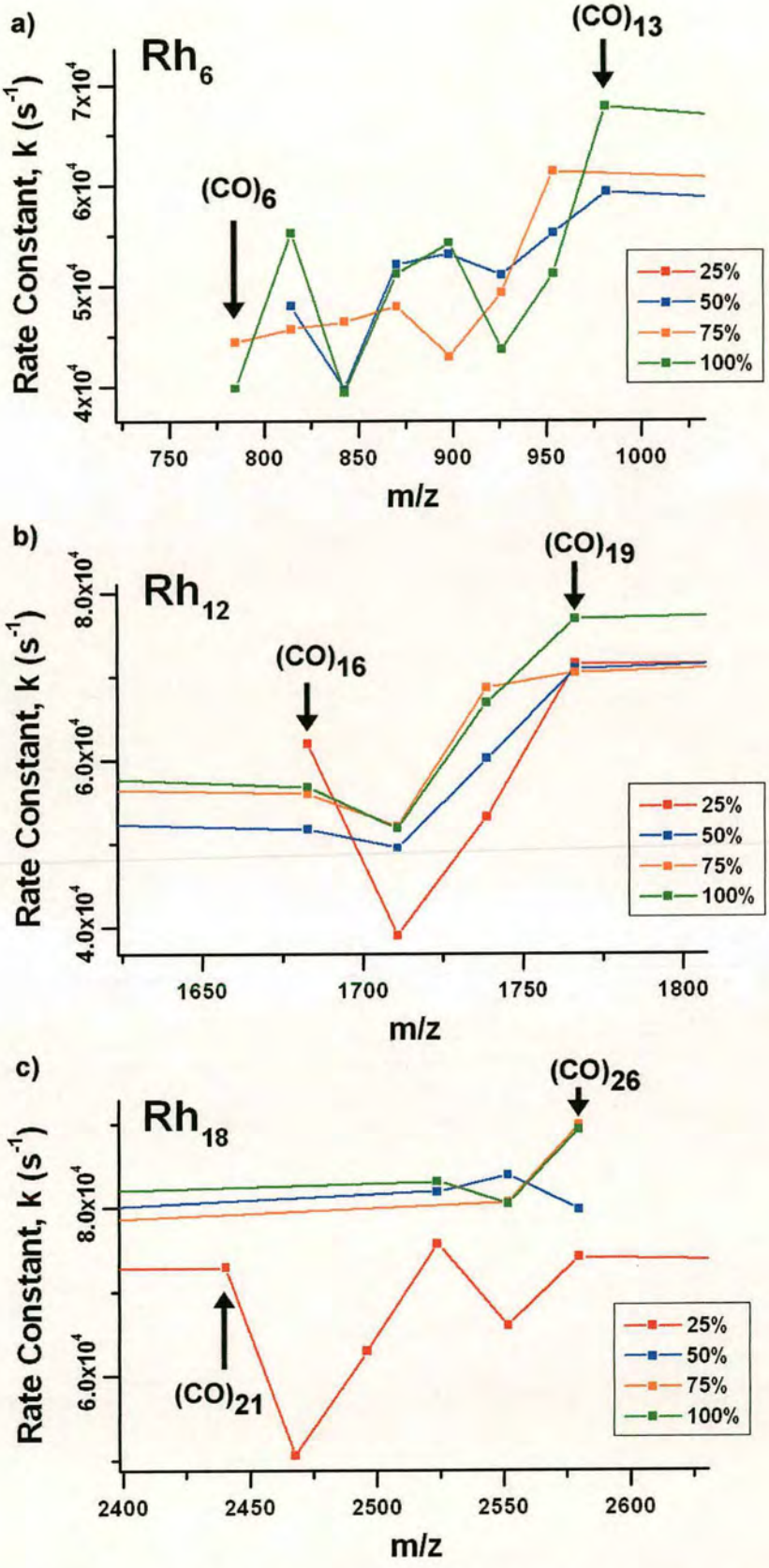

Figure 5-24 A close up of the metastable decay plot in Figure 5-22 showing the variation in the rate with cluster core and ligand size.

It is feasible that the removal of only two ligands can significantly alter the electron density of the cluster in some way that the cluster relaxes into a new geometry, perhaps involving new metal-metal bonds or an arrangement of bridging or capping ligands that improves the overall stability of the cluster, and makes it more tolerant of higher internal energies before dissociation occurs. Moving onto the Rh_{18} clusters, it is harder to make any judgement on the relative stability or instability of any of the clusters due to the fewer number of species that appear at all laser fine values.

It is therefore clear that while there exists a general trend of increasing metastable decay with increasing cluster core and ligand size, certain configurations prove to be more stable than others and create a local minimum in the data. These clusters could be analogous to the incidence of 'magic numbers' observed in organic van der Waal's clusters and metal atom clusters, where certain cluster systems feature an uncharacteristic greater stability than others of neighbouring sizes. It must be realised that the values of the rate represent an average over all the possible configurations a cluster $Rh_n(CO)_x$ can have with regards to the ion's internal energy, upon which the core geometry, ligand positions and dissociation reactions are dependent. This is a reflection on the nature of the ion formation and dissociation mechanism, which occurs on a purely probability based mechanism (the probability of a cluster receiving a certain amount of energy to become active, to collide with a neutral molecule, for bonds to be formed, for dissociation to occur within a given time scale). With no fixed reaction mechanism the output itself is not fixed. Therefore it is unlikely that a given dissociation step will occur with the removal of the exact same ligand from each cluster, since the dissociation path is dependent upon the internal energy of the cluster at the time prior to dissociation. It is therefore quite difficult to rationalise a structure for the $Rh_{12}(CO)_{17}^-$ cluster since there is no information within the mass spectra on the geometry of the dodecarhodium core. Without such information one cannot then rationalise the form the ligand shell may take that leads this cluster to be more stable than others of the same metal nuclearity. However, it may be possible to rationalise the structure of the $Rh_6(CO)_8^-$ cluster. If one assumes that the structure of the rhodium core is not distorted from its octahedral

structure under the laser field conditions, then on removal of half the ligand shell the remaining ligands may rearrange to cap each of the metal faces. While the removal of half the ligand shell represents a substantial depletion of the each metal's electron density, in this configuration the remaining ligands share their electron density equally around each metal.

5.7 Effect Of Ion Source Residence Time On Post-Source Decay

The determined rates of post-source decay are dependent upon the ion residence time within the mass spectrometer. While the mass spectrometer has no controllable means of storing the ions prior to analysis (for example by using a linear RF only quadrupole), it should be possible to manipulate the time the ions spend in the ions source by varying the potentials applied to the extraction optics. Increasing the focus potential will decrease the potential difference between the extraction electrode and the skimmer electrode. Since the ions will be moving quite slowly on passing the extraction electrode (kinetic energy of 50 eV, assuming singly charged species), such a decrease in the potential difference will increase the ion residence time within the ion source. The time within the ion source is much longer than the flight time of the ions, and thus by varying the focus potential, the time over which the ions can lose ligands within the source region can be increased. As such the rate of post-source decay to would be expected to decrease as the focus potential is increased. However, with an extended period within the ion source, those ions that previously just managed to reach the detector intact are more likely to decay post-source, and so such an effect will be offset against any decrease brought from decay within the ion source. It will therefore be interesting to see how these factors affect the overall observed rates of metastable decay.

5.7.1 Experimental Procedure

The time-of-flight instrument was set up as described earlier. The laser fine value was set to 50%, and the laser coarse value set to 100% as a compromise between reasonable resolution and an abundance of large supraclusters. The spectra were also recorded in negative ion mode only, as this produced the best population of larger nuclearity clusters. The source ion optics were set to their default values, except for the focus electrode, which was set to 15kV and increased to 18kV in 500V steps. Ten scans were recorded at each value of the focus electrode, followed by one other scan recorded with the laser fine level at 5% to record the background noise. The first ten scans were summed, followed by the subtraction of the final scan to remove the background noise from the resultant mass spectrum. The data was then smoothed by a 3-channel, 2-pass method. Each of these operations was performed by the MassLynx software.

5.7.2 Results

To begin with the mass spectra recorded for each of the different focus electrode values are shown in Figure 5-25. These spectra show a general pattern in the cluster population with focus electrode potential. For all but the highest focus potential, there would appear to be an increase in the population of the larger cluster species (metal core nuclearities 18 to 36) with a corresponding decrease in the population in the cluster precursor. Why the cluster precursor population is still the predominant cluster within the mass spectrum recorded for a focus potential of 18 kV is unknown at this stage. However, there is sufficient evidence to back the claims made previously in Chapter 5.4.2, that a greater population of larger clusters can be formed with sufficient time within the ion source.

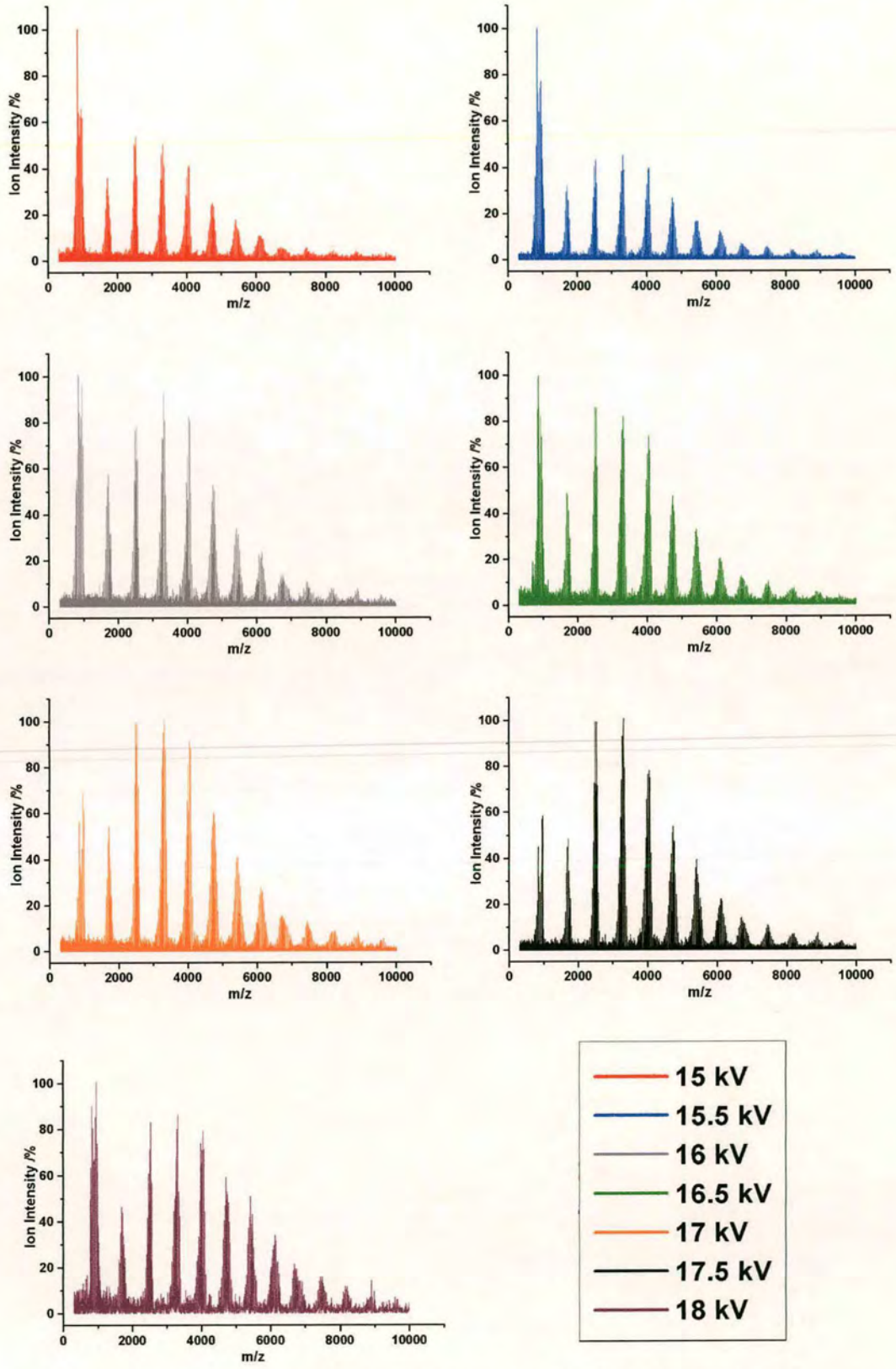

Figure 5-25 The mass spectra recorded for each value of the focus potential.

The recorded spectra were processed to determine the rates of metastable decay, as set out previously in Chapter 5.6.2. The rate is plotted against the mass-to-charge of the cluster for each value of the focus potential is given in Figure 5-26.

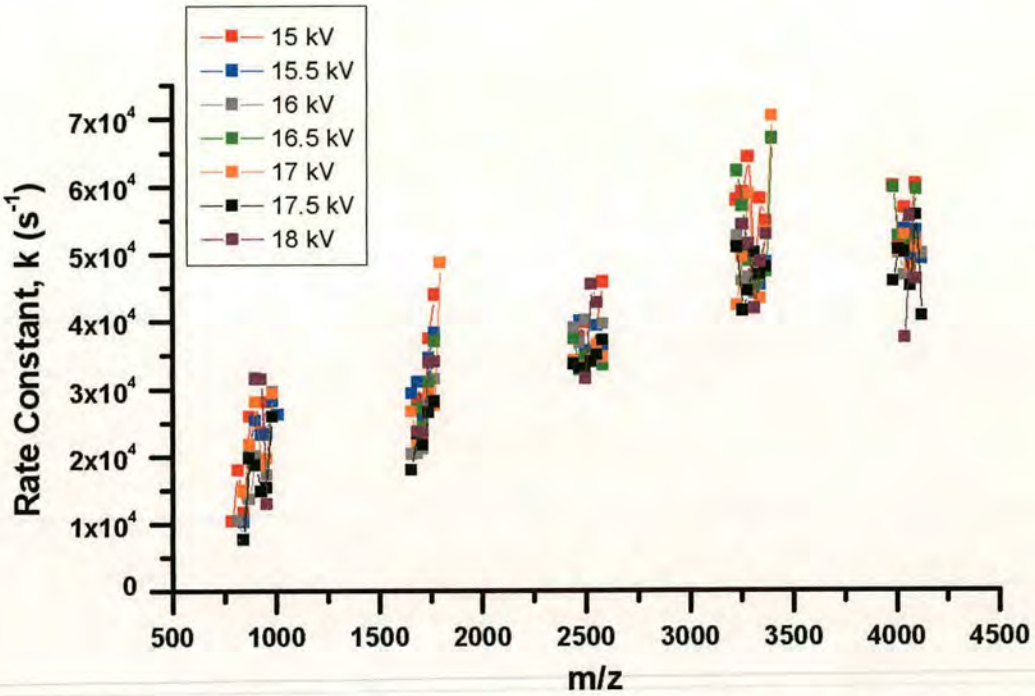

Figure 5-26 The change in metastable rate constant for various cluster sizes produced by different ion residence times within the ion source, controlled by the focus potential.

The plot above is rather a jumbled mess on this scale, but from this plot one can see that there is not a uniform increase in the metastable decay rate with increasing cluster core size, as was observed with the previous laser focus data. The metastable decay rates for the Rh_{30} clusters would appear to be slightly lower than would be expected if metastable decay increased with cluster size. This occurrence shall be reviewed later, after a look at the results pertaining to the change in metastable decay rates with varying ion residence time. The following figures show the data for each cluster core size in more detail.

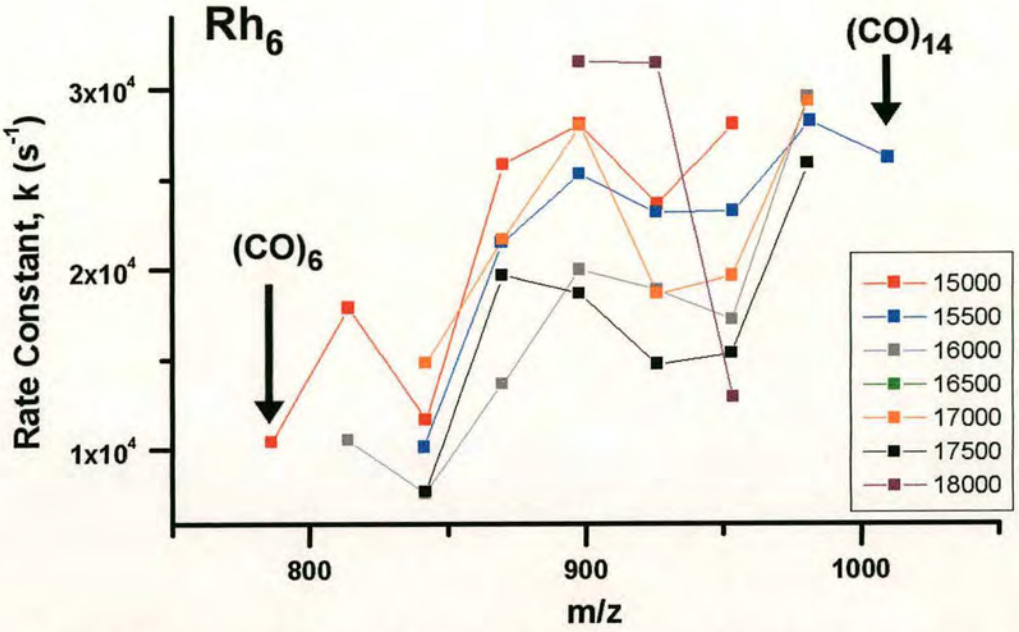

Figure 5-27 A close up of the metastable decay for the Rh_6 clusters from the plot in Figure 5-26.

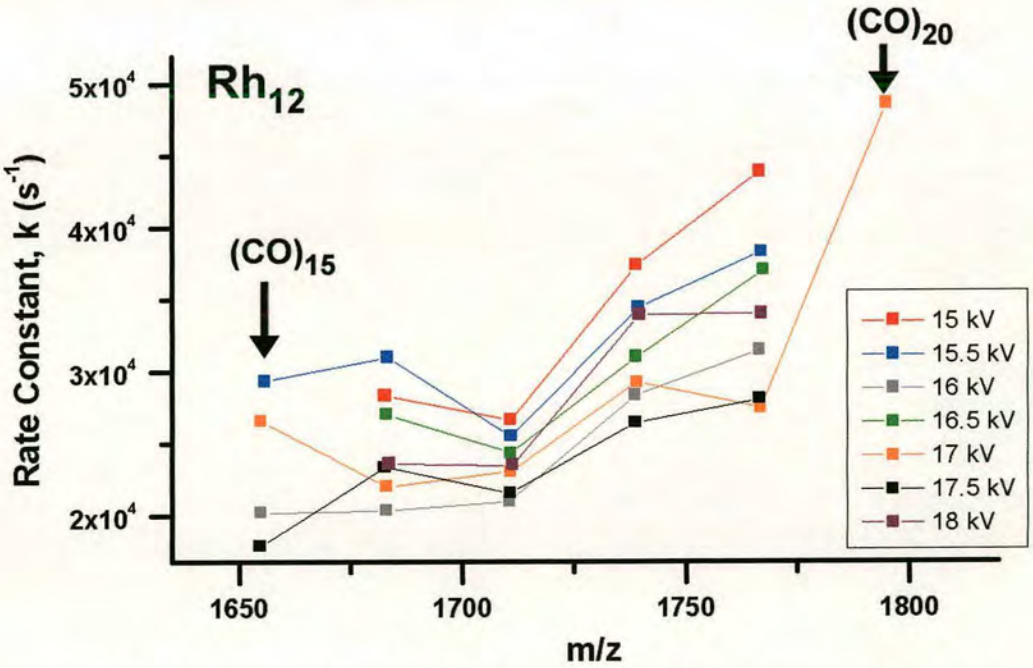

Figure 5-28 A close up of the metastable decay for the Rh_{12} clusters from the plot in Figure 5-26.

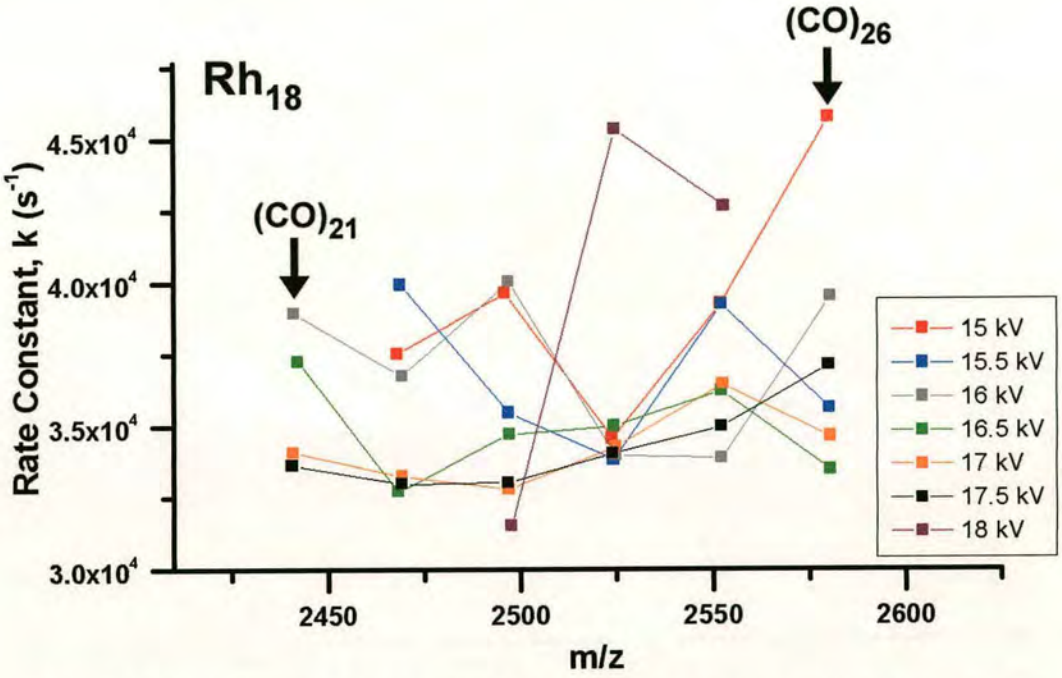

Figure 5-29 A close up of the metastable decay for the Rh_{18} clusters from the plot in Figure 5-26.

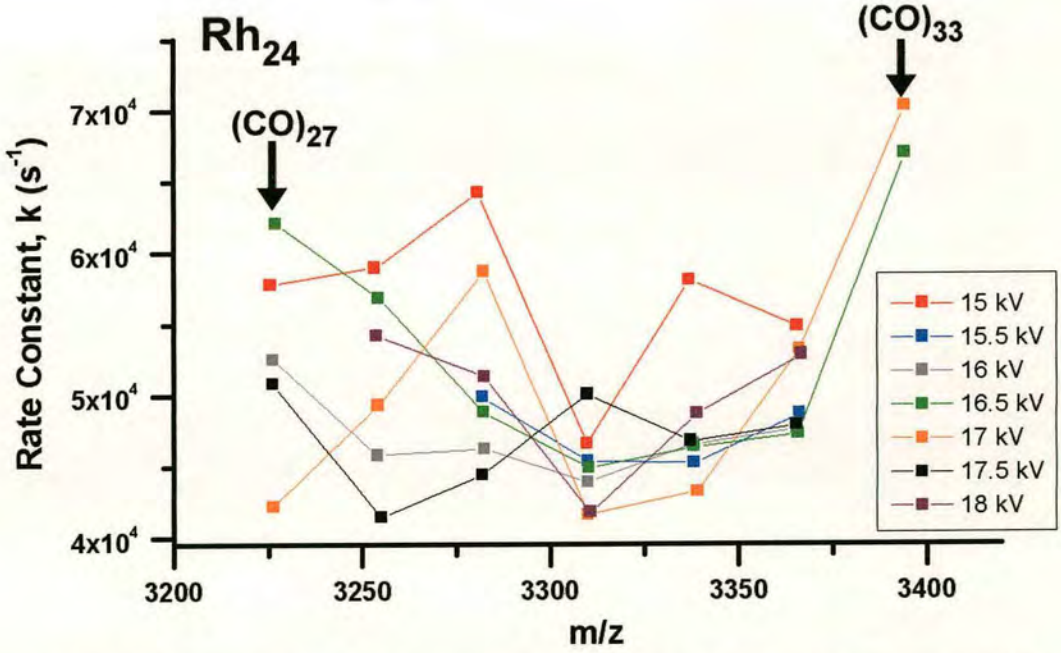

Figure 5-30 A close up of the metastable decay for the Rh_{24} clusters from the plot in Figure 5-26.

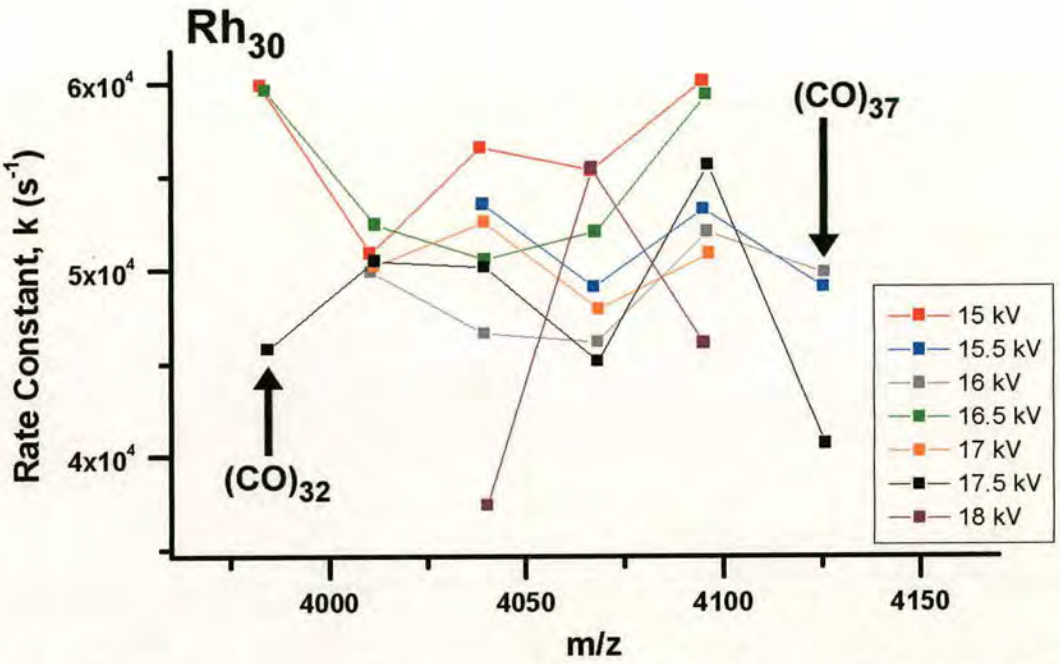

Figure 5-31 A close up of the metastable decay for the Rh_{30} clusters from the plot in Figure 5-26.

As the focus potential is increased so to is the ion residence time within the ion source, such that one would expect a slight decrease in the rate of metastable decay. With more time within the ion source there is more time for the cluster ions to undergo evaporative dissociations within the ion source. As such there will be an increase in the population of ions leaving the ion source with an internal energy that lies within the stable range (see Figure 5-19). Given that the focus potential is changed in a regular fashion one would reasonably expect there to be a regular decrease in the metastable decay. While a general trend can be observed, there is a distinct absence of a regular pattern for the varying ion focussing conditions. Once again this would appear to reflect the probabilistic nature of the cluster formation and dissociation mechanisms, such that what is observed in one experiment may not exactly reflect what is observed in a second or third experiment. However, there does appear to be an overall trend from which meaningful qualitative data can be drawn. The range of metastable decay rates for the current dataset is broader,

covering both lower and greater values for metastable decay than that observed in the laser focus experiments. Such behaviour is consistent with a variation in the ion residence time leading to different periods within which metastable decay can occur.

Returning to the observed dip in the metastable decay rate with the larger Rh_{30} clusters. This behaviour is not altogether unexpected if one considers that the minimum energy necessary for the cluster to exhibit metastable decay increases rapidly with increasing cluster size. Although multiple photons can be absorbed the time within which the ions remain in the source and can absorb photons is finite, such that the large clusters may not have enough time to absorb sufficient photons to promote the cluster to a level of energy consistent with metastable decay. Thus the efficiency of metastable decay will decrease with increasing cluster size, as observed in the current data, such that even larger clusters should be relatively stable [14].

Local Maxima And Minima In The Metastable Rate of Decay

There were some similarities observed between the local maxima and minima in the metastable decay rates recorded in the laser focus experiments and the current dataset. For instance it can be seen that once again $Rh_6(CO)_8$ exhibits an abnormally low rate of metastable decay within the current Rh_6 dataset, as previously observed in the laser focus data. This adds substance to the assumption that this particular configuration has a particularly stable configuration. The same is true for the $Rh_{12}(CO)_{17}$ ion, with both datasets exhibiting abnormally low rates of metastable decay. Considering points of local maxima in the metastable decay values, the laser focus dataset revealed $Rh_{12}(CO)_{19}$ to be the largest cluster observed with a 12 atom core, and with a particularly high rate of metastable decay. The current dataset reveals that the larger ion the $Rh_{12}(CO)_{20}$ is significantly more unstable, with a greater value of metastable decay (approximately $4E^{-4}$ s^{-1} for the $Rh_{12}(CO)_{19}$ cluster in the laser focus dataset, compared to $4.75E^{-4}$ s^{-1} for the $Rh_{12}(CO)_{20}$ cluster in the current dataset). The data for the remaining cluster cores, Rh_{18}, Rh_{24}, and Rh_{30} show no distinct local maxima and minima, instead following the general decrease in metastable rate with increasing ligand number, as discussed above.

5.8 Conclusion

It has been shown that the use of laser desorption ionisation, using ultraviolet radiation, is a potent method for the generation of large multi-nuclear unsaturated supraclusters. It is likely that the larger rhodium supraclusters resemble the form of fragments from a bulk material, and as such are an interesting proposition for future catalytic studies. A supracluster that resembles a bulk fragment may have the same properties of the bulk surface for catalysis, but for the same volume of material the cluster will have a much larger surface area than the bulk material, increasing the possible catalytic activity of the cluster over the bulk material. The evaluation of the unimolecular decay rates for the post-source decay of the clusters were observed to fall as the cluster became larger, suggesting a degree of thermodynamic stability, which will obviously be a necessity for solid-state catalysis. However, the total yield of supracluster species from this method is unclear, and the clusters have so far only been looked at in the gas-phase.

It was observed that the size of the ligand shell reduces as the metal core of the supraclusters becomes larger. This suggests that the cluster is approaching bulk-metal status, with the generation of a close-packed polyhedron structure and that the bonding within the core is more metallic like in character. Unfortunately the precise structure of the supraclusters cannot be determined from the mass spectrometry data, although one can conjecture possible structures as the data shows that the rhodium cluster is able to form larger clusters from the stepwise addition of the intact metal cores of the aggregation precursor ($Rh_6(CO)_{16}$). The precise geometry of the core will, however, have a degree of dependency upon the size of the ligand shell and the electrons they donate to the metal core. Osmium, on the other hand has shown that its aggregation precursor, $Os_3(CO)_{12}$ can have its metal core broken by the energy provided by the ultraviolet radiation, leading to the formation of clusters of various metal nuclearities.

5.9 Reference List

1. Wronka, J.; Ridge, D. P. *Journal Of The American Chemical Society.* **1983**, *106*, 67-71.

2. Meckstroth, W. K.; Ridge, D. P.; Reents Jr, W. D. *Journal Of Physical Chemistry* **1985**, *89*, 612-617.

3. Forbes, R. A.; Laukien, F. H.; Wronka, J. *International Journal Of Mass Spectrometry And Ion Processes* **1988**, *83*, 23-44.

4. Castleman Jr, A. W.; Hsieh, E.; Upschulte, B. L.; Schelling, F. J.; Keesee, R. G.; Holland, P. M. *International Journal Of Mass Spectrometry And Ion Physics* **1983**, *47*, 191-194.

5. Kettle, S. F. A.; Diana, E.; Rossetti, R.; Stanghellini, P. L. *Journal Of The American Chemical Society.* **1997**, *119*, 8228-8231.

6. Dyson, P. J.; Hearley, A. K.; Johnson, B. F. G.; McIndoe, J. S.; Langridge-Smith, P. R. R.; Whyte, C. *Rapid Communications In Mass Spectrometry* **2001**, *15*, 895-897.

7. Griffiths, W. J.; Yang, Y.; Sjovall, J.; Lindgren, J. A. *Rapid Communications In Mass Spectrometry* **1996**, *10*, 183-196.

8. Jackson, P.; Fisher, K. J.; Dance, I. G.; Gadd, G. E.; Willett, G. D. *Journal Of Cluster Science* **1902**, *13*, 165-187.

9. Armentrout, P. B. *Journal Of The American Society Of Mass Spectrometry.* **2002**, *13*, 419-434.

10. Bonner, P. L. R.; Lill, J. R.; Hill, S.; Creaser, C. S.; Rees, R. C. *Journal Of Immunological Methods* **1902**, *262*, 5-19.

11. Ervin, K. M. *Journal Of The American Society Of Mass Spectrometry.* **2002**, *13*, 435-452.

12. Wang, P. P.; Bartlett, M. G.; Martin, L. B. *Rapid Communications In Mass Spectrometry* **1997**, *11*, 846-856.

13. Leavell, M. D.; Leary, J. A.; Yamasaki, R. *Journal Of The American Society Of Mass Spectrometry.* **2002**, *13*, 571-576.

14. Ernstberger, B.; Krause, H.; Neusser, H. J. *Berichte der Bunsen Gesellschaft fur Physikalische Chemie* **1993**, *97*, 884-899.

15. www.waters.com . 2003.

16. Brown, J., Personal Communication: TofSpec 2E schematics.

17. Lewis, J.; Raithby, P. R. *Journal of Organometallic Chemistry* **1995**, *500*, 227.

18. Housecroft, C. E. *Metal-Metal Bonded Carbonyl Dimers and Clusters*, 1st ed.; Oxford University Press Inc.: New York, 1995.

19. Ohashi, K.; Adachi, K.; Nishi, N. *Bulletin of the Chemical Society of Japan* **1996**, *69*, 915.

6 Energy Dependent Electrospray Ionisation Mass Spectrometry of Transition Metal Carbonyl Clusters

6.1 Introduction

Small transition metal carbonyl clusters, of similar size to the precursors used in the laser-induced aggregation experiments, are known for their properties as catalysts and the associated models when the cluster is coordinatively unsaturated. The lauded catalytic properties of the transition metal carbonyl clusters are mostly present when the cluster is coordinatively unsaturated. The question is now one of producing unsaturated clusters that can be experimented upon. Stable coordinatively unsaturated metal species are not readily synthesised from scratch, and tend to be in the form of salts, with counter ions used to stabilise, and often neutralise, the species. The practical alternative is therefore to remove ligands from a saturated cluster. There are many viable means by which fragmentation can be induced, but one of the simplest to implement is through the use of collision-induced dissociation (CID) within the confines of a mass spectrometer. One such technique is *Energy Dependent Electrospray Ionisation Mass Spectrometry* (EDESI-MS) [1;23;4], which utilises CID to provide a complete map of all the fragments produced from a single species and provide raw data on the relative stability and point of formation of each fragment. Performing CID on a series of transition metal carbonyl clusters should provide an understanding of the stability of the unsaturated species, in addition to quantitative data regarding the bond energies of the different metal-carbonyl bonds, and observe how they change with a varying size of ligand shell.

The use of CID has been performed on organometallics to a good degree of success, but mostly with either pure metal clusters, or small clusters with first row transition metal species [5;6]. Little had been done on second and third row transition metal clusters until the work of Henderson (New Zealand), Johnson and McIndoe (Cambridge), and Dyson (York) [4;7;8], of whom both McIndoe and Dyson are collaborators with this project. Originally their work focussed on the synthesis of novel transition metal carbonyl materials and their subsequent analysis by X-ray diffraction (XRD) and mass spectrometry. However it was discovered that the use of an electrospray ion source to introduce their samples to the mass spectrometer for characterisation would often result in the cluster undergoing in-source CID, with the

dissociation of the metal-to-carbonyl bonds. Therefore it is evident that the bonding energy was sufficiently weak to be broken by in-source fragmentation. This discovery led to the development of Energy Dependent Electrospray Ionisation Mass Spectrometry.

The Principles Of EDESI-MS

The main focus of the EDESI-MS technique is direct control over the CID conditions within the electrospray source via the kinetic energy of the ions. This is achieved by controlling the electrostatic ion optic lenses within the source. By gradually increasing the kinetic energy of the ions in the source, one promotes collisions between the ions and the neutral bath gas molecules of increasing energy and number, leading to the production of more fragments. A mass spectrum is recorded for each incremental step in the ion kinetic energy over a desired range, which can lead to the production of over 100 mass spectra. Examining each mass spectrum in turn is a long task, but by doing this one can observe precisely how the population of each ion, parent and fragment, varies with the different energy conditions. Thankfully there is a far simpler means of presenting the data that reveals all of this information in one plot.

The first step is to sum each of the recorded mass spectra. The intensity of each fragment ion is summed over all the values of the cone voltage at which the ion is present, with the resultant mass spectrum providing a good measure of the relative population of each ion over the entire energy range. For instance a fragment ion that is present over a broad range of increasing collision energy shall have a correspondingly greater contribution to the summed spectrum than an ion that dissociates easily and does not appear for long. Therefore the relative intensity of the ion peaks in the summed mass spectrum provide a measure of their relative stability, with those ions that can remain intact for longer despite increasing collision energies having a suitably high intensity in the mass spectrum.

In summing the mass spectra all information on how the ion population varies with energy is removed. To counter this problem a two-dimensional map is constructed

that plots the variation in intensity with m/z and energy. From this data the energy range over which each fragment ion was formed can be directly observed. The intricacies of the construction of these EDESI-MS maps shall be covered in due course. The success of the EDESI-MS maps in quickly characterising the fragmentation pattern of transition metal carbonyl species and other analytes has been phenomenal [1-4;9-11].

By using the technique of EDESI-MS the stability and possible chemistry of the transition metal carbonyl clusters of $Ir_4(CO)_{12}$, $Os_3(CO)_{12}$, and $Rh_6(CO)_{16}$, and their unsaturated analogues shall be investigated. It is further hoped that the threshold energies for the formation of the associated fragments can also be determined, of which no experimental data currently exists for these systems.

6.2 The Micromass® Platform™ II Electrospray Ionisation Quadrupole Mass Spectrometer

The experiments were performed on a Micromass® Platform™ II electrospray ionisation mass spectrometer, which uses a quadrupole ion trap as the mass analyser. This instrument is shown in Figure 6-1.

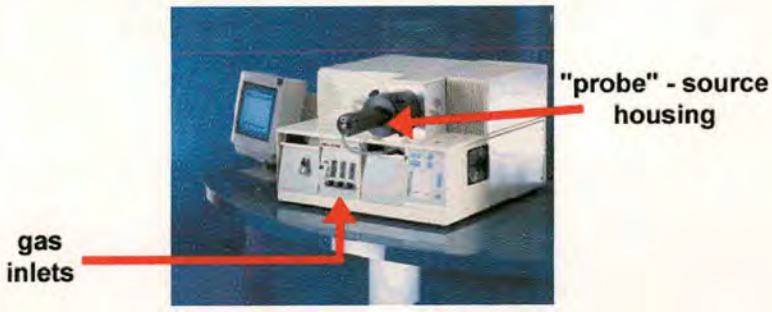

Figure 6-1 The Micromass® Platform™ II electrospray ionisation quadrupole mass spectrometer. Taken from Reference 12.

The instrument underwent a systematic tune to provide a good quality, reproducible mass spectrum for which the following parameters were found to provide the best output for the transition metal carbonyl clusters. It is fortunate that the Platform is a particularly stable instrument, and the same values could be used on different runs with minimal changes to the quality of the output.

6.2.1 Sample Introduction

The cluster ion solution is introduced into the electrospray interface from a 100 µl, gas tight syringe, manufactured by SGE, connected to a motorised syringe pump to provide a steady flow of analyte solution, normally 2 µl per minute. Flow rates can have an important affect on the quality of the mass spectrum produced. If the flow rate is rapid and the concentration of the solution is high then the over abundance of ions entering the mass spectrometer can have a detrimental affect on the quality of the mass spectrum, as ion intensities will tend to fluctuate wildly. The solution was transported from the syringe to the electrospray source via a length of narrow bore (100 µm) fused silica capillary tubing. The electrospray probe is the point of entry for the solution into the mass spectrometer.

6.2.2 The Internal Configuration Of The Electrospray Source

A schematic of the internal ion optics within the electrospray ion source, leading to the quadrupole analyser, is given in Figure 6-2.

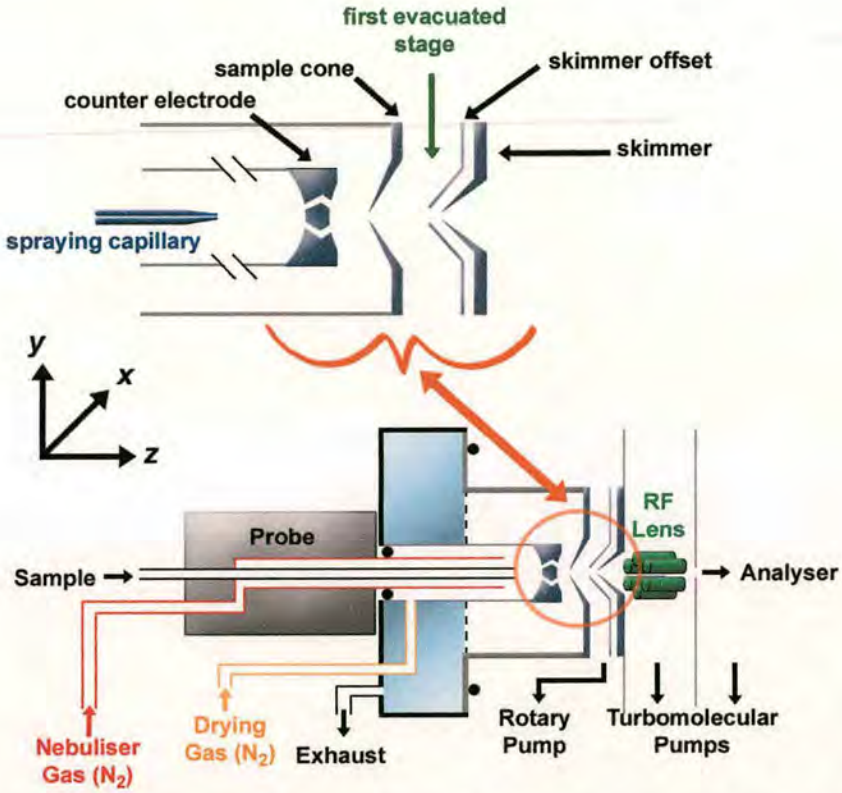

Figure 6-2 The interior of part of the Platform instrument, showing where the gases are introduced and the arrangement of the electronic plates and skimmers Diagram adapted from Reference 13.

Figure 6-2 shows that the electrospray interface of the Micromass Platform is similar to first model discussed in Chapter 3.4.2 (Figure 3-9). The sample cluster ion solution is transported through the probe to eventually be sprayed from the narrow-bore, tapered spraying capillary. The instrument was set for the analysis of negative ions, and as such the spraying capillary was given a fixed potential of –3.8 kV, while the counter electrode had the much lower potential of –0.5 kV. The counter electrode is also known as the high voltage lens, and features four apertures, each of which are aligned slightly off the *z*-axis so as to aid desolvation. The sample cone is next, and the potential applied to the skimmer cone, known as the *cone voltage*, has a range of possible values from 0V to –200 V when operating in negative ion mode. The region between the spraying capillary and the sample cone is defined as the *ion source* region of the electrospray interface. The source region is maintained at a fixed temperature of 90^0C to aid desolvation. Both the nebulising and drying gas are nitrogen, which is pumped through a series of lines, as shown in Figure 6-2, at a

constant flow rate (30 litres per hour for the nebulising gas and 200 litres per hour for the drying gas). This typically makes the working pressure of the nitrogen within the source region approximately 7 bar [13]. The vast majority of the ions will be completely desolvated on leaving the source region.

Beyond the sample cone the ions enter the first evacuated region, where the pressure is approximately 0.2 mbar, provided by a rotary pump. The ions then reach a second set of skimmers. The first skimmer lens is known as the skimmer-offset, with a value that is dependent upon the cone voltage. The Micromass manual states, "*This lens optimises at a set voltage (typically 5 V) higher than the sample cone.*" [13] From this description one would reasonably assume that the potential applied to the skimmer offset lens would be greater than that of the sample cone, creating a small potential incline in each ion mode. Thus in positive ion mode one would expect that with the default offset value of 5 V, a cone voltage of +25 V applied to the sample cone would result in a voltage of +30 V applied to the skimmer offset, while a cone voltage of –25 V would give a voltage of –30 V applied to the skimmer offset lens, especially given that the polarity of the optics are normally reversed when going from positive to negative ion mode. However, in working with the instrument in negative ion mode it soon became apparent that the polarity of the offset value had not been reversed, and so under the default setting, the skimmer offset was given a potential of –20 V for a cone voltage of –25 V! Therefore the actual value of skimmer offset denotes the absolute potential difference applied between the sample cone and the skimmer offset lens, regardless of lens polarity and the potential on the sample cone.

The second, and final, skimmer cone is grounded, has a slightly narrower aperture and is placed almost directly behind the skimmer-offset lens. The ions pass through this skimmer and enter a greater evacuated region, of approximately $8E^{-6}$ mbar, provided by a turbomolecular pump. The higher vacuum region features a R.F. hexapole to act as a final ion guide and to focus the beam before being set to the quadrupole analyser and detector.

The MassLynx software was used to set all of the electric potentials applied to the ion optics described above. The program showed that the greater potentials applied to the ion optics, such as the spraying capillary and the counter electrode and even the sample cone, were subject to momentary fluctuations from the power supply. The fluctuations were relatively infrequent and lasted under a second, changing the potential by anything from one to five percent. Given that the time frame for the fluctuations was far less than the scan time it was thought that the fluctuations would not lead to any major discrepancies between different scans.

6.2.3 Remaining Parameters

Mass Range

Since the quadrupole is a scanning analyser one can specify the range of m/z values within which one is interested. Limiting the observed range of m/z to the expected range of the sample ions can sometimes be problematic as it may prevent the detection of unexpected fragment ions or aggregations that would appear outwith the specified range. The electrospray source produces only ions of one polarity, thereby making an aggregation reaction highly unlikely. Therefore one can safely presume to place an upper limit of the range just beyond the mass-to-charge ratio of the parent ion. However, both the lower and upper range limits of the calibration file placed restrictions on the possible limits of the experimental spectra. The calibration files consisted of pre-recorded, accurate mass spectra of known species over a broad range of m/z values. A suitable calibration file from a negative salt solution was chosen for each experiment as it covered the expected m/z range of the cluster species.

Instrument Resolution

The resolution of the recorded mass spectrum is controlled by two parameters, which deal with the lower and higher mass areas within the scanned range of the mass spectrum. These fields control the magnitude of the a/q ratio for both the low- and high-pass mass filter on the quadrupole (as discussed in Chapter 3.5.2). This feature allows one to specifically enhance the resolution of the mass spectrum in the region of most interest, or augment both to get the best resolution over the whole mass range. A higher value of the resolution control results in an increased resolution of

the mass spectrum. The initial resolution settings were 15.0 and 15.5 out of a defined range of 0 to 25 for both the lower mass and the higher mass resolution respectively.

Scan Duration

The scan duration defines the length of time, in seconds, over which the quadrupole scans through the incoming ions and determines the mass-to-charge ratios. Since the quadrupole operates on a continuous influx of ions, the scan time does not provide any long-term measure of the thermodynamic stability of the ions. The ions need only last as long as the time taken for them to traverse the ion optics from the source and into the quadrupole analyser, which should be of the order of microseconds. However, the scan time is important since enough time must be allowed for the parameters to be changed on the computer, and for the change to be applied to the relevant component(s) of the instrument. As such, the scan duration was set to ten seconds, with an inter-scan "grace" period of one second. There was no significant difference observed in mass spectra recorded when the scan duration was altered to values of between five and fifteen seconds.

6.3 Sample Preparation

As discussed previously (Chapter 2.4), the transition metal carbonyl clusters were to be made suitable for electrospray ionisation by the derivatisation of the cluster with a sodium alkoxide solution. The production of an experimental solution for analysis by electrospray was a three-stage process:

1. Making the sodium alkoxide solution.
2. Reacting the sodium alkoxide with the cluster.
3. Dilution of the solution to a suitable level for analysis by mass spectrometry.

Methanol was used to create a methoxide derivatising agent, chosen because of its relative stability in normal laboratory conditions. The methanol was purchased from Fisher Chemicals with a purity of 99.9%. The sodium was in the form of large sticks

held under oil (supplied by Sigma Aldrich). Sodium quickly oxidises in air, and the presence of a large quantity of the oxide was found to hinder the formation of the methoxide anion. This fact dictated the way in which the methoxide solution was made.

Sodium Methoxide Solution

Firstly, 4 ml of the methanol was placed in a small glass container from a mechanical pipette, and placed on an electronic balance. A small portion of sodium was carved from a stick with a blade, and the portion dried on towelling to remove the oil. Once dried the surface of the sodium was noted to be a dull grey, indicating the presence of the oxide. A fresh blade was used to split the sodium chunk open and a smaller chunk was quickly carved out and deposited in the methanol held on the balance, quickly noting the corresponding change in mass. The smaller chunks had little time to form the oxide during this procedure, and the surface of the metal maintained a shiny lustre up to the point of entry into the methanol. Once the solution had stopped fizzing the container was sealed with a stopper. With the mass of the sodium and the volume of methanol known it was a simple task to determine the concentration of the solution. The mass of the sodium was typically of the order of 0.01 g. In 4 ml of alcohol this would give a solution of just over 0.1 M. It was a simple matter of determining how much extra methanol was required to take the solution back down to 0.1 M.

Addition Of The Cluster

An accurate balance was used to weigh out roughly 0.005 g of the specific cluster on a weigh boat. From the mass, the number of moles present was determined, and the volume of alcohol needed to make a 0.1 M solution was determined. The volume was typically over 50 µl, which was dispensed into an Eppendorf tube from a mechanical pipette. With two solutions of known concentration it was a simple matter of taking aliquots from each solution to make up mixtures of varying molar ratios held in a separate 1 ml Eppendorf tube. The resultant solution was then diluted in methanol to the 1 ml mark. Accuracy at this point need not be as strict as no qualitative work from the number of ions present would be determined from the mass

spectrometry instruments. The mixture was sonicated in an ultrasonic bath to aid both the mixing and the solvation of the cluster species, which are relatively insoluble.

Dilution For Mass Spectrometry

The concentration of the above solution would typically be of the order of $1E^{-3}$ M, or 1 μmole-per-millilitre. This is a little high for mass spectrometry purposes, so the solution was diluted ten fold to $1E^{-4}$M, or 0.1 μmole-per-millilitre. This was done by taking 100 μl from the above solution and simply making into 1ml with the alcohol. The syringe used to store the solution for use in the experiments had a capacity of 100 μl, thus making the total number of ions entering the instrument of the order of $1E^{-8}$ moles.

It was soon discovered through trials of differing molar ratios that little significant difference was discovered between solutions where the methoxide was in excess to the cluster, except that mixtures featuring a very high concentration of methoxide had to be diluted more before use in the instrument. These contained too many free alkoxide anions in the solution and produced an unstable mass spectrum. In addition it was observed that the solution would strip the inner coating of the transfer capillary tubing between the syringe and the mass spectrometer inlet. It was undesirable to have the cluster in excess of the methoxide since this would leave neutral cluster species in the solution, and lower the yield. It was then decided that generic solutions could be made, where the exact values of the reagents were not so meticulously determined, to speed up the experiment turn-around time. The experience from creating the above solutions allowed them to be quickly made where the molar concentration of the alkoxide was between two and five times greater than that of the cluster. The solutions were tested for reproducibility and showed favourable results. Once a solution had been made, it was kept in a fridge and re-used. The results provided in this thesis use these generic solutions. The resultant derivatised clusters then have the form $[Ir_4(CO)_{11}COOMe]^-$, $[Os_3(CO)_{11}COOMe]^-$, and $[Rh_6(CO)_{15}COOMe]^-$. Three independently prepared derivatised cluster solutions were made for each of the iridium, osmium and rhodium clusters. Each

one was used in the following experiments to monitor the repeatability of the experiments and the coherence of the data.

6.4 Energy Dependent Electrospray Ionisation Mass Spectrometry Of Derivatised Transition Metal Carbonyl Clusters

6.4.1 Experimental Procedure

The fundamental assumption governing in-source CID is that it occurs in the first intermediary evacuated region [14]. This would then place the activating collisions occurring between the sample cone and the skimmer. The velocity of the ions leaving the pressurised region of the ion-source will be maintained at a level corresponding to the velocity of the bath gas flow, as discussed in Chapters 3.4.2. Although the flow rates are known in terms of volume of gas per unit time (given in Chapter 6.2.2), it is difficult to convert this to a velocity value in metres per second. Despite not knowing the gas velocity, it is clear that it is only the post-source ion optics (sample cone, skimmer offset and skimmer) that provides the principal source of kinetic energy for the ions prior to the activating collisions, and it is known that the ions leave the source vibrationally cool [15]. As such it should be possible to alter the energy of the collisions by manipulating the ion velocity in this region through the use of the ion optics, namely the sample cone, and affect the subsequent activation. The action of increasing the cone voltage (making it more negative) will accelerate the ions to greater kinetic energies.

The cone voltage has a range of 0 V to –200 V in one-volt increments, which should provide plenty of scope to significantly alter the collision conditions and observe the difference this makes to the dissociation products from the derivatised molecular ions. If the instrument is set up as described in Chapters 6.2.2 and 6.2.3, with the skimmer offset applying a potential difference of +5 V between the sample cone and

the skimmer offset, the potential energy diagram for the instrument will look something the plot in Figure 6-3.

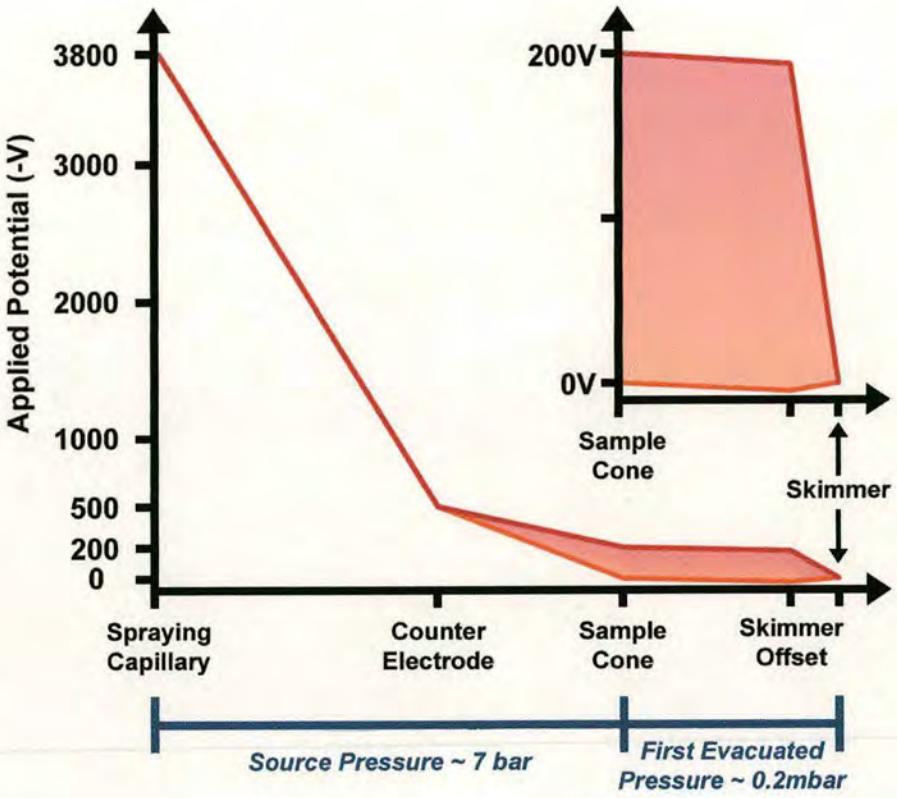

Figure 6-3 The potentials applied to the various ion optics within the Platform electrospray interface. The region between the sample cone and the final skimmer has been enlarged to show more clearly the shallow decline in potential between the sample cone and the skimmer offset lens with the default offset value of +5 V. The shaded region denotes the spread in energies from the maximum and minimum values of cone voltage.

The clusters $Ir_4(CO)_{12}$, $Os_3(CO)_{12}$ and $Rh_6(CO)_{16}$ were derivatised with a solution of sodium methoxide (Chapter 6.3), and then analysed in turn on the Micromass Platform instrument. For each derivatised sample solution, mass spectra were recorded for each step-wise increase in the cone voltage over the full possible range. The MassLynx software allows the series of mass spectra recorded for one sample to be compiled into one data set, allowing the software to perform a number of different functions on the spectra to show the complete fragmentation pattern for each cluster

ion. The experiments were then repeated using two new derivatised cluster solutions for each cluster species to test the reproducibility of the results.

6.4.2 Confirming Derivatisation Of The Clusters

The first observed trend in the results was the increase in CID with increasing cone voltage, producing fragment ions of progressively smaller mass-to-charge. To determine the composition of the daughter ions, the MassLynx software could be used to generate models corresponding to the isotopic distribution of a given molecular formula for comparison against the recorded spectra. An example of the recorded molecular ions for each methoxide derivatised species and the respective isotope model is given in Figure 6-4.

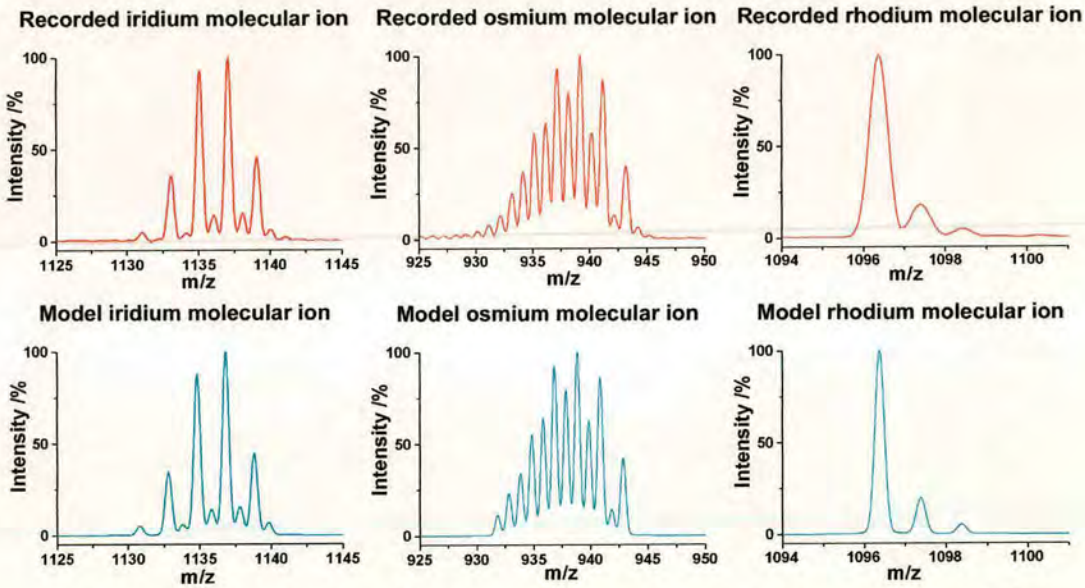

Figure 6-4 A comparison of the recorded mass spectrum of the parent ion of the methoxide derivatised iridium and osmium cluster and the isotope model for these same ions.

The recorded mass spectra very closely match the isotopic models, thus confirming the presence of the carbomethoxy ligand on the cluster. The complicated nature of the spectra reflects the number of atoms within the cluster ion, and their individual isotopic contribution. Osmium has seven isotopes, compared with the two of iridium and the monoisotopic rhodium [16]. One must also include the trace abundance of the heavier isotopes of carbon and oxygen. A change in the number of atoms will

normally have a distinct effect upon the isotope distribution. However, the dominance of the metals on the overall isotope distribution and the fact that their number remains constant throughout the experiments means that a change in the number of ligands present on the cluster has a negligible effect on the distribution.

6.4.3 Generating The EDESI-MS Ion Fragmentation Charts

General Trends In The EDESI-MS Data

Examples of the mass spectra recorded for one of the derivatised iridium, osmium and rhodium clusters for a range of applied cone voltage are shown in Figure 6-5 as a waterfall plot. Each of the peaks can be resolved to show similar characteristic isotope patterns to those shown above. The waterfall plots start from a cone voltage value of –10 V, since the mass spectra at zero volts produced little in the way of a quality mass spectrum. A reasonably regular pattern of ions and relative intensities for different derivatised solutions of each cluster species was observed, demonstrating good concordance between different solutions and the reproducibility of the results. The individual peaks are evenly spaced and tie in with the sequential loss of carbonyl ligands from the molecular ion.

As the cone voltage is increased (made more negative) fragment ions of progressively lower mass are produced. At the early stages, with low cone voltages between –10 and –30 V, the energy of the collisions is sufficient to cause a portion of the total molecular ion population to fragment between leaving the source and reaching the detector, while the remainder are detected intact. Beyond a cone voltage of –40 V the energy regime is such that the molecular ions cannot stay intact and the entire population fragments. This cycle is repeated for all of the fragment ions detected: as the cone voltage is increased further the daughter ions also fragment. The fact that dissociation products are only observed for non-zero values of the cone voltage shows that that no dissociation is occurring prior to the ion's presence in the accelerating field between the sample cone and the skimmer cone.

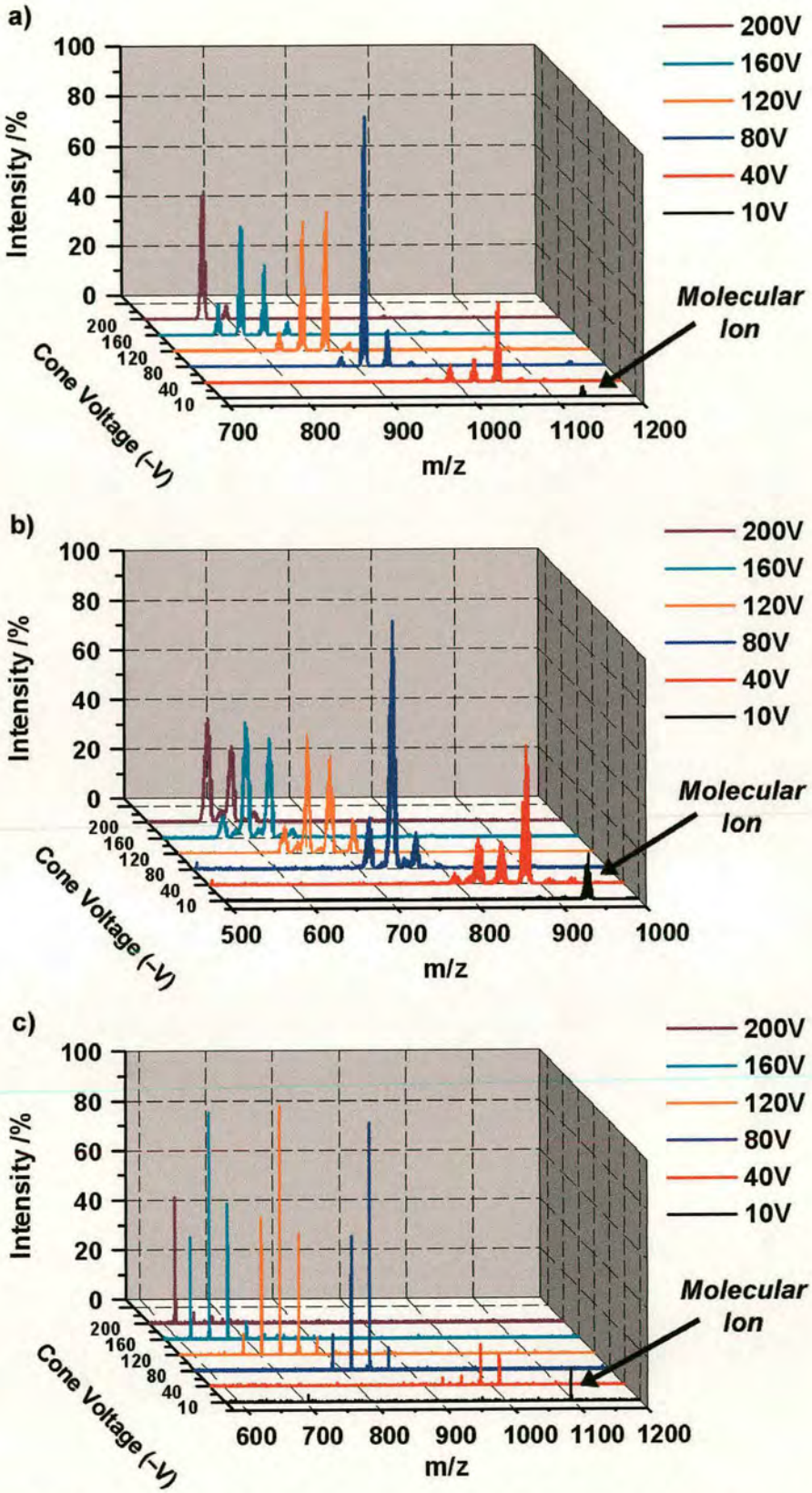

Figure 6-5 Waterfall diagrams showing the mass spectra recorded for the methoxide derivatised a) iridium, b) osmium, and c) rhodium carbonyl clusters.

This evidence proves that the high pressure of the nitrogen gas in the region between the capillary and the sample cone reduces the kinetic energy of the free ions formed to thermal levels, much too low for collisions to transfer a significant amount of energy into the internal energy of the cluster ion. Therefore the principal source of energy for the collision process is confirmed as the potential gradient between the sample cone and the grounded skimmer cone. However, it should be stressed that the pressure of the nitrogen gas within the collision region is still high enough to result in the thermalisation of the ions. The activating collisions will only be the first few that the ion experiences as it begins its short-lived acceleration by the potential difference.

It was also observed that the resultant product ion distribution from the CID of the cluster species was only dependent upon the actual value of the cone voltage at the point of dissociation – the previous value of cone voltage had no bearing on the product ion distribution observed at the present value. That is to say that the distribution of daughter ions on a mass spectrum recorded where the cone voltage is set to a value of *i* will be the same regardless of what the previous cone voltage value was. While the experiments increase the cone voltage in a step-wise fashion from 0 V to –200 V, the same results would be produced if the cone voltage was reduced from –200 V to 0 V, or the cone voltage values chosen at random. Therefore it has been proven that there is no accumulative energy effect in gradually increasing the cone-voltage and the values of cone voltage at which the daughter ions appear.

The nature of these patterns can be explored by considering the physical processes that are occurring in the ion source and collision region, which shall be discussed later in Chapter 6.4.4.

Variation Of Ion Intensity With Cone Voltage

It was earlier remarked that the waterfall spectra started at a cone voltage value of -10 V because there was little in the way of a discernible spectrum at 0 V. It should also be noted from the waterfall spectra in Figure 6-5 that the molecular ion intensity

in each of the mass spectra is less than the intensity of some of the daughter ions, whereas one would expect that the number of daughter ions produced would be equal to or less than the number of molecular ions present to begin with. This is due to the function of the sample cone and skimmer offset lens as a means to tune the mass spectrometer to obtain the best quality mass spectrum in terms of resolution and intensity, and so variation of the cone voltage can have an affect on both of these parameters. Therefore the intensity of the molecular ion at –10 V only represents the number of ions reaching the detector at that particular value of the cone voltage, and not the intensity over the entire cone voltage scale. Fortunately, this should have little influence on the interpretation of the mass spectra and the observations of the decay channels from the in-source dissociation.

Generating The EDESI-MS Maps

The first step is to sum the mass spectra recorded for each value of the cone voltage, as this will provide a general overview of the relative ion stability over the available collision energy range controlled by the cone voltage. Rather conveniently the MassLynx software has a function that allows one to perform the summation effortlessly to any chosen data set. Figure 6-6 shows an example summed spectrum for the fragmentation products of the derivatised iridium cluster $[Ir_4(CO)_{11}COOMe]^-$.

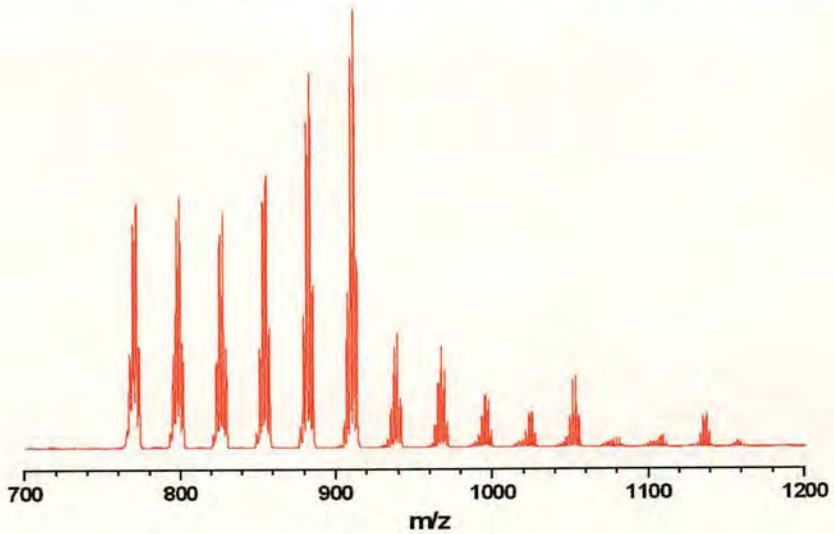

Figure 6-6 A combined mass spectrum for the methoxide derivatised iridium cluster produced from the summation of all mass spectra recorded over each step-wise increase in the cone voltage.

Now the summed spectrum must be complimented with the EDESI-MS map in which will be shown the variation of ion intensity with changing energy conditions. The generation of the map is performed by the MassLynx software, which automatically stores such information as the mass spectra are being recorded. Consider the example waterfall plot of the derivatised iridium cluster shown in Figure 6-5 a). A coloured intensity scale is overlaid onto each of the mass spectra to give another visual guide to the relative intensity of each peak in the spectrum. The chosen scale goes from black at 0% intensity, through blue, red, yellow and then white at 100% intensity. An example of this scale applied to the waterfall plot is given in Figure 6-7.

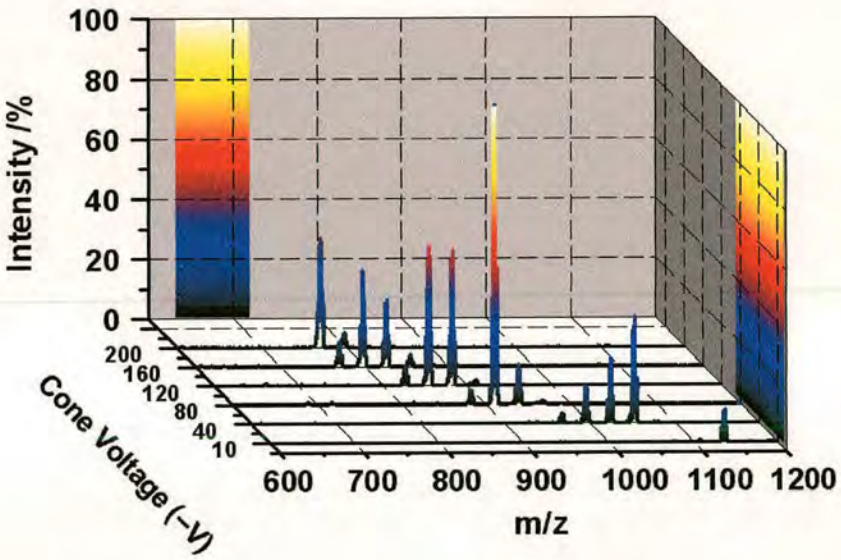

Figure 6-7 The colour scale applied to the waterfall plot of the cluster $[Ir_4(CO)_{11}COOMe]^-$.

If all of the recorded mass spectra were represented on the waterfall plot with the same colour coding, and the plot was tipped forward (with the mass-to-charge and cone voltage still the *x* and *y*-axis respectively) a colour coded contour plot that shows the variation of ion intensity with the cone voltage is generated. An example of this is given in Figure 6-8. As the collision conditions change with the cone voltage, the population of parent and daughter ion will vary, increasing and decreasing as they are formed and then spent from the dissociation reactions. This variation in the intensity of any given fragment ion cone voltage can also be studied

independently, where the resultant plots can be thought of as stability profiles of the individual ions. An example of two of these stability profiles are given in Figure 6-9, with the intensity normalised against that of the fragment ion with the highest recorded intensity.

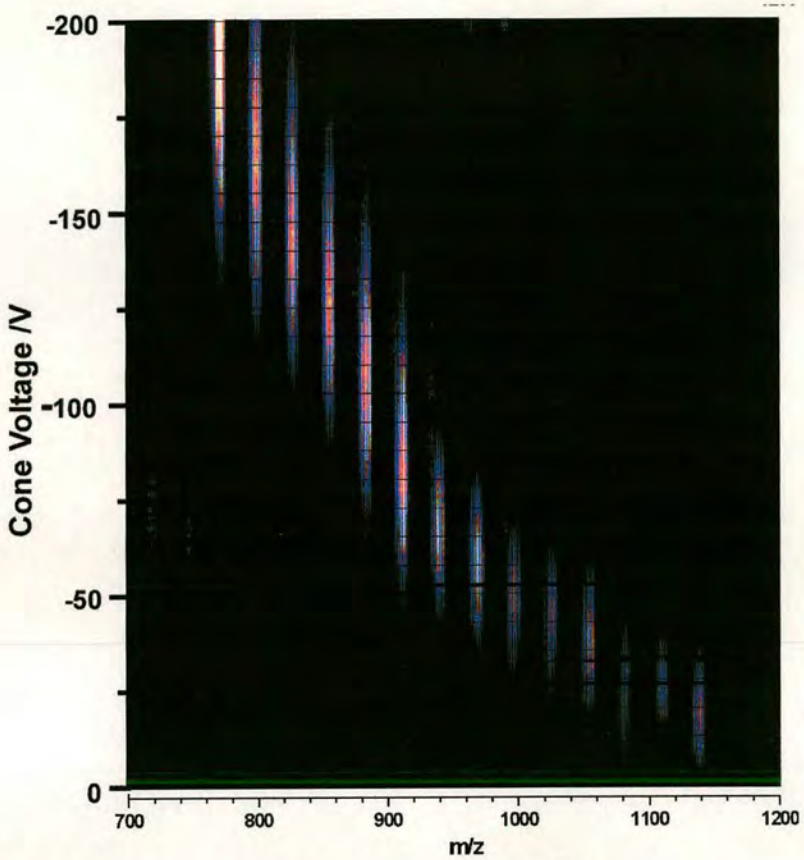

Figure 6-8 The resultant EDESI-MS map for $[Ir_4(CO)_{11}COOMe]^-$.

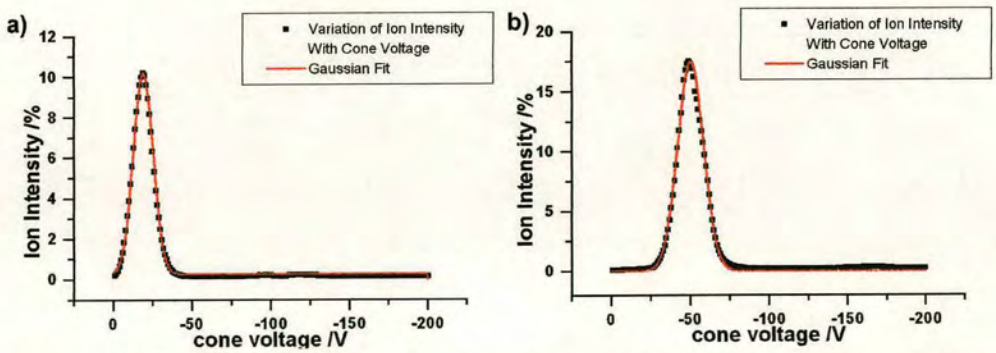

Figure 6-9 The stability profiles of a) the iridium molecular ion $[Ir_4(CO)_{11}COOMe]^-$, and b) the fragment ion $[Ir_4(CO)_6COOMe]^-$.

The data to plot the stability profiles were first smoothed within the MassLynx software using a mean 3-channel, 2-pass method. These were then exported into Micocal Origin 5 and plotted as scatter plots. The stability profiles for each cluster fragment were observed to vary very smoothly with the changing energy conditions. To emphasise this fact models of Gaussian curves were fitted to all of the stability profiles using the Microcal Origin 5 software, and those Gaussian curves have been superimposed over the scatter plot in Figure 6-9. These Gaussian curves fit the data exceptionally well, and show that the growth and decay of the ions as they are produced and later spent follows a very regular and smoothly varying pattern.

Each of these elements can be scaled and fitted together to form one chart that provides all the data on the production of fragment ions and their changing population with changing energy conditions, controlled by the cone-voltage. An example EDESI-MS chart is given for each of the derivatised cluster species experimented on in Figure 6-10 to 6-12. The charts are constructed from the summed mass spectrum on top, with the EDESI-MS map underneath. To the right hand side of the map, the stability profiles can be shown, which mimic the contours of ion variation in the EDESI-MS map. In each case only a small number of the stability profiles are given, purely for ease of visualisation. It is unfortunate that due to the monoisotopic nature of the rhodium clusters, the false colour contour plots are only around one mass unit wide, and thus can be quite hard to see.

The EDESI-MS charts provide a very useful "at-a-glance" look at the entire fragmentation process as the cone voltage is varied from its minimum to maximum levels. From this data it is hoped that useful thermodynamic data about the dissociation of the derivatised transition metal clusters under study shall be discovered.

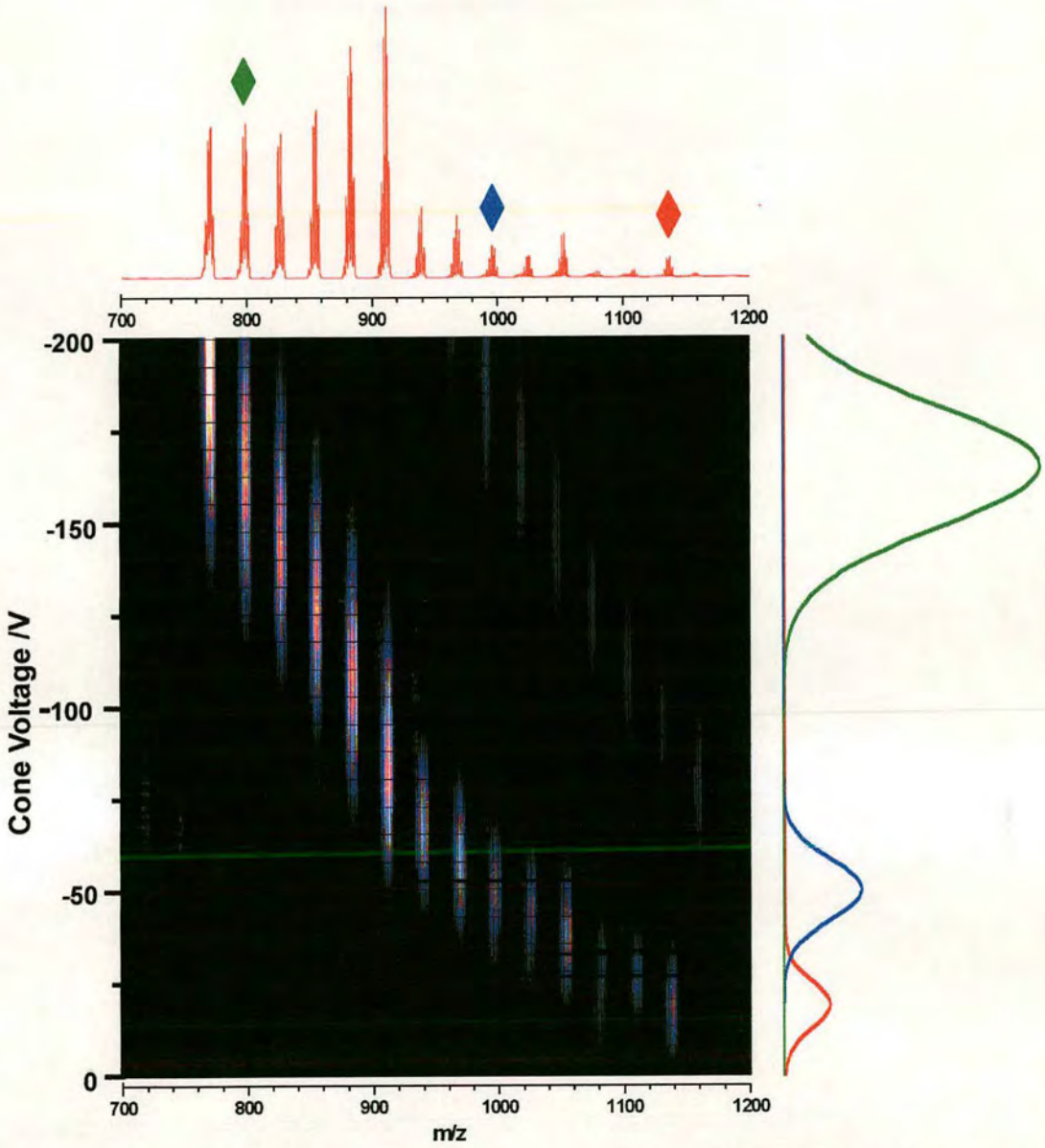

Figure 6-10 The EDESI-MS chart for the fragmentation of the derivatised cluster $[Ir_4(CO)_{11}COOMe]^-$. The stability profiles correspond to the molecular ion $[Ir_4(CO)_{11}COOMe]^-$ (red), and the fragments $[Ir_4(CO)_6COOMe]^-$ (blue) and $[Ir_4(CO)H]^-$ (green) as indicated on the summed mass spectrum.

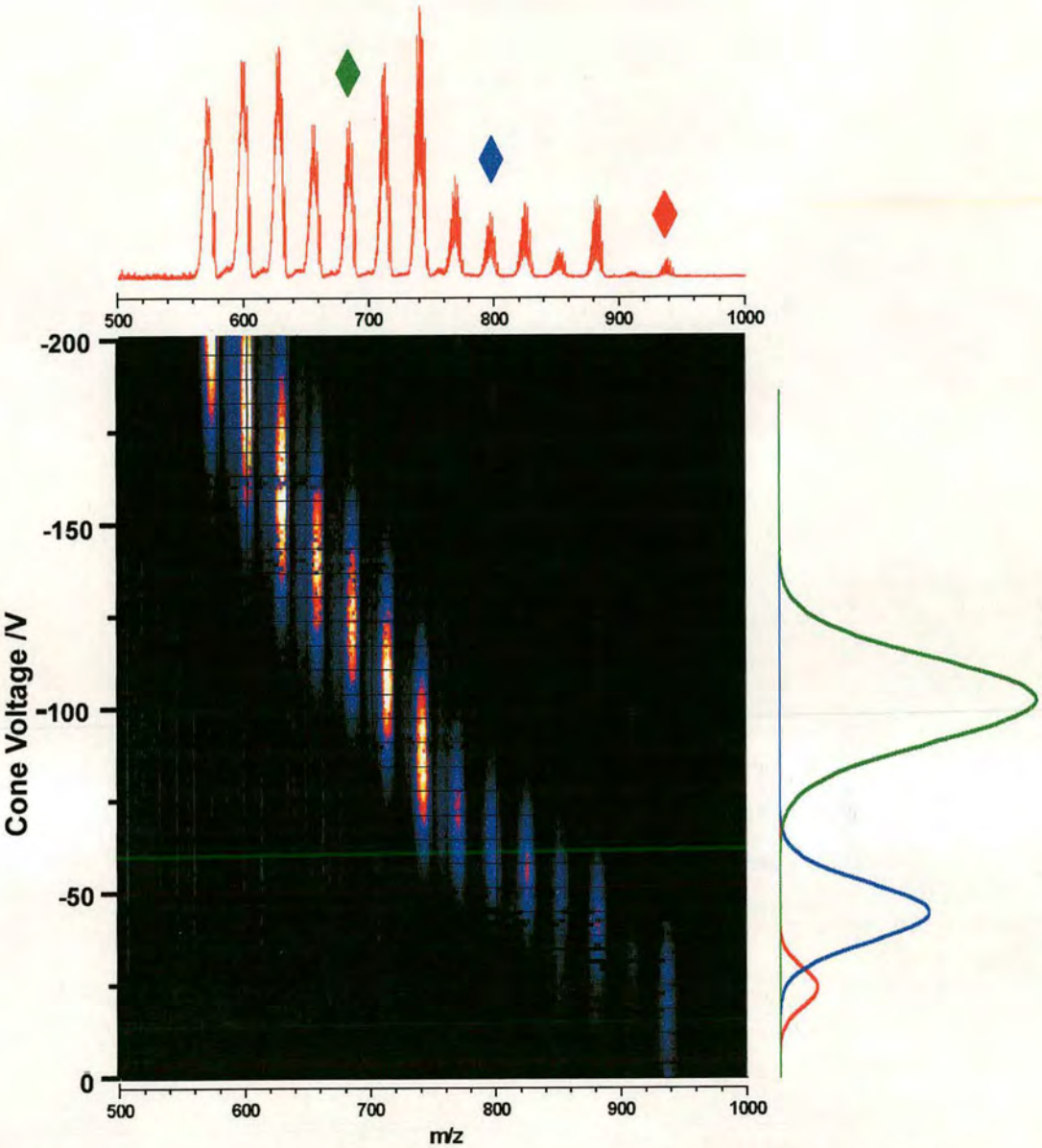

Figure 6-11 The EDESI-MS chart for the fragmentation of the derivatised cluster $[Os_3(CO)_{11}COOMe]^-$. The stability profiles correspond to the molecular ion $[Os_3(CO)_{11}COOMe]^-$ (red), and the fragments $[Os_3(CO)_7COOMe]^-$ (blue) and $[Os_3(CO)_4H]^-$ (green) as indicated on the summed mass spectrum.

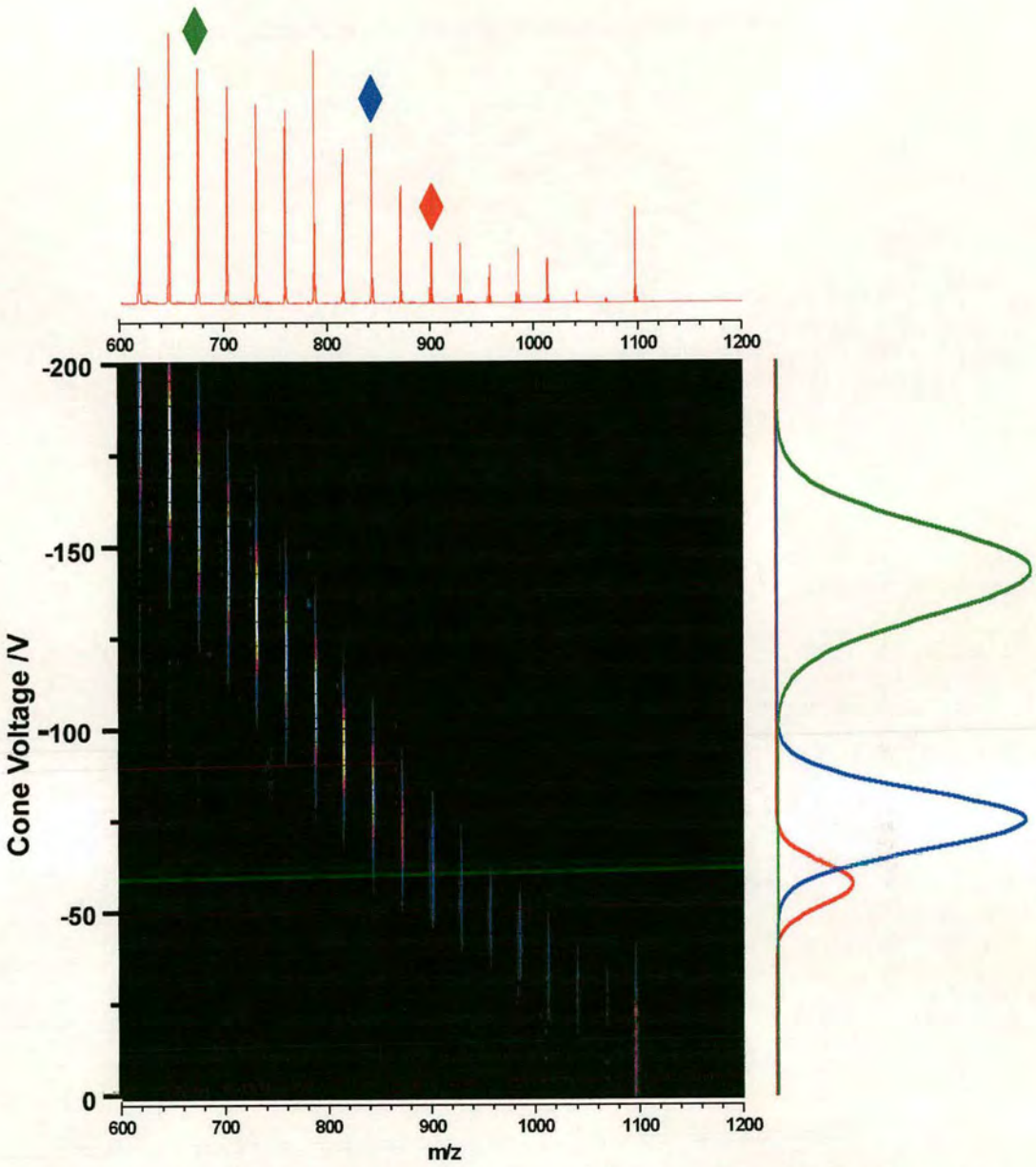

Figure 6-12 The EDESI-MS chart for the fragmentation of the derivatised cluster $[Rh_6(CO)_{15}COOMe]^-$. The stability profiles correspond to the fragment ions $[Rh_6(CO)_8COOMe]^-$ (red), $[Rh_6(CO)_8H]^-$ (blue) and $[Rh_6(CO)_2H]^-$ (green), as indicated on the summed mass spectrum.

6.4.4 The Mechanics Of EDESI-MS In The Micromass Platform

In the energy regime within the Platform instrument, the desorbed ions will be given an initial kinetic energy of the order of $10^1 - 10^2$ electronvolts by the potential difference between the skimmer cone and the skimmer offset. However, it can be rationalised that only the initial collisions transfer a significant amount of energy into the ion. Each collision will lower the kinetic energy of the ion, and thus also lower the maximum amount of energy that can be transferred, such that the latter collisions will be transferring only a very small quantity of energy and therefore the most potent collisions in terms of energy transfer are likely to the be the earliest. In addition, the vast number of collisions within this region will result in the ions quickly becoming thermalised, reinforcing the concept that it is only the initial collisions that provide any energy transfer. As the cone voltage is increased the maximum amount of energy that can be transferred in each of the initial collisions shall also increase, as will the collision frequency, such that the energy needed for each dissociation reaction is reached sooner, allowing for the observed sequential loss of ligands from the cluster at higher cone voltage values.

The initial kinetic energy of the desorbed ions suggests that electronic excitation will be precluded, and that vibrational excitation is far more likely. The energy regime also suggests that vibrational excitation from the formation of a long lived complex is also unlikely. Therefore at this stage it can be assumed that the excitation of the ion occurs via an impulse collision. Given that initially the metal core is completely surrounded by a ligand shell, all collisions and collision complexes occur between the carbonyl ligands and the nitrogen. One would therefore expect that the lifetime of the collision complex to be in accordance with the vibrational modes of the carbonyl ligand and the metal-to-carbonyl bond.

Infrared spectroscopy of $Ir_4(CO)_{12}$ has shown that the vibrational frequencies for the carbonyl bond to be on average 2046 cm^{-1}, while the Ir-C modes have been measured between 440 cm^{-1} and 550 cm^{-1} [17]. Similar values have been recorded for $Os_3(CO)_{12}$

[18]. If one assumes that these modes remain roughly the same for the derivatised iridium and osmium cluster, and that the same order of magnitudes can be applied to the respective modes of the rhodium cluster, then the period of the vibrational modes, and consequently an estimate of the interaction time can be determined to be of the order of 10^{-13}-10^{-14} s. This is considerably longer than the average period of electronic excitation, which is of the order of 10^{-15} s. The spectra presented in Figures 6-5 show that with increasing cone voltage, and hence ion kinetic energy, the amount of dissociation from the molecular ion increases, suggesting the excitation occurs from an impulse collision, and not a long lived complex (Chapter 4.3.5). With increasing ion kinetic energy, the lab energy (and hence the centre-of-mass energy), and the collision frequency will also increase accordingly (Chapter 4.3.6).

It would be prudent to determine the likely number of collisions that will occur within the collision region. A rough estimate of the mean free path of the ion can be made by applying a Langevin model of ion-molecule collisions, as discussed in Chapter 4.2.2. We can reasonably assume that there is no energy barrier to the reaction, since the dissociation reaction occurs after the collision event, and that there exists a strong attraction between the ion-molecule collision pair. We can then use Equations 4-15 and 4-16 to determine the mean free path for ions within this region. Thus the impact parameter is evaluated from:

$$b_{\max}^2 = \frac{q}{4\pi\varepsilon_0}\sqrt{\frac{2\alpha}{E_{rel}}}$$

and is dependent upon the polarisability of the neutral bath gas and the relative kinetic energy of the collision. The polarisability of dinitrogen can be taken to be of the order of 10^{-39} $J^{-1}C^2m^2$ [19]. It shall be sufficient at this stage to determine the impact parameter for the extreme limits of the initial collision energy, namely cone voltages of 1 and 200 V. Thus the squared impact parameters for these limits are $1.61E^{-19}$ and $1.140E^{-20}$ m. The mean free path of the ion is then determined from:

$$\lambda = \frac{1}{\sqrt{2}\sigma}\left(\frac{V}{N}\right) = \frac{1}{\sqrt{2}\pi b_{\max}^2}\left(\frac{k_B T}{p}\right) \qquad (6\text{-}1)$$

The pressure between the sample cone and the skimmer offset is held at 0.2 mbar, which on conversion to SI units is 19.6 Nm^{-2}, while the temperature within this

region is taken to be 90^0 C (363 K). This gives the mean free path to be $3.58E^{-4}$ m at a cone voltage of 1 V, and $5.04E^{-3}$ m at 200 V. Over a distance of a few millimetres this gives the number of collisions to be between $6E^6$ and $4E^5$ between these two limits. However, since the ions will rapidly be slowed by the numerous collisions with the neutral bath gas molecules, these figures are misleading and should not be taken as a definitive value to the actual number of collisions, being as they do not account for the pressure differential, nor the rapidly slowing ion velocity.

Although the efficiency of excitation does not necessarily increase with relative velocity, the centre-of-mass energy will increase with increasing relative kinetic energy. Therefore as a certain ion is given a greater kinetic energy from the increase in cone voltage, a point will be reached where the collisions will almost certainly provide sufficient energy to promote bond dissociation in the whole population of that ion, and hence beyond –40V the molecular ion has a very small lifetime and the entire population has dissociated, a cycle that is repeated for all other daughter ions which are subsequently activated to the point of complete fragmentation. It can reasonably be assumed that the dissociation reactions are sequential in nature. For example the reaction to produce the daughter ion, $M_n(CO)_{x-3}R$, from the molecular ion, $M_n(CO)_xR$, occurs from the sequential loss of three ligands:

$$M_n(CO)_x R \xrightarrow{\partial E_1} M_n(CO)_{x-1} R \xrightarrow{\partial E_2} M_n(CO)_{x-2} R \xrightarrow{\partial E_3} M_n(CO)_{x-3} R$$

The internal energy of the ion is built up gradually from the collisions, eventually attaining the necessary energy to cross the first threshold energy δE_1, and losing one ligand. The product daughter ion is then exposed to further collisions and dissociates a ligand on reaching an internal energy in excess of the threshold energy δE_2, and so on.

Large polyatomic species are known to survive the excitation of many vibrational modes before a dissociation event occurs [15]. This is justified from the fact that within the collision region the ions are subjected to over 10^5 collisions yet at the most efficient energy transfer we only see up to the order of 10 or more dissociation events for any one ion. Polyatomic species can act as an energy sink through which the

excitation energy can be redistributed rapidly, as predicted by the quasi-equilibrium theory. It could also be argued that since activation occurs via an impulse collision, part of the ion is acting as a spectator though the duration of the collision complex, although with multiple collisions it is likely that the whole ion is sampled. Indeed, if the cluster is being activated by an impulse collision, then it is likely that the carbonyl ligands are lost by direct activation of the metal-carbonyl bond from collisions between the N_2 and the surface ligand shell surrounding the metal core. As more ligands are lost from the shell, this target surface area reduces, such that more N_2 molecules are likely to strike the metal core than hit the few remaining carbonyl ligands still left attached. Uggerud and Derrick derived a relationship to quantify energy transfer in impulse collisions, as discussed in Chapter 4.3.5, in which the amount of centre-of-mass energy transferred on any one collision is maximised if the mass of the target bath gas molecules is equal to that of the atom(s) struck on the ion, as determined by the efficiency coefficient [20;21]:

$$\chi = 4\frac{m_a m_g}{(m_a + m_g)^2}$$

For a nitrogen molecule (m_g = 28 u) striking the oxygen of a carbonyl ligand (m_a = 16 u), the efficiency coefficient, χ, is equal to 0.9. If the nitrogen molecule strikes a full carbonyl ligand, the efficency coefficient is equal to unity. Now, if one considers the case of the nitrogen molecule striking the metal core of a rhodium cluster (m_a = 103 u), the efficiency coefficient is now equal to 0.67. Thus in striking the metal core the efficiency of energy transfer in an impulse collision is reduced, therefore with a greater degree of ligand loss energy transfer shall also be reduced for each collision. However, the complete removal of the ligands from the metal core is always observed. This is due to a number of reasons. Firstly the cluster experiences a great number of collisions, which increases the probability of the carbonyls being struck. Secondly, the cone voltage is approaching its maximum values when the cluster is mostly unsaturated, and as such the velocity of the ions is greater, resulting in an increase in collision density. Lastly, as the cone voltage is increased, the centre-of-mass energy also increases from the increase in lab energy (from the cone voltage) and from the removal of the ligands, making the ion lighter (see Chapter 4.3.4, Equation 4-36). Thus the molecular and subsequent daughter ions take fewer,

but more energetic collisions, before dissociation occurs at higher cone voltage values.

The Persistence Of Negative Ions In Energetic Collisions

Negative ions are renowned for being particularly fragile, with the additional electron usually being less well bound than the electrons on the respective neutral molecule. The collisional detachment of the charge-giving electron on the anion is a facile and common reaction in negative ion chemistry. Therefore one would expect that the threshold for electron detachment would be lower than any bond-breaking threshold. However, parent and daughter ions have been recorded in abundance, and therefore the neutralisation step would appear to be less facile than bond dissociation in this case. It is therefore clear that the negative charge is tightly bound to the cluster.

The carbomethoxy ligand introduces the negative charge to the neutral cluster, but it is uncertain whether the charge remains localised around the ligand, or is "absorbed" into the metal core of the cluster. Recalling the proposed bonding scheme for the carbomethoxy ligand discussed in Chapter 2.4.2, the additional electrons from the methoxide anion had been placed into one of the anti-bonding π orbitals of the carbonyl ligand, used for back-bonding to a metal atom. As such these electrons will possibly be used as part of the back-bonding between the metal and the carbomethoxy ligand, and consequentially may be assimilated into the metal core. Such an action would undoubtedly protect the electron from dissociation so long as the metal core remained intact.

6.5 The Presence of Cluster Hydride Anions

6.5.1 Irregular Isotope Distributions

A closer inspection of the mass spectra revealed that the isotope patterns of some of the iridium and osmium daughter ions exhibited a minor distortion in their isotope distribution, with the inclusion of additional low-intensity isotope peaks at the lower

m/z range of the distribution. As an example the recorded mass spectrum for the daughter ions $[Ir_4(CO)_6COOMe]^-$ and $[Os_3(CO)_4COOMe]^-$ are compared to the respective isotope models in Figure 6-13.

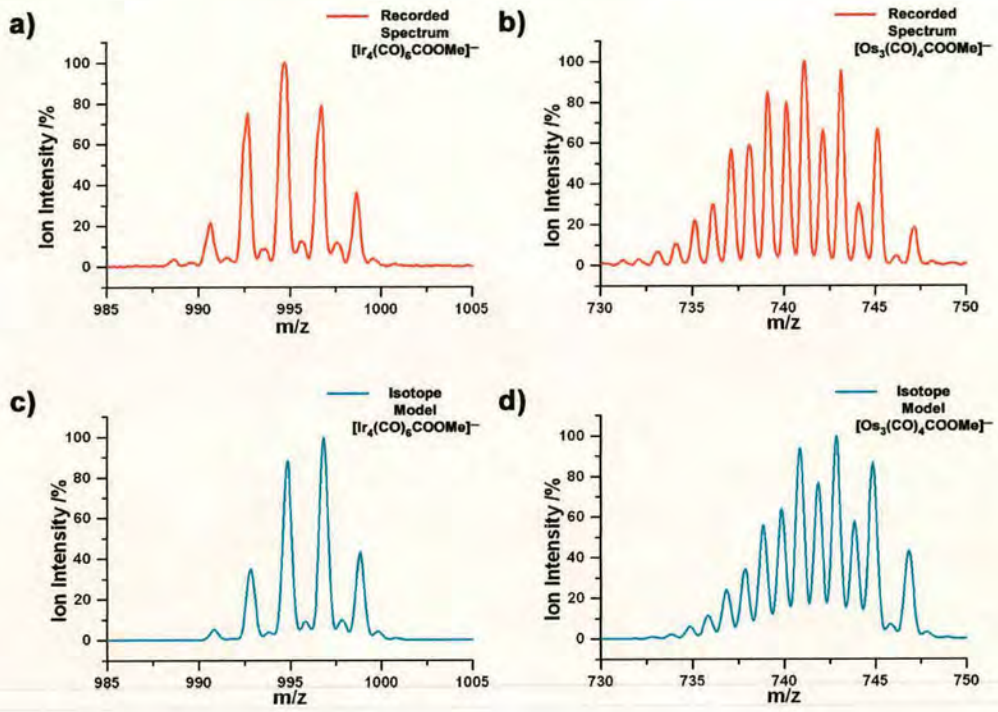

Figure 6-13 a) and b) show the typical recorded mass spectra for the daughter ions $[Ir_4(CO)_6COOMe]^-$ and $[Os_3(CO)_4COOMe]^-$ respectively. c) and d) show the expected isotope pattern for these ions. Comparisons show a minor perturbation in the recorded isotope patterns, most notably for the iridium cluster.

The perturbation is most obvious for the iridium daughter ion, with a clear alteration of the relative abundance of its component isotope peaks. The daughter ion of the osmium cluster shows only a minor variation in the relative abundance of the isotope peaks at the heavier end of the isotope pattern.

From these spectra it is difficult to determine a reason for this disruption and its significance to the current understanding of the dissociation pathways followed through the course of the CID experiments. A closer inspection of the rhodium data reveals the reason for this occurrence. A series of additional, unexpected peaks are to be found two mass-to-charge units less than those for the daughter anions

produced by carbonyl loss from the derivatised cluster, as illustrated by the mass spectrum in Figure 6-14.

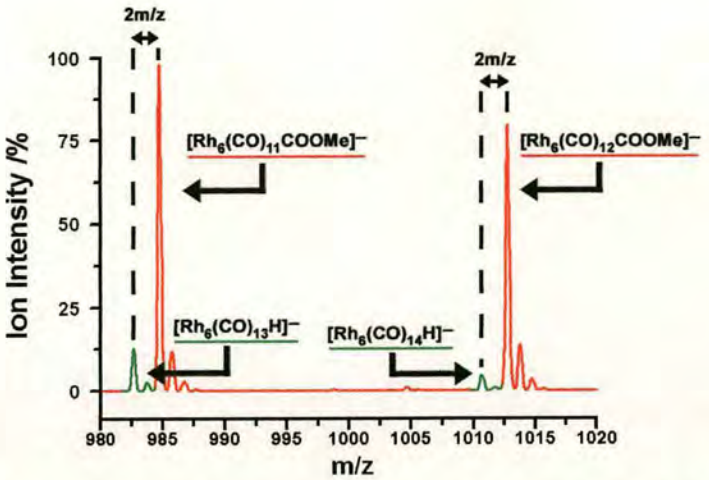

Figure 6-14 The CID mass spectra of the Rhodium cluster reveals the presence of a series of peaks that are two mass-to-charge units less than those of the daughter ions of the methoxide derivatised rhodium clusters. These ions have been attributed to rhodium carbonyl hydride anions.

Isotope modelling of these peaks in the rhodium spectra has lead to the empirical assignment of a rhodium carbonyl cluster hydride anion, $[Rh_6(CO)_nH]^-$. It is therefore likely that the presence of iridium and osmium hydride anions is the cause of the perturbation in the isotope pattern: the broad number of isotopes make it markedly difficult to differentiate between adjacent between two species whose mass differs by only two amu. For simplicity, those cluster ions that bear the carbomethoxy ligand shall generally be referred to as cluster carbomethoxy ions, whereas those clusters that feature the hydride shall be referred to as cluster hydride ions.

It is possible to prove the occurrence of cluster hydrides is the cause of the isotope perturbation in the iridium and osmium clusters by superimposing the relevant isotope models of the cluster carbomethoxy and cluster hydrides in an attempt to match the altered isotope pattern of the recorded spectra. This has been done for both the iridium and osmium daughter ions shown previously in Figure 6-13, and the results can be seen in Figures 6-15 and 6-16 respectively.

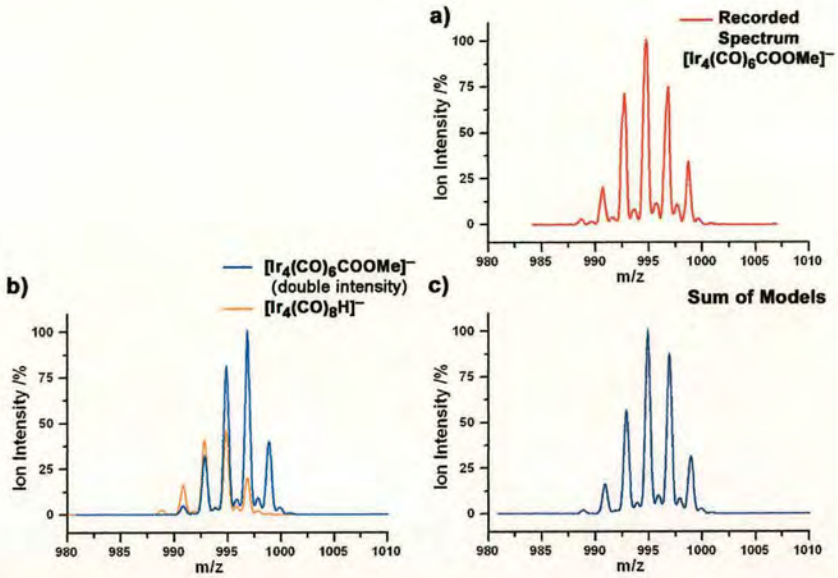

Figure 6-15 a) The recorded isotope distribution for the daughter ion $[Ir_4(CO)_6COOMe]^-$ b) The superimposed isotope models of $[Ir_4(CO)_6COOMe]^-$ and $[Ir_4(CO)_8H]^-$, with the former having double the intensity of the latter. c) The sum of the superimposed isotope models make an effective match to the recorded isotope distribution, giving a strong indication of the existence of the hydride anion and its effect on the isotope pattern for $[Ir_4(CO)_6COOMe]^-$.

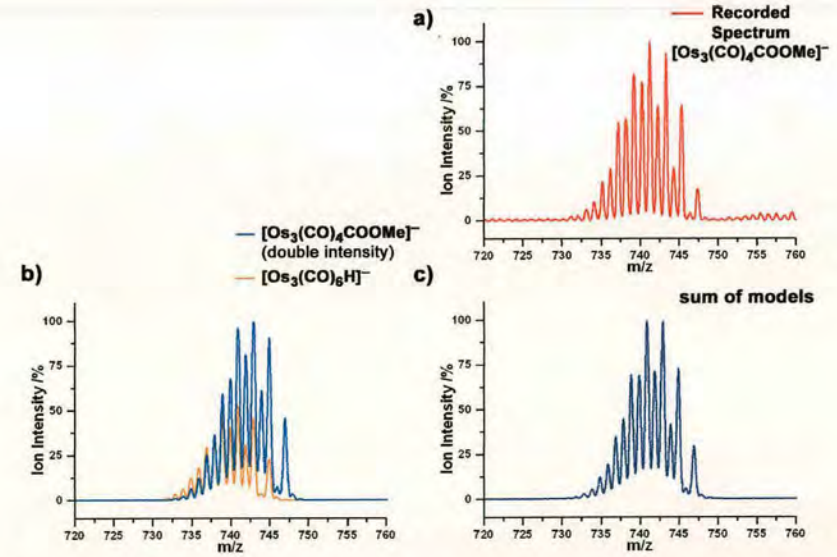

Figure 6-16 a) The recorded isotope distribution mass spectrum for the daughter ion $[Os_3(CO)_4COOMe]^-$. b) The isotope models of $[Os_3(CO)_4COOMe]^-$ and $[Os_3(CO)_6H]^-$, with the former having double the intensity of the latter. c) The sum of the superimposed isotope models is an effective match to the recorded isotope distribution, giving a strong indication of the existence of the hydride anion and its effect on the isotope pattern for $[Os_3(CO)_4COOMe]^-$.

In order to produce a reasonable match with the recorded isotope distribution of the relevant iridium and osmium daughter ions, the isotope model for the cluster carbomethoxy was made double that of the cluster hydride, as depicted in Figures 6-15 b) and 6-16 b). The resultant sum of these isotope models, shown in Figures 6-15 c) and 6-16 c) correspond to the recorded isotope distribution quite well, and prove that hydride anions exist for all the cluster species examined. The need to make the intensity of the cluster hydride much lower than that of the cluster carbomethoxy daughter ions is in accordance with the observations of the rhodium data, where the hydride ion intensity would be of considerably less intensity than cluster carbomethoxy neighbours on the spectrum for the daughter ions with fuller ligand shells. However, a general increase in the occurrence of the cluster hydrides was observed to occur as more ligands were removed.

The clarity of the rhodium CID data further proves the significance of the hydride anions within the CID process. All the rhodium spectra show that the daughter ion $[Rh_6(CO)_8COOMe]^-$ is the smallest daughter ion to contain the carbomethoxy ligand, with all subsequent daughter ions found to be hydride anions that undergo successive carbonyl loss as before. The intensity of the latter hydride anion peaks is equivalent to the earlier cluster carbomethoxy daughter ions. The threshold point is illustrated in Figure 6-17.

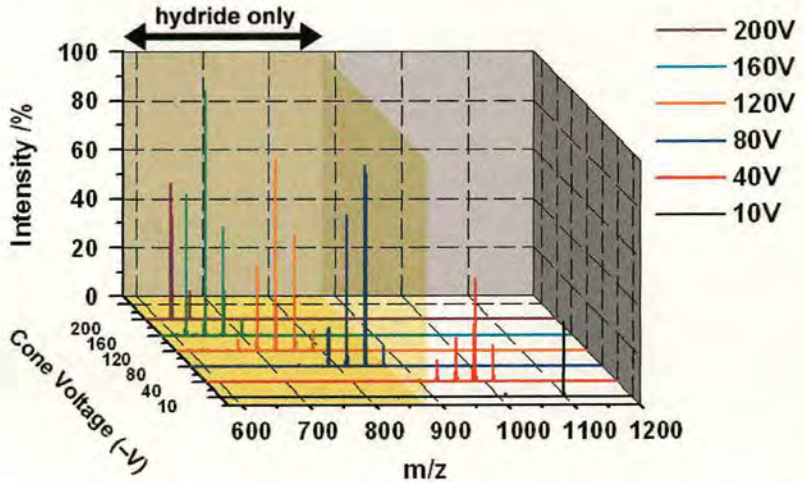

Figure 6-17 The shaded area in the waterfall plot for the CID of $[Rh_6(CO)_{15}COOMe]^-$ shows the region in which all the daughter ions are rhodium carbonyl hydride anions.

The iridium and osmium data show similar behaviour, with each set of cluster solutions suddenly producing only hydride anions at which point in the dissociation process. This suggests that a threshold exists at which only hydride anions are found, although the exact nature and reason behind this threshold is not obvious at this stage. Before trying to answer this problem it is pertinent to determine the origin of the hydride cluster first.

6.5.2 Possible Sources Of The Cluster Hydride Anions

There are two possible explanations for the presence of the hydride anions within the mass spectra:

1. Contaminant within the derivatising solution.
2. A secondary decay channel, other than carbonyl loss and perhaps involving some form of ligand activation, which produces the hydride anions.

Contamination As A Source Of Cluster Hydride Anions

The first possibility is that of contamination in the source of the derivatised clusters. The contamination could come from the un-derivatised clusters or from the derivatising solution. Before trying to rule any of these possibilities out a quick examination of the spectra and the trends observed in the CID experiments can reveal a lot of information over the probability of such contamination. To begin with the first hydride anions to appear in the experiments are $[Ir_4(CO)_{10}H]^-$, $[Os_3(CO)_{10}H]^-$ and $[Rh_6(CO)_{14}H]^-$. There was no indication of hydride bearing parent ion, i.e. $[Ir_4(CO)_{11}H]^-$, $[Os_3(CO)_{11}H]^-$, or $[Rh_6(CO)_{15}H]^-$. From the absence of any apparent hydride parent ion it would seem unlikely that the clusters had reacted with some contaminant within the derivatising solution prior to analysis. For instance a well known reaction in organometallic chemistry is the reaction between a transition metal carbonyl and sodium hydroxide (which can easily be formed from the addition of sodium to water). The hydroxide unit is a nucleophile and attacks the polar carbon of one of the ligands, in a similar manner to that of the sodium methoxide. However, the hydroxide can cause carbon dioxide to leave the metal, leaving the

hydrogen behind to bond to the metal. The reaction is shown for iron pentacarbonyl in Figure 6-18.

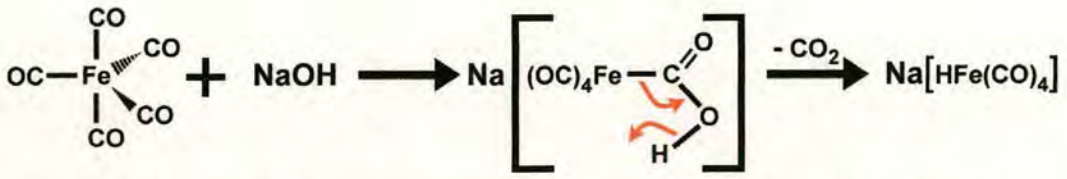

Figure 6-18 The nucleophilic attack of sodium hydroxide on one of the carbonyl ligands of iron pentacarbonyl. The subsequent loss of carbon dioxide from the reaction complex produces the iron carbonyl hydride anion [22].

One can draw other arguments against the possibility of contamination from the dominance of the hydride anions in the later stages of the dissociation reaction. Not only do the hydride ions become dominant at fixed points in the reaction pathway, but also their intensity is equivalent to that of the carbomethoxy ligand bearing clusters at the earlier stages of the dissociation reaction, at which point the hydride anions appeared in comparatively lower quantities. Such a sudden dominance in hydride anions at the expense of the carbomethoxy bearing clusters could not be satisfactorily explained by the tuning effect of the sample cone.

To ensure the validity of these arguments a set of solutions was made to try and remove any possible source of contamination. A quantity of methanol was distilled to remove any water, which was used to make the derivatising solution and also to wash the glassware and other utensils. It was unlikely that any contaminants came from the oil the sodium sticks were held under, since a clean blade was used each time to remove chunks of sodium from the inner surface of the stick. The end result was a series of mass spectra for all cluster species that were indistinguishable from those already shown, and showed the hydride anion phenomenon as reported above.

Secondary Decay Channel As A Source Of Cluster Hydride Anions

The evidence so far suggests that the hydride anions are produced directly from the methoxide derivatised molecular ion during the CID process. The formation of the hydride anions must result from an elimination reaction from the carbomethoxy

ligand, since it is the only bearer of hydrogen on the cluster and there appears to be no hydride anions that are associated with clusters still bearing the carbomethoxy ligand. This fact would also seem to rule out the possibility of an association or ligand transfer reaction to produce the hydrides, especially given the prior removal of possible contaminants from the solutions and that the only gas present within the source should be nitrogen.

It would seem that a secondary decay channel is present, in addition to the principal carbonyl loss channel, which leads to the formation of the cluster hydrides. The first detected hydride anions are $[Ir_4(CO)_{10}H]^-$, $[Os_3(CO)_{10}H]^-$ and $[Rh_6(CO)_{14}H]^-$, which corresponds to the loss of three carbon, three oxygen, and two hydrogen atoms (86 mass-to-charge units). Unfortunately, the mass spectra recorded on the Platform Instrument do not provide sufficient information to allow for an accurate judgment on the nature of the decay channel, as one cannot be sure of the parent ion. This would require the use of the isolation techniques used in tandem mass spectrometry, on an instrument such as a Fourier-Transform Ion Cyclotron Resonance mass spectrometer. However, it can be proposed from the current data that the cluster hydride anions have one decay channel only: the successive loss of carbonyl ligands, whereas the cluster carbomethoxy anions have two decay channels: the successive loss of carbonyl ligands, and the fragmentation that leads to the formation of the cluster hydrides.

The structure of the first cluster hydrides can be rationalised from the fact that hydrogen must bond to the metal core. This fact is clear from the present mass spectra, since the last product of the dissociation process for each cluster has had all carbonyl ligands removed, and matches isotope models for the respective bare metal core plus one hydrogen. The hydrogen can only bond to the metal if there is a vacant bonding site available, and therefore the formation of the cluster hydride can only occur if the cluster has undergone at least one dissociation event. Thus the cluster shall necessarily be excited to some degree for the metal-to-hydrogen bond to be formed.

6.5.3 The Threshold For Cluster Hydride Dominance

The threshold for cluster hydride dominance is almost certainly linked to the chemistry and physical properties of the molecular ion as it undergoes CID. The sudden dominance of the cluster hydride ions cannot be satisfactorily explained by the efficiency of transmission for the different focussing conditions in the mass spectrometer as the cone voltage is increased. Although the focussing conditions are dependent upon the cone voltage, it seems unlikely that the focus would be able to preferentially discriminate between the hydride and carbomethoxy anions, since their masses are roughly equivalent, and their charge state is identical. The efficiency of transmission would therefore be nearly the same for both types of ion for given cone voltages. In addition, the point of total cluster hydride dominance does not occur for a set value of cone voltage, and so the threshold is not an issue of the energetics of the CID.

To try and understand how this threshold arises, the configuration of the last observed cluster daughter ion to bear the carbomethoxy ligand is compared against that of the respective molecular ion, documented in Table 6-1.

Molecular Ion	Last Cluster Carbomethoxy Ion	Number of Carbonyl Ligands Lost From Parent
$[Ir_4(CO)_{11}COOMe]^-$	$[Ir_4(CO)_5COOMe]^-$	**6**
$[Os_3(CO)_{11}COOMe]^-$	$[Os_3(CO)_4COOMe]^-$	**7**
$[Rh_6(CO)_{15}COOMe]^-$	$[Rh_6(CO)_8COOMe]^-$	**7**

Table 6-1 A list of the last observed cluster carbomethoxy from the CID of methoxide derivatised clusters $[Ir_4(CO)_{11}COOMe]^-$, $[Os_3(CO)_{11}COOMe]^-$, and $[Rh_6(CO)_{15}COOMe]^-$, and the difference in the number of carbonyl ligands between them.

This does not immediately seem to provide any useful evidence with which to hypothesise a unified theory for the observed threshold point in the dissociation pattern for all the clusters. Similar studies into the electron density of the parent ion

and the clusters around the threshold limit also reveal little in the way of illuminating evidence. The significance and reasons behind this threshold would become clearer after investigations into the dissociation pathway that produces the cluster hydride by FT-ICR MS.

6.5.4 Properties Of Transition Metal Carbonyl Hydrides

Hydride ligands are common in transition metal carbonyl cluster chemistry, and are able to bond to clusters in a variety of different ways, such as terminal (M-H), bridging (M-H-M, denoted as μ-H) and face-capping (denoted as μ_3-H). However, polyhedral clusters such as $Rh_6(CO)_{16}$ and $Ir_4(CO)_{12}$ contain cavities in the inner regions surrounded by the metal-metal bonds. The size and shape of the cavity is dependent upon the geometry of the metal core and the internuclear separation. An atom that occupies such a cavity is said to occupy an *interstitial* site [23]. Due to the small size of the hydrogen atom it is possible to fit it into almost any polyhedron core, and is the only atom that can be accommodated in the cavity within a tetrahedral metal core[22;24-32]. While a terminal metal-to-hydride bond can be considered to be a two centre/two electron interaction, the bond between the hydride and more than one metal atom requires the bonding to be described by a delocalised bonding structure [22;24;25]. Thus the likely formations of the transition metal carbonyl clusters produced in these experiments are given in Figure 6-19 showing a general overview of their structure and the overlap between the 1*s* atomic orbital of the hydrogen with the suitable hybrid orbitals on the metal centres.

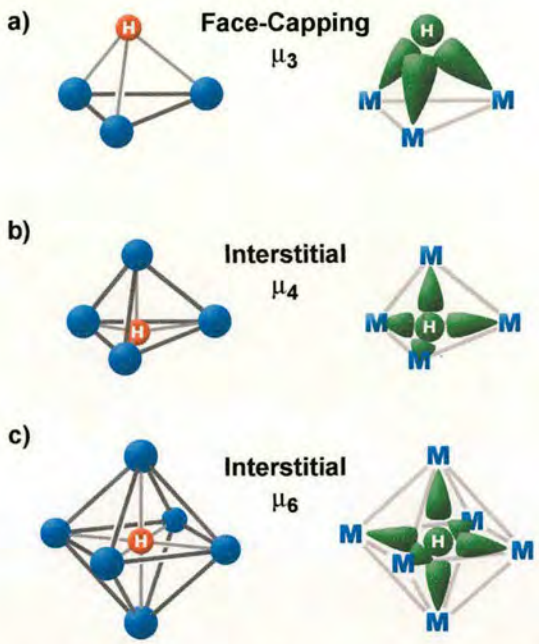

Figure 6-19 The suspected structures of the a) osmium, b) iridium, and c) rhodium carbonyl hydride anions produced from the CID experiments, including the overlap of atomic and hybrid orbitals which lead to the structure. Diagram adapted from Reference 25.

The thermal stability of the transition metal carbonyl hydrides should be reasonably good as the stability increases with the row of the metal species, with first row metal hydrides being particularly unstable. In addition, the electron-withdrawing nature of the carbonyl ligand polarises the metal-to-hydrogen bond, such that the species tend to act as acids in aqueous solution, with an activity that increases as the number of metal-to-hydrogen bonds increases. More importantly, metal hydrides are very reactive, with uses in the creation of metal hydrocarbons from the insertion of alkenes and alkynes and other agents [22], and as such have been the subject of many investigations [33-39]. Examples of the various common reactive routes are documented in Figure 6-20.

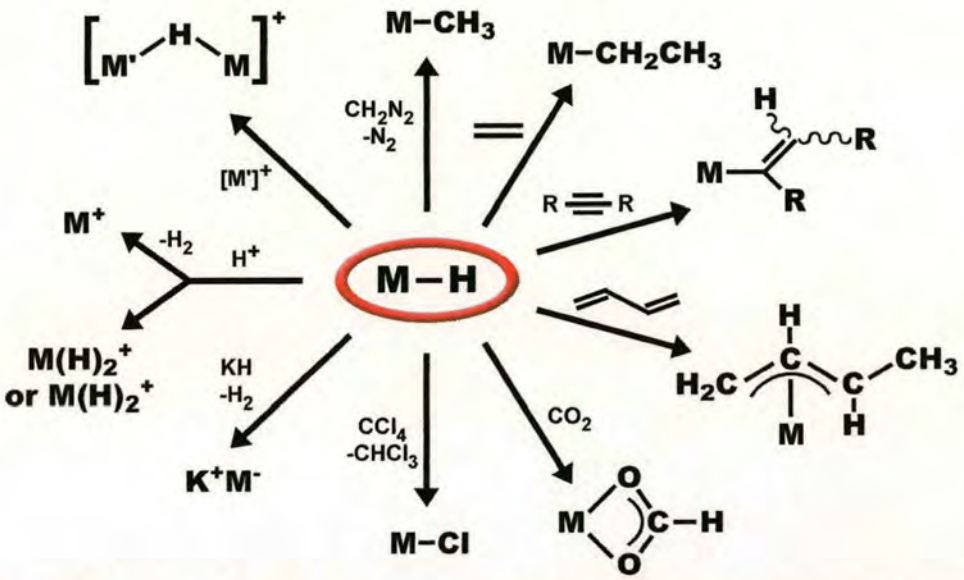

Figure 6-20 Some examples of the possible reactions that metal hydrides can undergo. Diagram adapted from Reference 22.

The insertion of carbonyl ligands into the bonds between the metal and the hydrogen has been proposed as a possible mechanism for the reduction of carbonyl to form hydrocarbons. Such a reaction is an example of the Fischer-Tropsch process, which converts mixtures of CO and hydrogen (known as "synthesis gas") into hydrocarbons:

$$nCO + 2nH_2 \longrightarrow -(CH_2)_n - + nH_2O \qquad (6\text{-}15$$

This reaction proceeds in the presence of heterogeneous metal catalysts such as iron and ruthenium under high pressure and temperature conditions. The outcome is generally a mixture of saturated and unsaturated hydrocarbons, but can also include products that incorporate oxygen, such as alcohols and esters [22]. Another possible outcome is in the water-gas shift reaction, the means by which hydrogen is produced on an industrial scale. The reaction has already been examined for the case of the iron pentacarbonyl species, where the metal hydride bind is formed from the addition of sodium hydroxide to species, as shown previously in Figure 6-18. The addition of a proton to metal hydride then leads to the formation of a hydrogen molecule from the metal. The cluster system has been able to produce the hydride cluster ion by another method (the precise mechanics of which are as yet not clear).

It can therefore be seen that the production of the metal hydride ion, while an unexpected side reaction in the CID experiments, could prove to be a potent reagent for a variety of chemical reactions. In addition, its formation shows that the transition metal carbonyl clusters are in themselves potent vehicles for the transformation of hydrocarbon species. An understanding of the metal hydride forming reaction would show exactly how this ability is realised.

6.6 Determining The Bond Dissociation Energies Of The Derivatised Cluster Ions

6.6.1 Variation Of Ion Intensity With Cone Voltage

It is known from previous discussion that the cone voltage has a tuning effect on the mass spectrum, and that at certain cone voltage values, ions of a given range of mass-to-charge will be preferentially focussed into the quadrupole at the expense of ions outwith this range. If any meaningful physical values are to be drawn from the EDESI-MS data, some attempt should be made to chart and then account for the tuning effect of the sample cone. In the absence of a tuning effect, and given constant solution flow rates, the total detected ion current should be the same for each value of the cone voltage: the same number of ions enter the source region, a number undergo dissociation reactions, and all ions then enter the quadrupole. Therefore the total number of daughter ions would be equal to the total number of parent ions that left the ion source. However, this has proven not to be the case. In addition to the tuning effect of the cone voltage, there is also the issue of the large angle scattering expected with impulsive collisions (as discussed in Chapter 4.3.5). Such scattering would reduce the number of ions entering the quadrupole if they occurred in stringent vacuum conditions. However the high pressure of bath gas within the collision region, and the forced flow of the gas along the axis of the instrument suggest that ion loss to scattering should be minimised. The tuning effect of the cone voltage sweep can be observed by summing the intensity of each ion recorded for given values of the cone voltage, plots of which can be seen for each

cluster species in Figure 6-21. Each of the derivatised sample solutions made for each cluster species have been sampled, and the curves represent the mean variation in total ion intensity with cone voltage, with the error bars representing the standard deviation.

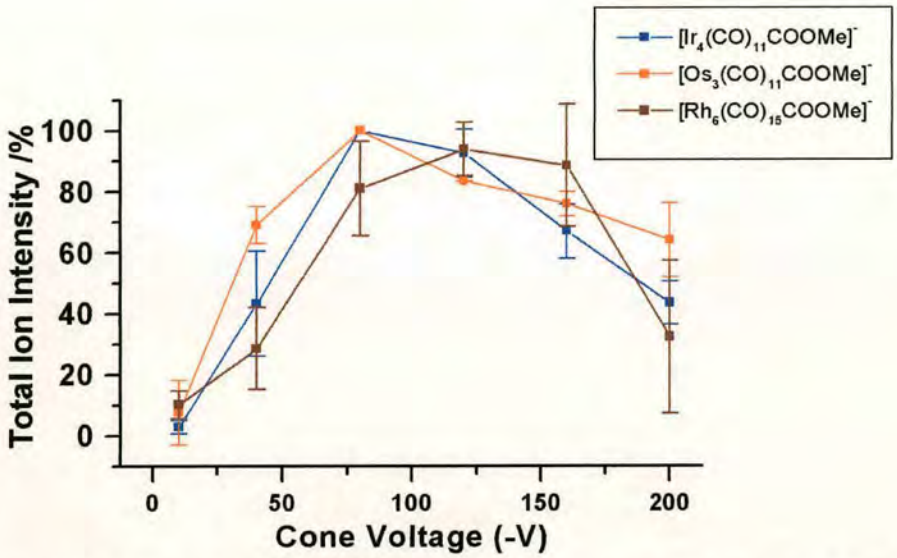

Figure 6-21 The intensity of each ion recorded at given cone voltages has been summed, and then normalised to produce curves showing the variation in ion intensity with the cone voltage. These curves thus visually represent the tuning effect of the cone voltage on ion transmission in the mass spectrometer.

In the absence of a tuning effect, the curves would be straight horizontal lines at 100%. However, the plots for the iridium, osmium, and rhodium derivatised clusters show a similar trend, forming a general curve shape over the cone voltage scale.

These curves can be used to calibrate the mass spectra, such that total ion transmission is made to be constant. The intensity plots in Figure 6-21 can be regarded as measures of ion transmission, x_i, at each cone voltage value, i, expressed as a percentage, such that $0 \leq x_i \leq 100$. The inverse of the ion transmission, defined as c_i, can be simply determined from:

$$c_i = \frac{100}{x_i} \tag{6-2}$$

This new variable, c_i, can be used as a calibration coefficient to equalise the total ion intensity over the whole cone voltage range, and thus mimicking conditions where

the molecular ion intensity is constant prior to fragmentation. Multiplying the ion intensity by c_i produces a new set of calibrated waterfall plots, with examples provided in Figures 6-22 a), b), and c) for iridium, osmium and rhodium methoxide derivatised clusters. These can be directly compared against the original waterfall plots given in Figure 6-5.

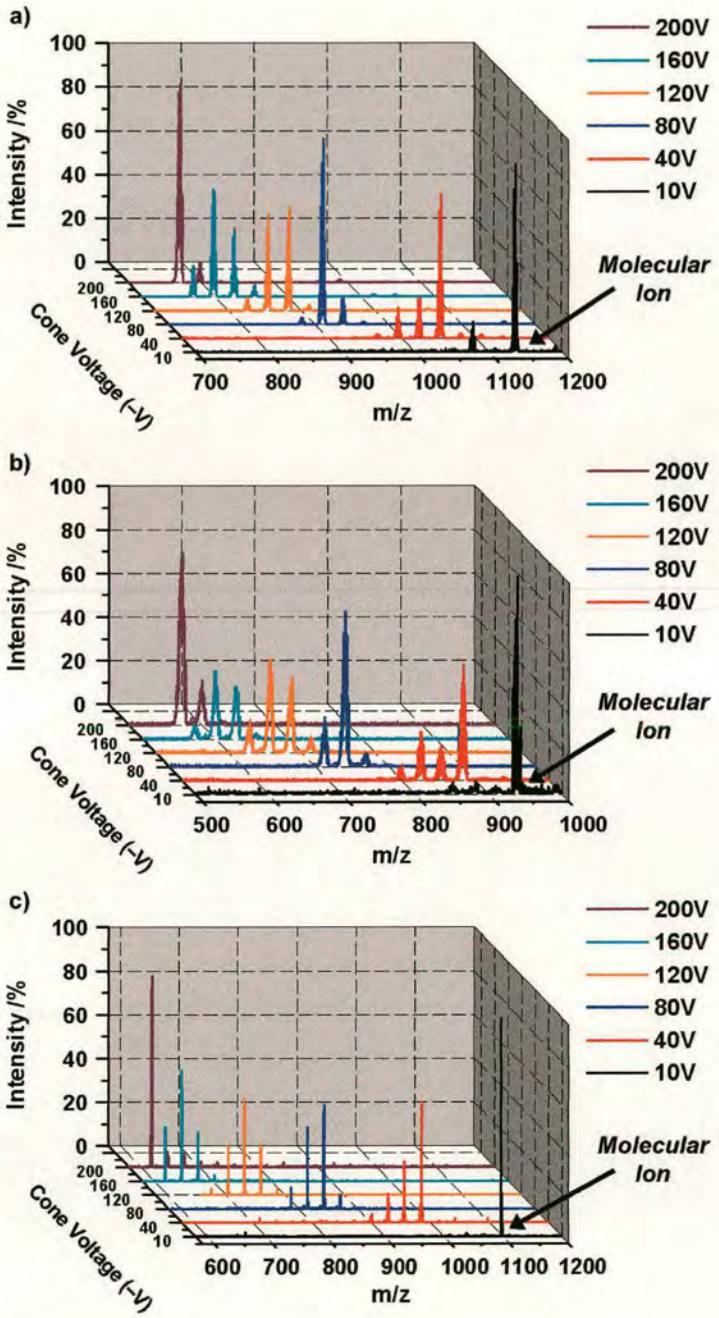

Figure 6-22 Waterfall diagrams showing the calibrated mass spectra recorded for the methoxide derivatised a) iridium, b) osmium, and c) rhodium of carbonyl clusters to mimic constant molecular ion intensity over cone voltage range.

6.6.2 Calibrating The Ion Stability Profiles

With the calibration mechanism in place, the stability profiles of all the ions recorded in the mass spectra can be calibrated. From these new plots a measure of the influence of the tuning effect on the stability profiles can be obtained by comparing those from the raw and calibrated data. Thus the stability profiles for various ions from the chromatograms of the iridium, osmium and rhodium derivatised clusters are presented in Figures 6-23 to 6-25 as scatter plots, for both the raw and calibrated. As a reminder the chromatograms were first smoothed within the MassLynx software using a mean 3-channel, 2-pass method, before being imported into Microcal Origin 5 for the fitting of Gaussian curves to all of the stability profiles.

The differences between the raw and calibrated data are most pronounced for the heavier ions (most notably the derivatised iridium molecular ion in Figure 6-23 a) which is the heaviest cluster species experimented on) produced at the early stages of the experiment with low cone voltage values. As the cone voltage is increased and the species become smaller the different datasets are observed to converge to very similar patterns. Such a result is to be expected. At low cone voltage values the electric field is very weak, such that there is little to no focussing effect of the field, and only those ions of the correct orientation will pass through the skimmer, while the rest strike the surroundings. With an increasing cone voltage the electric field becomes stronger around the skimmer and will have a greater effect on the deflection and focussing of the ions through the skimmer.

The calibration used to counter the ion focussing conditions was only concerned with equalising the ion intensity across the cone voltage range. Thus the only change made to the curves would be in their overall intensity. The relatively uniform curves used for the calibration of the data (Figure 6-21) would make it unlikely that they would drastically change the way in which the ion intensity varied with the cone voltage (i.e. make the peaks narrower or broader). However, given the observed effect of the calibration on the stability profiles, from this point only the calibrated data shall be reviewed.

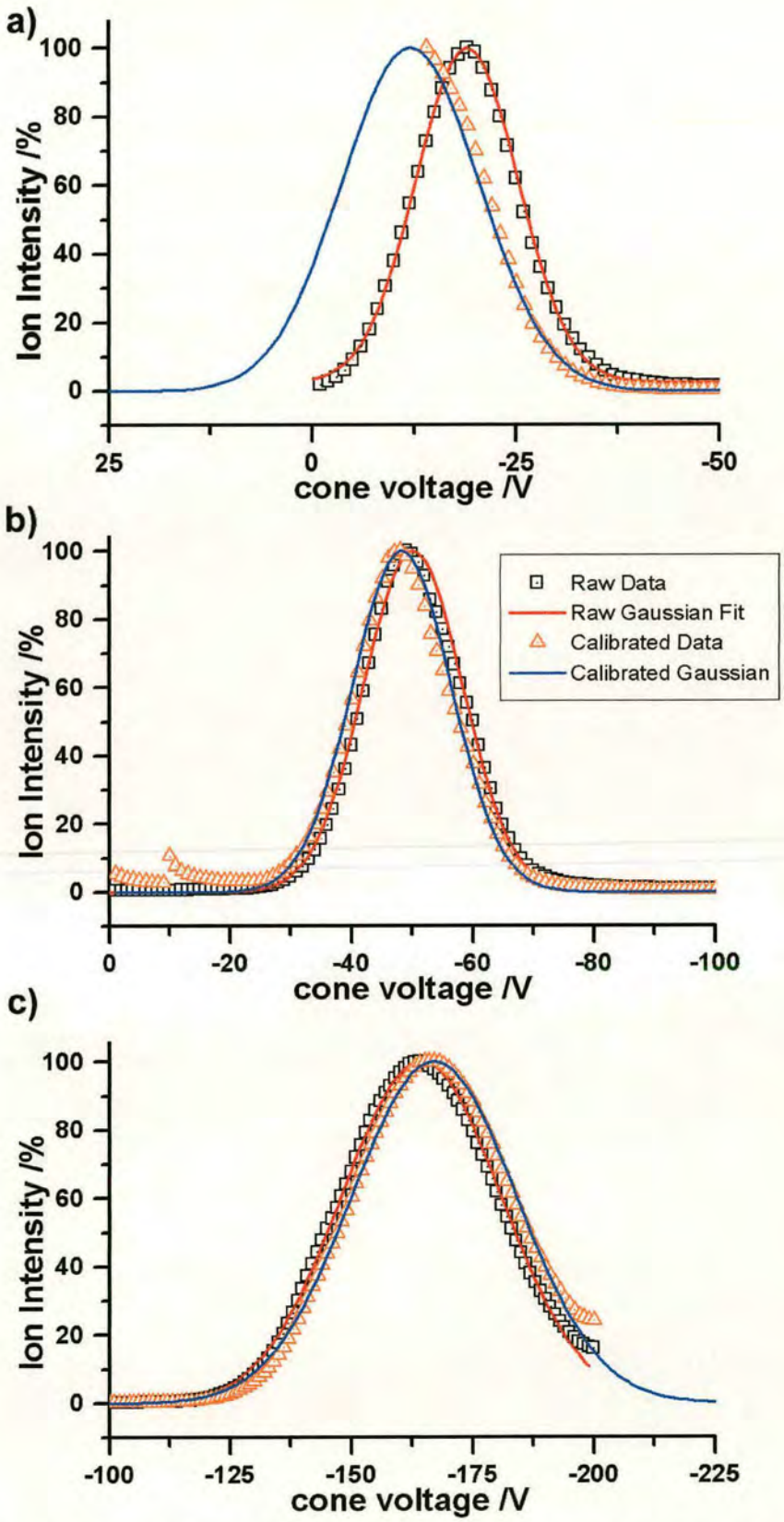

Figure 6-23 The stability profiles of a) The iridium molecular ion $[Ir_4(CO)_{11}COOMe]^-$, b) $[Ir_4(CO)_6COOMe]^-$, and c) $[Ir_4(CO)_4H]^-$.

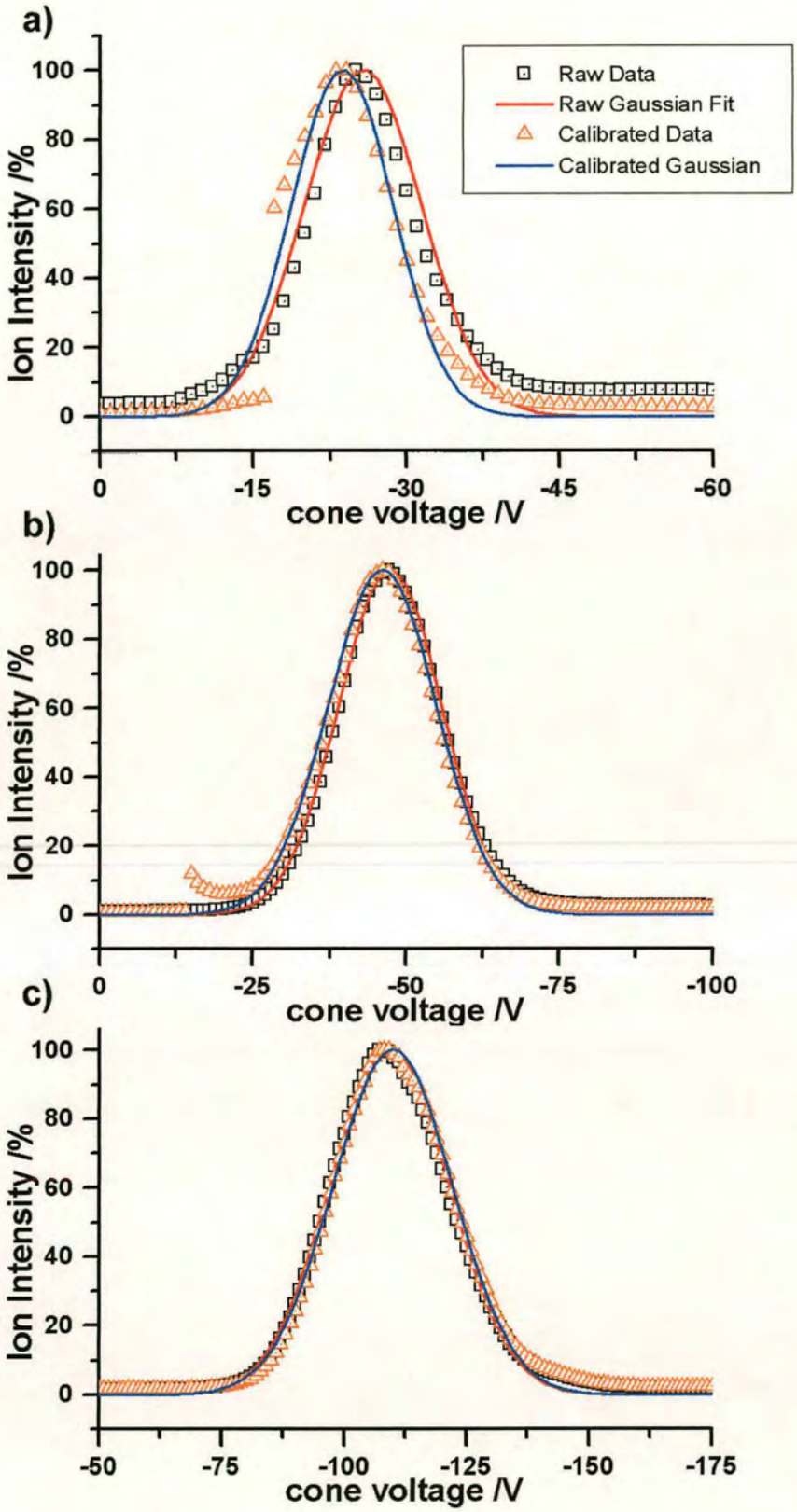

Figure 6-24 The stability profiles of a) The osmium molecular ion $[Os_3(CO)_{11}COOMe]^-$, b) $[Os_3(CO)_7COOMe]^-$, and c) $[Os_3(CO)_4H]^-$.

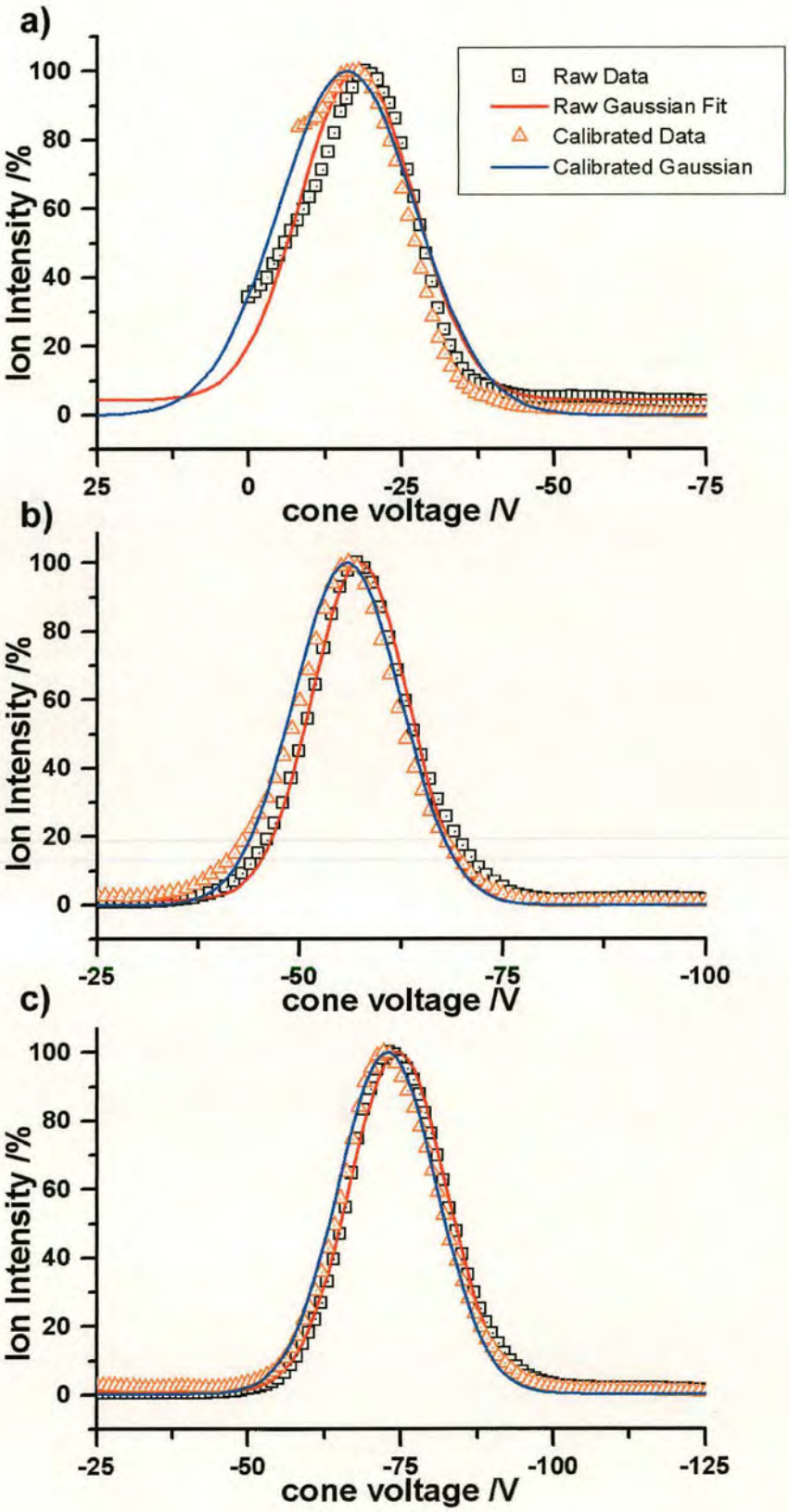

Figure 6-25 The stability profiles of a) The rhodium molecular ion $[Rh_6(CO)_{15}COOMe]^-$, b) $[Rh_6(CO)_8COOMe]^-$, and c) $[Rh_6(CO)_8H]^-$.

It was found that for the most part there seems to be a slight increase in the widths of the stability profiles as the cluster ions become smaller in both the recorded and calibrated data. At first one may imply that the breadth of such peaks is an indication of the stability of the cluster ion. Since the cone voltage provides a measure of the ion kinetic energy in the lab frame, the range over which an ion appears from its creation till its complete removal by dissociation could indicate how resilient the ion is to increasingly energetic collision conditions, with a particularly stable ion having a lifetime over a broad cone voltage range. Thus a gradual increase in the breadth of the stability profile peak as more ligands are removed would suggest that the ion is gradually becoming more stable. However, one must also account for the fact that the observed increase in the breadth of the stability curves is a factor of the assumed impulse method of activation. As discussed earlier in Chapter 6.4.4, the chance of a ligand being struck in any one collision is reduced as the ligand shell becomes smaller, with the associated reduction in collision energy transfer efficiency. Despite this, the stability profiles should provide some useful information for the determination of the thermochemistry of the cluster ions

6.6.3 Cone Voltage And Cluster Internal Energy

The principal source of ion kinetic energy, and therefore energy for the collision activation process, is confirmed as being provided by the potential gradient between the sample cone and the grounded skimmer cone. As such it would be relatively simple to determine the kinetic energy of the ions leaving the skimmer in the absence of any collisions from the value of the cone voltage and the charge on each ion. However, the ions undergo of the order of 10^5 collisions, with varying degrees of energy transfer, and there is no accurate means of determining the ion's kinetic energy beyond the skimmer cone. One could try to elucidate the energy transfer for single collision conditions by performing the experiment at different collision gas pressures and extrapolating the energy required for dissociation in each case to zero pressure, as performed by the Armentrout group as discussed in Chapter 4.3.7. Unfortunately the nature of the CID reaction within the electrospray source is such that by trying to reduce the pressure of the gas within the source region can hamper the efficiency with which the ions are desorbed from the solution droplets, and

thereby also having a detrimental effect on the resultant mass spectrum. Thus the study of the behaviour of the ions in the CID experiments is limited to the observations made from the cone voltage values at which the ions are observed.

It may be possible to calibrate the cone voltage values against known values of the metal-to-ligand bond energies. As far as we are aware, there has been very little work on determining the exact bond dissociation energies of such transition metal carbonyl complexes as those experimented on here. However, Hughes and Wade have determined average values of the bond energies for a series of transition metal carbonyl species, including those studied here, from a comprehensive study of the present thermochemical data that exist in the literature [40]. Each of these values should provide a good estimate of the bond dissociation energy for the loss of the first carbonyl ligand from the cluster, and are shown in Table 6-2. It should then be possible to calibrate the cone voltage to these values, and then extrapolate the remaining bond dissociation energies for the clusters under study. While by no means a perfect, or strictly accurate, method of determining such values it would appear to be the best available with the current data, and also at the very least provide a general estimate value for the thermodynamic data that has never been determined. It is important to realise that one cannot purely apply these energy values to the bond dissociation energies for each of the carbonyl losses from the clusters: the average energy will change with the metal-carbonyl ratio, owing to the high π-acidity of the carbonyl ligand [23]. Individual values for each of the dissociation reactions are required.

Cluster	E(M-CO) (kJ mol^{-1})	E(M-CO) (eV)
$Ir_4(CO)_{12}$	196	**2.0314**
$Os_3(CO)_{12}$	201	**2.08322**
$Rh_6(CO)_{16}$	182	**1.8863**

Table 6-2 The calculated bond dissociation energies for the cluster species under study, taken from Reference 40.

The stability profiles show the growth and decay of the ions with the cone voltage, but it is not clear which point of the curve should be considered to represent the point at which a cluster is formed from the dissociation of its parent ion. The peak of the stability profile curve represents the value of the cone voltage at which the population of the ion is greatest throughout the experiment. However, this does not necessarily represent the energy at which the ion was formed. A more likely option is the cone voltage value that corresponds to the point at which that ion first appears, which could be taken as the 10% value of the height of the stability profile curve, as demonstrated in Figure 6-26.

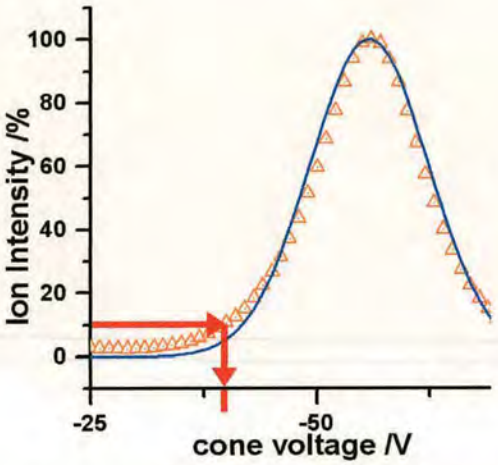

Figure 6-26 The point (in terms of energy) at which a daughter ion first appears can be extracted from the stability profile for that ion, from the cone-voltage value that corresponds to 10% of the height of that peak, as indicated.

For the sake of convenience all cone voltage values discussed from here onwards refer to those extracted from the 10% height of the stability profiles of the daughter ions. The cone voltage values can be compared with the bond dissociation energies in Table 6-2 to determine a form of "collision coefficient" for the reaction system, representative of the number of collisions experienced by a parent ion, leading to the dissociation of one carbonyl ligand. The maximum amount of energy that can be transferred in any one collision is defined by the centre-of-mass energy, and therefore the cone voltage values must be converted to the appropriate value in the centre-of-mass frame. The centre-of-mass energy can be determined from the following relationship (from Chapter 4.3.4, Equation 4.36):

$$E_c = \left(\frac{m_{N_2}}{m_I + m_{N_2}} \right) E_{LAB} = \delta E_{\max} \qquad (6\text{-}3)$$

where m_{N_2} is the mass of the neutral nitrogen molecule, and m_I is the mass of the cluster ion. Since the ions are singly charged and their kinetic energy is mostly provided by the potential difference set by the cone voltage and the grounded skimmer, the cone voltage values can be translated into the lab energies in electronvolts. Unfortunately, this can only give an insight into the collision conditions experienced by the parent ion as it dissociates its first ligand, since there is no more data on the bond dissociation energies for the removal of other ligands from the cluster. It is reasonable to expect that the bond dissociation energies shall change as the ligand shell becomes smaller due to the reduction of electron density around the metal core, and so the tabled values would not be strictly valid. Despite the fact that the collision conditions change as the cone voltage is increased and as the ligand shell decreases, this is the best means currently available to evaluate the bond dissociation energies for the complete removal of ligands from the core from the current data. In determining this collision coefficient, and applying it to the cone voltage values at which the other fragment ions appear, a useful approximation to their bond dissociation energies should be determined.

Determining The Collision Coefficient

The cone voltage values for the first produced daughter ions from the calibrated data were averaged over all three solutions for the respective cluster species, and are given in Table 6-3. Errors are determined from the standard error from the standard deviation in the determination of the average value for each ion. The energy required to produce this ion would depend upon the energy acquired by its parent. Thus the centre-of-mass energy for the collision system of the molecular ion (the ion from which the first daughter ion is formed) and the nitrogen target molecule is calculated, with the associated error determined from the equivalent translation of the standard error.

Cluster Daughter Ion	10%Peak CV	Standard Error	CM Energy (eV)	Associated Error
$[Ir_4(CO)_{10}COOMe]^-$	14.55821	2.80724	0.35111	0.0677
$[Os_3(CO)_{10}COOMe]^-$	11.14145	0.864	0.32413	0.02514
$[Rh_6(CO)_{14}COOMe]^-$	10.95586	3.36901	0.27408	0.08428

Table 6-3 The cone voltage values corresponding to the 10% peak height value from the stability profiles, and the energy of the ions of equivalent kinetic energy expressed in the centre-of-mass frame (CM energy).

A direct comparison of the centre-of mass energy and the bond calculated bond dissociation energies, is given in Table 6-4. To determine the collision coefficient, the value of the known bond dissociation energy is divided against the calculated centre-of-mass energy.

Cluster Daughter Ion	CM Energy (eV)	E(M-CO) (eV)	Collision Coefficient	Associated Error
$[Ir_4(CO)_{10}COOMe]^-$	0.35111	2.0314	**5.78568**	**1.11564**
$[Os_3(CO)_{10}COOMe]^-$	0.32413	2.08322	**6.42715**	**0.69841**
$[Rh_6(CO)_{14}COOMe]^-$	0.27408	1.8863	**6.88229**	**2.11636**

Table 6-4 Determination of the collision coefficient from which all other bond-dissociation energies can be extrapolated from the 10% peak height cone voltage values.

A better appreciation of these values can be gained by viewing them as a plot, with associated errors, for each cluster species, given in Figure 6-27.

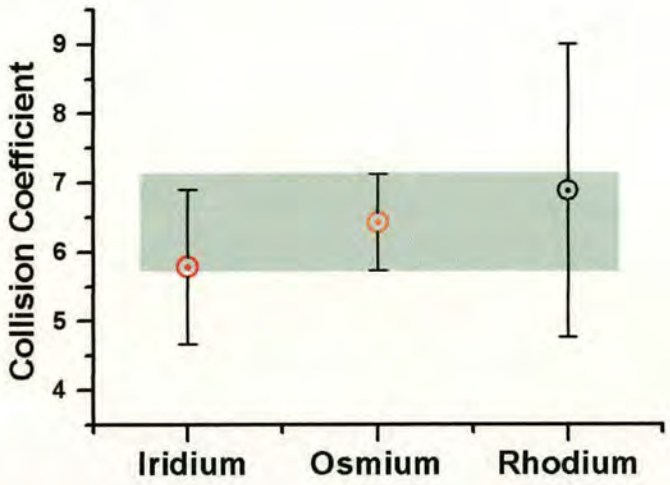

Figure 6-27 The determined collision coefficient for each cluster species with associated error bars, taken from Table 6-4.

Figure 6-27 shows that there is a good degree of similarity between the different collision coefficient values for the different cluster species, with each value lying within the boundaries of each other's error limits. Indeed, each value of the collision coefficient lies within the error limits for the osmium cluster, as indicated by the shaded area on the plot. However, one would not necessarily expect there to be a common collision coefficient between each species, since each species has its own collision conditions due to the differences in size and mass.

The collision coefficient can then be used to determine an estimate of the total energy acquired by the cluster to form specific daughter ions, relating to the higher energy collisions experienced by the molecular ion. From this data it may then be possible to extract the bond dissociation energies for the sequential removal of each ligand from the cluster. Unfortunately this relies upon a linear extrapolation from just this one point of reference to determine these energies, and cannot account for changes in collision frequency as the cone voltage increases the kinetic energy of the ions. Nevertheless, a rough estimate of the energy of the cluster system as it undergoes the CID reactions, and the overall thermochemistry of the unsaturated carbonyl clusters should be gained.

Energy Of The Cluster System During The Dissociation Reactions

Thus far reasonably it has been assumed that the dissociation reactions are sequential in nature. However, one must realise that the value of cone voltage associated with the formation of any given daughter ion does not represent the energy of the immediate parent ion as it passes the threshold for the dissociation reaction, but rather is a measure of the total energy that has been absorbed by the molecular ion as it has undergone the sequential dissociation of ligands and finally stabilised to give the current daughter ion. For example, the reaction scheme:

$$M_n(CO)_x R \xrightarrow{\partial E_1} M_n(CO)_{x-1} R \xrightarrow{\partial E_2} M_n(CO)_{x-2} R \xrightarrow{\partial E_3} M_n(CO)_{x-3} R$$

produces the daughter ion $M_n(CO)_{x-3}R$ at a cone voltage value of γ. This cone voltage value provides a measure of the energy ($\delta E_1 + \delta E_2 + \delta E_3$), and not the energy δE_3 for the reaction $M_n(CO)_{x-2} R \xrightarrow{\partial E_3} M_n(CO)_{x-3} R$. Unfortunately, the average number of collisions required to reach each energy stage, δE_1, δE_2, and δE_3 is unknown, and so the contributions of each stage to produce the final daughter ion for this sequence $M_n(CO)_{x-3}R$ cannot be accurately evaluated. Since the collision coefficient can be considered to represent an average of the collision conditions, one may be justified in taking the mean value for the individual centre-of-mass energy contributions for each sequential dissociation step to reach a given daughter ion at a given cone voltage value. Multiplying this value by the collision coefficient for the relevant cluster would then provide an estimated value for the total energy acquired by the cluster that lead to the production of that daughter ion.

Unfortunately to determine this value, the reaction path that leads to the production of each daughter ion must necessarily be known. For the principal decay channel, namely the sequential loss of carbonyl ligands, the identification of the parent ion is facile. However, a determination of the parent ion for the observed transition metal carbonyl hydride ions cannot be determined from this data, and therefore the energy contribution from each parent ion that leads to the production of the cluster hydride species cannot be determined. Only by knowing that can the energy acquired by the cluster at each stage of the dissociation reaction be evaluated.

The parent of the cluster hydride ions can be determined by tandem mass spectrometry experiments, such as those that can be performed on a Fourier-transform ion cyclotron resonance mass spectrometer. Therefore this stage of the analysis must be left until verification of the hydride formation mechanism is made from experiments performed on such an instrument, as described in Chapter 7.3.

This method of determining such thermodynamic data is not ideal. While there are certain limits placed on the equipment available, there are a number of possible means by which the accuracy of such calculations could be improved. The most fundamental of these is a calibration of the energy scale by using EDESI-MS to observe the points of dissociation for species with known bond-dissociation energies. A suitable test subject is iron pentacarbonyl, which has had its bond-dissociation energies evaluated by laser pyrolysis [41] and low energy collisional activation of the protonated form $HFe(CO)_n^+$ [42]. From this a more accurate scale of cone voltage and real energy transfer could be constructed. Unfortunately there was insufficient time to perform such a calibration, and so the subsequent analysis is dependent upon the current calibration.

6.7 Conclusion

The technique of energy dependent electrospray ionisation mass spectrometry has produced stable, small-scale unsaturated transition metal carbonyl clusters, to the extent that a cluster with a given size of ligand shell can be produced at will. From these experiments there has been some indication of the ability of these transition metal carbonyl clusters to interact with hydrocarbons, making and breaking bonds, which has lead to the formation of the hydrides from the originally carbomethoxy ligand bearing cluster. As yet the precise mechanism for this reaction is unknown. Despite this it has been shown that it is possible to produce stable, unsaturated and hence reactive small transition metal clusters, a feat that was thought to be unlikely due to the strong stabilising influence of the carbonyl ligands on clusters of this size

By using available data on the bond energies of the metal-carbonyl bond for the cluster species under study here, it is hoped to correlate the initial laboratory frame kinetic energy of the ions prior to undergoing multiple activating collisions to the energy available to the species within the centre-of-mass frame, but this step first requires knowledge of the reaction mechanism by which the cluster hydride ions are formed from the cluster carbomethoxy ions. From this data it may then be possible to extract the threshold energies required for the formation of each of the cluster fragments detected.

6.8 Reference List

1. Dyson, P. J.; Johnson, B. F. G.; McIndoe, J. S.; Langridge-Smith, R. R. *Rapid Communications In Mass Spectrometry.* **2000**, *14*, 311-313.

2. Dyson, P. J.; Feeder, N.; Johnson, B. F. G.; McIndoe, J. S.; Langridge-Smith, P. R. R. *Journal Of The Chemical Society-Dalton Transactions* **2000**, 1813-1815.

3. Dyson, P. J.; Hearley, A. K.; Johnson, B. F. G.; McIndoe, J. S.; Langridge-Smith, P. R. R.; Whyte, C. *Rapid Communications In Mass Spectrometry* **2001**, *15*, 895-897.

4. Dyson, P. J.; Hearley, A. K.; Johnson, B. F. G.; Khimyak, T.; McIndoe, J. S.; Langridge-Smith, P. R. R. *Organometallics.* **2001**, *20*, 3970-3974.

5. Katta, V.; Chowdhury, S. K.; Chait, B. T. *Journal Of The American Chemical Society.* **1990**, *112*, 5348-5349.

6. Hao, C.; March, R. E.; Croley, T. R.; Smith, J. C.; Rafferty, S. P. *Journal Of Mass Spectrometry.* **2001** , *36*, 79-96.

7. Henderson, W.; McIndoe, J. S.; Nicholson, B. K.; Dyson, P. J. *Chemical Communications* **1996**, 1183-1184.

8. Henderson, W.; McIndoe, J. S.; Nicholson, B. K.; Dyson, P. J. *Journal of the Chemical Society, Dalton Transactions* **1998**, 519-525.

9. Butcher, C. P. G.; Dyson, P. J.; Johnson, B. F. G.; Khimyak, T.; McIndoe, J. S. *Chemistry-A European Journal* **2003**, *9*, 944-950.

10. Butcher, C. P. G.; Dyson, P. J.; Johnson, B. F. G.; Langridge-Smith, P. R. R.; McIndoe, J. S.; Whyte, C. *Rapid Communications In Mass Spectrometry* **2003**, *16*, 1595-1598.

11. Dyson, P. J.; Johnson, B. F. G.; McIndoe, J. S.; Langridge-Smith, R. R. *Rapid Communications In Mass Spectrometry* **2000**, *14*, 311-313.

12. www.waters.com . 2003.

13. Micromass *Platform II Users Guide*.

14. Fenn, J. B.; Mann, M.; Meng, C. K.; Wong, S. F. *Mass Spectrometry Reviews.* **1990**, *9*, 37-70.

15. Douglas, D. J. *Journal Of Physical Chemistry* **1982**, *86*, 185-191.

16. Stark, J. G.; Wallace, H. G. *Chemistry Data Book*, 2nd Edition in SI ed.; John Murray (Publishers) Ltd: London, 2001.

17. Adams, D. M.; Taylor, I. D. *Journal Of The Chemical Society Faraday Transactions.* **1982**, *78*, 1573-1579.

18. Adams, D. M.; Taylor, I. D. *Journal Of The Chemical Society Faraday Transactions.* **1981**, *78*, 1561-1571.

19. Atkins, P. W. *Physical Chemistry*, 6th ed.; Oxford University Press: 1998.

20. Cooper, H. J.; Derrick, P. J.; Jenkins, H. D. B. *Journal Of Physical Chemistry* **1993**, *97*, 5443-5444.

21. Uggerud, E.; Derrick, P. J. *Journal Of Physical Chemistry* **1991**, *95*, 1430-1436.

22. Bochmann, M. *Molecular Organometallics 1 Complexes with Transition Metal-Carbon σ-Bonds*, 3rd ed.; Oxford University Press: Avon, 1999.

23. Chini P.; Longoni, G.; Albano, V. G. 1974; pp. 285-344.

24. Dyson, P. J.; McIndoe, J. S. *Transition Metal Carbonyl Cluster Chemistry*, Gordon and Breach Science Publishers: 2000.

25. Housecroft, C. E. *Metal-Metal Bonded Carbonyl Dimers and Clusters*, 1st ed.; Oxford University Press Inc.: New York, 1995.

26. Baumann, W. G. *Journal of the Less Common Metals* **1982**, *88*, 245-250.

27. Cribb, P. H.; Nordholm, S.; Hush, N. S. *Chemical Physics* **1980**, *47*, 135-149.

28. Fukai, Y. *Journal of the Less Common Metals* **1991**, *172-174*, 8-19.

29. Norskov, J. K.; Besenbacher, F. *Journal of the Less Common Metals* **1987**, *130*, 475-490.

30. Opitz, C.; Grunler, B.; Muller, H. *Journal of the Less Common Metals* **1987**, *128*, 73-77.

31. Schober, H. R.; Stoneham, A. M. *Journal of the Less Common Metals* **1991**, *172-174*, 538-547.

32. Stott, M. J. *Journal of Nuclear Materials* **1978**, *69-70*, 157-175.

33. Backvall, J. E. *Journal of Organometallic Chemistry* **2002**, *652*, 105-111.

34. Dedieu, A. *Abstracts of Papers of the American Chemical Society* **1988**, *195*, 14-HYS.

35. Elkind, J. L.; Armentrout, P. B. *Inorganic Chemistry* **1986**, *25*, 1078-1080.

36. Hoskin, A. J.; Stephan, D. W. *Coordination Chemistry Reviews* **2002**, *233*, 107-129.

37. King, R. B.; Ohene, F. *Annals of the New York Academy of Sciences* **1983**, *415*, 135-147.

38. King, R. B. *Coordination Chemistry Reviews* **2000**, *200*, 813-829.

39. Srivastava, R. S. *Applied Organometallic Chemistry* **1993**, *7* , 607-611.

40. Hughes, A. K.; Wade, K. *Coordination Chemistry Reviews* **2000**, *197*, 191-229.

41. Lewis, K. E.; Golden, D. M.; Smith, G. P. *Journal Of The American Chemical Society.* **1984**, *106*, 3905-3912.

42. Ekeberg, D.; Hagen, S. I.; Hvistendahl, G.; Schulze, C.; Uggerud, E.; Vedde, J. *Organic Mass Spectrometry* **1993**, *28*, 1547-1554.

43. Whetten, R. L.; Cox, D. M.; Trevor, D. J.; Kaldor, A. *Surface Science* **1985**, *156*, 8-35.

7 Fourier Transform Ion Cyclotron Resonance Mass Spectrometry of Transition Metal Carbonyl Clusters

7.1 Introduction

The previous experiments have revealed interesting data on the reactivity of transition metal carbonyl clusters in laser fields and collision-induced dissociation conditions. However, the capabilities of the mass spectrometers used in the experiments were limited in terms of experimental scope and resolution. Fourier-transform ion cyclotron resonance mass spectrometry offers many more experimental options for the study of clusters, such as tandem mass spectrometry, and a much higher resolution. The higher resolution allows the unambiguous assignment of high nuclearity supracluster species, something that was made more complicated within the time-of-flight mass spectrometer.

Each of the experiments performed so far in this thesis can be performed on a FT-ICR MS instrument, albeit in a slightly modified form, hopefully allowing us to further probe the data already accumulated. In the laser-induced aggregation experiments, the problems with low-resolution at higher masses should be eradicated. In addition, it is possible to probe the stability of the formed supraclusters under infrared laser conditions. Secondly, further collision-induced dissociation experiments can be performed to determine the reaction path that leads to the formation of the observed cluster hydride anions from the methoxide derivatised transition metal cluster precursors.

7.2 Laser-Induced Cluster Aggregation On FT-ICR MS

7.2.1 The Bruker® Apex II™ Fourier Transform Ion Cyclotron Resonance Mass Spectrometer

The experiments were performed on a Bruker® Apex II™ instrument at the Bruker facility in Bremen, Germany, by supervisor Dr. Pat Langridge-Smith with the assistance of Dr. Gokhan Baykut and Dr. Mathias Witt. The instrument was

equipped with a seven Tesla, actively shielded superconducting magnet. A general schematic of the instrument is provided in Figure 7-1.

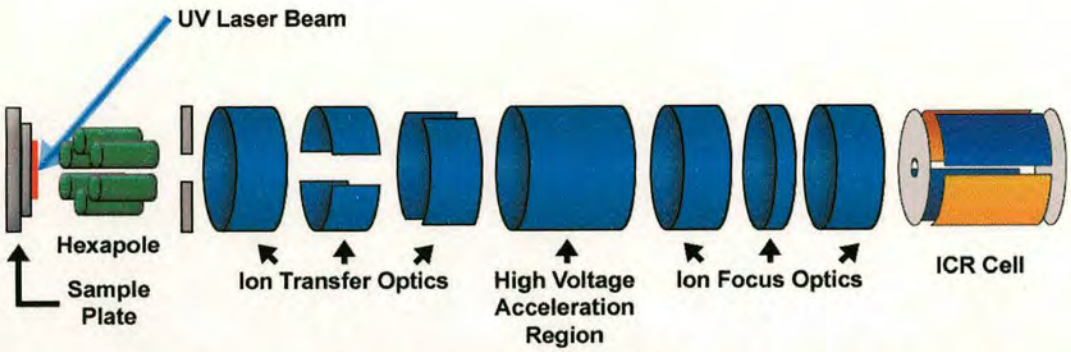

Figure 7-1 The basic components of the Bruker® Fourier-transform ion cyclotron resonance mass spectrometer. Adapted from Bruker Training Materials [1].

The instrument was also host to a prototype of the new MALDI Scout 100 source, depicted in Figure 7-2.

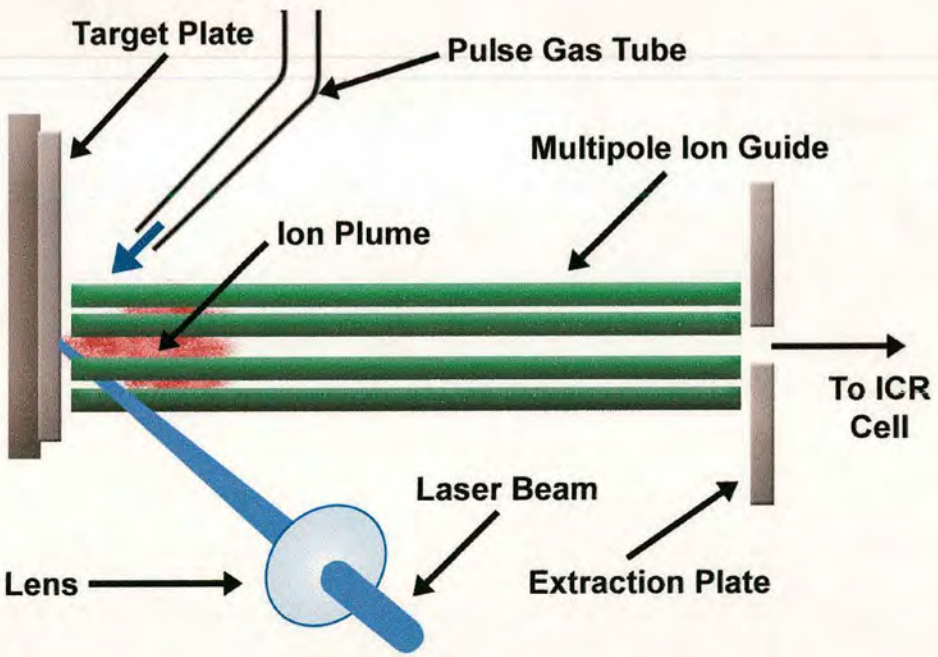

Figure 7-2 Schematic diagram of prototype MALDI source. Diagram adapted from Reference 2.

The source consists of the metallic sample plate, a nitrogen laser of wavelength 337nm (provided by Laser Science Inc.®), and a 6cm long hexapole for ion

accumulation. The method by which the mass spectrometer works requires one compact packet of ions to enter the cell at a time for analysis. The product of several laser shots, between ten and thirty, were accumulated in the hexapole, before the hexapole was flushed and the ion packet sent through the ion optics into the ICR cell. This was achieved by applying a 3kV potential to the sample plate [3].

A neutral inert bath gas (argon) was injected into the hexapole cell using a pulsed valve. Its purpose is to promote energy quenching collisions between the excited product ions from the laser irradiation. The pressure within the source chamber near to the target plate was approximately 10^{-2} mbar [3]. Thus the ions should be significantly cooled to stable levels, assisting cluster formation by quenching and hopefully eradicating the occurrence of post-source decay (although such an occurrence would not be detected by the instrument). The hexapole acts as a linear multipole ion trap, and so the ions are constrained to specific patterns of motion within the hexapole (similar to that of ions within a linear quadrupole, as described in Chapter 3.5.2). As such reactive ion-molecule collisions within the hexapole are precluded, so cluster aggregation within the hexapole is also precluded. Thus there is a time delay of the order of microseconds between the laser shots and the application of the RF field to allow cluster formation to occur.

Ion Transfer Optics

The ion transfer optics normally requires continuous tweaking to get the best output from the mass spectrometer. The values of the potentials applied to the many of ion transfer electrostatic lenses within the instrument were varied through the experiments to produce the best quality output. Such tuning had little effect on the actual processes that were of importance to this work, and so their values have not been documented here.

Sample Preparation

Clusters species $Ir_4(CO)_{12}$ and $Os_3(CO)_{12}$ were available for use in these experiments. The sample preparation procedure is the same as that for the laser

desorption ionisation experiments in Chapter 5. Dichloromethane was used as the solvent, and evaporative layers built up onto the sample plate.

7.2.2 Results of Laser-Induced Cluster Aggregation

Once again, the products of the positive ion clusters were disappointing, showing only sporadic cluster formation. Fortunately the negative ion spectra show evidence of a denser population of supracluster ions. Thus all the reported results are of negatively charged cluster species.

Laser-Induced Aggregation Of $Ir_4(CO)_{12}$

An example of a mass spectrum of the clusters generated by the laser-induced aggregation of $Ir_4(CO)_{12}$ is given in Figure 7-3.

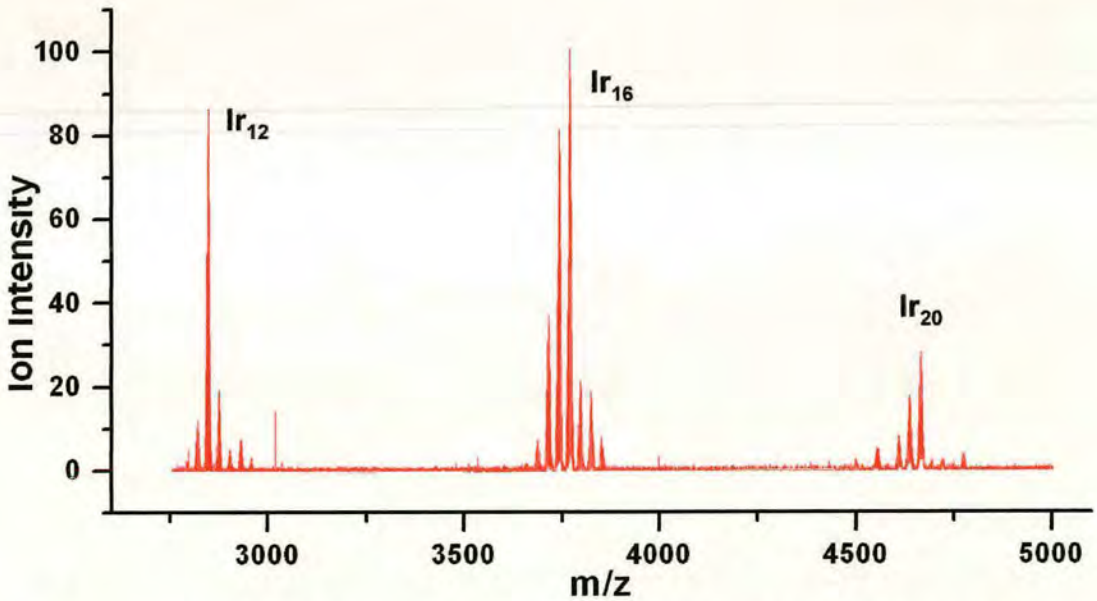

Figure 7-3 LDI-FTICR mass spectra produced from the aggregation of the $Ir_4(CO)_{12}$ precursor.

The increased resolution of the FT-ICR instrument allows us to instantly differentiate the peaks pertaining to the different sizes of ligand shell for each size of cluster core. The mass spectrum shows that the iridium cluster aggregates through the addition of intact precursor cluster metal cores, similar to clustering mechanism observed for the

rhodium precursor $Rh_6(CO)_{16}$ in the time-of-flight experiments of Chapter 5. There are several similarities between the rhodium and iridium cluster precursors: both iridium and rhodium are d^8 metals, and the cluster core is a three-dimensional polyhedron. However, the iridium cluster precursor is much closer in size to the trigonal osmium precursor, which has been shown to fragment under ultraviolet laser conditions in the time-of-flight experiments. Therefore a more direct comparison between the aggregation of the iridium and osmium clusters can be made to determine why it is that the osmium cluster fragments.

The average metal-metal bond strength in an iridium carbonyl system has been determined to be the same as that for osmium: 130 $kJmol^{-1}$ [4]. The iridium cluster precursor is a three-dimensional polyhedral structure, similar to the rhodium cluster precursor, such that there exists more metal-metal bonds than osmium: each iridium atom is bound to three others in the tetrahedral geometry in comparison to the two of osmium. In addition the iridium cluster precursor will have access to a slightly larger array of internal energy modes in which it can store energy, due to the presence of the additional metal atom in the core. It is difficult to determine precisely the relative importance that each of these factors plays in the increased stability of the iridium cluster precursor over the osmium, but one would reasonably conjecture that they are they most fundamental of reasons for seeing the three-dimensional core structures of iridium and rhodium remain intact under exposure to ultraviolet radiation of this wavelength, whereas the planar osmium can be fragmented.

Figures 7-4, 7-5 and 7-6 shows the Ir_{12}, Ir_{16}, and Ir_{20} clusters in more detail. The individual isotope contributions can instantly be observed, due to the high resolution of the mass spectrum over this range. The high resolution aids in the unambiguous identification of each of the cluster ion species and the size of their ligand shells.

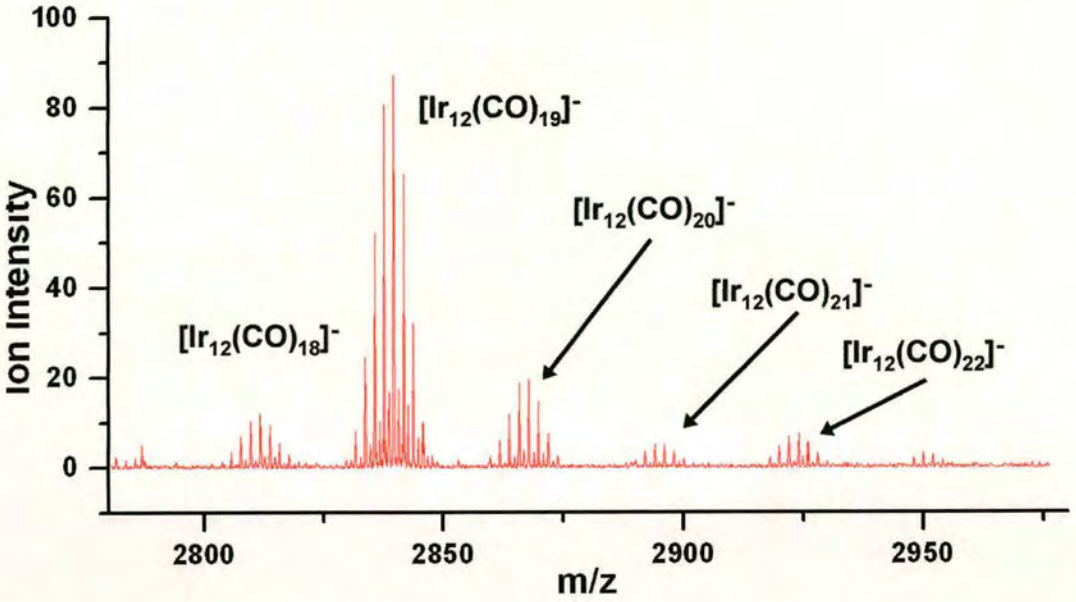

Figure 7-4 A close up of the Ir_{12} clusters from the spectrum in Figure 7-3.

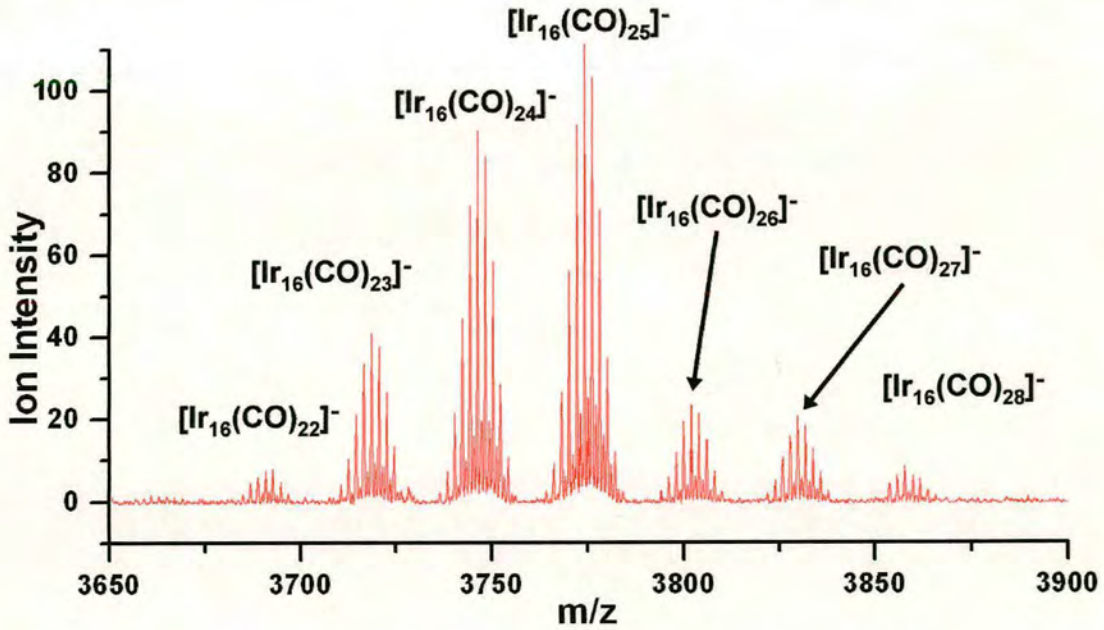

Figure 7-5 A close up of the Ir_{16} clusters from the spectrum in Figure 7-3.

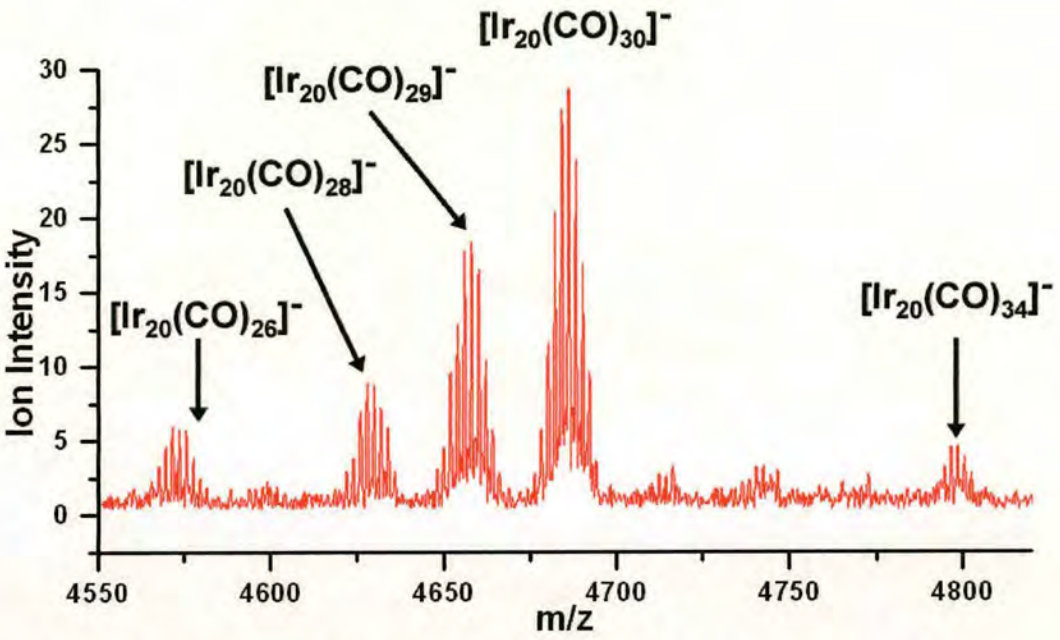

Figure 7-6 A close up of the Ir_{20} clusters from the spectrum in Figure 7-3.

As before in the time-of-flight data given in Chapter 5.4.2 the ratio of the ligand to metal nuclearity can be seen to gradually decrease with increasing metal nuclearity. The iridium cluster growth is not as prolific as that observed for the rhodium cluster in Chapter 5, which could be observed to grow up to ten times their original size. The iridium clusters on the other hand, are observed only to grow to five times their original size. Possible reasons are more likely to reside with the different conditions within the ion sources of the two instruments where the cluster growth occurs, as opposed to any physical differences and limitations posed to aggregation by the chemical properties of the cluster precursors.

Laser-Induced Aggregation Of $Os_3(CO)_{12}$

The clusters generated from the osmium cluster precursor displayed a variety of metal nuclearities, suggesting that once more the precursor had been fragmented within the source region of the mass spectrometer. While the wavelength of the incident laser beam was identical to that used in the earlier laser-induced cluster generation experiments, the conditions within the ion source were slightly different due to the presence of the inert cooling gas and different residence times within the laser focus. Evidently such factors did not have a significant effect against the

factors necessary to promote the fragmentation of the cluster core. However, the addition of the hexapole and the cooling gas did have an effect regarding the extent of cluster formation observed. Within the FT-ICR MS system the aggregation of the precursors has been more prolific, generating a larger array of supraclusters. An example of the typical mass spectra recorded for the osmium clusters is given in Figure 7-7. The designation of the peaks has been confirmed by isotope modelling.

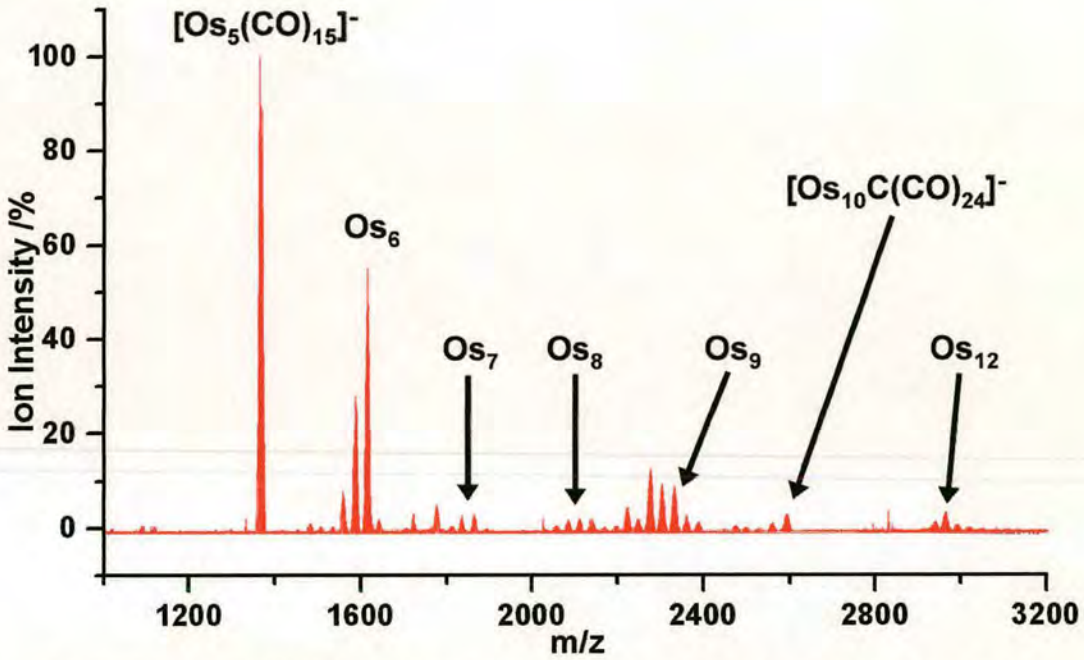

Figure 7-7 LDI-FTICR mass spectra produced from the aggregation of the $Os_3(CO)_{12}$ precursor.

Although the mass spectrum is dominated by the smaller clusters (Os_5 and Os_6), the resolution of the FT-ICR MS instrument allows the full examination and verification of the identity of the other cluster peaks, something that was just not possible on the time-of-flight mass spectrometer. Figures 7-8 to 7-11 show the various clusters detected with core nulcearities of 6, through to 12 respectively and the different sizes of ligand shells. This form of clustering has been observed in the pyrolysis of $Os_3(CO)_{12}$ at 200°C, which produces such neutral clusters as$Os_4(CO)_{13}$, $Os_5(CO)_{16}$, $Os_6(CO)_{18}$ and the carbide $Os_8C(CO)_{24}$ [5].

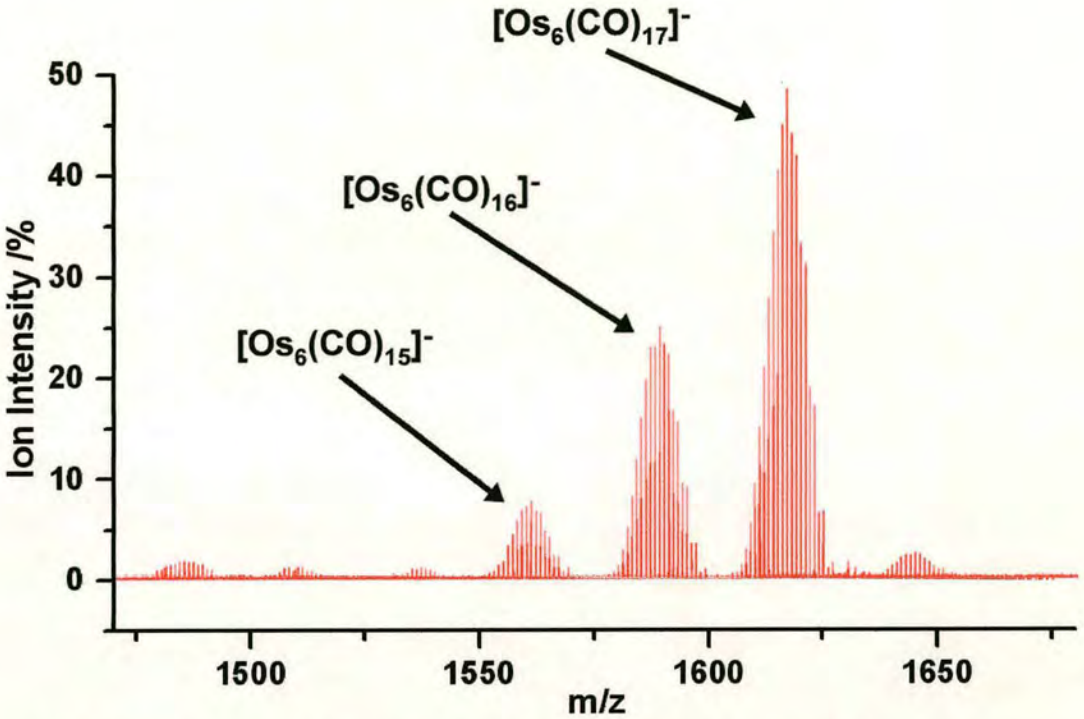

Figure 7-8 The clusters recorded with a core nuclearity of 6 osmium atoms.

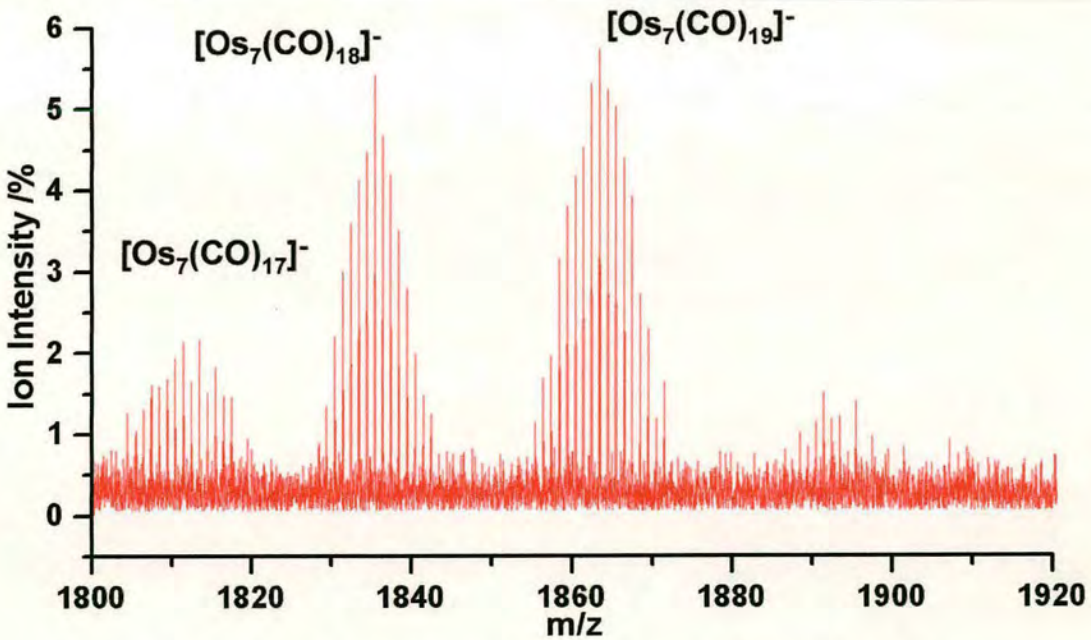

Figure 7-9 The clusters recorded with a core nuclearity of 7 osmium atoms.

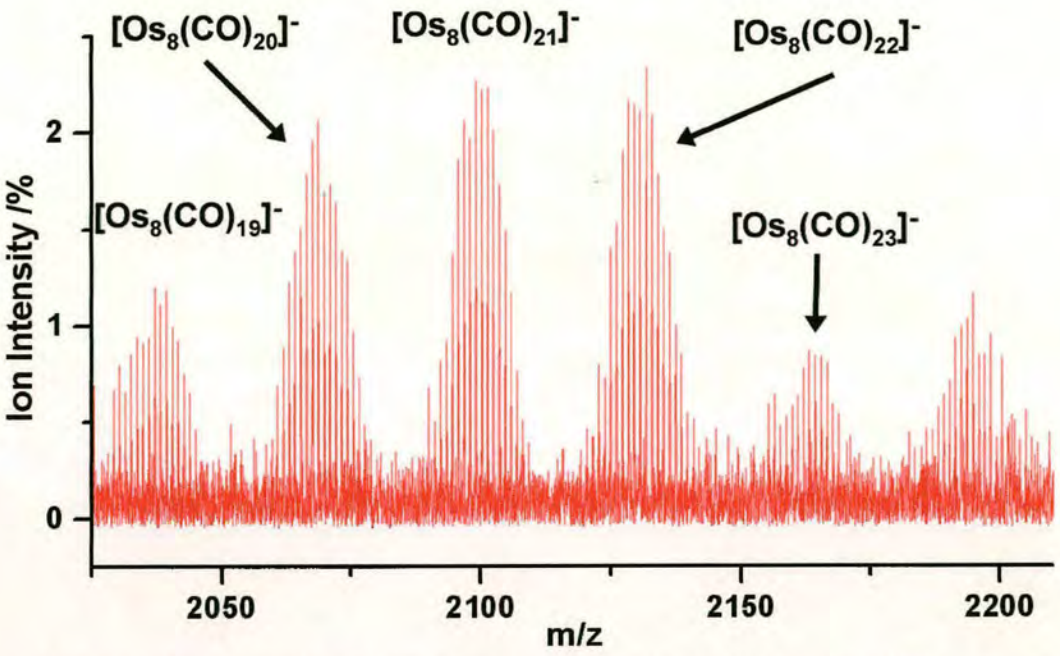

Figure 7-10 The clusters recorded with a core nuclearity of 8 osmium atoms.

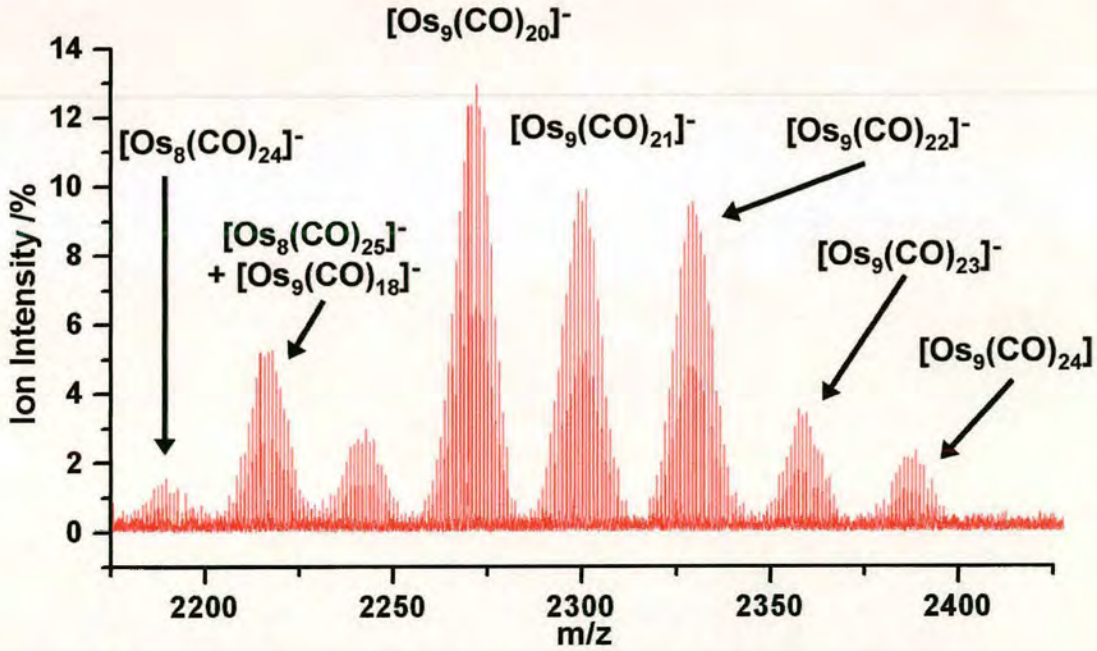

Figure 7-11 The clusters recorded with a core nuclearity of 9 osmium atoms.

At this point there appears a standalone cluster with a metal nuclearity of 10 osmium atoms. While such a cluster may not be unexpected given the current experimental results, the peak can be attributed to a carbide cluster ion, $[Os_{10}C(CO)_{24}]^-$. The peak is shown in Figure 7-12, alongside an isotope model for this cluster generated by the

Xmass software. It can be seen that the recorded mass spectrum is in excellent agreement with the isotope model, to within nearly ten parts per million absolute agreement. The production of this ion is very interesting, since the production of the singly charged $[Os_{10}C(CO)_{24}]^-$ has not knowingly been recorded before, and has not been generated by any synthetic method. A dianionic form of the cluster can be produced from the pyrolysis of $Os_3(CO)_{10}(NCMe)_2$ at around 280^0C, stabilised in the solid state with Ph_3PNPPh_3 (represented by $[PPN]^+$), such that it has the form of $[PPN]_2[Os_{10}C(CO)_{24}]$, [6-8]. The dianionic species has been crystallographically identified as a tetracapped carbide-centred octahedron (where the carbon atom occupies an interstitial site, similar to the cluster hydrides observed in the EDESI experiments in Chapter 6.5.4), although it is not clear from the current mass spectrum whether the singly charged analogue has the same structure. The difference in charge and the different methods of synthesis could produce different structures, especially given the very rapid heating that occurs with laser irradiation in comparison to pyrolysis.

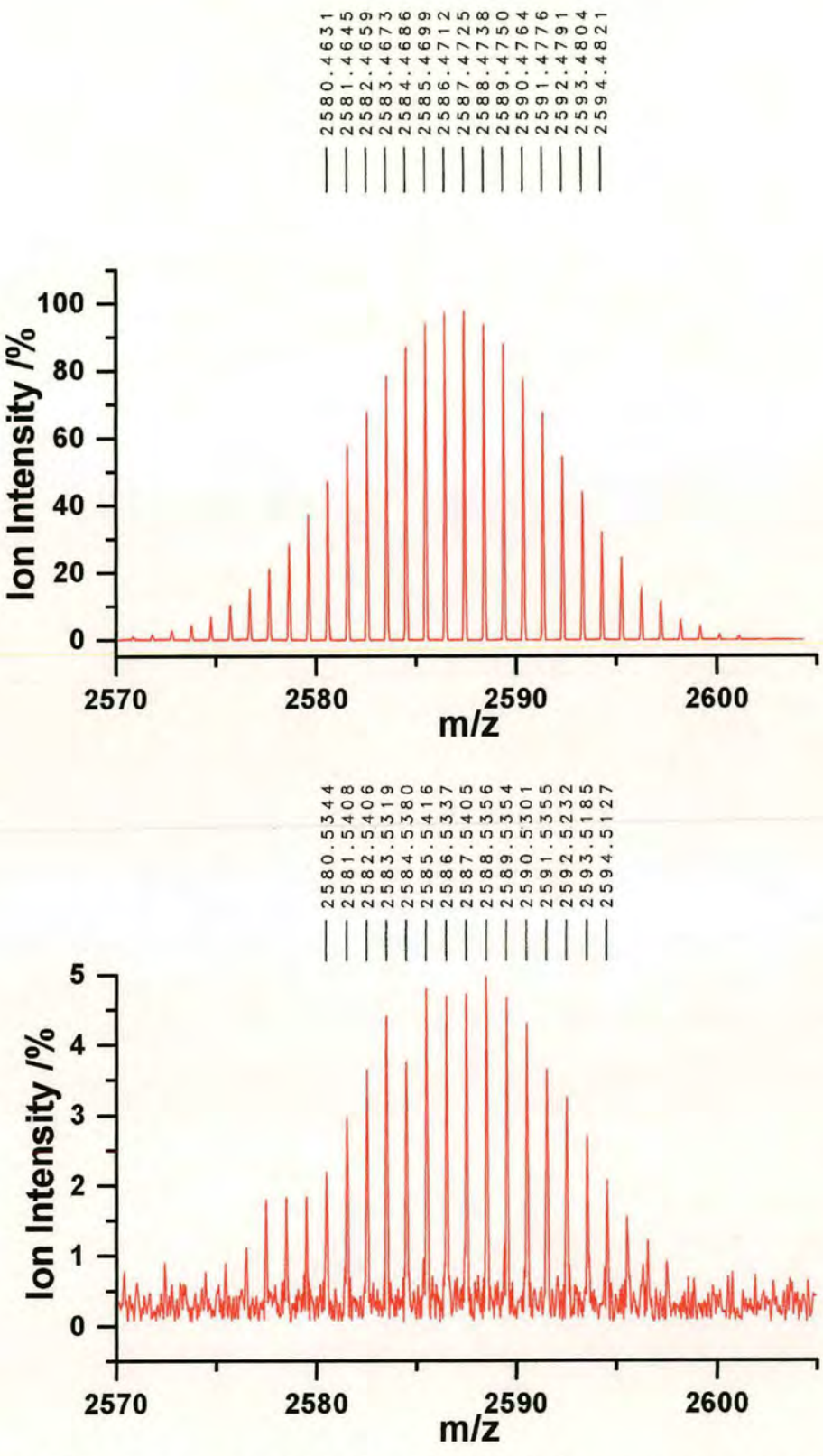

Figure 7-12 An isotope model (top) and the recorded mass spectrum (bottom) of the osmium carbide cluster $[Os_{10}C(CO)_{24}]^-$.

The formation of transition metal carbonyl cluster carbides is quite a common occurrence via a number of different reaction systems involving the thermolysis or refluxing of transition metal carbonyl clusters, but this is the first known instance of a carbide ion being formed from a neutral transition metal carbonyl cluster under laser field conditions. Metal carbides, like metal hydrides have also generated some interest in their reactivity and possible use in catalysis [9-20].

The formation mechanism itself is thought to occur from the dissociation of a carbonyl ligand, with the subsequent (or associated) loss of an oxygen atom from another carbonyl ligand to form CO_2, as given below:

$$2CO \rightarrow C + CO_2$$

The mechanism by which the carbon-oxygen triple bond is broken is thought to involve an intermediate state in which both the carbon *and* the oxygen atoms of a carbonyl ligand are bonded to the metal core, most likely along one of the vertices. This method of coordination, which can be considered as a form of bridging carbonyl ligand, weakens the carbon-oxygen triple bond to the extent that a free carbon monoxide molecule released from the cluster can react with the prone carbonyl ligand and extract the oxygen to form carbon dioxide. The remaining carbon atom can then migrate into the core of the cluster. It is a possibility that the carbide was formed from a smaller cluster species, such as Os_7, and then reacted with another cluster precursor to form the larger Os_{10} cluster. Such a mechanism would easily explain the migration of the carbon through the core, as it could simply just become surrounded by additional osmium units that react and bond to form the larger cluster. However, one would then expect to see evidence of the additional cluster carbides for the smaller metal nuclearities, but no such evidence exists. It would then seem that the decaosmium provides the correct conditions for the formation of the carbide, in terms of the size of the cluster, the geometry of the metal-metal bonds and the size of ligand shell to allow one of the ligands to bridge across the metals. While it is a possibility that more than one of the carbonyl ligands within the cluster ligand shell may be activated in the way described above, there has been no indication of the presence of multiple carbons associated with the cluster. A possible explanation is

that there would be insufficient room to accommodate two main group atoms within the core polyhedron.

To further enforce the potency of laser-induced cluster aggregation as a means to produce novel materials, there were clear examples of dodecaosmium supraclusters of various different ligand shell sizes. There has been no evidence in the literature to suggest that such species have ever been produced previously. From the mass spectrum these clusters would appear to be stable (at least in comparison to the other clusters produced). Therefore this is the first ever recording of a homoleptic dodecaosmium cluster, and within one single mass spectrum is conclusive evidence of the "exotic" conditions within the laser field, conducive for the production of novel species that are unattainable in standard laboratory synthetic processes.

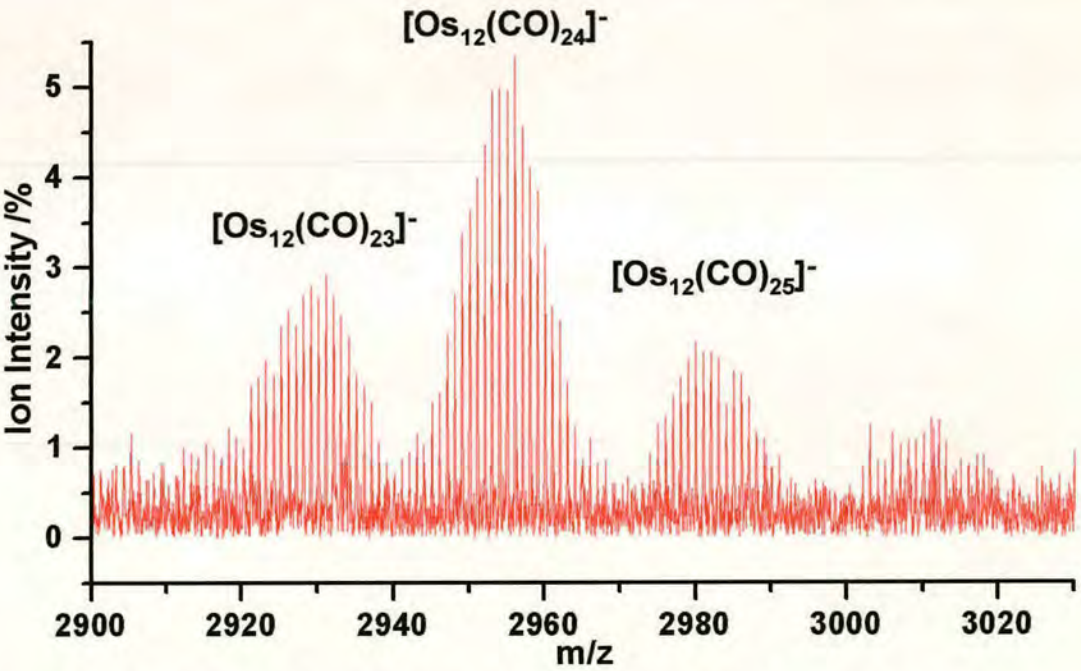

Figure 7-13 The clusters recorded with a core nuclearity of 12 osmium atoms.

The production of these new species is all very well, but they have no practical use within the mass spectrometer. Fortunately methods do exist for the collection and extraction of clusters generated in this way for further testing outside of the mass spectrometer. One of the leading figures in this field is Christopher Binns at the

University of Leicester. Using apparatus very similar in nature to a time-of-flight mass spectrometer, cluster species are made to land onto a surface coated with a suitable substrate, instead of flying through to the detector and being lost. The mass selection process can be performed by tandem mass spectrometry, provided by a quadrupole for instance, or from size selection provided by suitable apertures between the cluster source and the substrate. The cluster ions are slowed prior to landing on the substrate, and altering the kinetic energy of deposition onto the substrate produces cluster surfaces with different properties. Low energy deposition (energies of around 0.1 eV/atom) lead to a sooty film of clusters that is easily removed from the surface, while a high energy deposition (energies greater than 10 eV/atom) produces a hard shiny metallic coating [21]. After collection of the clusters, the solid sample film can be removed from the mass spectrometer, allowing it to be used in a variety of different experiments to test its physical properties, from electrical conductivity to magnetic susceptibility.

7.2.3 Testing The Stability Of Clusters By IRMPD

A selection of the iridium supraclusters underwent further investigation, using the technique of infrared multiple photon dissociation (IRMPD) to probe their relative stability. A carbon dioxide laser, with a wavelength of 10.6 Å, provided the infrared radiation, which was channelled along the central axis of the ICR cell through the rear trapping electrode, as discussed in Chapter 3.5.3. A cluster ion, or selection of cluster ions, can be isolated within the ICR cell (also discussed in Chapter 3.5.3). On exposure to the infrared radiation one can then accurately observe the subsequent effect on the isolated species and draw meaningful conclusions from the results on the stability and dissociation mechanism.

The iridium cluster ion $[Ir_{12}(CO)_{19}]^-$ was isolated by SORI and exposed to 5 seconds of pulsed infrared laser shots, firing at a frequency of 10Hz, over which time no change in the ion population was observed. Therefore this particular cluster anion exhibits an extraordinary degree of stability, which could be explained by the composition of the cluster: its molecular makeup and internal energy modes make it a less efficient absorber of this wavelength of radiation than some others. The mass

spectrum of the isolated $[Ir_{12}(CO)_{19}]^-$ ion is given in Figure 7-14 as a further demonstration of the high resolution capabilities of the instrument. The resolution of the mass spectrum is in the order of 15000, measured from the ratio of the mass against mass separation ($m/\Delta m$). Each isotopic contribution can be clearly defined, with the average FWHM values for each peak being approximately m/z 0.1.

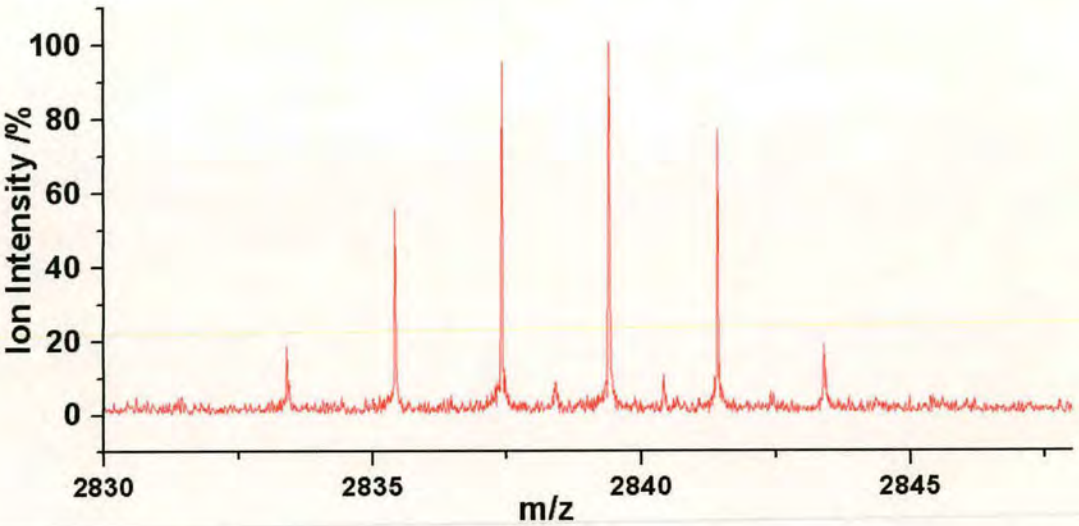

Figure 7-14 The isolated $[Ir_{12}(CO)_{19}]^-$ cluster ion, recorded with a resolution of approximately 15000.

For comparison, a small selection of Ir_{16} clusters were isolated, and exposed to similar radiation conditions. The mass spectra representing the before and after cases are given in Figure 7.15.

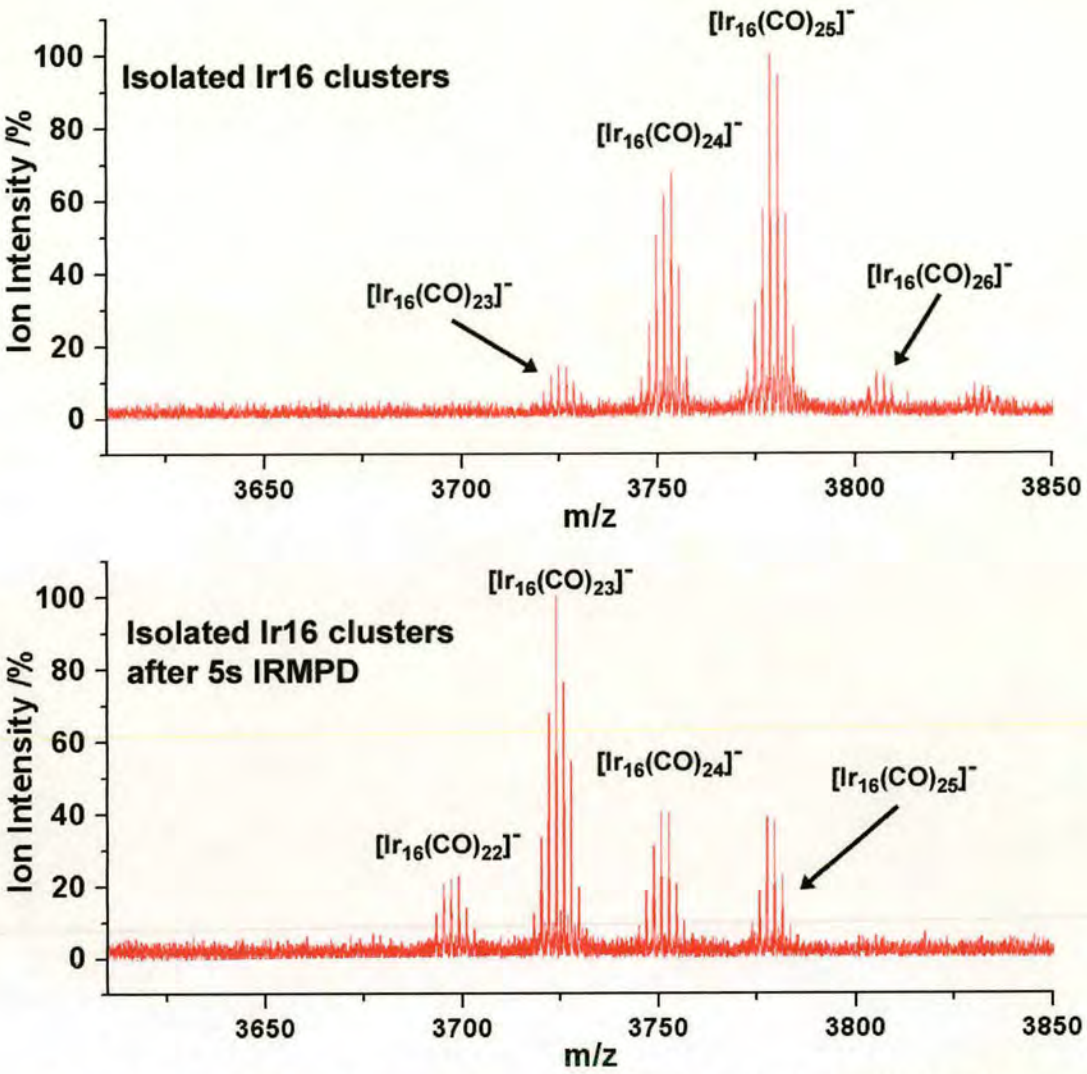

Figure 7-15 The top mass spectrum shows the iridium clusters isolated by SORI within the ICR cell. The bottom mass spectrum shows the change in the cluster population following 5 seconds of infrared irradiation.

After IRMPD there is a complete alteration in the population of ions within the cell. Thus it would appear that infrared absorption has been much more efficient for the larger Ir_{16} clusters than for the $[Ir_{12}(CO)_{19}]^-$ cluster ion. The population of cluster ions has shifted to lower masses corresponding to a reduction in the size of the ligand shell by one carbonyl ligand. This suggests that each cluster received sufficient energy from the infrared radiation to at least exceed the threshold for the dissociation of a single carbonyl ligand.

This outcome could be a direct result of changes in the photochemical properties of the two cluster species, brought about by the difference in the *d*-electron configuration of the Ir_{12} and Ir_{16} cluster cores. The additional metal atoms will produce a different separation in the highest occupied molecular orbital (HOMO) and the lowest unoccupied molecular orbital (LUMO), the main source of the optical properties of organometallic clusters. Thus it is a distinct possibility that the Ir_{16} clusters were greater absorbers of the infrared radiation than the Ir_{12}, leading to the observed dissociation reactions

7.3 Collision-Induced Dissociation on FT-ICR MS

Chapter 6 was left at an impasse. The collision-induced dissociation experiments on the Micromass Platform instrument had shown that it was possible to produce cluster ions of a given ligand number between that of the molecular ion, down to the bare metal core, by controlling the collision-induced dissociation conditions from the ion's kinetic energy on exiting the electrospray ion source. The experiments also verified the existence of a secondary decay channel, which leads to the formation of hydride bearing cluster anions. Unfortunately the nature of this secondary decay channel could not be determined from this data alone, a fact that prevented us from determining an estimate of the energy available to each cluster daughter ion at the point of its formation.

The loss of carbonyl ligands was observed to be the principal decay channel, from which it was concluded that this occurred via a process of sequential ligand loss. The identification of the parent ion in this case is facile. However, a determination of the parent ion for the observed transition metal carbonyl hydride ions could not be solved so easily. By knowing the identity of the parent ion for the cluster hydrides one can then conjecture the mechanism by which it was formed. Such a problem can be solved through use of the ion isolation that can be performed in an FTICR-MS.

7.3.1 Instrument Setup

The experiments were performed at the University of Edinburgh on a Bruker® Apex II™ FT-ICR MS. While similar to that used previously in the laser-induced aggregation experiments, the current instrument was equipped with a three Tesla actively shielded superconducting magnet. The lower strength of the magnetic field means that the maximum possible resolution of the instrument is reduced, but is still far higher than that offered by any of the other mass spectrometers used within this thesis. In addition the instrument was connected to an electrospray ionisation source, of a type that corresponds to the second model discussed in Chapter 3.4.2 (Figure 3-10). The operating conditions of the electrospray ion source were necessarily much different from those within the Micromass Platform. The temperature of the source was maintained at a far higher temperature of 250°C (compared to 90°C), while the pressure of the nitrogen desolvation gas was kept at a lower pressure of approximately 1 bar (compared to 7 bar). Directly after the electrospray source and capillary there is a hexapole ion trap, used to collect and form ions into a coherent ion packet to be sent to the ICR cell. The ion residence time within the hexapole can be directly controlled from the Xmass software. The remainder of the ion optics in the instrument are the same as those provided in Figure 7-1. The following experiments were performed with assistance from Dr Adriana Dinca and Mr Nick Polfer.

Sample Preparation

Given that it was only from the rhodium data that any quantitative energy values were determined from the EDESI experiments for both carbomethoxy and hydride ligated clusters, it was decided that the investigation of the hydride formation process would be limited to the methoxide derivatised rhodium cluster only. The sample preparation procedure was the same as that for the EDESI experiments in Chapter 6.4.

7.3.2 Isolation Of Derivatised Rhodium Clusters

In-Source CID

The ion optics within the electrospray source permitted CID within the ion source of the FTICR-MS instrument, but controlling the fragmentation reactions was far less precise than could be achieved on the Micromass Platform. For instance it was frequently observed that the in-source dissociation was so prolific that only the rhodium carbonyl hydrides of $[Rh_6(CO)_9H]^-$ and lower could be observed, with no $[Rh_6(CO)_nCOOMe]^-$ ions. This posed a problem in that to understand the formation of the hydride clusters required the isolation of one of the carbomethoxy ligated clusters. Several attempts were made to reduce the extent of in-source CID by altering the potentials on the ion optics that have most influence on the ion kinetic energy in the activating collision region (from the desolvation capillary and beyond). Unfortunately this produced little change in the ion population. It was subsequently discovered that the ions were still subject to activating collisions within the hexapole ion trap. The ions were held here for accumulation into a coherent ion packet for anything upto a period of one second, within which time countless number of low energy collisions would be occurring, gradually increasing the internal energy of the ions leading to the extensive fragmentation observed. A new pulse program was written for the operation of the hexapole, in which the ions were only held for a matter of microseconds before being sent to the ICR cell. To ensure that there was enough ions in the cell to give a reasonable ion signal several ion packets were sent to the ICR cell before the analysis procedure began. The implementation of this system dramatically improved the ion population to suit the current requirements. An example of the in-source CID is given in Figure 7-16. As can be seen, the parent ion is quite prominent, with many of the carbomethxy ligated and hydride cluster ion fragments visible.

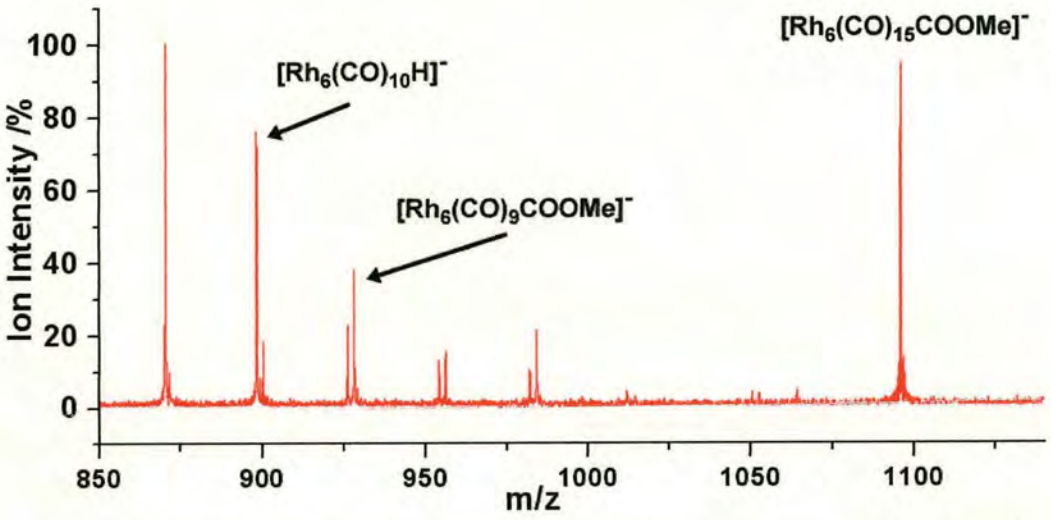

Figure 7-16 In-source CID observed within the electrospray source of the FTICR-MS.

It should also be noted that the population of the hydride species increases with a decreasing size of ligand shell, upto the point where the threshold is reached and all the remaining fragments are hydrides.

7.3.3 Determining The Source Of The Hydride Ions

Results Of Isolation/Collision-Induced Dissociation

With the successful detection of the rhodium carbomethoxy ligated clusters within the ICR cell, it was now possible to selectively isolate any chosen cluster and promote collision-induced dissociation within the cell by SORI CID, using argon as the target gas. The back pressure of the argon gas was typically of the order of several mbar, and the gas was pulsed into the ICR cell in 3 ms shots every two seconds. The following mass spectra show the results for a series of cluster fragments. Figures 7-17 to 7-20 show the results of isolating the ions $[Rh_6(CO)_{15}COOMe]^-$, $[Rh_6(CO)_{12}COOMe]^-$, $[Rh_6(CO)_{11}COOMe]^-$, and $[Rh_6(CO)_8COOMe]^-$, and the following fragments produced from SORI CID of these ions.

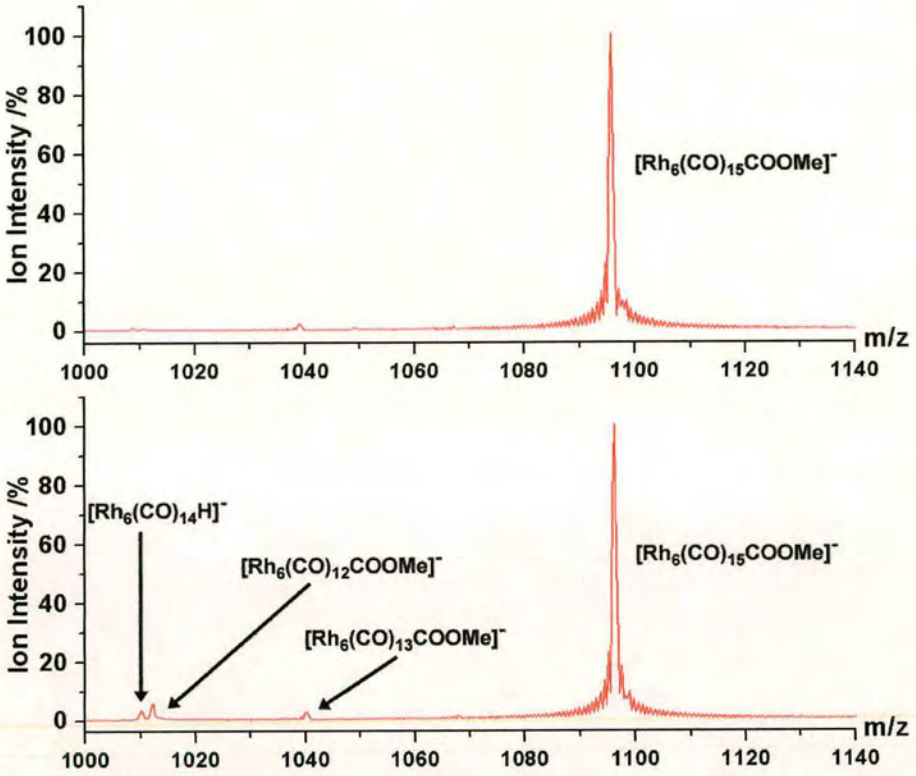

Figure 7-17 The isolation and fragmentation of $[Rh_6(CO)_{15}COOMe]^-$.

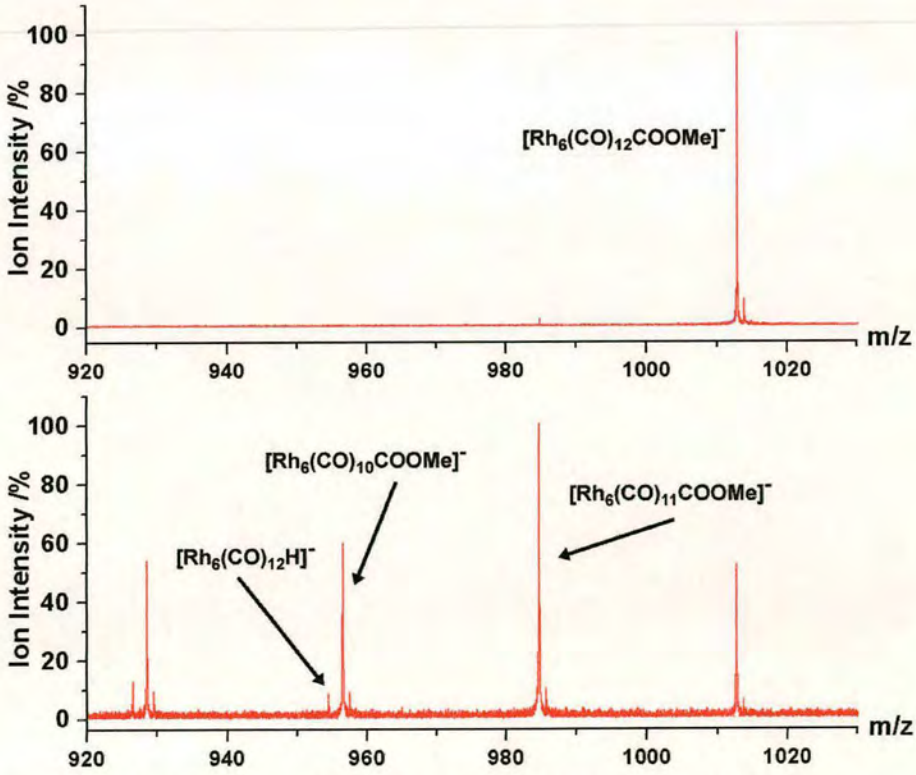

Figure 7-18 The isolation and fragmentation of $[Rh_6(CO)_{12}COOMe]^-$.

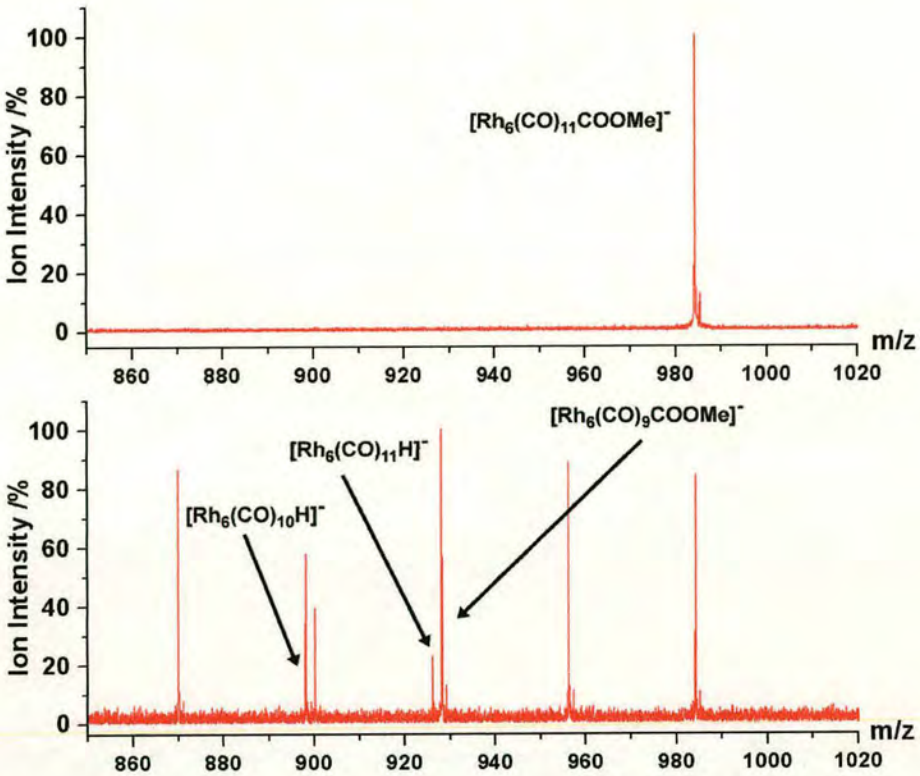

Figure 7-19 The isolation and fragmentation of $[Rh_6(CO)_{11}COOMe]^-$.

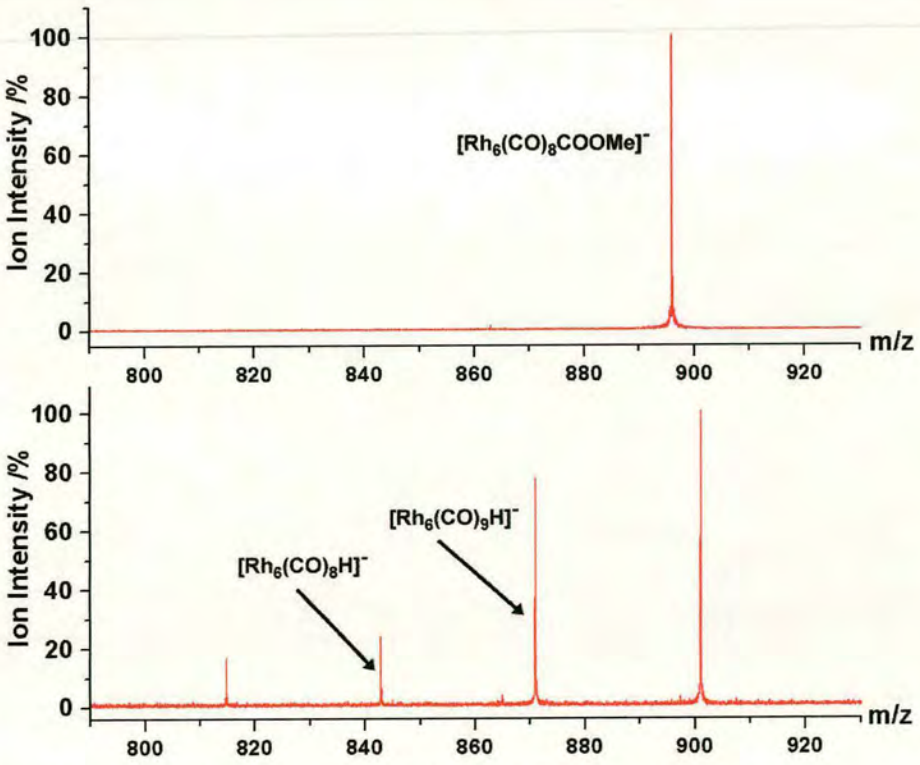

Figure 7-20 The isolation and fragmentation of $[Rh_6(CO)_8COOMe]^-$.

Figure 7-17 shows that the fragmentation of the molecular ion under these conditions yields little in the way of fragments, but from those that are produced it can be seen that the first observed hydride ion is the $[Rh_6(CO)_{14}H]^-$. This was also the first observed hydride ion observed in the EDESI experiments. Since only the carbomethoxy derivatised molecular ion was present in the cell prior to the dissociation reaction, the possibility that the hydride anions are produced from some contaminant within the electrospray source in the Platform mass spectrometer can now be ruled out. The remaining mass spectra in Figures 7-18 and 7-19 show that for the isolation of ion $[Rh_6(CO)_nCOOMe]^-$, the first detected hydride ion is $[Rh_6(CO)_nH]^-$. Although this does not seem to apply for the fragmentation results of the molecular ion, one must remember that the first hydride anion has been confirmed to be $[Rh_6(CO)_{14}H]^-$, and so it is possible that molecular ion $[Rh_6(CO)_{15}COOMe]^-$ may first dissociate one carbonyl ligand to form $[Rh_6(CO)_{14}COOMe]^-$, before dissociating to form either $[Rh_6(CO)_{13}COOMe]^-$ or $[Rh_6(CO)_{14}H]^-$. These spectra are representative of the reactions observed for all carbomethoxy bearing cluster ligand shell sizes, with the notable exception of the isolation of $[Rh_6(CO)_8COOMe]^-$. Figure 7-20 appears to show only the removal of 30 mass units, corresponding to the loss of OCH_2 from the ion to give $[Rh_6(CO)_9H]^-$. The relevance of this outcome shall be explored in due course, but for now it shall be treated as a special event, and the focus shall be fixed upon the more common result, namely the loss of 58 mass units from the cluster to form the hydride. Thus for the molecular ion $[Rh_6(CO)_nCOOMe]^-$, the possible dissociation pathways available to the methoxide derivatised rhodium cluster are:

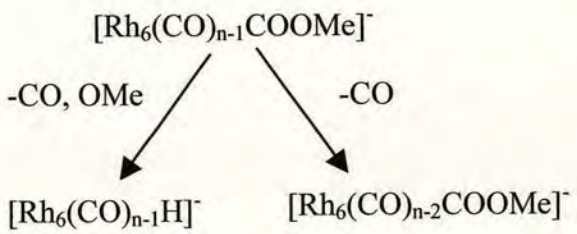

(7-1)

Dissociation Mechanisms For The Production Of Hydrides

It would be prudent to begin with a reminder of the connectivity of the carbomethoxy ligand to the rhodium atom on the cluster, as shown in Figure 7-21, which shall later be used as a basis for the determination of the possible dissociation mechanism.

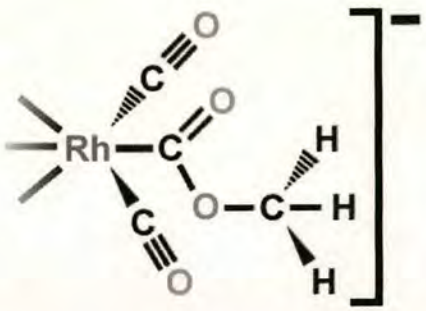

Figure 7-21 A general illustration of the connectivity of the carbomethoxy ligand to the rhodium atom on the cluster.

Given the previous observations it is clear that the hydrides are formed from the carbomethoxy ligand in some way, being the only source of hydrogen on the cluster. The results from the majority of the isolation experiments are coherent with the loss of the entire carbomethoxy ligand, minus one hydrogen atom, so by what mechanism does such a reaction occur? A feasible reaction mechanism may be conjectured by examining the known mechanism of dissociation of hydroxylated transition metal carbonyl systems in the water gas shift reaction. This is shown below in Figure 7-21 for the iron pentacarbonyl system.

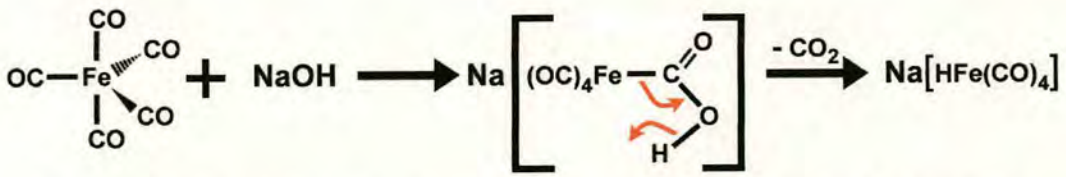

Figure 7-22 The nucleophilic attack of sodium hydroxide on one of the carbonyl ligands of iron pentacarbonyl. The subsequent loss of carbon dioxide from the reaction complex produces the iron carbonyl hydride anion [22].

If one assumes for the sake of convenience at this stage that the first carbonyl ligand was removed from the carbomethoxy bound rhodium atom. The proposed reaction

mechanism could then be projected as occurring via the mechanism given in Figure 7-23.

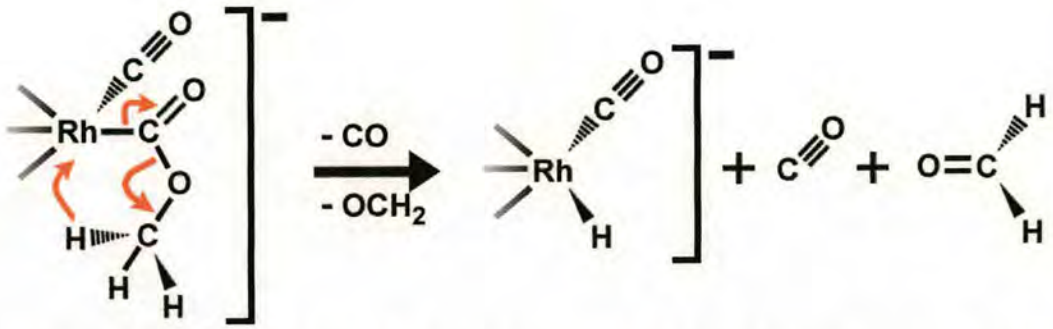

Figure 7-23 An outline of the possible reaction that leads to the formation of the hydride anion, producing carbon monoxide and formaldehyde (OCH_2).

This reaction mechanism leads to the formation of two stable neutral species, formaldehyde (OCH_2) and carbon monoxide. As such the reaction would be the most energetically favourable possibility for the loss of $COOCH_2$ from the cluster. Unfortunately the fragments are neutral and cannot be detected by mass spectrometry, so the validity of this mechanism cannot be verified from the current data. This mechanism can possibly explain why the first observed hydride ion is $[Rh_6(CO)_{14}H]^-$, since it would appear that the cluster must first lose one carbonyl ligand to provide a free bonding site for the metal-hydrogen bond to be formed. The reaction mechanism for the formation of the hydride (excluding carbonyl loss from another hydride) is

$$[Rh_6(CO)_x COOMe]^- \xrightarrow{-CO,-OCH_2} [Rh_6(CO)_x H]^- \qquad (7\text{-}2)$$

There is, however, another possible reaction mechanism, which can not only account for the formation of the hydride species, but also account for observed threshold from where all subsequent dissociation fragments are hydrides. This proposed mechanism is analogous to that of the formation of the carbide clusters observed for the osmium supraclusters in Chapter 7.2.2. Let us suppose that a carbonyl ligand is lost from a rhodium atom adjacent to the rhodium bound to the carbomethoxy ligand. The vacant site is suitable to allow the carbon-oxygen single bond of the carbomethoxy ligand to bridge across the two metals as an intermediate state. This

would weaken the bond, leading to the release of formaldehyde in a similar mechanism to that given in Figure 7-23. The remaining hydrogen is then in a suitable place to migrate into the core polyhedron, as shown in Figure 7-24.

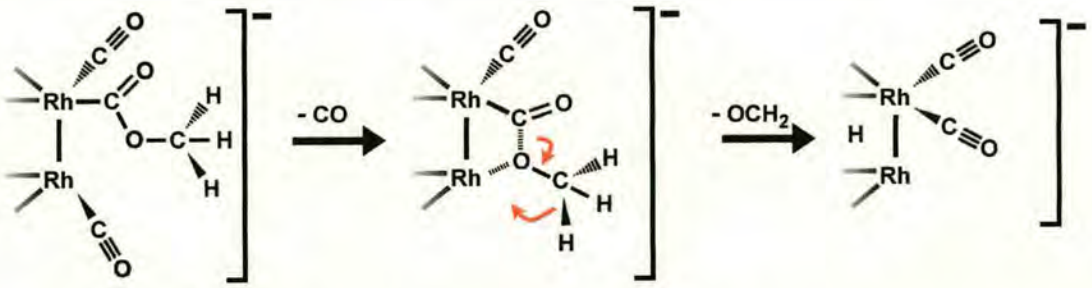

Figure 7-24 A second possible reaction mechanism for the formation of the hydride anions, which also comes from the loss of a suitable carbonyl ligand, followed by formaldehyde elimination.

Under such a reaction mechanism, at least one suitable carbonyl must first be lost to allow the bridging of the carbomethoxy ligand to occur, matching the observations. Only the removal of certain ligands from around the core allow the bridging reaction to occur, and so the population of the heavy cluster hydride anions is dependent upon just which carbonyls have been removed from a given cluster. In addition the reactions may also follow one another very quickly, so that they can be viewed as a quick, single reaction in the current experimental timeframe. The carbomethoxy ligated clusters that have been isolated could not have had a substantial population of ions that had a suitable vacant site for the bridging reaction to occur, otherwise from the isolation of ion $[Rh_6(CO)_xCOOMe]^-$ a population of ions of the form $[Rh_6(CO)_{x+1}H]^-$ would be observed in the fragment mass spectrum.

From this bridging reaction mechanism, it then follows that the designation of the parent ion for any one cluster hydride is:

$$[Rh_6(CO)_xCOOMe]^- \xrightarrow{-OCH_2} [Rh_6(CO)_{x+1}H]^- \qquad (7\text{-}3)$$

since the reaction is only dependent upon the removal of a suitable ligand from the cluster to allow the bridging reaction to occur. When such a vacancy does occur, it can be assumed that the ensuing bridging reaction occurs very rapidly, such that the reaction mechanism is indistinguishable from the first proposed decay pattern (the

simultaneous loss of carbon monoxide and formaldehyde) in the experimental time-frame.

This mechanism is radically different from the first proposed mechanism in Equation 7-2. It can be seen that as the number of ligands removed increases so to will the probability that the carbomethoxy can bridge and form the hydride, again matching the observations that hydride ion intensity increases as more carbonyl ligands are removed. This reaction mechanism may also explain the observation made of the decay of $[Rh_6(CO)_8COOMe]^-$ to give $[Rh_6(CO)_9H]^-$ as shown in Figure 7-20.

Correlation With The Hydride Formation Threshold

It is now time to consider the significance of the threshold point for the formation of cluster hydride fragments only. Previously in Chapter 6.6.3 various possibilities were explored to explain this occurrence. The first attempt to correlate the point of cluster hydride dominance for all the cluster species experimented on considered the number of carbonyl ligands lost prior to the threshold point. To recap, the last observed carbomethoxy ligated clusters are given in Table 7-1.

Molecular Ion	Last Cluster Carbomethoxy Ion	Number of Carbonyl Ligands Lost From Parent
$[Ir_4(CO)_{11}COOMe]^-$	$[Ir_4(CO)_5COOMe]^-$	**6**
$[Os_3(CO)_{11}COOMe]^-$	$[Os_3(CO)_4COOMe]^-$	**7**
$[Rh_6(CO)_{15}COOMe]^-$	$[Rh_6(CO)_8COOMe]^-$	**7**

Table 7-1 The last observed carbomethoxy ligated clusters from the CID of $[Ir_4(CO)_{11}COOMe]^-$, $[Os_3(CO)_{11}COOMe]^-$, and $[Rh_6(CO)_{15}COOMe]^-$.

For the bridging mechanism for hydride formation to take place, there are certain conditions that must be met before the reaction can occur. The carbomethoxy ligand can only bridge across to a metal centre adjacent to the one it is bonded to. There must therefore be a vacancy on one of these metals. However, the geometry of the

vacancy must also be suitable. For instance, if the carbomethoxy ligand is bonded in an equatorial position, it will be unable to bridge onto an axial vacancy.

Thus the number and position of carbonyl ligands lost plays a fundamental role in the viability of this reaction mechanism. Since the dissociation process is essentially random, at least in terms of which ligand is removed per dissociation step, the occurrence of this reaction is a probabilistic function of the number of ligands lost. However, there will come a point where the sequential removal of the ligands will remove all those that, on leaving the metal, would not leave a suitable vacancy for the reaction (such as those not on an adjacent metal and those of the wrong geometry). Therefore the probability of the reaction would then become a certainty.

This issue is best explored by an example. Beginning with the simplest derivatised cluster species $[Os_3(CO)_{11}COOMe]^-$. The trigonal structure of the cluster means that the carbomethoxy ligand can theoretically bridge to either of the metal centres surround the one to which it is bonded. If it is assumed the carbomethoxy ligand occupies an axial position, then the removal of the two equatorial ligands on both of the other osmium metals will not produce a suitable vacancy to allow the carbomethoxy ligand to bridge across. In addition the removal of all the carbonyl ligands bonded to the carbomethoxy bound metal will serve no use in assisting the bridging reaction. The removal of these specific ligands, a total of seven overall, will not generate conditions suitable for the formation of the hydride. This number would be the same if the carbomethoxy ligand occupied an equatorial position on the metal. If all seven of these ligands were to be removed from the osmium cluster, the removal of any one of the remaining ligands would produce a suitable vacancy for the bridging reaction to occur. This is illustrated for the osmium cluster in Figure 7-25. The left hand side of the diagram shows the full molecular ion $[Os_3(CO)_{11}COOMe]^-$, with the trigonal arrangement of metal atoms and the bonds to the ligands that surrounds them. The carbomethoxy ligand is indicated by a circle at the end of one of these bonds. The right hand side of the diagram shows which carbonyl ligands are removed that do not generate the necessary vacancy for the

bridging reaction, as discussed above. Those carbonyl ligands removed from the cluster are represented as hollow bonds.

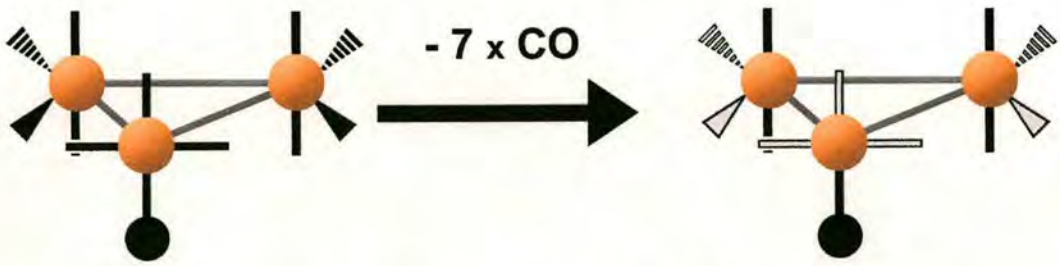

Figure 7-25 The maximum number of carbonyl ligands that can be removed from the derivatised osmium cluster that do not generate a suitable vacancy for the bridging of the carbomethoxy ligand to produce the hydride cluster species.

The maximum number of ligands that could be removed from the methoxide derivatised osmium cluster without producing a suitable vacancy to allow the bridging reaction to occur is equal to the amount removed to produce the last observed osmium carbomethoxy cluster $[Os_3(CO)_4COOMe]^-$, as shown in Table 7-1. Beyond this particular configuration, all subsequent daughter ions were cluster hydrides.

A similar process of elimination can be applied to the iridium cluster. From the XRD representation of the derivatised structure (as given in Chapter 2.4.3), the carbomethoxy ligand occupies an axial position on one of the metals that are bridged by carbonyl ligands. These bridged carbonyl ligands can be removed since they are equatorial. The two equatorially orientated carbonyls can also be removed from the top iridium atom. Finally the carbonyl ligand is removed from the metal bound to the carbomethoxy ligand. This is represented below in Figure 7-26.

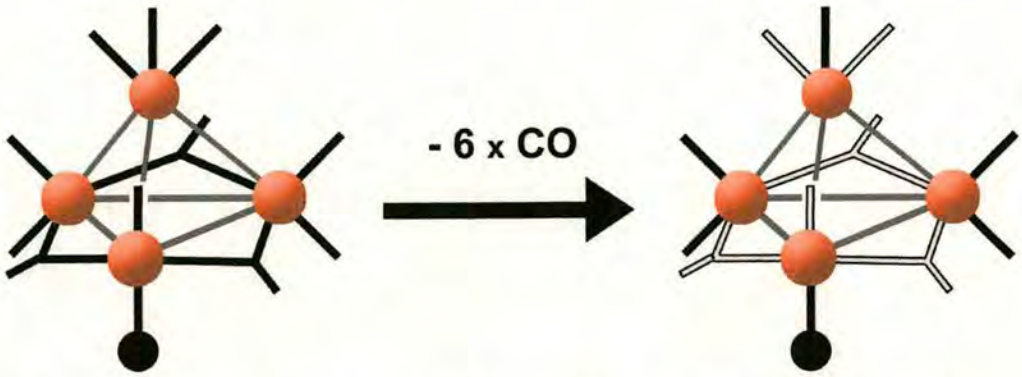

Figure 7-26 The maximum number of carbonyl ligands that can be removed from the derivatised iridium cluster that do not generate a suitable vacancy for the bridging of the carbomethoxy ligand to produce the hydride cluster species.

The total number of carbonyl ligands removed so far is six. The removal of any other remaining carbonyl ligand will allow the carbomethoxy ligand to bridge across two metal centres, leading to the formation of the hydride. The number of carbonyls removed that do not generate a suitable vacancy once again matches the number removed to produce the last observed iridium carbomethoxy cluster $[Ir_4(CO)_5COOMe]^-$, as shown in Table 7-1.

Finally, consider the rhodium cluster. The orientation (axial or equatorial) of the carbomethoxy ligand is somewhat ambiguous from the XRD data (see Chapter 2.4.3). However, it is clear that the four capping carbonyl ligands that surround the octahedral core would not provide a suitable vacancy for the bridging reaction to occur. In the same respect the carbonyl ligand bonded to the carbomethoxy bound rhodium atom, and the two carbonyl ligands bonded to the rhodium diametrically opposite are equally redundant. However, the removal of any other ligand will leave the desired vacancy for the hydride formation., as given in Figure 7-27. For ease of visualisation the capping carbonyl ligands have not been shown on the rhodium cluster.

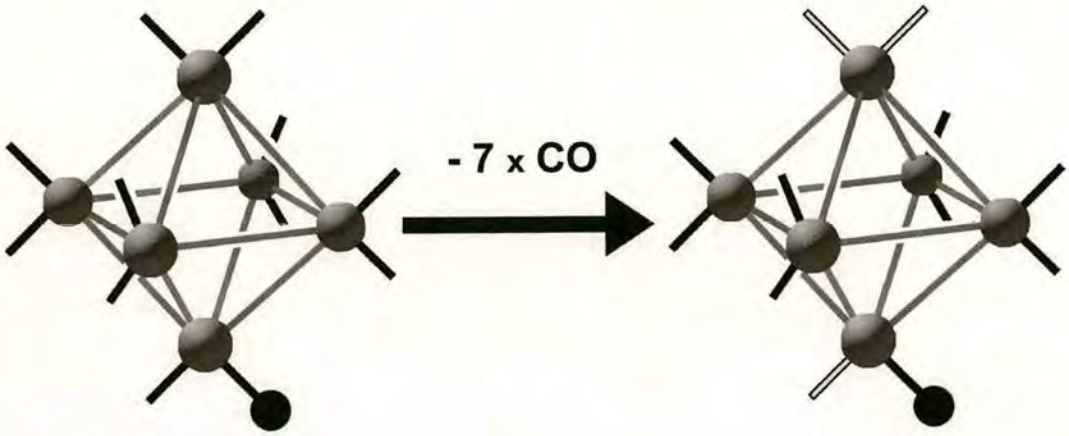

Figure 7-27 The maximum number of carbonyl ligands that can be removed from the derivatised rhodium cluster that do not generate a suitable vacancy for the bridging of the carbomethoxy ligand to produce the hydride cluster species.. The four capping carbonyls are not shown for ease of visualisation.

Once again, the maximum number of ligands that can be removed that do not permit the bridging reaction, seven in this case, matches that lost to form the last observed carbomethoxy cluster daughter ion in the CID of rhodium, $[Rh_6(CO)_8COOMe]^-$.

There is a distinct correlation between the conditions that must be met to permit the bridging formation of the cluster hydrides and the observations made from the spectra. The threshold point for cluster hydride dominance can be unambiguously tied in with the conditions necessary for the bridging reaction formation of that species. As more carbonyl ligands are removed the probability that a vacancy of the correct geometry will appear increases, a fact that can be seen in the observed increase in the relative intensity of the cluster hydrides with reducing ligand shell size.

However, there is the issue of the mobility of the ligands around the metal core, such that an axial to equatorial bridging mechanism may not be precluded, as has been assumed so far. In the case of the rhodium cluster such factors are not a significant issue. The ligands cannot really be separated into axial and equatorial orientations, and those ligands that have been removed in the example will obviously not generate

the required vacancy for bridging on steric grounds. These arguments can also be, in part, applied to the iridium cluster with the removal of the bridging carbonyls. However, there are questions on the possibility of axial-equatorial bridging with both the iridium and osmium clusters. It is likely that with the loss of only one or two ligands from the cluster core, such axial-equatorial bridging reactions are sterically forbidden. The removal of more ligands generates more space around the metal core, increasing the possibility of axial-equatorial bridging, such that the number of ligands that must be removed to allow such free movement approximates the evaluated maximum number of ligands that must be removed to guarantee the bridging of the carbomethoxy ligand. The case remains for the existence of a threshold for the total formation of cluster hydride fragment ions, which does match the proposed mechanism for the formation of these cluster hydride species. It is also the case that the discussed bridging mechanism seems to be the most reasonable mechanism for formation of these hydride species.

7.3.4 Determining The Energy of Formation

Now that a reaction mechanism for the formation of the cluster hydrides has been established, the data accumulated in Chapter 6 can now be used to determine the energy of the system at the point of formation of each daughter ion.

Knowledge of the reaction mechanism for the production of each daughter ion allows for the determination of the mean value for the individual centre-of-mass energy contributions for each sequential dissociation step to reach a given daughter ion at a given cone voltage value. These values can then be multiplied by the value of cone voltage at which the ions were formed (taken from the 10% peak value from the EDESI-MS breakdown plots) to give the mean centre-of-mass energy contribution per collision. This is then multiplied by the collision coefficient determined for each cluster species and the collision-induced dissociation conditions (5.78568 for iridium, 6.42715 for osmium, and 6.88229 for rhodium, as taken from Chapter 6.6.3).

Tables 7-2 to 7-5 show the outcome of these operations to determine the energy of the system at the point of formation of each daughter ion. For ease of identification each daughter ion has been numbered. The monoisotopic nature of rhodium permitted the direct observation of all of the cluster hydride ions and cluster carbomethoxy ions, such that individual cone voltage values can be attributed to each species. With the iridium and osmium data however, the isotope distributions for the early cluster hydrides were mixed with those of the cluster carbomethoxy ions, preventing the allocation of cone voltage values to each fragment ion. The knowledge of the point in formation of each of the rhodium hydride clusters allows for the determination of the energy values associated with their production from the carbonyl decay channel (Table 7-4) and rapid formaldehyde loss channel (Table 7-5), and from carbonyl loss from a pre-formed hydride species. The energy values for each cluster daughter ion are then plotted in Figures 7-28 to 7-30.

Ion No.	Cluster Species	m/z	Cone Voltage	Energy (eV)	Standard Error
1	$[Ir_4(CO)_{10}COOMe]^-$	1108.812	14.56	**2.03**	0.39
2	$[Ir_4(CO)_9COOMe]^-$	1080.817	8.22	**1.16**	0.82
3	$[Ir_4(CO)_8COOMe]^-$ & $[Ir_4(CO)_{10}H]^-$	1052.8221	21.73	**3.11**	0.17
4	$[Ir_4(CO)_7COOMe]^-$ & $[Ir_4(CO)_9H]^-$	1024.8271	26.28	**3.80**	0.29
5	$[Ir_4(CO)_6COOMe]^-$ & $[Ir_4(CO)_8H]^-$	996.8323	31.37	**4.60**	0.12
6	$[Ir_4(CO)_5COOMe]^-$ & $[Ir_4(CO)_7H]^-$	968.8373	40.48	**6.01**	0.15
7	$[Ir_4(CO)_6H]^-$	938.8268	48.73	**7.27**	0.09
8	$[Ir_4(CO)_5H]^-$	910.8318	58.91	**8.91**	0.08
9	$[Ir_4(CO)_4H]^-$	882.8369	77.71	**11.61**	0.22
10	$[Ir_4(CO)_3H]^-$	854.842	97.13	**14.48**	0.12
11	$[Ir_4(CO)_2H]^-$	826.8471	113.37	**16.91**	0.12
12	$[Ir_4(CO)H]^-$	798.8522	127.52	**19.07**	0.20
13	$[Ir_4H]^-$	770.8572	149.49	**22.47**	0.14

Table 7-2 The variation and error in the average energy acquired by the molecular ion $[Ir_4(CO)_{11}COOMe]^-$ to produce each designated daughter ion, first observed at the marked value of the cone voltage.

Ion No.	Cluster Species	m/z	Cone Voltage	Energy (eV)	Standard Error
1	$[Os_3(CO)_{10}COOMe]^-$	910.8414	11.14	**2.08**	0.16
2	$[Os_3(CO)_9COOMe]^-$	882.8464	20.55	**3.89**	0.25
3	$[Os_3(CO)_8COOMe]^-$ & $[Os_3(CO)_{10}H]^-$	854.8515	24.13	**4.64**	0.49
4	$[Os_3(CO)_7COOMe]^-$ & $[Os_3(CO)_9H]^-$	826.8566	32.20	**6.28**	0.42
5	$[Os_3(CO)_6COOMe]^-$ & $[Os_3(CO)_8H]^-$	798.8616	33.19	**6.58**	0.44
6	$[Os_3(CO)_5COOMe]^-$ & $[Os_3(CO)_7H]^-$	770.8667	39.10	**7.88**	0.20
7	$[Os_3(CO)_4COOMe]^-$ & $[Os_3(CO)_6H]^-$	742.8717	48.93	**10.03**	0.28
8	$[Os_3(CO)_5H]^-$	712.8611	71.85	**14.81**	0.43
9	$[Os_3(CO)_4H]^-$	684.8662	85.60	**17.94**	0.54
10	$[Os_3(CO)_3H]^-$	656.8712	91.79	**19.58**	0.83
11	$[Os_3(CO)_2H]^-$	628.8763	101.29	**22.11**	0.51
12	$[Os_3(CO)H]^-$	600.8813	129.51	**28.93**	0.55
13	$[Os_3H]^-$	572.8864	156.38	**35.74**	0.72

Table 7-3 The variation and error in the average energy acquired by the molecular ion $[Os_3(CO)_{11}COOMe]^-$ to produce each designated daughter ion, first observed at the marked value of the cone voltage.

Ion No.	Cluster Species	m/z	Cone Voltage	Energy (eV)	Standard Error
1	$[Rh_6(CO)_{14}COOMe]^-$	1068.3751	10.96	**1.89**	0.58
2	$[Rh_6(CO)_{13}COOMe]^-$	1040.3802	17.01	**2.96**	0.04
3	$[Rh_6(CO)_{12}COOMe]^-$	1012.3853	20.23	**3.57**	0.15
5	$[Rh_6(CO)_{11}COOMe]^-$	984.3904	24.67	**4.41**	0.08
6	$[Rh_6(CO)_{13}H]^-$	982.3748	21.88	**3.89**	0.27
7	$[Rh_6(CO)_{10}COOMe]^-$	956.3954	29.81	**5.39**	0.17
8	$[Rh_6(CO)_{12}H]^-$	954.3798	27.51	**4.95**	0.44
9	$[Rh_6(CO)_9COOMe]^-$	928.4006	34.87	**6.40**	0.09
10	$[Rh_6(CO)_{11}H]^-$	926.3849	31.42	**5.72**	0.23
11	$[Rh_6(CO)_8COOMe]^-$	900.4056	42.26	**7.86**	0.21
12	$[Rh_6(CO)_{10}H]^-$	898.39	38.38	**7.08**	0.12
13	$[Rh_6(CO)_9H]^-$	870.3951	47.85	**8.94**	0.05
14	$[Rh_6(CO)_8H]^-$	842.4001	56.83	**10.77**	0.03
15	$[Rh_6(CO)_7H]^-$	814.4053	66.64	**12.81**	0.04
16	$[Rh_6(CO)_6H]^-$	786.4103	75.87	**14.87**	0.08
17	$[Rh_6(CO)_5H]^-$	758.4154	88.67	**17.71**	0.07
18	$[Rh_6(CO)_4H]^-$	730.4205	97.64	**19.87**	0.08
19	$[Rh_6(CO)_3H]^-$	702.4256	107.09	**22.21**	0.08
20	$[Rh_6(CO)_2H]^-$	674.4307	118.04	**24.95**	0.34
21	$[Rh_6(CO)H]^-$	646.4357	132.17	**28.49**	0.10
22	$[Rh_6H]^-$	618.4409	142.81	**31.41**	0.35

Table 7-4 The variation and error in the average energy acquired by the molecular ion $[Rh_6(CO)_{15}COOMe]^-$ to produce each designated daughter ion from successive carbonyl loss, first observed at the marked value of the cone voltage.

Ion No.	ClusterSpecies	m/z	Cone Voltage	Energy (eV)	Standard Error
4	$[Rh_6(CO)_{14}H]^-$	1010.3696	17.72	**3.08**	0.06
6	$[Rh_6(CO)_{13}H]^-$	982.3748	21.88	**3.86**	0.27
8	$[Rh_6(CO)_{12}H]^-$	954.3798	27.51	**4.91**	0.44
10	$[Rh_6(CO)_{11}H]^-$	926.3849	31.42	**5.68**	0.23
12	$[Rh_6(CO)_{10}H]^-$	898.39	38.38	**7.04**	0.12
13	$[Rh_6(CO)_9H]^-$	870.3951	47.85	**8.90**	0.05
14	$[Rh_6(CO)_8H]^-$	842.4001	56.83	**10.72**	0.03

Table 7-5 The variation and error in the average energy acquired by the molecular ion $[Rh_6(CO)_{15}COOMe]^-$ to produce each designated daughter ion from carbonyl loss followed by rapid carbomethoxy ligand bridging and subsequent formaldehyde loss, first observed at the marked value of the cone voltage.

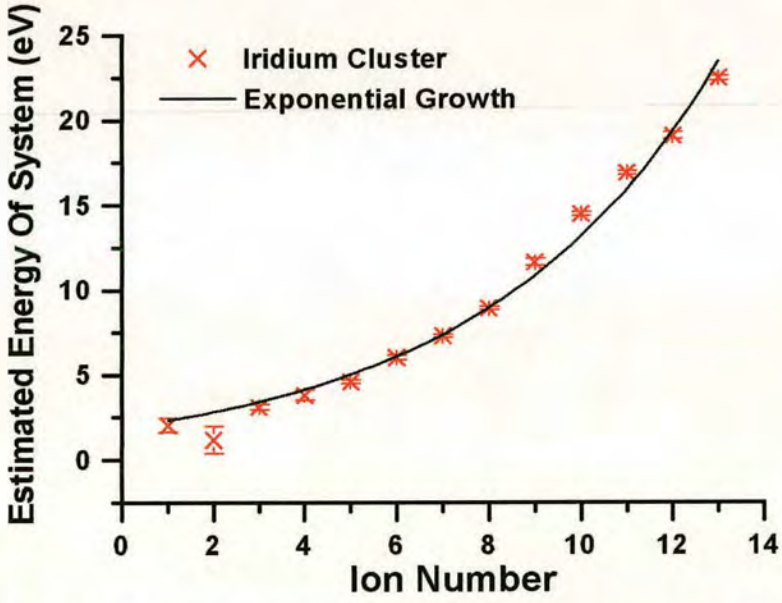

Figure 7-28 The estimated energy of the methoxide derivatised iridium cluster system leading to the production of the labelled daughter ions. An exponential growth curve has been fitted to the data.

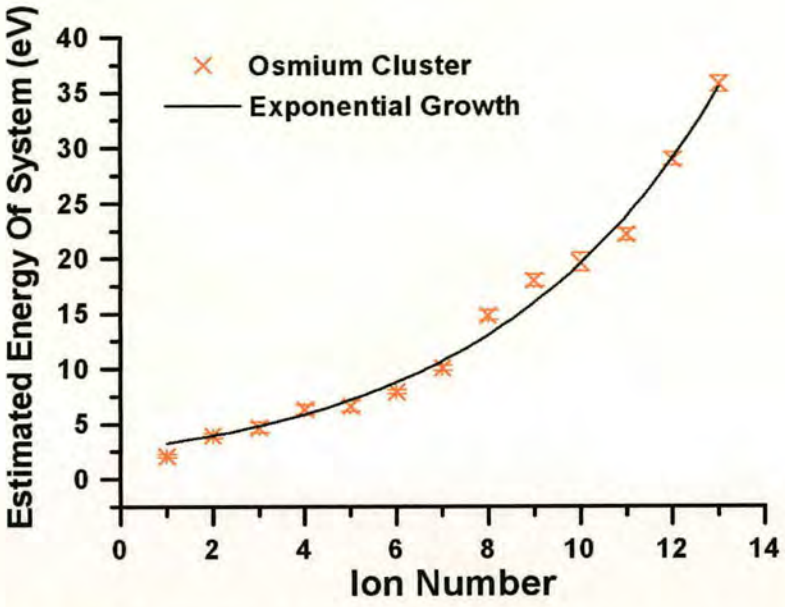

Figure 7-29 The estimated energy of the methoxide derivatised osmium cluster system leading to the production of the labelled daughter ions. An exponential growth curve has been fitted to the data.

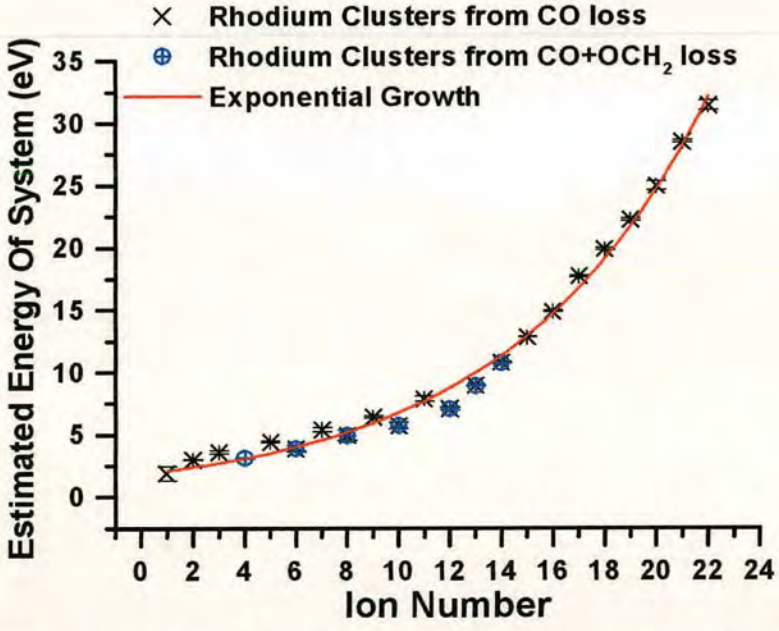

Figure 7-30 The estimated energy of the methoxide derivatised rhodium cluster system leading to the production of the labelled daughter ions from both carbonyl loss and carbonyl followed by rapid formaldehyde loss. An exponential growth curve has been fitted to the data.

The energy of the system at the time of ion formation can be seen to gradually increase as the daughter ions become smaller. To illustrate the point, first order exponential growth curves have been fitted to the raw data, purely to show that the data seems to follow a smoothly varying curve. A similar result is achieved for a quadratic curve fitted to the data as well, but not for a linear fit.

The curves plotted in Figures 7-28 to 7-30 suggest that as more ligands are removed from the cluster core, the more energy that is required to remove the remaining ligands. Similar reports on the relationship between successive ligand loss and the energy required for removal have been made for $Fe(CO)_5$ [23]. Such an occurrence could be rationalised by considering the nature of the bond between the carbonyl ligand and the metal core. In breaking the carbonyl-metal bond the metal is no longer able to back-donate electrons from its filled *d* orbitals, and the dative bond is also broken so the metal no longer receives electrons into the empty *d* orbitals. This has the overall effect of making the metal core relatively more electropositive as more ligands are lost. Therefore the metal will draw more electron density from the remaining dative bonds of the carbonyl ligands.

While the energy available to each cluster system at the point of its formation is knonw, this does not provide a great deal of information about the actual threshold energy that must be reached by each fragment to decay again: the individual bond dissociation energies of each of the ligands. To determine the threshold energy for the formation of any of the cluster fragments from any of the possible parents, the energy values for the fragment can be compared against the values of the possible parents. The difference can then be taken as a measure of the threshold energy for the formation of that particular cluster fragment from the parent. The two decay channels are thus carbonyl loss, and the loss of formaldehyde to produce the cluster hydride. It should be noted that carbonyl loss occurs for both the carbomethoxy ligated clusters and the cluster hydrides. However, there currently only exists unambiguous data on the points of formation of the rhodium hydride clusters; the position of the hydrides of iridium and osmium overlapped with those bearing

carbomethoxy ligands, and so an assignment of their point of formation cannot be made.

Thus the energy of dissociation for each of the possible dissociation reactions that occur to the derivatised rhodium cluster at each point in the EDESI experiment can be evaluated. Taking the data from Table 7-4 and Table 7-5 the energy necessary for the carbonyl dissociation and subsequent rapid formaldehyde loss can be calculated, as given in Table 7-6 (which also accounts for just carbonyl loss from the fully derivatised clusters). In addition the energy necessary for the sequential carbonyl dissociation reactions from the cluster hydride ions can also be determined, given in Table 7-7. The energy values for the carbonyl dissociation reactions to form each of the possible daughter ions has been plotted in Figure 7-31. It should be noted that since the cluster contains various different types of carbonyl ligands (terminal, capping etc.), and there is no specificity in the type that is removed, these energy values express the average bond dissociation energy of a given number of ligands from the cluster.

	Parent Ion	Subsequent CO loss Daughter Ion	Subsequent OCH_2 loss Daughter Ion
Cluster	$[Rh_6(CO)_{15}COOMe]^-$	$[Rh_6(CO)_{14}COOMe]^-$	N/A
Energy of Formation / eV	0	1.89 ± 0.58	N/A
Energy For Dissociation Reaction /eV	**1.89 ± 0.58**	N/A	
Cluster	$[Rh_6(CO)_{14}COOMe]^-$	$[Rh_6(CO)_{13}COOMe]^-$	**$[Rh_6(CO)_{14}H]^-$**
Energy of Formation / eV	1.89 ± 0.58	2.96 ± 0.04	3.08 ± 0.06
Energy For Dissociation Reaction /eV	**1.07 ± 0.62**	**0.12 ± 0.1**	
Energy For Overall $CO+OCH_2$ Decay /eV	**1.17 ± 0.64**		
Cluster	$[Rh_6(CO)_{13}COOMe]^-$	$[Rh_6(CO)_{12}COOMe]^-$	**$[Rh_6(CO)_{13}H]^-$**
Energy of Formation / eV	2.96 ± 0.04	3.57 ± 0.15	3.86 ± 0.27
Energy For Dissociation Reaction /eV	**0.61 ± 0.19**	**0.29 ± 0.42**	
Energy For Overall $CO+OCH_2$ Decay /eV	**0.90 ± 0.31**		
Cluster	$[Rh_6(CO)_{12}COOMe]^-$	$[Rh_6(CO)_{11}COOMe]^-$	**$[Rh_6(CO)_{12}H]^-$**
Energy of Formation / eV	3.57 ± 0.15	4.41 ± 0.08	4.91 ± 0.44
Energy For Dissociation Reaction /eV	**0.84 ± 0.23**	**0.50 ± 0.52**	
Energy For Overall $CO+OCH_2$ Decay /eV	**1.34 ± 0.59**		

Continued next page.

	Parent Ion	Subsequent CO loss Daughter Ion	Subsequent OCH_2 loss Daughter Ion
Cluster	$[Rh_6(CO)_{11}COOMe]^-$	$[Rh_6(CO)_{10}COOMe]^-$	**$[Rh_6(CO)_{11}H]^-$**
Energy of Formation / eV	4.41 ± 0.08	5.39 ± 0.17	5.68 ± 0.23
Energy For Dissociation Reaction /eV		**0.98 ± 0.25**	**0.29 ± 0.40**
Energy For Overall CO+OCH_2 Decay /eV	**1.27 ± 0.31**		
Cluster	$[Rh_6(CO)_{10}COOMe]^-$	$[Rh_6(CO)_9COOMe]^-$	**$[Rh_6(CO)_{10}H]^-$**
Energy of Formation / eV	5.39 ± 0.17	6.40 ± 0.09	7.04 ± 0.12
Energy For Dissociation Reaction /eV		**1.01 ± 0.26**	**0.64 ± 0.21**
Energy For Overall CO+OCH_2 Decay /eV	**1.65 ± 0.29**		
Cluster	$[Rh_6(CO)_9COOMe]^-$	$[Rh_6(CO)_8COOMe]^-$	**$[Rh_6(CO)_9H]^-$**
Energy of Formation / eV	6.40 ± 0.09	7.86 ± 0.21	8.90 ± 0.05
Energy For Dissociation Reaction /eV		**1.46 ± 0.30**	**1.04 ± 0.26**
Energy For Overall CO+OCH_2 Decay /eV	**2.50 ± 0.14**		
Cluster	$[Rh_6(CO)_8COOMe]^-$	$[Rh_6(CO)_7COOMe]^-$	**$[Rh_6(CO)_8H]^-$**
Energy of Formation / eV	7.86 ± 0.21	N/A	10.72 ± 0.03
Energy For Overall CO+OCH_2 Decay /eV	**2.86 ± 0.21**		

Table 7-6 The energy required for each of the described dissociation reactions, calculated from the formation energies determined in Tables 7-4 and Table 7-5.

	Parent Ion	Subsequent CO loss Daughter Ion
Cluster	$[Rh_6(CO)_{14}H]^-$	**$[Rh_6(CO)_{13}H]^-$**
Formation Energy / eV	3.08 ± 0.06	3.89 ± 0.27
Dissociation Energy /eV	**0.81 ± 0.33**	
Cluster	$[Rh_6(CO)_{13}H]^-$	**$[Rh_6(CO)_{12}H]^-$**
Formation Energy / eV	3.89 ± 0.27	4.95 ± 0.44
Dissociation Energy /eV	**1.06 ± 0.71**	
Cluster	$[Rh_6(CO)_{12}H^-$	**$[Rh_6(CO)_{11}H]^-$**
Formation Energy / eV	4.95 ± 0.44	5.72 ± 0.23
Dissociation Energy /eV	**0.77 ± 0.67**	
Cluster	$[Rh_6(CO)_{11}H]^-$	**$[Rh_6(CO)_{10}H]^-$**
Formation Energy / eV	5.72 ± 0.23	7.08 ± 0.12
Dissociation Energy /eV	**1.36 ± 0.35**	
Cluster	$[Rh_6(CO)_{10}H]^-$	**$[Rh_6(CO)_9H]^-$**
Formation Energy / eV	7.08 ± 0.12	8.94 ± 0.05
Dissociation Energy /eV	**1.86 ± 0.17**	
Cluster	$[Rh_6(CO)_9H]^-$	**$[Rh_6(CO)_8H]^-$**
Formation Energy / eV	8.94 ± 0.05	10.77 ± 0.03
Dissociation Energy /eV	**1.83 ± 0.08**	
Cluster	$[Rh_6(CO)_8H]^-$	**$[Rh_6(CO)_7H]^-$**
Formation Energy / eV	10.77 ± 0.03	12.81 ± 0.04
Dissociation Energy /eV	**2.04 ± 0.07**	
Cluster	$[Rh_6(CO)_7H]^-$	**$[Rh_6(CO)_6H]^-$**
Formation Energy / eV	12.81 ± 0.04	14.87 ± 0.08
Dissociation Energy /eV	**2.06 ± 0.12**	
Cluster	$[Rh_6(CO)_6H]^-$	**$[Rh_6(CO)_5H]^-$**
Formation Energy / eV	14.87 ± 0.08	17.71 ± 0.07
Dissociation Energy /eV	**2.84 ± 0.15**	

Continued next page.

	Parent Ion	Subsequent CO loss Daughter Ion
Cluster	$[Rh_6(CO)_5H]^-$	**$[Rh_6(CO)_4H]^-$**
Formation Energy / eV	17.71 ± 0.07	19.87 ± 0.08
Dissociation Energy /eV	**2.16 ± 0.15**	
Cluster	$[Rh_6(CO)_4H]^-$	**$[Rh_6(CO)_3H]^-$**
Formation Energy / eV	19.87 ± 0.08	22.21 ± 0.08
Dissociation Energy /eV	**2.36 ± 0.16**	
Cluster	$[Rh_6(CO)_3H]^-$	**$[Rh_6(CO)_2H]^-$**
Formation Energy / eV	22.21 ± 0.08	24.95 ± 0.34
Dissociation Energy /eV	**2.74 ± 0.42**	
Cluster	$[Rh_6(CO)_2H]^-$	**$[Rh_6(CO)H]^-$**
Formation Energy / eV	24.95 ± 0.34	28.49 ± 0.10
Dissociation Energy /eV	**3.54 ± 0.44**	
Cluster	$[Rh_6(CO)H]^-$	**$[Rh_6H]^-$**
Formation Energy / eV	28.49 ± 0.10	31.41 ± 0.35
Dissociation Energy /eV	**2.92 ± 0.45**	

Table 7-7 The energy required for each of the carbonyl loss dissociation reactions, calculated from the formation energies determined in Tables 7-4 and Table 7-5.

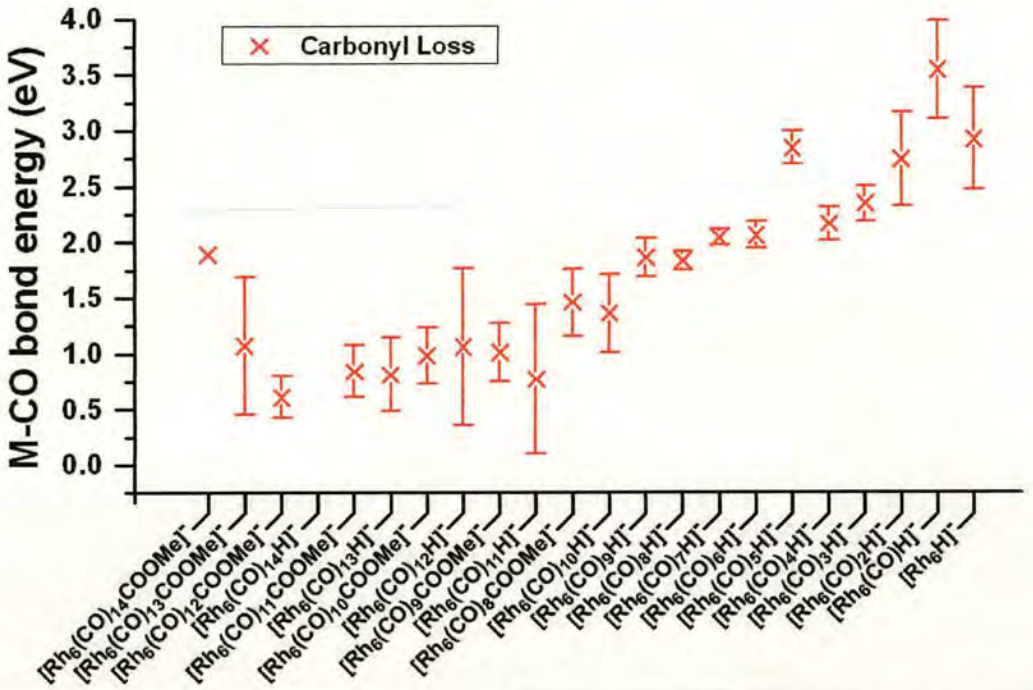

Figure 7-31 The threshold energies for the formation of the different rhodium cluster fragments from the carbonyl dissociation pathways.

As expected, one of the largest threshold energies to be overcome is that corresponding to the removal of the first carbonyl ligand from the cluster. Once this barrier is overcome the removal of successive ligands is very facile, but as more ligands are lost the metal core becomes more electropositive, making the bonds to the very small number of ligands that much stronger.

It can be seen that the additional energy necessary to perform the bridging of the carbomethoxy ligand, and the subsequent loss of formaldehyde from the carbomethoxy group requires little extra energy compared to the energy for the carbonyl ligand dissociation reaction that permits the reaction. However, it is unfortunate that in some instances the evaluated errors in these values are sometimes in excess of the actual energy value, raising some doubts about the veracity of these calculations. Despite this, these lower energy values are expected given the way in which the carbomethoxy becomes activated during the reaction. One may expect that with such low energy thresholds the hydride fragments would be more prolific in the EDESI MS experiments at lower cone voltage values. However, the

formaldehyde elimination reaction is dependent upon the removal of a suitable carbonyl ligand from an adjacent metal to allow the reaction, and as such the reaction is dependent upon the probability that just such a carbonyl will be removed. As the ligand shell decreases in size so this probability increases, with an associated increase in the population of hydride fragments. It is also striking how much more energy is needed to form the fragments $[Rh_6(CO)_5H]^-$ and $[Rh_6(CO)H]^-$. This indicates once more that given arrangements of carbonyl ligands around the cluster core can have a dramatic effect on the relative stability of the species, especially given that the formation of $[Rh_6(CO)_5H]^-$ requires an appreciably greater amount of energy to remove another ligand to form $[Rh_6(CO)_4H]^-$. Thus the fragment ion $[Rh_6(CO)_6H]^-$ must be far more stable than its daughter ion $[Rh_6(CO)_5H]^-$, but in losing a number of other ligands the fragment $[Rh_6(CO)_2H]^-$regains some of that stability.

Unfortunately, where a fragment can be produced from either carbonyl loss or formaldehyde elimination, the methods of determining the threshold for reactions are not perfect. Although the energy values determined for each of the fragments, and their possible parent ion, have been calculated it is not known for certain by which mechanism these fragments were formed. In addition the calibration of the energy scale is inadequate for accurate data acquisition, as discussed previously. There are other means by which these values could be determined. One possibility is the guided ion beam experiments with which the Armentrout group has produced a wealth of similar data for a range of species [24;25]. Another is the use of controlled collisions within the ICR cell of the FT-ICR mass spectrometer. Unfortunately time and the resources available limited the study to its current form. Nonetheless, in a field where such little information of this type exists, especially for these clusters, this is an informative first step.

7.4 Conclusion

The use of the advanced capabilities of Fourier-transform ion cyclotron resonance mass spectrometryhas been successful in improving the current investigations of transition metal carbonyl clusters. In the laser-induced cluster aggregation experiments large multi-nuclear supraclusters of both iridium and osmium were generated, with the result that two novel supracluster species were generated , $[Os_{10}C(CO)_{24}]^-$, and $[Os_{12}(CO)_{23\text{-}25}]^-$ that have previously never been constructed by traditional synthetic methods. In addition, the tandem mass spectrometry capabilities of the FT-ICR MS instrument allowed the investigation of the dissociation reactions that were observed in Chapter 6, prompting the formulation of the most likely dissociation mechanism for the production of the observed cluster hydride species. The proposed bridging mechanism for the liberation of formaldehyde from the carbomethoxy ligand tied in with the observations made in the EDESI-MS experiments of a threshold for the complete dominance of the cluster hydride anions. This knowledge lead to the further analysis of the data gathered from the EDESI-MS experiments in Chapter 6 into the energy accumulated by the cluster species in the production of each daughter ion, and estimations to the average bond dissociation energies for the rhodium carbonyl clusters for each individual ligand loss process.

7.5 Reference List

1. Bruker. Bruker Training Materials. 2000.

2. Baykut, G.; Jerzt, R.; Witt, M. *Rapid Communications In Mass Spectrometry* **2000**, *14*, 1238-1247.

3. Witt, M., Personal Communication: MALDI-FTMS experiments Bruker Bremen.

4. Lewis, J.; Raithby, P. R. *Journal of Organometallic Chemistry* **1995**, *500*, 227.

5. Eady, C. R.; Johnson, B. F. G.; Lewis, J. *Journal of Organometallic Chemistry* **1972**, *37*, C39.

6. Dyson, P.; Johnson, B. F. G.; McIndoe, J. S.; Langridge-Smith, P. R. R. *Inorganic Chemistry* **2000**, *39*, 2430-2431.

7. Dyson, P. J.; McIndoe, J. S. *Transition Metal Carbonyl Cluster Chemistry*, Gordon and Breach Science Publishers: 2000.

8. Housecroft, C. E. *Metal-Metal Bonded Carbonyl Dimers and Clusters*, 1st ed.; Oxford University Press Inc.: New York, 1995.

9. Aizawa, T.; Hayami, W.; Souda, R.; Otani, S.; Tanaka, T.; Ishizawa, Y. *Surface Science* **1996**, *358*, 645-650.

10. Desikan, A. N.; Sherif, F. G. *Abstracts of Papers of the American Chemical Society* **1997**, *214*, 10-CATL.

11. Fernandez-Torres, L. C.; Perry, S. S.; Didziulis, S. V.; Frantz, P. P. *Surface Science* **2002**, *511*, 121-132.

12. Homma, Y.; Kobayashi, Y.; Ogino, T.; Takagi, D.; Ito, R.; Jung, Y. J.; Ajayan, P. M. *Journal of Physical Chemistry B* **2003**, *107*, 12161-12164.

13. Iyer, M. V.; Norcio, L. P.; Kugler, E. L.; Dadyburjor, D. B. *Industrial & Engineering Chemistry Research* **2003**, *42*, 2712-2721.

14. Johnsson, M.; Carlsson, M.; Nygren, M. *Advanced Ceramics and Composites* **2003**, *247*, 145-148.

15. Lau, J. P. K.; Wong, W. T. *Inorganic Chemistry Communications* **2003**, *6*, 733-736.

16. Naito, S. *Catalysis Surveys from Japan* **2000**, *4*, 3-15.

17. Oyama, S. T.; Dhandapani, B. *Abstracts of Papers of the American Chemical Society* **1996**, *212*, 29-ETR.

18. Zurer, P. *Chemical & Engineering News* **2001**, *79*, 16.

19. Kovalchuk, V. I.; Mikova, N. M.; Chesnokov, N. V.; Naimushina, L. V.; Kuznetsov, B. N. *Journal of Molecular Catalysis A: Chemical* **1996**, *107*, 329-337.

20. Oxton, I. A.; Kettle, S. F. A.; Jackson, P. F.; Johnson, B. F. G.; Lewis, J. *Journal of Molecular Structure* **1981**, *71*, 117-120.

21. Binns, C. *Surface Science Reports* **2001**, *44*, 1-49.

22. Bochmann, M. *Molecular Organometallics 1 Complexes with Transition Metal-Carbon σ-Bonds*, 3rd ed.; Oxford University Press: Avon, 1999.

23. Ekeberg, D.; Hagen, S. I.; Hvistendahl, G.; Schulze, C.; Uggerud, E.; Vedde, J. *Organinc Mass Spectrometry* **1993**, *28*, 1547-1554.

24. Aristov, N.; Armentrout, P. B. *Journal Of Physical Chemistry* **1986**, *90*, 5135-5140.

25. Ervin, K. M.; Armentrout, P. B. *Journal Of Chemical Physics.* **1985**, *83*, 166-189.

8 Conclusion

8.1 Conclusion Of Thesis

It has been shown from all of the reported experiments performed that transition metal carbonyl clusters can provide a wealth of useful chemical and physical data from a series of relatively simple experiments performed on mass spectrometers.

The laser-induced cluster aggregation experiments were incredibly successful in the production of large, coordinatively unsaturated supraclusters, produced from reactive ion-molecule collisions between labile species, themselves generated from the photo-induced dissociation of the cluster precursors. The supraclusters appear to aggregate in a stepwise fashion, judging from the supraclusters that were produced from the iridium and rhodium cluster precursors. The three-dimensional polyhedral core of these two cluster precursors would appear to have given them increased stability in the laser field conditions, in comparison to the osmium cluster precursor which was observed to fragment. Whereas the iridium and rhodium supraclusters were formed from the stepwise addition of their intact metal cores, the osmium supraclusters had a much broader range of metal nuclearities.

Nonetheless this fragmentation of the osmium core led to two of the most intriguing finds of this thesis, namely the production of hitherto uncharacterised cluster species: the mono-anionic osmium carbonyl carbide cluster $[Os_{10}C(CO)_{24}]^-$ and the dodecaosmium carbonyl clusters $[Os_{12}(CO)_{23\text{-}25}]^-$. This has proven the ability of laser field conditions to promote reactions that are not viable with other, more traditional synthetic methods. Due to the ease of use of laser-assisted synthesis, the generation of a myriad of novel species with these and other precursor species could be very facile.

The stability of the clusters were investigate in two ways, through the measurement of the unimolecular post-source decay of ions in the time-of-flight mass spectrometer, and with infrared multi-photon dissociation in the Fourier transform ion cyclotron resonance mass spectrometer. It was observed that the rate of unimolecular post-source decay initially rose with increasing metal nuclearity and

ligand shell, but levelled off as the cluster became larger and the carbonyl ligand-to-metal atom ratio approached unity. This suggested that the larger clusters were able to hold larger amounts of internal energy before reaching the dissociation threshold. Such abilities as an energy sink may be attributed to the production of close-packed metal core structures at higher metal nuclearities, with the increased number of internal metal atoms with a corresponding increase in the number of metal-metal bonds providing a greater number of modes in which energy can be stored.

The infrared multi-photon dissociation data revealed that a larger cluster, with its potential ability to act as a stronger energy sink, is not always more stable. The hexadecairidium carbonyl clusters were observed to decay through carbonyl ligand loss under infrared laser irradiation, whereas the dodecairidium cluster $[Ir_{12}(CO)_{19}]^-$ withstood similar conditions with no change to the ion population. This was perhaps a direct reflection of the different optical properties of these two clusters, produced from the differences in their *d*-electron configurations, specifically the separation between highest occupied molecular orbital and the lowest unoccupied molecular orbital. The Ir_{16} clusters were possibly greater absorbers of the infrared radiation than the Ir_{12} as a consequence of this difference.

The energy dependent electrospray ionisation mass spectrometry (EDESI-MS) experiments were able to produce stable forms of unsaturated small transition metal carbonyl clusters. Such species are relatively rare in traditional cluster experiments. The reactivity of these unsaturated cluster precursors were made abundantly clear from the EDESI-MS data with the detected formation of transition metal carbonyl hydrides. These in themselves are useful and reactive reagents for a number of organic reaction mechanisms, such as the Fischer-Tropsch and Water-Gas Shift reactions. However, the dissociation mechanism that lead to the hydrides could not be deduced from the EDESI-MS data, and it was only with the tandem mass spectrometry capabilities of the Fourier Transform Ion Cyclotron Resonance mass spectrometer (FT-ICR MS) that the isolation and dissociation of selected clusters was possible. Correlating the isolation dissociation data with the observations already

made in the EDESI experiments revealed that the cluster hydrides were formed from the loss of a carbon monoxide of the correct geometry on a metal atom adjacent to that bound to the carbomethoxy ligand. This allowed the ligand to bridge the two metal centres, leading to the release of formaldehyde from the carbomethoxy ligand. This chain of reactions is assumed to occur very rapidly, such that the overall decay channel appears to be a loss of 58 mass units (equal to the nominal mass of carbon monoxide and formaldehyde together).

In addition the data produced fragmentation plots which provided quick access to the fragmentation patterns of the methoxide derivatised transition metal carbonyl clusters. From these plots useful physical data was extracted leading to the first quantitative assessment of the threshold energies for the for the complete removal of ligands from the metal core of the derivatised rhodium carbonyl cluster $[Rh_6(CO)_{15}COOMe]^-$. This showed that the hydride formation reaction was very facile, demonstrating the ease with which transition metal carbonyl species can make, break and manipulate organic species, and their deserved popularity as catalysts in organic reactions.

These findings pave the way for a wealth of a possible future experiments.

8.2 Future Work

Firstly it would be desirable to confirm the mechanism which leads to the formation of the transition metal carbonyl hydrides through the use of isotopically tagged methanol, such as CD_3OH, CH_3OD and possibly $C^{13}H_3OH$ and $CH_3O^{18}H$, and further isolation / dissociation experiments. It would then be possible to observe the composition of the leaving group leading to the formation of the hydride species, whether it comes from the carbomethoxy ligand, and just what bonds are being broken.

It would then be most useful to recalibrate the energy scale used in the EDESI-MS experiments with a species for which current and reliable data was available for the bond dissociation energies, such as $Fe(CO)_5$. In addition the cluster species could also be studied by other means, such as photo-electron spectroscopy, to further investigate the bonding energies and provide a full and accurate brief on the thermodynamic properties of these cluster species.

It would also be of fundamental interest to test the reactivity of the unsaturated transition metal carbonyl hydrides through the isolation of a given species in the ICR cell and the addition of suitable reagent gases such as unsaturated hydrocarbons. Initial experiments in this field have been performed on a mixed metal transition metal carbonyl cluster. The ligand shell was completely removed and the methane injected into the ICR cell. The observed products showed that the methane was bonding to the bare metal cluster, as a methyl group (CH_3) and as the radical form $CH_2^{\bullet}$ and as a bare carbon atom. In a similar manner, the production of clusters with a specific degree of ligand desaturation could be made to react with a vapour pressure of the neutral cluster precursors to observe the change in the rate of clustering with the composition of the cluster ions. One might also be able to generate mixed metal clusters in this way.

One could also try different derivatising alcohols, such as ethanol, pentanol, etc. to observe whether the derivatised cluster will react in a similar way as they did to the methoxide derivatisation, what species would be eliminated, and what would remain on the cluster.

Reactivity of the larger transition metal carbonyl clusters generated by the laser-induced aggregation experiments could also be performed on the FT ICR mass spectrometer. The supraclusters, with their unsaturated nature should prove to be reasonably acceptable to reaction with organic molecules. In addition, the chemistry could be significantly different from that observed in the smaller precursors, as they share more in common with bulk surfaces of transition metal species, than the smaller precursors which are more akin to thin metal films. This has implications for

fields such as catalysis, especially for the removal of toxic and harmful chemicals from engine emissions, such as NO and CO.

It can be seen that the field of transition metal carbonyl clusters is one rich in chemistry. There are numerous possibilities for the use of clusters in performing organic transformation reactions, as shown by this thesis. This has possible implications for their use in assisting reactions, as well as their possible function as catalysts. There is also a wealth of information that can be learned about the nature of matter from their unique size in relation to the molecular and bulk limits, information that is of important fundamental interest. Despite this, clusters have yet to be fully investigated and their properties exploited, but with each observation and experiment made that deficit is being eradicated.

9 Acknowledgements

This experiments reported within this thesis could not have performed without the assistance of the following people, whose contributions were always gratefully received. My gratitude to you all.

Dr Pat Langridge-Smith,	Primary Supervisor.
Dr Kenneth Lawley,	Secondary Supervisor.
Dr Scott McIndoe	Collaborator, University of Cambridge.
Dr Paul Dyson	Collaborator, University of York.
Dr Tony Jackson	ICI Wilton
Dr Mathias Witt	Bruker Daltoniks, Bremen.
Dr Ghokan Baykutt	Bruker Daltoniks, Bremen.
Miss Sally Shirran	University of Edinburgh MS facility

The People of The Exploratory Measurement Science Group
At The University of Edinburgh

Dr Adriana Dinca, Dr. Sandy Yates, Dr David Kilgour,
Dr. David Simpson, Dr Nick Polfer, Dr Logan Mackay

10 Courses And Conferences

Over the course of this post-graduate study, the following courses and conferences have been attended.

Courses

X-Ray Crystallography:

Mass Spectrometry:

Seminars

Royal Society Of Chemistry Lectures within the Department Of Chemistry

Physical Chemistry Weekly Seminars, requiring contributions per term.

Physical Chemistry Mini-Conference at Firbush, including Oral Presentations and Posters.

Conferences:

Annual Northern Meeting Of Chemical Physics, Liverpool 2001:

Oral Presentation: "Laser Desorption Ionisation: A Novel Route To Supraclusters".

British Mass Spectrometry Society Annual Conference, Southampton 2001:

Poster: "Studies Of Cluster Formation Using FT-ICR MS". Winner of the Barber-Bordoli Prize for Best Poster

Poster: "Ligand Stripping Dynamics In Transition Metal Clusters". Second Prize in Best Poster Competition.

American Society For Mass Spectrometry Annual Conference, Florida 2002:

Oral Presentation: "Analysing Transition Metal Carbonyl Clusters By Energy Dependent Electrospray Ionisation Mass Spectrometry".

Paper Contributions:

"On the use of breakdown graphs combined with energy-dependent mass spectrometry to provide a complete picture of fragmentation processes" Butcher,C.P.G.; Dyson,P.J.; Johnson,B.F.G.; Langridge-Smith,P.R.R.; McIndoe,J.S.; Whyte,C. Rapid Communications In Mass Spectrometry, **2003**, 16, (16), pp1595-1598.

"Combining energy-dependent electrospray ionisation with tandem mass spectrometry for the analysis of inorganic compounds" Dyson,P.J.; Hearley,A.K.; Johnson,B.F.G.; McIndoe,J.S.; Langridge-Smith,P.R.R.; Whyte,C. Rapid Communications In Mass Spectrometry, **2001**, 15, (12), pp895-897.